Control Strategies in an Islanded Microgrid with High Penetration of Renewables

Jiahui Jiang

B.E. (Elec.)(Hons. 1)

September 2020

A thesis submitted to embody the research carried out to fulfil the requirements for the degree of:

Doctor of Philosophy

in **Electrical Engineering**

at **The University of Newcastle**

Callaghan, NSW, 2308, Australia

Declaration

I hereby certify that the work embodied in the thesis is my own work, conducted under normal supervision. The thesis contains no material which has been accepted, or is being examined, for the award of any other degree or diploma in any university or other tertiary institution and, to the best of my knowledge and belief, contains no material previously published or written by another person, except where due reference has been made. I give consent to the final version of my thesis being made available worldwide when deposited in the University's Digital Repository, subject to the provisions of the Copyright Act 1968 and any approved embargo.

Jiahui Jiang

B.E. (Elec.)(Hons. 1)

September 2020

THE UNIVERSITY OF NEWCASTLE AUSTRALIA

Acknowledgements

The work presented in this thesis was undertaken during the author's Ph.D. candidature at the University of Newcastle, Australia in the School of Electrical Engineering and Computing.

I would firstly like to thank my parents for the unconditional love and support that was offered since the beginning of my Ph.D. It would not have been possible for me to start this journey without your encouragements. I would also like to thank my younger brother, Jiachang for your faith in me. Your thoughtfulness and humour has made my life much brighter.

I would like to acknowledge the support and guidance of my primary supervisor Doctor Colin Coates. Your wisdom, encouragement, patience, and kindness have not only made my Ph.D. journey meaningful and memorable, but also shown me the secrets of living a happy life.

I would also like to thank my co-supervisor Doctor Terrence Summers. The knowledge and network you provided was invaluable.

I would like to thank Professor Frede Blaabjerg and Doctor Saeed Peyghami for the academic visit opportunity at Aalborg University, Denmark. Your insights and support have helped me tremendously in understanding research and perfecting my Ph.D. project.

I would like to express my appreciation to Doctor David Harcombe and Doctor Kevin Sun for your expertise, talent and kindness. You are the colleagues and friends that I can always turn to for help. I would also like to thank electrical technicians, Ian, Roy and Jerry, for the assistance during the hardware setup.

To my gorgeous international friends, Zhaorong, Iryna and Bo, you have made Newcastle a lovely and memorable place.

Lastly, I am grateful to everyone that have accompanied me through this adventurous Ph.D. journey.

Contents

List of Figures

List of Tables

Abstract

This thesis presents the control and performance of a hybrid Microgrid (MG) which integrates photovoltaic (PV), battery and conventional sources. A hybrid MG offers advantages in improving system reliability, economic efficiency and renewable penetration level. For a MG with a high penetration level of PV, system requirements and constraints are different to traditional electric grid. In particular, traditional grid-following PV sources are expected to provide ancillary services, e.g. frequency regulation and voltage support. However, the intermittent, varying and uncertain nature of PV generation imposes challenges on its realization.

The coordination strategy for multiple parallel connected MG sources are presented, with the aim of improving renewable penetration level, system reliability while considering power characteristics of individual sources. In detail, an innovative real power sharing scheme is first proposed which prioritizes renewable power sources in power supply. Meanwhile, a decentralized implementation strategy is also investigated which enables "peer to peer' and "plug and play" functionalities. The issues in reactive power sharing are then reviewed and two new approaches for reactive power sharing are proposed to improve system reliability and applicability. The reactive power sharing accuracy is also improved by a new method and its performance relative to the established virtual impedance method is evaluated. Small-signal models for the proposed control strategies are established to evaluate the stability.

Simulation and experimental results are both presented that evaluate and validate the performance of the proposed control strategies. The results show that the proposed control techniques offer desired performance.

Nomenclature

$\Delta\omega$	Maximum alllowable grid frequency deviation, page 9
$\delta\omega$	Frequency deviation, page 47
$\delta\omega_{BAT}$	Frequency deviation value of a battery source, page 58
$\Delta\omega_{CVS}$	Frequency deviation range of CVS, page 43
$\delta\omega_{CVS}$	Frequency deviation value of a conventional source, page 58
$\Delta\omega_{ESS}$	Frequency deviation range of ESS, page 43
$\delta\omega_{PV}$	Frequency deviation value of a PV source, page 58
$\Delta\omega_{RES}$	Frequency deviation range of RES, page 43
δSOC	SOC range of constant voltage charging, page 37
ΔV	Voltage drop, page 121
δV	Voltage increment in modified Q-V droop, page 112
ΔV_{max}	Maximum alllowable grid voltage deviation, page 9
δV_{PV}	Increment of PV voltage reference, page 63
$\Delta^{+}\omega$	Maximum frequency deviation, page 47
$\Delta^{-}\omega$	Minimum frequency deviation, page 47
$\mathcal{P}(\theta)$	Park transformation matrix, page 49
ω	Angular frequency, page 8

ω_c	Cut off angular frequency of digital LPF in power management, page 49
ω_0	Angular frequency set point, page 8
ϕ	phase angle across the coupling inductor, page 7
$\Re\omega_{CVS}$	Frequency region of CVS, page 43
$\Re\omega_{ESS}$	Frequency region of ESS, page 43
$\Re\omega_{RES}$	Frequency region of RES, page 43
τ_{dc}	Time constant of DC bus voltage regulation, page 34
C_{bat}	Battery capacity, page 38
D_i	Accumulated thermal damage of ith VSI, page 105
E	LC filter output voltage magnitude, page 8
E_0	Inverter voltage set point, page 8
E_{ref}	Voltage magnitude reference in droop control, page 122
f_c	Cut off frequency of LC filter, page 33
f_g	Grid frequency, page 33
f_{nom}	Nominal grid frequency , page 54
f_{sw}	Switching frequency, page 33
I_o	Output current after the LC filter, page 48
I_r	Solar irradiance, page 35
I_{bat}	Battery discharging current, page 38
m	Droop coefficient of real power, page 8
n	Droop coefficient of reactive power, page 8
P	Real power, page 7

P_B	Power generation from battery source, page 40
P_C	Power generation from conventional source, page 40
P_L	Real power demand, page 40
P_0	Real power set point, page 8
P_{B-max}	Battery maximum discharging rate, page 38
P_{B0}	Manufacturer recommended discharging rate, page 37
P_{C-max}	Maximum conventional power generation, page 43
P_{ch}	Battery reference chaging rate, page 37
P_{max}	Upper power limit, page 47
P_{min}	Lower power limit, page 47
P_{nom}	Nominal real power, page 8
P_{PV-MPP}	Maximum PV generation, page 15
P_{PV-nom}	Nominal PV power generation, page 45
P_{PV}	PV power output, page 35
Q	Reactive power, page 7
Q_L	Reative power demand, page 80
Q_0	Reactive power set point, page 8
Q_{nom}	Nominal reactive power, page 9
S_i	Apparent power rating of the VSI, page 20
SOC_0	Initial SOC level, page 38
SOC_{low}	SOC lower threshold, page 38
SOC_{ref}	SOC reference value after constant current charging, page 37

T_a	Ambient temperature, page 20
T_j	Junction temperature, page 20
V_g	Grid voltage, page 120
V_o	Output voltage after the LC filter, page 48
V_{dcref}	DC bus voltage reference value, page 34
V_{dc}	DC bus voltage, page 14
V_{g-est}	Estimated grid voltage, page 122
$V_{i,ref}$	Voltage reference for the inverter, page 10
V_{MPP}	Voltage at the maximum power point, page 35
V_{nom}	Nominal grid three-phase voltage, page 54
V_{PV}	PV output voltage, page 35
V_{ref}	LC filter output voltage reference, page 116
X_{est}	Estimated coupling reactance, page 126
Z_c	Coupling impedance, page 119
Z_o	VSI output impedance, page 117
Z_v	Virtual impedance, page 22
Z_{est}	Estimated coupling impedance, page 124
AGC	Automatic Generation Control, page 18
CC	Constant Current, page 37
CERTS	the Consortium for Electric Reliability Technology Solutions, page 2
CHP	Combined Heat and Power, page 2
CV	Constant Voltage, page 37

CVS	Conventional Sources, page 13
DAPI	Distributed Averaging PI, page 19
DG	Distributed Generation, page 1
EMS	Energy Management System, page 4
ESS	Energy Storage Systems, page 15
IC	Incremental Conductance, page 64
ICtrl	Current Control, page 10
IGBT	Insulated Gate Bipolar Transistor, page 30
LPF	Low Pass Filter, page 48
MCU	Microcontroller, page 90
MG	Microgrid, page 1
MPC	Model Predictive Control, page 12
MPP	Maximum Power Point, page 35
MPPT	Maximum Power Point Tracking, page 5
P&O	Perturb and Observe, page 64
PCC	Point of common coupling, page 21
PCM	Power control mode, page 5
PCtrl	Power Control, page 10
PLL	Phase Locked Loop, page 11
PV	Photovoltaic, page 13
PWM	Pulse Width Modulation, page 10
RE	Renewable Energy, page 1

RES	Renewable Energy Sources, page 1
SOC	State of Charge, page 16
TI	Texas Instruments, page 90
VCM	Voltage control mode, page 6
VCtrl	Voltage Control, page 11
VDC	Voltage Drop Compensation, page 104
VSI	Voltage Source Inverter, page 4

Chapter 1

Introduction

Due to the increasing demand for electricity, depleting fossil fuel reserves and catastrophic impacts of climate change, there is urgent need to integrate more Renewable Energy Sources (RES) into the electric grid. This chapter discusses the concept of a Microgrid (MG) which enables a high penetration level of Renewable Energy (RE). The MG control strategy is critical to the success of RE integration. MG control is generally hierarchical in structure with primary, secondary and tertiary levels of control. This chapter reviews the power management strategies in a MG with a particular focus on the primary control. In addition, the challenges during the integration of RE are also discussed and existing solutions reviewed. Finally, the objectives and outlines of this thesis are given.

1.1 Background

1.1.1 Microgrid and Hierarchical Control

The microgrid concept allows for more RES or Distributed Generation (DG) units to be integrated into the grid. This has the potential to improve energy efficiency, grid reliability, power quality and reduce carbon emissions. Global electricity demand has consistently increased in recent decades and is expected to remain on this trajectory [4]. This trend asks for alternative sources of energy rather than continued reliance on depleting fossil fuel reserves. Climate change has also driven people's attention to RES.

The traditional centralized electric network is suffering issues in many aspects: aging infrastructure and facilities, low energy efficiency, low reliability and power quality [5, 6]. A large amount of RE integration will severely impact the condition of the existing electric grid because of the intermittent and uncertain nature of RE generation. Thus. the RE integration level achievable in the traditional grid is limited. The MG provides a framework to raise the RE penetration level.

There are many definitions of the MG featuring different functionalities [7–9]. The concept of MG proposed by the Consortium for Electric Reliability Technology Solutions (CERTS) provides an early picture [7]. It summarizes some general features of a MG as:

(1) It behaves as a single, self-controlled entity to the surrounding distribution grid.

(2) It seamlessly separates from the grid when faults occur and reconnects once they are resolved.

(3) DG units in the MG are "peer to peer". There are no such components as master controllers or central generation units. The system can continue to operate with the loss of any unit, under the principle of $N + 1$ redundancy.

(4) DG units are featured with "plug and play". They provide a unified dynamic performance with a local controller. This enables any unit to be placed at any point of the grid without re-engineering.

(5) Combined Heat and Power (CHP) process is highlighted, which means utilizing the waste heat during the process of primary fuel combustion. This significantly improves energy efficiency.

These features provide MGs with some advantages. As the MG regulates DG units internally, it can connect to the main grid without introducing great disturbances. This enables the grid to integrate a higher level of RE. In addition, the MG can operate autonomously in islanded mode. It disconnects from the grid under some special events: grid faults, over-voltages or outages of the bulk supply [10]. This action protects the critical load in a MG from power outages or voltage distortions. It improves the grid reliability and power quality. Last but not least, transmission line losses can be reduced across the power system as the MG locates generation geographically close to loads, so that energy loss in transmission systems is saved. All of these benefits, provided by a MG network, rely on stable and proper internal control strategies.

As the generation units and load are distributed geographically, a MG in common-bus topology is most commonly discussed. Multiple DG units connect to a common bus in parallel, as shown in Figure 1.1. The benefits of a MG can be achieved by a hierarchical control mechanism, as shown in Figure 1.2 [11]. The control strategy interacts with power electronics, power generation units and loads to achieve secure and reliable power supply. Each higher level controller distributes reference values to its lower level controller in a supervisory fashion. The controllers on each level realize different objectives with different time constants.

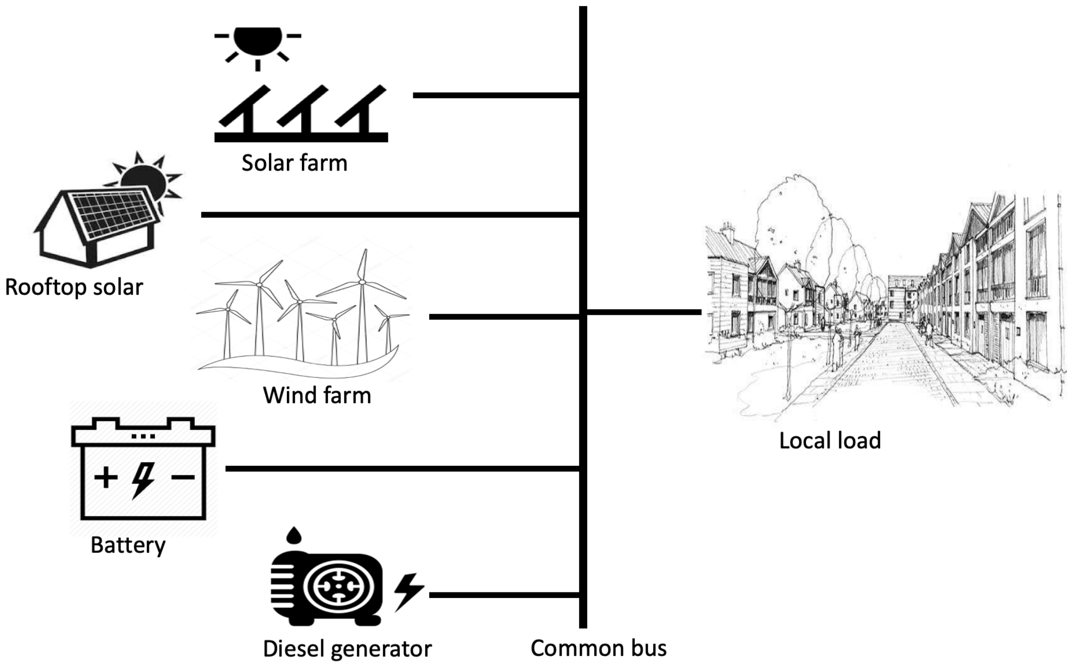

Figure 1.1: Topology of a common-bus MG

The primary control is responsible for instantaneous load-generation balance in a decentralized manner. The controller is located in each source and operates autonomously based on local information. In a synchronous generator, the governor controller regulates the grid frequency and voltage magnitude so as to maintain system stability. In an electronics-based power source, the generation unit interfaces with the grid through a Voltage Source Inverter (VSI), which can also regulate output voltage magnitude and phase angle. Because no inter-unit communication or a central controller is needed, it significantly improves the grid reliability and response speed. The time frame of this control level is in the order of seconds [9]. The secondary control aims to achieve an optimal power sharing pattern, to compensate for voltage/frequency deviation, and to synchronize the MG with the main grid before connection [11–13]. It adjusts power reference values provided by the tertiary control after processing the information collected from all DG units and the system loading condition. It responds at a slow speed, with a time interval of around 5 min. The tertiary control implements an Energy Management System (EMS) which realizes load forecasting, power generation prediction, unit commitment, demand side management and market participation [8]. The response time interval is at a 30-min level. A communication system is necessary for the hierarchical control and the bandwidth decreases at the higher levels of control, as shown in Figure 1.3.

The primary level control interacts with the power sources directly. It is thus critical to system stability especially in islanded systems when the support from main grid is absent. The following discussion mainly focuses on MG primary control.

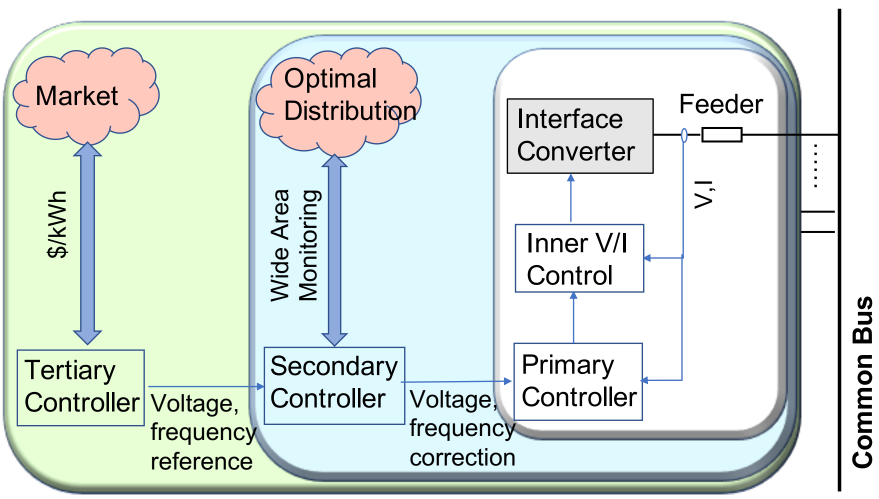

Figure 1.2: Structure of MG hierarchical control

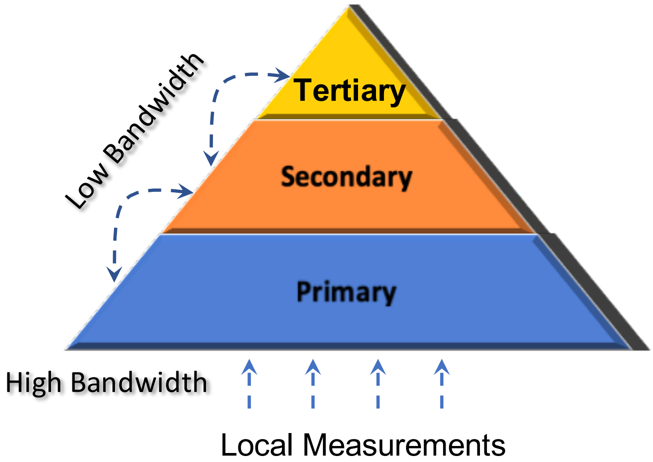

Figure 1.3: Bandwidth in hierarchical control

1.1.2 Microgrid Power Management

Power management in an autonomous MG is different from that in a grid-connected MG. If a MG is supported by the main grid, the power distribution within the MG can be determined by an optimization algorithm with great flexibility. The secondary level control can adopt a multi-objective power management algorithm, with the aim of minimizing economic cost, reducing greenhouse gases emissions, increasing power efficiency, while considering fluctuating power generation [8,14–19]. The power references generated at the secondary level are distributed to the dispatchable DG units through a communication network. Upon receiving reference values, the DG units regulate their power output at primary level. As for undispatchable power sources, e.g. RES, they operate in Maximum Power Point Tracking (MPPT) mode at primary level. All the DG units in a grid-connected MG operate as grid-following units as they operate in Power Control Mode (PCM).

In an islanded MG, the total power generation must match local power consumption for system stability. If the local power generation is sufficient to support the local load, an islanded MG provides some advantages, e.g. no transmission line losses, high energy efficiency, high reliability, environmentally friendly and so on. Islanded MGs also have a great potential in housing estates, industrial parks and remote communities. However, their power management strategies should not only consider cost efficiency and environmental impacts but also grid voltage/frequency regulation and stability issues. Some of the DG units in an islanded MG should be able to regulate grid voltage/frequency in Voltage Control Mode (VCM) effectively operating as grid-forming units. Other interfaced DG units can operate either in VCM or PCM, depending on the power management strategy.

Master-Slave control has been proposed to coordinate grid-forming units and grid-following units in an islanded MG [10]. The grid-forming unit is called the master unit and the grid-following units are defined as slaves. The master can be formed by one single source or multiple DG units which can be selected dynamically [20]. The power reference values for slaves are from either a supervisory controller or from the controller in the master unit [21]. While the master unit regulates the grid and maintains power balance, the slaves are responsible for power quality and energy efficiency of the MG. These power management strategies rely on extensive communication links to collect local information and distribute power references to DG units. They also rely on a supervisory controller or a master unit. These requirements reduce the system reliability by being exposed to communication interruption, cyber-attacks, single-point-failures, etc.

Alternatively, droop control has been widely discussed in an electronics-based MG for power management and grid regulation. Imitating the synchronous generator, droop control is firstly proposed to manage paralleled inverters in [22]. The droop-controlled units share the total power demand proportionally to the interfaced VSI ratings [23–25]. The detailed principle of droop control and proportional power sharing are demonstrated as follows.

The inverter generates an output voltage: $E\angle\phi$. It is coupled to the common bus through a series impedance $Z\angle\theta = R + jX$, shown in Figure 1.4. The voltage at the common bus is defined as the grid voltage represented as $V\angle 0^o$. The power supplied by the inverter can then be represented as:

$$
\begin{aligned}
P &= \frac{E^2}{Z} cos\theta - \frac{EV}{Z} cos(\theta + \phi) \\
Q &= \frac{E^2}{Z} sin\theta - \frac{EV}{Z} sin(\theta + \phi)
\end{aligned}
$$

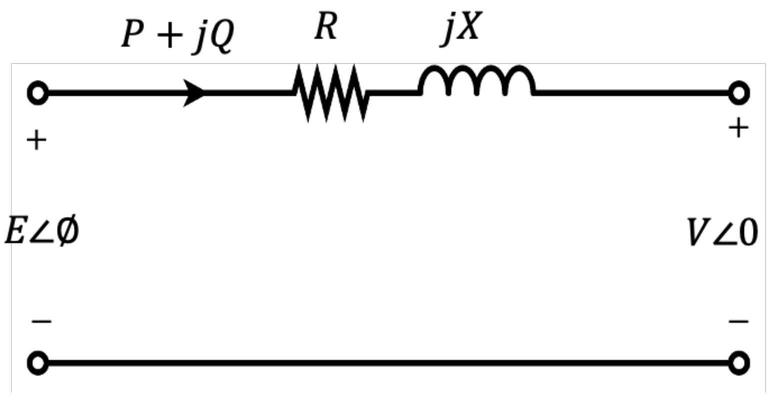

Figure 1.4: Diagram of the VSI coupling network

The coupling impedance normally consists of the VSI output impedance and the line impedance. The LC filter after the VSI combined with the regulation loop makes the VSI output impedance predominantly inductive (details in Chapter 5). In addition, the relatively short feeder lengths in MGs makes the line impedance much smaller than the inverter output impedance [23]. It is thus reasonable to assume that the coupling network is predominantly inductive. Consequently, the network impedance phase angle is $\theta \approx 90°$, and the real power (P) and reactive power (Q) equations can thus be simplified as:

$$P = \frac{EV}{X} sin\phi \tag{1.1}$$

$$Q = \frac{E^2 - EVcos\phi}{X} \tag{1.2}$$

The phase angle across the coupling inductor ϕ is kept small to allow a largely linear relationship with real power. The value of ϕ should be large enough that the power control is not too sensitive to its value. Considering these requirements, X is normally sized to guarantee ϕ smaller than 10°, indicating $sin\phi \approx \phi$ and $cos\phi \approx 1$. As a result, we can see from the following equations that real power depends heavily on phase angle (ϕ) while reactive power depends heavily on voltage difference ($E - V$).

$$P \approx \frac{EV\phi}{X} \tag{1.3}$$

$$Q \approx \frac{E(E - V)}{X} \tag{1.4}$$

Typical droop control equations can be expressed as:

$$\omega = \omega_0 - m\,(P - P_0) \tag{1.5}$$

$$E = E_0 - n\,(Q - Q_0) \tag{1.6}$$

where ω_0 and E_0 are set points for angular frequency and voltage magnitude respectively; P_0 and Q_0 are set points for real and reactive power of the unit; m and n are corresponding real and reactive droop coefficients.

Imitating the synchronous generator, droop control allows a drop in frequency (ω) when real power output increases. This is reasonable as real power mainly depends on ϕ which is the integral of ω. The reason ω is chosen instead of ϕ is that an individual unit is not able to know the initial phase angle of other units, while ω is a common value within the system. The unit with a larger phase angle ϕ can share more power than the one with a smaller ϕ. As a result, power sharing among units can be achieved by adjusting ω, and effectively, ϕ. As for reactive power flow, a small mismatch in VSI output voltages will cause uneven distribution of reactive currents or even reactive current circulation amongst sources. It imposes the risk of overloading to the VSI. The voltage reference E is reduced when reactive power flow becomes more inductive. It increases as the reactive power becomes more capacitive. This principle minimizes the mismatch of reactive power sharing. Traditionally, we set the desired value of reactive power as zero for a unity power factor.

To realize proportional power sharing, the droop control for paralleled inverters should be appropriately designed, as shown in Figure 1.5. Assuming the sources share the same ω_0, E_0 and the same grid frequency and voltage at steady state, the power sharing pattern becomes

$$m_1(P_1 - P_{01}) = m_2(P_2 - P_{02}) = \cdots = m_i(P_i - P_{0i}) \tag{1.7}$$

$$n_1(Q_1 - Q_{01}) = n_2(Q_2 - Q_{02}) = \cdots = n_i(Q_i - Q_{0i}) \tag{1.8}$$

If the real power rating and reactive power rating for a VSI are represented by P_{nom} and

Q_{nom} respectively, proportional sharing among i number of units means:

$$\frac{P_1}{P_{nom1}} = \frac{P_2}{P_{nom2}} = \cdots = \frac{P_i}{P_{nomi}} \tag{1.9}$$

$$\frac{Q_1}{Q_{nom1}} = \frac{Q_2}{Q_{nom2}} = \cdots = \frac{Q_i}{Q_{nomi}} \tag{1.10}$$

If the power reference is chosen as the nominal value, i.e. $P_0 = P_{nom}$ and $Q_0 = Q_{nom}$, the selection of droop gains based on (1.11),(1.12) will achieve proportional power sharing.

$$m_1 P_{nom1} = m_2 P_{nom2} = \cdots = m_i P_{nomi} \tag{1.11}$$

$$n_1 Q_{nom1} = n_2 Q_{nom2} = \cdots = n_i Q_{nomi} \tag{1.12}$$

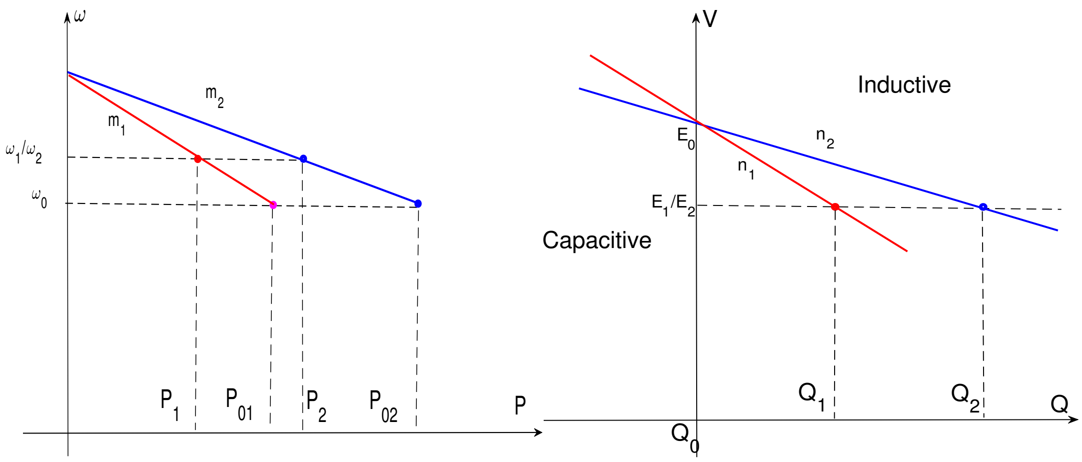

Figure 1.5: $P - \omega$ (left), $Q - V$ (right) droop curve

The selection of droop coefficients should also assure that grid frequency/voltage specifications, according to grid codes, are met. In practice, combined with (1.11) and (1.12), the droop coefficients can usually be decided by the following principle:

$$m = \frac{\Delta\omega_{max}}{P_{nom}} \tag{1.13}$$

$$n = \frac{\Delta V_{max}}{Q_{nom}} \tag{1.14}$$

where $\Delta\omega_{max}$, ΔV_{max} are the maximum allowed deviations of frequency and voltage magnitude.

Under this power management strategy, when there is an increase of power demand, the unit with the smaller droop slope would share a higher portion of the additional load. The advantage of droop control is that only local information is required. By avoiding inter-unit communication, the system is easily expanded without re-engineering which realizes “plug and play” functionality. The droop-controlled units can regulate grid voltage/frequency cooperatively in “peer to peer” manner. They do not necessarily rely on a master unit, which greatly improves the grid reliability. In addition, these grid-forming units coordinate with each other in order to track the power demand of the whole MG.

1.1.3 Control Strategies for Voltage Source Inverters

In VSI-based MGs, the discussed power management strategies can be realized by regulating the interfaced VSIs. A VSI operates either in PCM as a grid-following unit or in VCM as a grid-forming unit. The fundamental control methods, in both modes, will be utilised in this thesis and are introduced here.

1.1.3.1 Power Control Mode

If a primary controller aims to regulate the power flow of the controlled source to a reference value, the corresponding VSI operates in PCM. The control loop for PCM is shown in Figure 1.6, where P_{ref}, Q_{ref} represent real power and reactive power references, respectively. In the power regulator, the Power Control (PCtrl) regulates the power flow to the reference value and it generates the current reference. The Current Control (ICtrl) then regulates the output current to the reference value and generates a voltage reference for the inverter, $V_{i,ref}$. It is realized by Pulse Width Modulation (PWM). The PCtrl is the outer control loop while the ICtrl is the inner control loop. The phase angle ϕ is

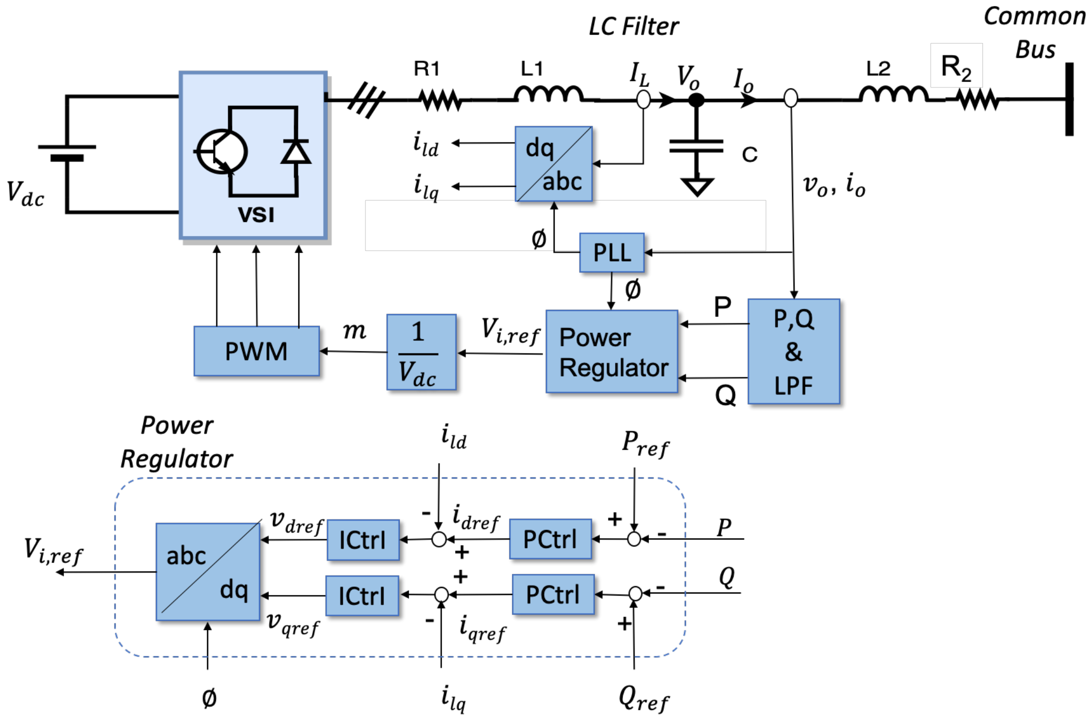

Figure 1.6: Control loop for VSI in PCM

obtained from Phase Locked Loop (PLL), which is to synchronize the VSI to the grid.

1.1.3.2 Voltage Control Mode

If the power source provides ancillary services, e.g. voltage support, frequency regulation, the interfaced VSI operates in VCM. Its control diagram is shown in Figure 1.7. The voltage and frequency references can be generated from droop control and then fed into the voltage regulator. The voltage regulator tracks voltage reference commands and produces an inverter voltage reference for PWM. Many control principles have been reported for voltage regulation: repetitive control [26], hysteresis regulation [27], predictive control [28] and feedback control [29, 30]. Particularly, feedback control is widely used due to its simplicity and ease of implementation. There are two types of voltage regulator: single-loop and double-loop.

In single-loop control, the Voltage Control (VCtrl) loop regulates the LC filter output voltage to the reference value with zero error at steady state, as shown in Figure 1.8. The output of the VCtrl is the inverter input reference voltage. Single-loop control has

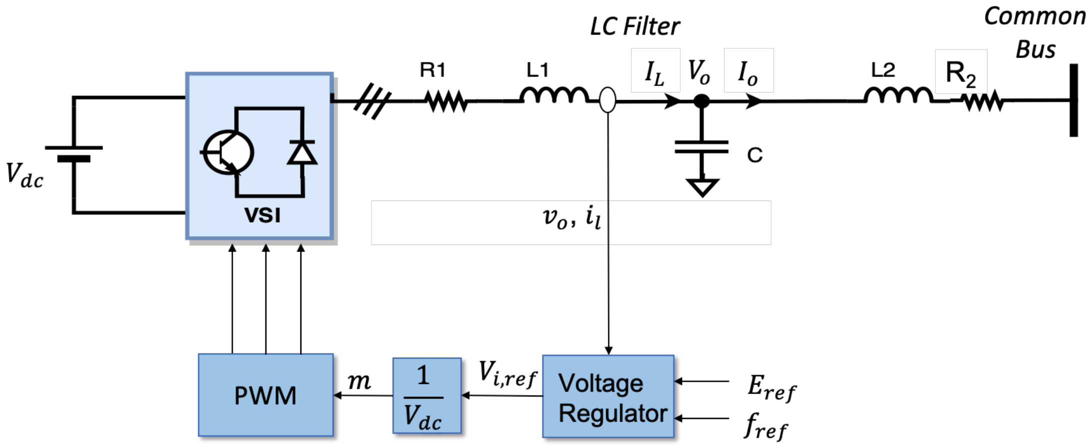

Figure 1.7: Control loop for VSI in VCM

reduced the controller's sensitivity to impedance-related stability [31]. Double-loop is usually composed of inner Current Control (ICtrl) loop and outer voltage control loop, as shown in Figure 1.9. In the outer loop, the LC filter output voltage and frequency are regulated under VCM. Its output provides a current reference value to the inner ICtrl loop. The output of ICtrl loop provides the inverter reference voltage. The outer voltage loop ensures the steady state reference tracking and the inner loop provides superior dynamic response to disturbances [32,33]. Moreover, the inner current loop has inherent current limiting capability.

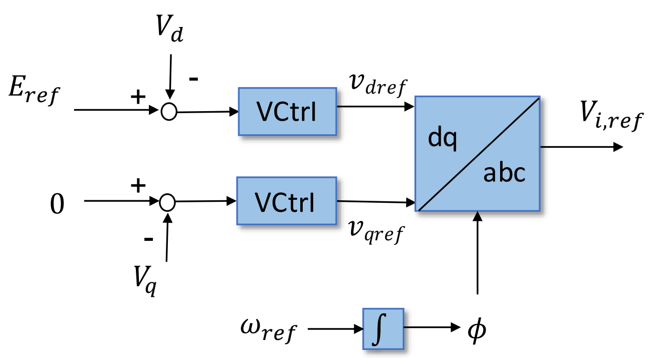

Figure 1.8: Single-loop structure of VSI voltage regulator

Recently, Model Predictive Control (MPC) has attracted much attention in inverter applications. MPC predicts the system future behaviour based on a discrete model and a proper cost function. In hierarchically organized loop control, the transient response

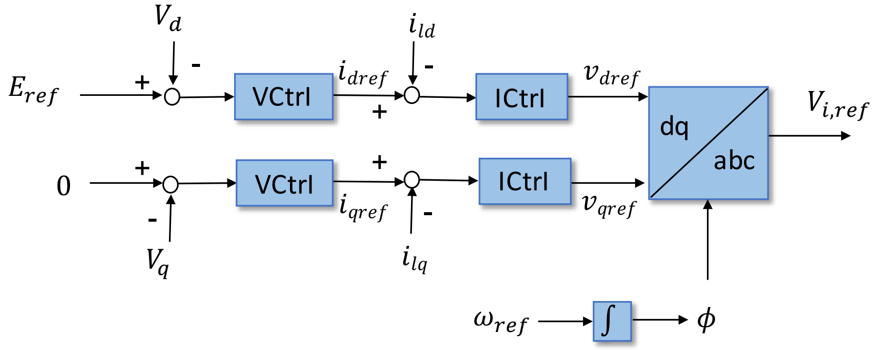

Figure 1.9: Double-loop structure of VSI voltage regulator

speed is limited because the bandwidth of the outer loop is approximately an order of magnitude smaller than the inner one. MPC is adopted to mitigate this problem [34,35]. It provides a rapid response and distributed operation. However, the drawbacks of MPC are that it requires high computation capacity and the cost function is hard to determine.

1.2 Challenges and State of the Art in Photovoltaic Integration

In this thesis, Conventional Sources (CVS) are considered as those where power can be dispatched on demand (e.g. diesel generator, micro-turbine). Compared to conventional sources, renewable sources pose some challenges to maintain grid stability. Because RES interface with the grid through power electronics, the system inertia is reduced. The intermittent, uncertain and fluctuating nature of RE generation results in serious grid frequency fluctuation and DC bus voltage deviation [36–38]. In a MG, there are more challenges during the integration of RES. According to International Energy Agency, solar Photovoltaic (PV) cost is consistently decreasing and below new coal- or gas fired power plants in most countries [4]. It also suggests that solar is the main driver of growth in renewable deployment for electricity. This thesis particularly focuses on PV integration. Note that the discussed strategies also apply to other RES.

Traditionally, PV sources operate in MPPT mode as grid-following units. In a modern power system, PV sources comprise an increasing portion of total power supply, they are expected to provide some ancillary services, e.g. voltage support and frequency regulation. It requires PV sources to track the load power demand when necessary rather than to continuously output maximum available power. Consequently, PV sources should be able to operate as grid-forming units in VCM. As droop control enables grid-forming functionality, it is of great interest to apply droop control to PV sources. Traditional droop control assumes an ideal source is present that can supply sufficient dispatchable power. However, PV sources provide limited and non-dispatchable power. This section discusses these challenges from different perspectives.

1.2.1 Overloading Issues

In this context, an overload issue refers to the situation when a VSI attempts to supply more power into the grid than is available from the associated RES. As traditional droop control shares power demand proportionally to the VSI rating, it overlooks the actual available RE generation which varies with weather conditions. After an increase in load demand or a reduction in source supply (e.g. a cloud passing over solar panels), the droop-controlled VSI may require more power than the source can supply. This mismatch between power generation and consumption will cause the DC bus voltage (V_{dc}) to drop, which may drive the system unstable.

If solar panels directly connect to the VSI, overloading issues may drive the PV output voltage below the stability boundary (reasons are explained in Chapter 2). The strategies proposed in [39, 40] integrate MPPT and V_{dc} regulation to the traditional droop control. The maximum PV power output can be realized after a power disturbance and the additional power demand is supported by other existing sources. Dynamic droop coefficients are also proposed in [41, 42]. While [41] proposes S-shaped droop control, the strategy in [42] adjusts $P - \omega$ droop coefficient based on

$$m = \frac{\Delta\omega}{P_{PV-MPP}} \tag{1.15}$$

where $\Delta\omega$ is the allowed frequency deviation range based on grid codes and P_{PV-MPP}

is the predicted maximum available power.

The above strategies require knowledge of the maximum power generation of PV sources, i.e. P_{PV-MPP}. The value of P_{PV-MPP} can only be predicted by an appropriate model of PV arrays and proper measurements of surrounding weather conditions. It is not cost effective to install solar irradiance sensors on every PV system, especially on rooftop PV. As a result, the value of P_{PV-MPP} should not be treated as a priori knowledge in most cases and neither is it a constant value under varying weather conditions.

In order to avoid using P_{PV-MPP}, MPPT and droop control is cooperatively managed in a two-stage PV source according to [43, 44]. The strategy switches control configuration between MPPT and the proposed universal controller which integrates the MPPT function into a droop controller. It can effectively solve the overloading issue but introduces another stability issue due to the transients during configuration switching. The enhanced dual droop control scheme proposed in [45] avoids this issue. If PV sources interface through a DC/DC converter, the traditional $P-\omega$ characteristic is modified to

$$\omega = \omega_0 - m(P - P_0) + k(V_{dc} - V_{dcref}) \tag{1.16}$$

where the term $k(V_{dc} - V_{dcref})$ has an upper limit of zero. This second droop term ensures the frequency of PV source drop when it is overloaded such that other sources pick up the additional load. It needs to be noted that this strategy only focuses on the control of the VSI but the operation of the intermediate DC/DC converter has not been specified.

1.2.2 Cooperation with Energy Storage Systems

Since RES cannot support a power system independently, they are usually equipped with Energy Storage Systems (ESS). One advantage of ESS is the fast response provided by the generation unit under primary control. ESS can connect to the grid in parallel to RES. Alternatively, it can connect to the DC bus in a renewable power source so as to compose a hybrid unit. The advantage of separate operation is that the ESS can serve multiple RES with lower cost. It, however, requires challenging control strategies as the ESS interact with the AC grid directly. The system operation should adapt to the status of ESS, e.g. the State of Charge (SOC), which is hard to be realized without inter-unit communications. Under the hybrid structure, RES is more friendly to the grid as it can provide a unified dynamic performance with the help of ESS [46]. It also makes the SOC level accessible to RES locally. However, the requirement of more ESS leads to high initial cost.

Scale and application are two main considerations when choosing the type of ESS. Pumped hydro or compressed air energy storage is location specific so they are not common options in MGs. Short-term storage devices, like super-capacitors, have high power density and also offer fast dynamics. However, their low energy density prevent them providing long-term power support [47]. High speed flywheels offer both high energy density and power density but with a high price [48]. Alternatively, batteries have high energy density and also desirable power density. In general, batteries are more preferable in MG applications in terms of their relatively fast response, low cost, flexible capacity and portability.

Batteries are usually equipped with their own power management system to regulate charging procedure. Meanwhile, their discharging rates should also be maintained below the suggested maximum value. The details of battery management are discussed in Chapter 2. These characteristics also restrict battery power output. As a result, the application of droop control to batteries is also worth studying. Moreover, the coordination of PV and battery sources in a droop-controlled MG is more challenging.

In [49] [50], PV and battery sources can seamlessly switch their operation modes between VCM and PCM under smooth switching droop control and frequency bus-signaling strategy. The switching is realized by varying the droop coefficient as:

$$m = m_p + m_d s + MD \cdot \frac{m_i}{s}, \quad MD \in [0, 1] \tag{1.17}$$

where m_p, m_i and m_d are the parameters of PID controller for power regulation. $MD = 0$ means the unit operating under VCM while $MD = 1$ means PCM. The selection of MD value is based on both frequency value and SOC of the battery. There are four possible modes in the system. The PV sources switch from PCM to VCM when the batteries are fully charged and meanwhile, the batteries switch from VCM to PCM. Conversely, when the power consumption is larger than PV generation, PV sources switch from VCM to PCM and batteries switch from PCM to VCM to discharge power. This strategy can effectively deal with disturbances from load demand. However, it is not responsive to varying weather conditions because the frequency bus-signal only changes with varying loading condition.

The autonomous decentralized load sharing strategy presented in [2] overcomes the restriction of frequency-bus signaling. The multisegment adaptive $P - \omega$ curve is designed and it adapts to the dynamics of available PV power, loading conditions and SOC of the battery in real time. All the units can operate both in VCM and PCM and they switch their operating modes autonomously based on real-time power condition. PV power is the basic power supply while the battery only supports peak load demand. The droop controlled units help to balance power. The weakness of this strategy is that it is not suitable to the grid with multiple PV units or batteries. However, it provides a new perspective in MG load sharing which is to prioritize the PV unit in power supply. As an improvement, a modified droop control is applied to parallel connected PV units and batteries in [51]. It is worth noting that the controller of PV units requires the information of battery conditions so the battery and PV is structured as a hybrid unit. Alternatively, [52] deals with parallel connected PV units and batteries with sophisticated multi loop control structure. However, the battery is in single-stage form which presents less flexibility in operation.

1.2.3 Frequency Restoration

As a result of primary droop control, the steady state frequency of an islanded MG deviates from the nominal value and the deviation depends on the load level as well as droop settings. Moreover, power disturbances from load or RE generation will introduce frequency fluctuation. In order to make the frequency less sensitive to power disturbances, and restored to the nominal value, a frequency restoration strategy needs to be incorporated into MG control.

Traditionally, in large power plants, the frequency control is carried out by Automatic

Generation Control (AGC) through two levels [53]. The primary level control is a local proportional controller and it produces a static error of local frequency (ω_i). In consequence, a central integral controller is needed at the secondary level to eliminate this error, which is shown below

$$\dot{\hat{\omega}} = b(\omega_{ref} - \frac{1}{n}\sum_{i=1}^{n}\omega_i) \tag{1.18}$$

where $\hat{\omega}$ is the frequency reference for the primary level control; ω_{ref} is the grid frequency reference; b is the integral gain. This central controller collects frequency measurements from all units in the network and distributes the output back to every local controller.

This strategy has also been adopted in electronics-based MGs. It requires two-way communication links between the central controller and every individual unit. In addition, the central controller requires a large computation capacity and the system is less reliable as it may suffer from single-point failures. To avoid a central controller, a distributed approach is proposed in [54]. However, every single unit asks for information from all the other units in order to calculate an average frequency value. It requires an even more complex communication network which means the strategy is not fully distributed. As a result, a fully distributed or decentralized secondary strategy without heavy communication has been investigated.

To clarify the definition, fully distributed control means the controller needs a communication network by which the individual unit can access information from its neighbouring units. On the other hand, decentralized control means no communication is needed and the control is conducted based on local information.

Decentralized PI control on secondary level can be adopted to restore frequency in MGs [55–57]. A low pass filter (with a time constant of T_{fres}) can be adopted to achieve time-scale separation between this secondary control and primary control, represented in (1.19). It prevents the frequency restoration process from interfering with primary control.

$$\delta\omega_{i-fres} = \frac{1}{T_{fres}s+1}(k_p + \frac{k_i}{s})(\omega_{ref} - \omega_i) \tag{1.19}$$

where $\delta\omega_{i-fres}$ is the frequency restoration term imposed to primary control in ith unit.

Since power sharing performance is dependent on the phase angle, the integration of frequency over the restoration period should remain the same for paralleled units. However, even with identical PI parameters, the integration terms can still be different. It can be attributed to many factors, e.g. different initial conditions, the connection/disconnection of a DG unit, load disturbances, measurement errors and different physical systems. As a consequence, a frequency restoration strategy without communication will introduce a risk of instability and a reduction in power sharing accuracy. Consequently, distributed frequency synchronization has been widely studied to solve this issue.

A Distributed Averaging PI (DAPI) controller collecting both local measurements and neighbour information is proposed in [58]. It can quickly regulate the network frequency under large and rapid power disturbances. The control variable u_i is generated to adjust the set point value P_{0i}:

$$P'_{0i} = P_{0i} + u_i \tag{1.20}$$

$$ki\ \dot{u}_i = \frac{1}{m_i}(\omega_{ref} - \omega_i) - \sum L_{c,ij}(m_i u_i - m_j u_j) \tag{1.21}$$

where the matrix $L_c \in \mathbb{R}$ is the Laplacian matrix corresponding to a weighted, undirected and connected communication graph. Some other methods based on consensus algorithm have also been studied in [59–61]. The advantage of these methods is that frequency can be restored with a high-bandwidth.

In summary, inter-unit communication is necessary to achieve accurate frequency restoration while maintaining accurate power sharing at primary level. Distributed strategy can achieve fast frequency restoration with a sparse communication network. In contrast, a totally decentralized restoration strategy can fulfill “plug and play” function of the MG by sacrificing power sharing accuracy. It is a result of de-synchronisation of integral terms among DG units.

1.2.4 Reactive Power Sharing Issues

For reactive sharing, most studies adopt droop control to distribute reactive power demand proportionally to VSI ratings [23, 62–64]. This principle aims to protect the VSI from overloading and reduces power losses by minimizing the possible circulating reactive current. However, due to the existing real power flow, the remaining VSI capacity for reactive power flow reduces [65, 66]. The limits of both real power and reactive power should be taken into account when designing power management and they can be defined as:

$$P_{i,max} = S_i \tag{1.22}$$

$$Q_{i,max} = min\{Q^C_{i,max}, Q^{PF}_{i,max}\} \tag{1.23}$$

where $Q^C_{i,max}$ and $Q^{PF}_{i,max}$ are maximum reactive power output limited by the VSI current rating and minimum power factor respectively. Their values are determined by the inverter's apparent power S_i, real power output P_i and minimum allowable power factor of the power source pf_{min}, and they are calculated based on the following equations:

$$Q^C_{i,max} = \sqrt{S_i^2 - P_i^2} \tag{1.24}$$

$$Q^{PF}_{i,max} = P_i \tan(\cos^{-1}(pf_{min})) \tag{1.25}$$

Droop control can effectively avoid overloading VSIs by considering their power capacity, but they cannot protect them from over-stressing. That is because the thermal stress on a converter depends on both its power loading as well as operational and environmental conditions [67, 68]. For example, ambient temperature (T_a) fluctuations will change junction temperature (T_j) of the critical components in a converter, and hence, affect their thermal damage. The over-stressing issue was explored in DC MGs by presenting a reliability-oriented power sharing strategy based on droop control [68]. It updates $P - \omega$ droop gains of the interfaced VSIs to shift real power from the high-stressed converters to the low stressed ones. In a RE-based MG, the intermittent nature of RE generation results in intermittent real power loading on the corresponding VSIs. Consequently, the thermal stresses on VSIs in RES may behave differently to VSIs in other interfaced sources. To balance thermal stresses, the $Q - V$ droop gains can be modified to shift reactive power flow, which will enhance overall system reliability.

Another concern on reactive power sharing is the inaccuracy issue based on traditional $Q-V$ droop control. This is because the voltage is not a global quantity as opposed to frequency in real power sharing. The voltage drop over line impedance has an impact on reactive power sharing [23, 62, 69, 70]. Methods on improving the accuracy of reactive power sharing in MG have been extensively studied.

An effective way to improve reactive power sharing is to increase $Q-V$ droop gain. The accuracy of power sharing can be improved according to the $Q-V$ characteristic. The drawback of this method is that it degrades the overall system stability and voltage regulation. Alternatively, a derivative loop is added to the conventional droop loop and the loop gain is attained by pole-placement technique to procure an adequate stability margin [71]. Also, the proposed $Q-V$ dot droop control is immune to the influence of mismatched feeder impedance [70, 72]. Injecting a small ac voltage signal also helps to accurately share reactive power since the signal frequency reduces as reactive power output increases [73]. Instead of regulating LC filter output voltage, regulating the grid voltage at Point of Common Coupling (PCC) was suggested in [23, 74]. This strategy essentially compensates for mismatched voltage drop. While [23] introduces integral control of the AC bus voltage, [74] employs a feedback loop with proportional control. However, the availability of grid voltage is critical in these methods. In a “plug and play” MG, high bandwidth communication links are not preferable.

As the inaccuracy issue originates from the mismatch of line impedances in paralleled units, the mismatch can be compensated by designing the coupling impedance. The feeder impedance can be estimated so that a specific control loop can be designed to compensate for the mismatch. Nevertheless, these methods are only applicable under some constraints, e.g. a requirement for a separate device, special numerical techniques, main grid availability [75, 76]. In a MG, the line impedance is normally a small value due to the short geographical distance between source and load. The total output impedance of an inverter can be essentially fixed by interfacing a relatively large impedance, so that the impact of the feeder impedance can be neglected. The concept of virtual impedance is thus proposed to imitate a physical impedance by modifying control algorithm [62], which is explained below.

Virtual impedance is realized by adding a feedback loop in voltage reference V_{ref} generation, which means:

$$V'_{ref} = V_{ref} - i_o Z_v \tag{1.26}$$

where i_o is the VSI output current and Z_v is the interfaced virtual impedance. For the purpose of improving reactive power sharing accuracy, a large Z_v can be incorporated, so that the impact of mismatched line impedance on reactive power sharing is attenuated

In [63,64,77], the virtual impedance can be designed into a flexible complex value and the droop control is modified based on the impedance phase angle. For example, to better share reactive power and harmonic power, the output impedance in [77] is designed to be proportional to unit ratings based on priori knowledge of feeder impedance. Moreover, [78] employed genetic algorithm to design optimized virtual impedance in networked MG for reactive power sharing, based on a thorough knowledge of network information (structure and feeder impedance). However, the requirement of a central controller or the knowledge of feeder impedance lessens the advantages of droop control.

Other studies try to realize accurate reactive power sharing at secondary level [10,12]. To avoid using a central controller or intensive communication-based control strategy, fully distributed control strategy has been studied. It only requires distributed communication between DG units based on consensus algorithms. A group of people proposed the following distributed voltage control u_i^V for an inverter at node $i \in N$:

$$u_i^V = V_i^* - k_i \int_0^t e_i(\tau) d\tau, \tag{1.27}$$

$$e_i = \sum_{k \sim C_i} \left(\frac{Q_i^m}{\lambda_i} - \frac{Q_k^m}{\lambda_k}\right) \tag{1.28}$$

where $V_i^* \in R_{>0}$ is the desired voltage amplitude and $k_i \in R_{>0}$ is a feedback gain. $\frac{Q_i^m}{\lambda_i}$ represents the per unit reactive power output and $\frac{Q_i^m}{\lambda_i} = \frac{Q_k^m}{\lambda_k}$ implies two units proportionally share reactive power. This study also provides a necessary and sufficient condition for local exponential stability [79]. Furthermore, [59] focuses on both voltage regulation and reactive power sharing. It highlights and clearly demonstrates a fundamental limitation of voltage control: precise voltage regulation and precise reactive power sharing are conflicting objectives. It proposes distributed averaging PI control to tune the compromise between voltage regulation and reactive power sharing.

Based on consensus algorithms, the value of virtual impedance can also be tuned to achieve accurate real power and reactive power sharing without knowing feeder impedance [80, 81].

1.3 Motivations and Objectives

On the journey of increasing RE penetration level in the electric network, there are some barriers. This thesis looks into these barriers and provides solutions from the perspective of the power-electronics control. This section lists the issues in RE integration and control objectives regarding each issue.

- The intermittent, uncertain and fluctuating RE generation makes RES undispatchable. A large amount of RE integration will lower power quality and grid stability. This thesis aims to achieve a high penetration level of RE in the grid with high reliability and power quality. While MG technology is equipped with these advantages, this thesis will investigate control strategies in the context of a MG.
- The characteristics of RE generation require back-up power supply in an islanded MG to maintain reliable power supply. Traditionally, the integrated ESS require a capacity equal or larger than the capacity of RES. This costly option limits the development of MGs. The restrictions imposed by the limited ESS need to be reconsidered. Additionally, minimizing fossil fuel usage is also one of the objectives. As a result, a power management approach coordinating different power sources in a MG needs to be designed.
- Traditional droop control is effective to share power supply from ideal DC sources. Utilizing traditional droop method in a RE-based MG will impose over-loading and over-stressing issues to interfaced power converters. This thesis will propose a power sharing strategy incorporating unique characteristics of individual power

sources based on traditional droop method. It aims to improve system reliability and stability.

- Inter-unit communications reduce the grid reliability by being exposed to cyber attacks. In addition, any strategy featuring a central controller or master units suffer from the potential of single-point failures. “Peer to peer” and “plug and play” is thus necessary in a MG for higher reliability and flexible integration of DG. This thesis will focus on decentralized MG primary control.

- There are some stability issues regarding the operation of RES and droop control: lack of inertia, fast dynamics in electronics-based system, limited and fluctuating power generation from RES and restricted droop coefficients in droop control. The stability analysis thus needs to be conducted.

1.4 Publications

In completing this thesis the following papers were presented and published.

1. “Voltage Collapse Issue in a Photovoltaic Source Operating in an Islanded Microgrid”, was published in the Australasian Universities Power Engineering Conference (AUPEC), Melbourne, Australia, November, 2017. This paper investigates the power characteristics of a PV source and identifies the unstable region of PV operation. The challenges of this possible voltage collapse issue are discussed and a control method is proposed. This observation leads to the discussions in Chapter 2.

2. “Droop Control Based Strategy for Photovoltaic Sources in an Islanded Microgrid”, was published in the Australasian Universities Power Engineering Conference (AUPEC), Auckland, New Zealand, November, 2018. The paper modifies a conventional control method, droop control, in order to be applied to power-electronics based PV power sources. The coordination of the DC/DC boost converter and DC/AC inverter is discussed, which can effectively adjust its power output. It forms the

first section of Chapter 3.

3. “Power Sharing Scheme for an Islanded Microgrid Including Renewables and Battery Storage”, was published in the IEEE 4th Southern Power Electronics Conference (SPEC), Singapore, December, 2018. This paper enables “peer to peer” and “plug and play” operation of a microgrid, which incorporates PV sources, batteries and conventional sources. The proposed power sharing strategy prioritizes renewable sources and improves renewable integration level of the grid, which is a summary of Chapter 2 and Chapter 3.

4. “Accurate Reactive Power Sharing in Renewable-Prioritized Islanded Microgrids”, was published in the 21st European Conference on Power Electronics and Applications (EPE’19 ECCE Europe), Genova, Italy, September, 2019. It aims to prioritize renewable sources in microgrid reactive power sharing based on modified droop control. In order to improve reactive power sharing accuracy, an interfacing inductor and grid voltage estimation strategy is used. This paper is the preliminary study of the second section of Chapter 5.

5. “A Decentralized Reliability-Enhanced Power Sharing Strategy for PV-Based Microgrids”, was published in the journal of IEEE Transactions on Power Electronics, November, 2020. This paper proposes a decentralized power sharing approach that restricts thermal damage of converter components to avoid over-stressing converters. The main goal is to improve overall system performance and reliability by appropriately sharing active and reactive power among different sources without using communication systems. It adopts the strategy proposed in the first section of Chapter 5, with the addition of extensive numerical simulations and analysis.

1.5 Thesis Outline

The remainder of this thesis is organised as follows:

- Chapter 2 discusses the unique power characteristics of PV and battery sources. Based on that, the RE-prioritized power sharing scheme is proposed for a hybrid MG, which gives RES the priority of power supply. The control implementation of the proposed scheme is based on droop control modification.

- Chapter 3 proposes the decentralized control strategies for PV sources and battery sources. It incorporates with the proposed modified droop control to achieve RE-prioritized power sharing scheme and at the same time, maintain stable operation of the source.

- Chapter 4 presents hardware experimental results which validate the proposed control strategies.

- Chapter 5 aims to improve reactive power sharing from different perspectives. A reliability-enhanced reactive power sharing strategy is proposed for system-level reliability improvement. Meanwhile, a RE-prioritized reactive power sharing strategy is also proposed which saves gen-sets operation time. Furthermore, the accuracy issue in reactive power sharing is discussed and an innovative compensation approach is proposed as opposed to traditional virtual impedance approach.

- Chapter 6 presents the modeling of PV and battery sources based on small-signal state space model. The stability analysis is evaluated for the proposed control strategies.

- Chapter 7 summarizes and highlights the main contributions in the thesis, and it also provides thoughts on future research work and directions.

Chapter 2

Renewable-Prioritized Real Power Sharing Strategy

One of the advantages of the MG topology is that it is capable of integrating various DG sources. As most of natural DG is from RES, power management in a MG with a high RE penetration level is attracting more and more attention. To maximize the RE penetration level, this thesis proposes a RE-prioritized power sharing strategy. It enables RES with grid-forming ability and gives them the priority in power supply. Since back-up energy sources are indispensable in RE-based MGs, RES also need to coordinate with other sources, e.g. ESS and CVS. This chapter introduces the concept of a hybrid MG and its topology is shown in Section 2.1. Under this context, the proposed power sharing strategy is demonstrated based on characteristics of power sources in Section 2.2. It is followed by the control implementation in Section 2.3. Last but not least, the simulation results are presented in Section 2.4.

2.1 Topology of a Hybrid Microgrid

A hybrid MG is defined as a MG incorporating a variety of power sources: RES, ESS and CVS. The proposed hybrid MG is shown in Figure 2.1. In this thesis, PV sources are used to represent the RES although the discussed methodology can be applied to other DC/AC interfacing converters when the connected power source has varying and limited generation. Although their front-end converters may vary, other renewable sources, e.g. wind power, tidal power, are also eligible candidates. Some modifications are normally necessary when applied to different sources since the characteristics of dynamic response and weather conditions may vary. Similarly, batteries are used to represent ESS but again the presented methodology could be extended to other types of ESS. The PV source is connected in the two-stage form: a unidirectional DC/DC boost converter coupled with a DC/AC VSI. The battery source is also connected in the two-stage form, through a bidirectional buck-boost converter coupled with a DC/AC VSI.

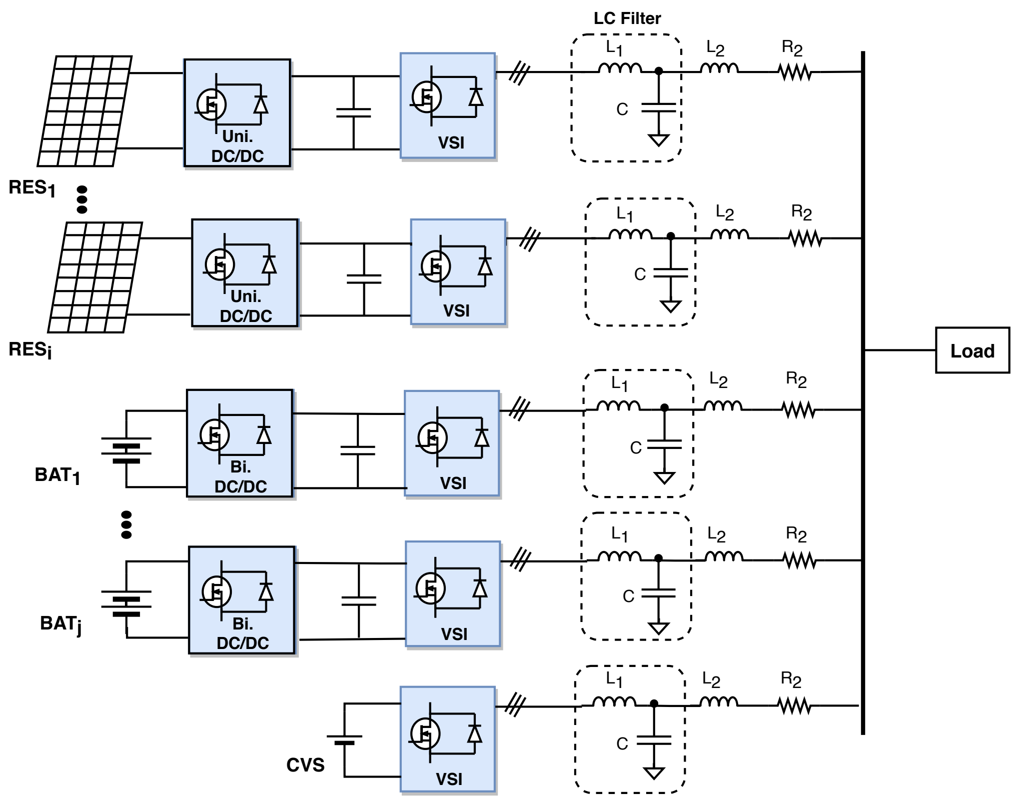

Figure 2.1: The hybrid microgrid system

A CVS is considered as a dispatchable fuel/gas powered source, most commonly in the form of a diesel generator or micro-turbine. A micro-turbine is normally connected to the grid through an inverter [82]. Conversely, diesel generators usually operate at lower speeds connecting to the grid through a rotating machine. This thesis' primary focus is on the coordinated operation of RES and ESS. Consequently, the CVS in this work is represented by an ideal DC voltage source interfaced through an inverter for simplicity. This assumption provides the CVS with unlimited capacity and faster dynamics than might otherwise be expected in the real source it is approximating. The investigation on coordinating power sources possessing significantly different dynamics is beyond the scope of this thesis. The inclusion of this dynamic behaviour could be readily included in future extensions of this work with the addition of control functionality that emulates source dynamics in the CVS inverter control. Some discussions on employing diesel generators in MGs can be found in [83–85].

At the output of each VSI, a LC filter is connected and its inductor and capacitor are represented as L_1 and C respectively. After that, each VSI connects to the common AC bus through a coupling impedance, L_2 & R_2.

2.1.1 Photovoltaic Sources

In wind power generation, wind turbines usually connect to the grid through a two-stage converter: front end AC/DC rectifier and DC/AC inverter. This topology decouples the fluctuating wind power from the main grid and gives flexibility to grid voltage regulation. On the other hand, for PV sources, there are two topologies: single-stage form and two-stage form.

In a PV source, DC power is produced from solar panels and then converted to AC by a DC/AC inverter. A DC link capacitor is connected at the input of the inverter and its voltage level should be maintained constant during steady state to maintain power balance. When there is an increase in load, additional energy is drawn from the capacitor instantaneously and V_{dc} drops as a result. Since the energy stored in the DC bus capacitor is relatively small, the DC bus voltage regulator should respond quickly to recover V_{dc}. In single-stage form, a VSI directly connects to solar panels through a DC capacitor, shown in Figure 2.2a. This structure is easy to implement and it achieves higher power conversion efficiency. Nevertheless, it requires a significant number of series connected solar panels to provide sufficient V_{dc}. This in turn increases the difficulty of tracking MPP in every individual panel. Additionally, the MPPT operation totally relies on VSI control. If a power disturbance occurs on the load side, there is poor transient performance on the grid due to the coupling between V_{dc} and PV power generation [44].

In contrast, the two-stage form consists of a front end DC/DC converter and a DC/AC

VSI, shown in Figure 2.2b. Due to the presence of blocking diodes, a boost converter is reported to perform better than other types of DC/DC converters [86]. DC/DC boost converter offers the flexibility to reduce the number of series connected solar panels. It can boost V_{dc} higher than the required peak AC voltage and the extra stored energy in the DC capacitor can decouple AC voltage from DC voltage. As a result, the transients after power disturbances can be improved. Meanwhile, a better performance in MPPT can be achieved [44]. However, it is undeniable that the power loss in the DC/DC converter reduces power efficiency of the two-stage form. A tradeoff between performance and efficiency has to be made when designing the system.

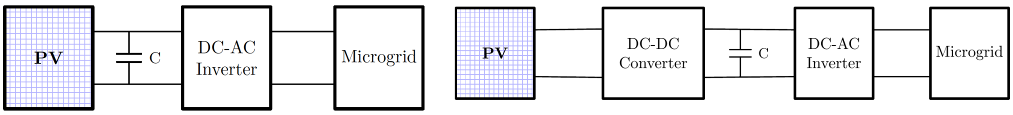

(a) Single-stage structure

(b) Two-stage structure

Figure 2.2: Topology of a PV source

Given the merits and drawbacks of the two PV source topologies, the two-stage form is preferred in the application of islanded MGs. To integrate solar energy into the MG, control strategies for both DC/DC boost converter and DC/AC VSI should be addressed. A basic boost converter topology is employed here, which is shown in Figure 2.3. There are four components of particular importance in the design of a boost converter: electronic switch, boost inductor L, output capacitor C_2 and blocking diode.

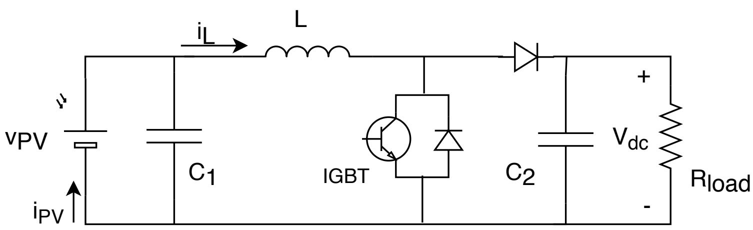

Figure 2.3: Topology of a DC/DC boost converter

An Insulated Gate Bipolar Transistors (IGBT) is most commonly used as the switch in medium- to high- power applications. It has a rapid turn on/off time so that it can synthesize complex waveforms with PWM. It is thus chosen in this application. Meanwhile, when selecting the diode, its ability to block the required off-state voltage, peak and average current limit, low reverse recovery and low forward voltage drop should be taken into account.

As for the selection of the inductor and output capacitor, maximum allowed current ripple and voltage ripple should be considered. Assuming the boost converter operates in continuous conduction mode, the inductor current never falls to zero and the minimum value of inductance L_{min} is derived, according to (2.1). Similarly, (2.2) gives the minimum capacitance value to get the desired output voltage ripple [87].

$$L_{min} = \frac{V_{PV}(V_{dc} - V_{PV})}{\Delta i_L f_{sw} V_{dc}} \tag{2.1}$$

$$C_{min} = \frac{V_{dc} D}{R f_{sw} \Delta V_{dc}} \tag{2.2}$$

where V_{PV} and V_{dc} represent the nominal input and output voltage respectively; f_{sw} is the switching frequency of IGBT; Δi_L is the acceptable inductor current ripple while ΔV_{dc} means the acceptable output voltage ripples. The input capacitor C_1 is selected during the PV control design. It helps to stabilize the PV output voltage. The detailed discussion can be found in Chapter 6.

2.1.2 Battery Sources

To allow more flexibility in DC bus voltage, a two-stage topology is also adopted in battery sources. The interfaced DC/DC converter is a bidirectional buck/boost converter whose topology is shown in Figure 2.4. When IGBT1 switches under PWM and IGBT2 is open, the converter operates under boost mode. Alternatively, when IGBT2 switches under PWM and IGBT1 is open, it operates under buck mode. The inputs $g1$ and $g2$ are the gate signals for IGBT1 and IGBT2 respectively. In buck mode, the inductor combined with the input capacitor C_1 operates as a low pass filter. Its cut off frequency needs to be significantly lower than switching frequency. On the other hand, the capacitor works as an energy storage in boost mode. The sizing of filter inductor and output capacitor follows the same principle as discussed in the PV source.

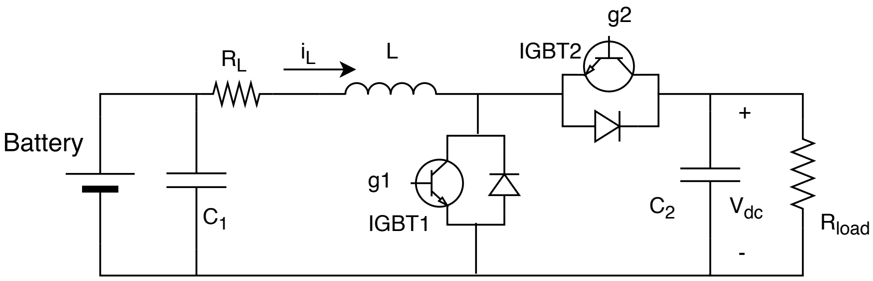

Figure 2.4: Topology of a buck/boost converter

2.1.3 LC Filter

PWM inverters are widely used in the applications of DG integration. As the IGBT in an inverter switch at a high frequency, there are high-frequency current and voltage ripples at the output of the inverter. Different configurations of passive filters are used to filter out the harmonics. First-order passive L-type filters are normally used to regulate the output AC current. It targets to attenuate the current ripples but is restricted to high-power low-switching-frequency applications due to the inevitable larger inductor size. Alternatively, second-order passive LC-type filters are widely used at the output of PWM inverters to attenuate the voltage ripples. In the design of a filter, the cut-off frequency needs to be specified while the filter size, the interfacing circuit and its impact on control bandwidth should also be considered [88].

In the proposed MG, the output voltage of the LC filter is controlled. Thus, an inverter coupled with its LC filter can be considered as an independently controlled voltage source. The LC-type filter only works effectively in circuits where the load impedance across the capacitor is relatively high at and above the switching frequency. The presence of coupling inductance between the filter output and the MG AC bus maintains a high level of load impedance, which guarantees an effective performance of the LC filter. It also performs as an LCL equivalent filter from the perspective of the grid [89]. The advantage of LCL-type filter is that it can extensively reduce output current ripples with relatively small inductors. It is also more immune to the variation of grid parameters. However, it is to be noted that the resonance frequency of LCL filter is different from that of LC filter. The design of LC filter should thus consider the value of coupling inductance.

As the phase angle difference between the inverter output and the MG bus should stay small for the sake of stability, we set 10^o as the upper limit. According to power transfer function $P = \frac{EVsin\delta}{X}$, the maximum value of coupling inductance can be derived. In the design of LC filter, the choice of cut-off frequency (f_c) is critical. It is usually chosen as 10 times lower than inverter switching frequency (f_{sw}) and specifically determined by (2.3).

$$f_c = \frac{1}{2\pi\sqrt{L_1 C}} \tag{2.3}$$

In addition, the resonance frequency of equivalent LCL filter (composed of the LC filter and the coupling inductor) should be considered. In LCL filter, L_1, L_2 represent the inverter side inductor and grid side inductor respectively, while C represents the filter conductor. The resonance frequency f_{res} and its normal range can be represented as below [90]:

$$f_{res} = \frac{1}{2\pi}\sqrt{\frac{L_1 + L_2}{L_1 L_2 C}} \tag{2.4}$$

$$10f_g < f_{res} < 0.5f_{sw} \tag{2.5}$$

where f_g is the nominal grid frequency. It is worth noting that the damping method of LCL filter is not considered in this thesis since the studied system simply connects to the RL type load through a coupling line. The resonance issue is not so critical provided that the resonance frequency is designed far from other critical values, i.e. control bandwidth and switching frequency. Once L_2 , f_c and f_{res} are reasonably determined, appropriate filter components L_1 and C can be derived. The detailed discussion of LCL damping methods can be found in other literatures [89].

2.1.4 DC Bus Voltage Level and Capacitor Size

At the input of a DC/AC inverter, a DC source should be connected. The high switching harmonics from PWM may cause current ripples on the DC bus voltage. A shunt DC capacitor can improve its steady state performance. It can also improve the transient when there is a power disturbance either from the grid or the power source. The larger the DC capacitor, the better the performance. A sensible DC capacitor should be selected considering both the size and economic efficiency.

The size of the DC capacitor is designed based on a time constant τ_{dc} which indicates the transient time the capacitor can endure during a disturbance. It is defined as the ratio of the stored energy in the capacitor over the inverter rating S_i [91]. As a result, the capacitor size can be chosen based on

$$C_{dc} \geq \frac{2\tau_{dc} S_i}{V_{dcref}^2} \tag{2.6}$$

where V_{dcref} is the nominal DC bus voltage. τ_{dc} is selected based on the specific application with a purpose of restricting voltage ripples, and 10 cycles of fundamental period is chosen as the minimum value in this thesis.

Meanwhile, the DC bus voltage should be maintained above a minimum value, in order to avoid over-modulation. That means:

$$V_{dc} \geq \frac{2\sqrt{2}}{\sqrt{3}} V_{LL} \tag{2.7}$$

where V_{LL} is the line-line fundamental voltage on the AC side. In the linear region, the modulation ratio is between 0 and 1.

2.2 Proposed Real Power Sharing in a RE-Prioritized MG

Since traditional droop control assumes the interfaced power sources as ideal DC sources, it cannot be applied to undispatchable sources, e.g. RES, without modifications. In practice, the maximum available PV generation is limited by the weather conditions. Meanwhile, the battery operation is also restricted to its capacity and power management specifications. The power characteristics of PV and battery sources play an important role in power management and they are demonstrated in this section. Furthermore, a novel power sharing strategy which prioritizes PV power is proposed. It aims to improve the RE penetration level of the grid.

2.2.1 Power Characteristics of a PV Source

Typical power characteristics of PV panels under different weather conditions are shown in Figure 2.5. It can be seen that both solar irradiance I_r and ambient temperature T_a can influence the point of maximum power (MPP). The increasing I_r increases the maximum available PV generation, P_{PV-MPP}, and the corresponding voltage V_{MPP} . On the contrary, the decreasing T_a leads to higher P_{PV-MPP} and V_{MPP}.

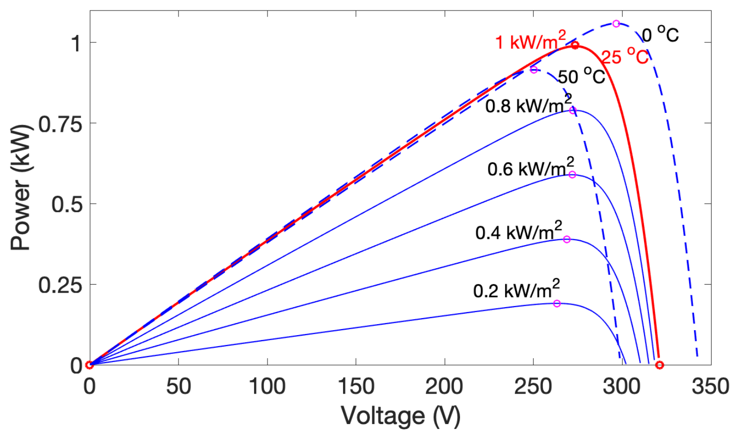

Figure 2.5: Power characteristics under various I_r and T_a

If we look closely at the power characteristic of PV arrays at one particular weather condition, the power vs. voltage ($P_{PV} - V_{PV}$) curve is shown in Figure 2.6. It represents the power characteristic of a $100kW$ PV array under the condition of $T_a = 25^oC$ and $I_r = 1000W/m^2$. When the PV array is connected to a MG, the operating region is composed of two sections: stable area and unstable area. The stable operating points occur at the right-hand-side of the $P_{PV} - V_{PV}$ curve, where $V_{PV} \geqslant V_{MPP}$. It is known that an increasing load leads to a drop of V_{dc} which will further lower V_{PV} in both the single-stage and the two-stage topology, if there is no additional regulation. When operating point is at the right-hand-side, namely $dP_{PV}/dV_{PV} < 0$, V_{PV} dropping means more power would be generated from the PV source. In this circumstance, a new power balance between source and load can be achieved. Conversely, power generation reduces with falling V_{PV} when the operating point is at the left-hand-side, namely $dP_{PV}/dV_{PV} > 0$. This enlarges the difference between power generation from PV arrays and the power demand by the load, which will make V_{PV} drop further and finally collapse. As a consequence, appropriate PV control loop should be designed to guarantee its stability. One simple method is to control V_{PV} operating higher than V_{MPP} at steady state. This stability issue will be validated by simulations in Section 3.1.3.1.

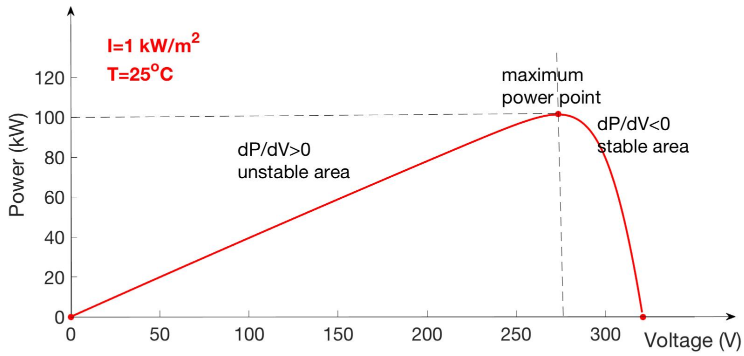

Figure 2.6: $P_{PV} - V_{PV}$ curve of a PV array under a certain environment condition

In conclusion, PV power generation and PV output voltage varies with weather conditions. The intermittent, uncertain and varying power output brings challenges to PV source control. What is more, the maximum power point on $P_{PV} - V_{PV}$ curve puts a upper limit on its power generation. It is thus more difficult to make PV power dispatchable. Traditional techniques which maintain PV operating under MPPT are no longer recommended in a MG with high penetration of PV. These techniques treat PV sources as current sources which deprives their ability to provide voltage regulation. Section (2.2.3) proposes a control strategy for PV sources considering its power characteristics and imposes new functionalities in the MG application.

2.2.2 Power Characteristics of a Battery Source

During the design of a battery source, there are several selection criteria: round trip efficiency, cycle life, maximum temperature rating, safety, environmental considerations and maintenance requirements. Among all types of battery storage, lead-acid and lithium-ion (Li-ion) are the two most common variants in the market. Although lead-acid battery technology is quite mature, Li-ion is emerging to have the greater potential. Li-ion has higher energy density, higher round trip efficiency and it can also be discharged to a lower level than lead-acid. The cycle times of Li-ion batteries are more than that of lead-acid [92]. Furthermore, the charging and discharging characteristics are of particular importance during the operation of batteries.

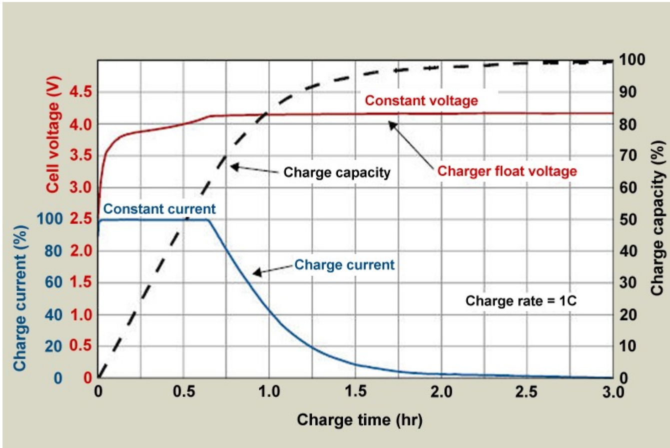

Figure 2.7: Standard charging procedure for Li-ion battery [1]

To assure long cycle lifetime, the battery charging curve for Li-ion cell normally involves two main stages: Constant Current (CC) and Constant Voltage (CV). During the CC stage, the battery is being charged by a current-limited power supply, usually at a rate of 0.5-0.7 times the nominal battery capacity, i.e. 0.5C-0.7C. Note that the charging rate is of unit A while capacity C is of unit Ah. It lasts until the battery voltage reaches its nominal value and the SOC is around 80% at this moment. If the battery keeps being charged, its voltage remains at nominal value while the charging current drops gradually. It is considered as fully charged when the charging current drops to 0.03C-0.1C [1]. The whole charging procedure is shown in Figure 2.7.

By approximation, this charging procedure can be translated into a relationship between reference charging rate P_{ch} and the SOC level. It is represented by an exponential function (2.8) and graphically shown in Figure 2.8 [2]. The recommended charging/discharging rate from the manufacturer can be represented by P_{B0}.

$$P_{ch} = \begin{cases} P_{B0} & if\ SOC < SOC_{ref} \\ P_{B0} e^{-\frac{SOC - SOC_{ref}}{\delta SOC / k_\delta}} & if\ SOC \geqslant SOC_{ref} \end{cases} \tag{2.8}$$

where SOC_{ref} is the threshold where CV charging starts; k_δ is a constant value determining the falling speed of charging rate, while δSOC specifies the range over which CV charging occurs before fully charged. These values are predefined by manufacturers and design specifications.

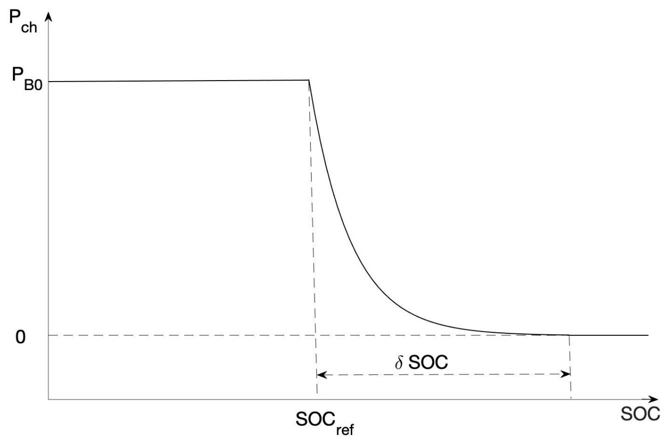

Figure 2.8: Battery charging reference curve with respect to SOC [2]

The SOC of a battery can be estimated by the ampere-hour (Ah) counting method expressed in (2.9)

$$SOC = SOC_0 - \int_0^t \frac{I_{bat}(\tau)}{3600C_{bat}} d\tau \tag{2.9}$$

where SOC_0 represents the initial SOC, C_{bat} is the capacity of the battery in Ah while I_{bat} is the charging current in A [93].

As a battery discharges, its voltage decreases. Figure 2.9 represents discharging characteristics under different discharging rates with respect to Ampere-hour (Ah) and time respectively. Once the voltage drops below the low-voltage threshold, the circuit should disconnect the battery. In practice, the discharging rate is dependent on the grid condition, control methodologies and limited by P_{B-max} (specified in (2.10)). It needs to be noted that the SOC needs to be monitored during discharging to prevent battery exhaustion.

$$P_{B-max} = \begin{cases} P_{B0} & if\, SOC > SOC_{low} \\ 0 & if\, SOC \leqslant SOC_{low} \end{cases} \tag{2.10}$$

where SOC_{low} is the lower threshold of SOC level, below which battery should stop discharging.

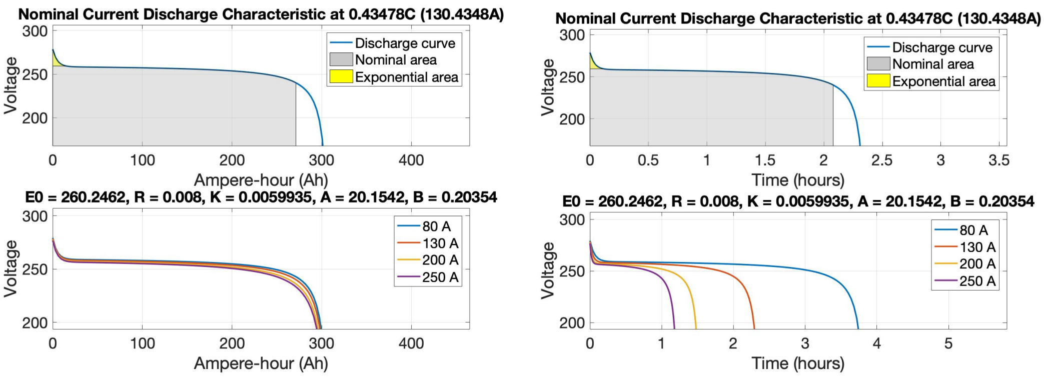

Figure 2.9: Battery discharging characteristics with respect to Ampere-hour (left) and time (right)

It can be seen that the SOC level restricts the battery charging/discharging rate. A higher SOC level corresponds to a lower charging rate but a normal discharging rate. A low SOC level corresponds to a normal charging rate but zero discharging capacity. Overall, the operation of batteries is restricted to preserve their lifetime. While power flow through the battery converter determines its operation mode, an effective power management strategy is critical to battery lifetime as well as system reliability.

2.2.3 Proposed Power Sharing Strategy

To improve the penetration level of RE, RES are enabled with grid-forming functionality and the priority in real power supply. Meanwhile, ESS and CVS operate as supplements to RES. In order to guarantee the quality and reliability of power supply, at least one type of supplements needs to exist in the system.

As CERTS originally proposed, a MG is a single, self controlled entity featuring “peer to peer” and “plug and play” functionalities [94]. Aiming to increase RE penetration level, an islanded hybrid MG is designed to meet the following operating requirements:

- All generation units in a MG are "peer to peer" which means every unit has the function of voltage regulation. There is no central generation unit, master unit or a central controller.
- All units are able to "plug and play" which requires a unified dynamic performance of every independent unit. Inter-unit communications are avoided and a decentralized control strategy is necessary.
- RES possess the priority of real power supply while ESS and CVS are only responsible for peak demand and complementing insufficient renewable generation.

RES traditionally operate under MPPT mode to maximize the utilization of solar panels. However, as RE penetration level increases, some ancillary services are required from RES, e.g. voltage support and frequency regulation. It means that RES can flexibly transfer between grid-following operation and grid-forming operation and should be able to operate at a condition other than MPP. Similarly, ESS also require a modified control to manage the charging/discharging rate with respect to different operating conditions.

To fulfill these functionalities, a specific real power sharing scheme is designed for the discussed hybrid MG. Its operating conditions are classified into four scenarios based on varying local load and available power generation:

i. If there is sufficient PV power generation to support both local load (P_L) and standard battery charging ($P_B = -P_{ch}$), CVS produce zero power ($P_C = 0$). Note that battery power output is represented by P_B while a positive P_B means discharging. Under this condition, PV curtails its power generation to maintain power balance of the whole system. As a result, PV sources perform grid-forming functionality and operate in VCM while batteries and CVS operate in PCM as grid-following units.

ii. When available PV power is insufficient to support both local load and the desired battery charging rate, PV sources generate their maximum available power

P_{PV-MPP} and battery charging rate decreases below P_{ch}. In this scenario, batteries operate under VCM and adjust their power output to keep power balance ($-P_{ch} < P_B < 0$). Meanwhile, PV and CVS operate in PCM ($P_{PV} = P_{PV-MPP}$ and $P_C = 0$).

iii. If the available PV power generation is lower than local load, PV sources operate at MPP to support as much load as possible. At the same time, batteries will start to discharge power to supplement the power shortage. It needs to be noted that the SOC should also be supervised to prevent battery exhaustion. Similar to Scenario ii, batteries still track the power demand ($P_B > 0$) and operate in VCM while other sources operate in PCM ($P_{PV} = P_{PV-MPP}$ and $P_C = 0$).

iv. If the load increases to a level higher than the total available power from PV and batteries, CVS pick up the additional load while batteries discharge at the maximum rate, P_{B-max}, the value of which is suggested by manufacturers. CVS maintain the power balance and regulate grid frequency in VCM and the other two types of sources operate in PCM ($P_{PV} = P_{PV-MPP}$ and $P_B = P_{B-max}$). Noting that CVS (gas turbines, diesel generators) have a minimum threshold of power demand which initiates the generator. This threshold is relevant to system specifications and can be incorporated into control design. For simplicity, the threshold is assumed to be zero in the following discussion without losing generality.

Scenarios	PV	Battery	CVS
i. $P_L \leq P_{PV-MPP} - P_{ch}$	VCM	PCM	PCM
ii. $P_{PV-MPP} - P_{ch} < P_L \leq P_{PV-MPP}$	PCM	VCM	PCM
iii. $P_{PV-MPP} < P_L \leq P_{PV-MPP} + P_{B-max}$	PCM	VCM	PCM
iv. $P_L > P_{PV-MPP} + P_{B-max}$	PCM	PCM	VCM

Table 2.1: Operating modes of different DG units in different scenarios

The designed operating scheme not only allocates grid-forming function to power sources but manages to balance power between generation and consumption with maximum RE penetration. The summary of operating modes is shown in Table 2.1. As can be seen, each source operates either in VCM or PCM and switches between them autonomously.

2.3 Modified Droop Control in a RE-Prioritized MG

As DG units scatter geographically in a MG, it is neither efficient nor reliable to rely on a central controller or extensive communication links. To implement the above power sharing scheme successfully requires an autonomous decentralized control method. As a result, only local information is available to the local controller. As the proposed real power sharing scheme suggested, each unit is able to switch between VCM and PCM. Droop control is the most popular decentralized control strategy in MG applications and it is adopted here. Imitating a synchronous generator, droop control introduces frequency and voltage droop in inverter-based sources for primary control. Its basic responsibility is to regulate voltage and frequency such that total power demand can be shared among parallel sources accordingly. Some other techniques, like virtual synchronous generator (VSG), were also proposed to provide grid-forming functionality [95]. It points out that droop method with a first-order lead-lag unit has an equivalent small-signal model to that of VSG method. However, droop control allows autonomous coordination of different sources while VSG technique focuses more on an individual unit.

2.3.1 Modified Droop Control

Traditional droop method enables power sources to share the power demand proportionally to their ratings. In order to achieve the proposed power sharing scheme, it is critical to design the set point of the droop controller in each unit cooperatively with that of others. According to RE-prioritized sharing strategy, $P-\omega$ droop curves are modified, as shown in Figure 2.10. The blue line represents the droop curve for a PV source (representing RES) while the red line that for a battery (representing ESS) and the yellow line that for a conventional source. To simplify the scenario, we use one line to represent the equivalent characteristics of each kind of source. In other words, the proposed strategy is suitable for a system with multiple PV/battery/conventional sources. In Figure 2.10, O_1 represents the operating point where the PV source outputs zero power at the upper limit of frequency. It means there is no load demand in the system. O_2 is the maximum available PV power output point which is decided by MPPT. This MPPT point moves along the droop curve as weather condition changes. When the power demand passes this maximum value P_{PV-MPP}, the frequency reference of this PV source should reduce so as to limit power output. In the frequency range across O_1O_2 in the PV source, the battery is operating along the vertical line at $-P_{ch}$. The frequency stays within region $\Re\omega_{RES}$ in this scenario.

The battery starts to take the responsibility of maintaining power balance once P_L passes P_{PV-MPP}. Its operating point moves between O_3 and O_4 (being charged on the left-half plane and discharging on the right-half plane). The location of O_3 varies with P_{ch} value and that of O_4 depends on the maximum discharging rate P_{B-max} of the particular battery. The frequency stays within region $\Re\omega_{ESS}$ in this scenario. If the load keeps increasing, the CVS starts to output power, driving its operating point to move towards right from point O_5. It is supposed to pick up all the additional load to maintain power balance. The power limit of the CVS is easy to control and usually pre-set before operation (say 0 and P_{C-max} for lower and upper power limit respectively). The frequency stays within region $\Re\omega_{CVS}$ in this scenario. In summary, the RE-prioritized power sharing scheme is guaranteed by allocating $\Re\omega_{RES}, \Re\omega_{ESS}, \Re\omega_{CVS}$ on top of one another. The frequency range covered by each region are $\Delta\omega_{RES}$, $\Delta\omega_{ESS}$ and $\Delta\omega_{CVS}$ respectively.

Different sets of operating points in Figure 2.10 correspond to the different scenarios classified in the previous section. Operating points a_1,a_2 operate in Scenario i, b_1,b_2 in Scenario ii, c_1,c_2 in Scenario iii and d_1, d_2, d_3 in Scenario iv. The operating points move around in different scenarios, as shown in Figure 2.11.

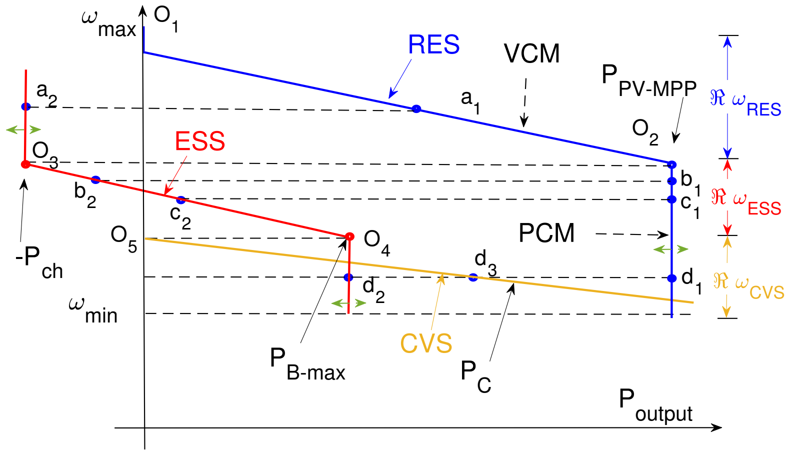

Figure 2.10: $P - \omega$ droop characteristics in a RE-prioritized MG

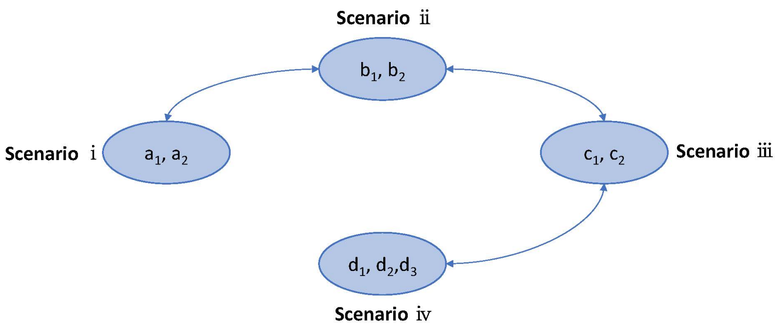

Figure 2.11: Operating points transfer between different scenarios

Unlike proportional power sharing, the allowed frequency deviation range is divided into three regions in the proposed strategy. The range of each frequency region is related with power rating of the corresponding source and the total allowed frequency deviation. In each region, VCM units determine the steady state grid frequency and PCM units adjust their own frequency reference to follow the steady state value. As frequency is a common variable in the system, no inter-unit communications are needed. For sources of the same type, they still share power proportional to their ratings. For example, if there are two PV sources with different nominal power $P_{pv1-nom}$ and $P_{pv2-nom}$, the set points can be designed as follows:

Variables	P_{0-pv1}	ω_{0-pv1}	P_{0-pv2}	ω_{0-pv2}	m_{pv1}	m_{pv2}
Set points	$P_{pv1-nom}$	ω_{nom}	$P_{pv2-nom}$	ω_{nom}	$\frac{\Delta\omega_{RES}}{P_{pv1-nom}}$	$\frac{\Delta\omega_{RES}}{P_{pv2-nom}}$

Table 2.2: Set points of two PV sources

As this section focuses on real power sharing, we assume each source has the same reactive power rating such that the sources equally share the reactive power load, i.e. average reactive power sharing. The set point (E_0 , Q_0), droop coefficient n and upper limits of reactive power in the interfaced sources are identical. The detailed discussion on reactive power sharing in a RE-prioritized MG is included in Chapter 5.

2.3.2 Analysis of Varying Maximum Power in PV Sources

As explained in Figure 2.10, the switching point for PV from VCM to PCM is the point of maximum available generation, which is dependent on weather conditions. On a cloudy day, P_{PV-MPP} drops below its nominal power, P_{PV-nom}, driving O_2 moving upward along the droop curve. In Scenario ii, iii, iv, PV sources operate under MPPT mode which is along the vertical characteristic. A MPPT technique can help to locate the maximum power point (V_{MPP}, P_{PV-MPP}) on the power source side, details discussed in Chapter 3.

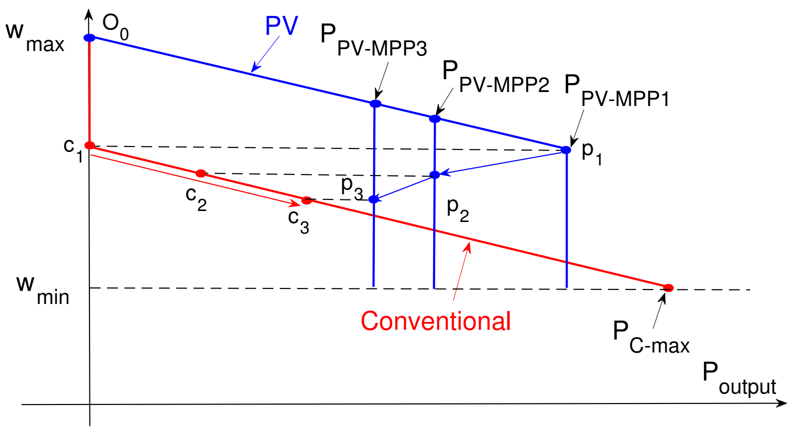

Figure 2.12: PV operation mechanism under varying weather conditions

The illustration of varying P_{PV-MPP} in the proposed strategy can be seen in Figure 2.12. The $P-\omega$ droop of PV is in blue and the single line can represent a single PV source or the equivalent characteristic of several PV sources. As the solar irradiance decreases or temperature increases around the solar panels, P_{PV-MPP} decreases from $P_{PV-MPP1}$ to $P_{PV-MPP2}$ to $P_{PV-MPP3}$ according to the power characteristics of PV generation. The caused power shortage is supplemented by the VCM unit, e.g. CVS (represented in red curve). Under the condition of $P_L = P_{PV-MPP1}$, the operating point of the PV source moves from p_1 to p_2 to p_3 while that of the CVS moves from c_1 to c_2 to c_3. PV source operates along the vertical line and the CVS moves along the droop line. Steady state frequency values are determined by the VCM unit (CVS in the discussed example). The performance of the proposed strategy under varying weather conditions will be shown by simulation and experimental studies in the following chapters.

2.3.3 Control Implementation

The proposed control strategy can be achieved by modifying traditional droop control. This section includes the control diagram of primary control based on modified droop control and that of inner voltage and current control loop. Since this section focuses on the control on grid side converter, the power source is represented by an constant DC voltage source. The source side converter control is discussed in the next chapter while considering the unique power characteristics of connected sources.

2.3.3.1 Overall Control Diagram

The control diagram for a single inverter is presented in Figure 2.13. It is the one-line diagram of a three-phase system and the power source is represented by a constant DC voltage source for simplicity. Without losing generality, the coupling line impedance is composed of both inductance (L_2) and resistance (R_2) and a parasitic resistance (R_1) is also included in the LC filter inductance.

The proposed control strategy discussed in Section 2.3.1 can be achieved by modifying the traditional $P - \omega$ droop. As can be seen in Figure 2.10, the unit in VCM operates under droop control and the unit in PCM is restricted by power limits. The transition point is at the lower/upper power limits of each source. Under PCM, operating frequency deviates from the original transition point (e.g. O_2 for PV source) and the deviation value in steady state is determined by the VCM units. If this frequency deviation is represented by $\delta\omega$, the modified droop control can be represented by:

$$\omega_{ref} = \omega_0 - m(P - P_0) + \delta\omega \tag{2.11}$$

where $\delta\omega$ is generated locally in each source and leads the frequency reference to a common steady state value.

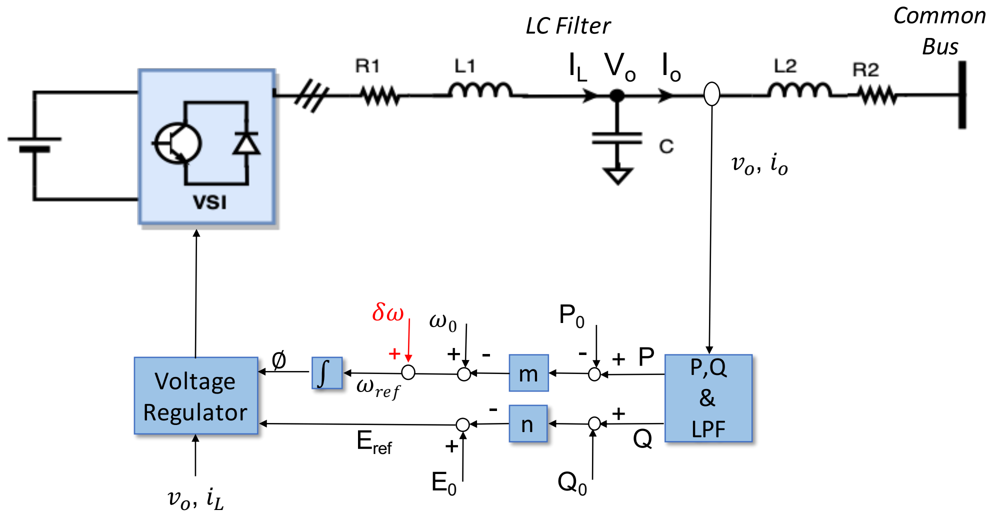

Figure 2.13: Control diagram of the modified droop control with power limiting functionality

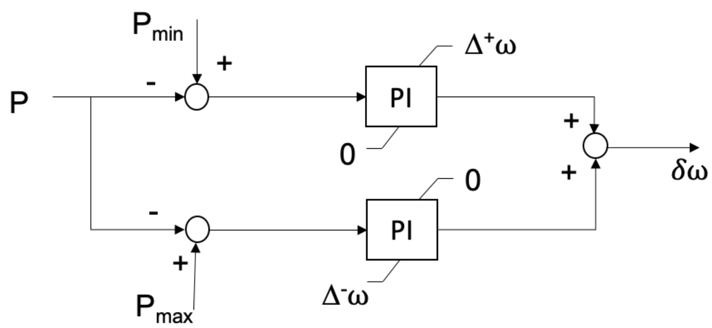

Figure 2.14: Control diagram of $\delta\omega$ generation

As $\delta\omega$ aims to regulate power output to a constant value at steady state, it can be generated from a PI controller. The control diagram of $\delta\omega$ generation can be designed as shown in Figure 2.14. P_{max} and P_{min} represent the upper power limit and lower power limit respectively. $\Delta^+\omega$ and $\Delta^-\omega$ represent respectively the positive and negative limits of frequency deviation.

It needs to be noted that the deviation limits are not only related back to the specific grid codes but also are dependent on the various types of sources. The $\delta\omega$ range in PV, battery and conventional sources are represented separately as below:

$$\Delta^{-}\omega_{PV} = \omega_{min} - \omega_{0PV} \; \& \\ \Delta^{+}\omega_{PV} = 0 \tag{2.12}$$

$$\Delta^{-}\omega_{BAT} = \omega_{min} - \omega_{0BAT} \; \& \\ \Delta^{+}\omega_{BAT} = \omega_{max} - \omega_{0PV} \tag{2.13}$$

$$\Delta^{-}\omega_{CVS} = \omega_{min} - \omega_{0CVS} \; \& \\ \Delta^{+}\omega_{CVS} = \omega_{max} - \omega_{0CVS} \tag{2.14}$$

In Figure 2.13, three-phase output voltage V_o and current I_o are measured at the output of LC filter. They are fed into a real-time power calculation module, which is followed by the modified droop controller generating the VSI reference voltage. The voltage regulator then generates PWM signals to regulate the VSI output voltage to the reference value. The module of power calculation consists of three parts: Park transformation, real-time power calculation, digital Low Pass Filter (LPF). The voltage regulator is described separately in the next section.

The Park transformation transforms a AC signal from three-phase (abc) reference frame to synchronous rotating ($dq0$) reference frame. It can effectively transfer three-phase-balanced sinusoidal signals into two constant components. A zero-sequence component can also be generated from un-balanced sinusoidal signals. The direct transformation can be seen in the equation:

$$\begin{bmatrix} f_d(t) \\ f_q(t) \\ f_0(t) \end{bmatrix} = \frac{2}{3} \begin{bmatrix} cos(\theta(t)) & cos(\theta(t) - \frac{2\pi}{3}) & cos(\theta(t) - \frac{2\pi}{3}) \\ sin(\theta(t)) & sin(\theta(t) - \frac{2\pi}{3}) & sin(\theta(t) - \frac{2\pi}{3}) \\ \frac{1}{2} & \frac{1}{2} & \frac{1}{2} \end{bmatrix} \begin{bmatrix} f_a(t) \\ f_b(t) \\ f_c(t) \end{bmatrix} = \mathcal{P}(\theta) \begin{bmatrix} f_a(t) \\ f_b(t) \\ f_c(t) \end{bmatrix} \tag{2.15}$$

where θ represents the angular position of $dq0$ reference frame and it is the integral of grid frequency; f_d, f_q and f_0 are direct, quadrature and zero-sequence components in the $dq0$ reference frame; f_a, f_b and f_c are the instantaneous three-phase values in the abc reference frame; $\mathcal{P}(\theta)$ is the Park transformation matrix. From the perspective of control strategy, tracking a sinusoidal signal usually requires a complex and high-order compensator. On the contrary, a simple PI compensator is effective to achieve zero steady-state error in tracking a DC value. It is thus advantageous to control a sinusoidal signal in rotating frame because the components on d and q axis can be regulated independently by simple PI control.

The real time power calculation is also easy to carry out based on $dq0$ reference frame. The equations are shown below:

$$p = \frac{3}{2}(v_d i_d + v_q i_q) \tag{2.16}$$

$$q = \frac{3}{2}(v_q i_d - v_d i_q) \tag{2.17}$$

The digital LPF is used to smooth the power value prior to being employed in the droop control algorithm. With a cut-off frequency at ω_c, the filtered power can be represented below:

$$P = \frac{\omega_c}{s + \omega_c} p \tag{2.18}$$

$$Q = \frac{\omega_c}{s + \omega_c} q \tag{2.19}$$

Note that the cut-off-frequency of LPF also has an impact on the system stability, which is analyzed in [33].

2.3.3.2 The Voltage Regulator

In the voltage regulator, the VSI output voltage is controlled in $dq0$ reference frame such that simple PI control is sufficient. The regulator has a double-loop structure which provides fast over-current protection and output disturbance rejection. In order to regulate the AC voltage in $dq0$ reference frame, the model of the LC filter and network dynamics need to be built. In abc reference frame, the dynamics of LC filter after the inverter can be represented in (2.20) and (2.21). Meanwhile, the network dynamics are represented in (2.22)

$$v_{i,abc} = L_1 \frac{di_{L,abc}}{dt} + R_1 i_{L,abc} + v_{o,abc} \tag{2.20}$$

$$i_{L,abc} = C \frac{dv_{o,abc}}{dt} + i_{o,abc} \tag{2.21}$$

$$v_{o,abc} = L_2 \frac{di_{o,abc}}{dt} + R_2 i_{o,abc} + v_{g,abc} \tag{2.22}$$

where $v_{i,abc}$ and $i_{L,abc}$ represent the vector of three-phase voltages and currents at the output of the inverter respectively; $v_{g,abc}$ represents the vector of three-phase voltages at the grid common bus; L_1, R_1 and C are values for inductance, resistance and capacitance in the LC filter respectively; L_2 and R_2 are inductance and resistance values across the coupling line.

Transform the above equations into $dq0$ reference frame using Park transformation $\mathcal{P}(\theta)$. Taking (2.20) as an example, it is transformed into (2.23).

$$\begin{aligned}
\mathcal{P}(\theta)v_{i,abc} &= \mathcal{P}(\theta)L_1 \frac{di_{L,abc}}{dt} + \mathcal{P}(\theta)R_1 i_{L,abc} + \mathcal{P}(\theta)v_{o,abc} \\
v_{i,dq0} &= \mathcal{P}(\theta)L_1\mathcal{P}^{-1}(\theta)\mathcal{P}(\theta)\frac{di_{L,abc}}{dt} + \mathcal{P}(\theta)R_1\mathcal{P}^{-1}(\theta)\mathcal{P}(\theta)i_{L,abc} + v_{o,dq0} \\
v_{i,dq0} &= L_1\mathcal{P}(\theta)\frac{di_{L,abc}}{dt} + R_1 i_{L,dq0} + v_{o,dq0} \\
v_{i,dq0} &= L_1\left\{\frac{d(\mathcal{P}(\theta)i_{L.abc})}{dt} - \frac{d\mathcal{P}(\theta)}{dt}i_{L,abc}\right\} + R_1 i_{L,dq0} + v_{o,dq0} \\
v_{i,dq0} &= L_1\left\{\frac{di_{L.dq0}}{dt} - \omega\frac{d\mathcal{P}(\theta)}{d\theta}i_{L,abc}\right\} + R_1 i_{L,dq0} + v_{o,dq0} \\
v_{i,dq0} &= L_1\left\{\frac{di_{L.dq0}}{dt} - \omega\frac{d\mathcal{P}(\theta)}{d\theta}\mathcal{P}^{-1}(\theta)i_{L,dq0}\right\} + R_1 i_{L,dq0} + v_{o,dq0}
\end{aligned} \tag{2.23}$$

Note that,

$$\frac{d\mathcal{P}(\theta)}{d\theta}\mathcal{P}^{-1}(\theta) = \begin{bmatrix} 0 & 1 & 0 \\ -1 & 0 & 0 \\ 0 & 0 & 0 \end{bmatrix}$$

Equation (2.23) can then be represented in component form:

$$v_{id} = L_1 \frac{di_{Ld}}{dt} - \omega L_1 i_{Lq} + R_1 i_{Ld} + v_{od} \tag{2.24}$$

$$v_{iq} = L_1 \frac{di_{Lq}}{dt} + \omega L_1 i_{Ld} + R_1 i_{Lq} + v_{oq} \tag{2.25}$$

Similarly, (2.21) and (2.22) can be transformed into $dq0$ form:

$$i_{Ld} = C \frac{dv_{od}}{dt} - \omega C v_{oq} + i_{od} \tag{2.26}$$

$$i_{Lq} = C \frac{dv_{oq}}{dt} + \omega C v_{cd} + i_{oq} \tag{2.27}$$

$$v_{od} = L_2 \frac{di_{od}}{dt} - \omega L_2 i_{oq} + R_2 i_{od} + v_{gd} \tag{2.28}$$

$$v_{oq} = L_2 \frac{di_{oq}}{dt} + \omega L_2 i_{od} + R_2 i_{oq} + v_{gq} \tag{2.29}$$

To graphically represent this dynamic model, a diagram is drawn below:

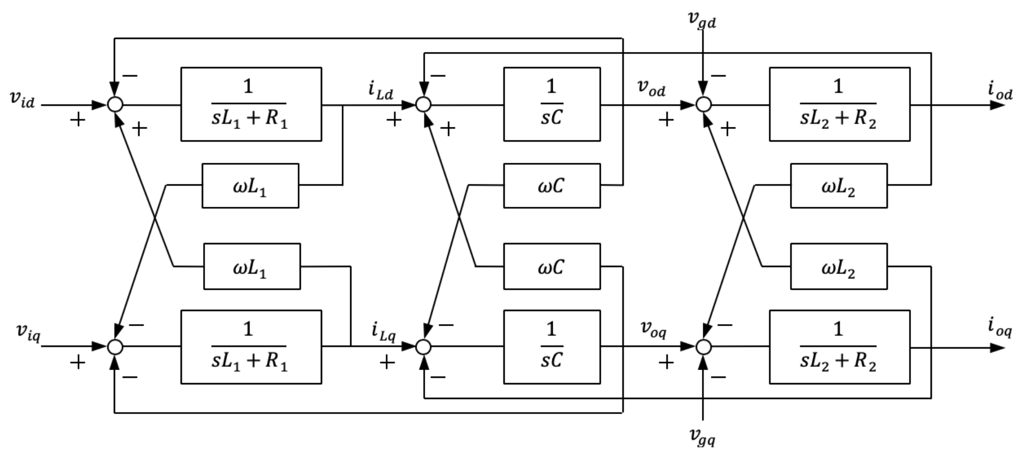

Figure 2.15: Model of the network in $dq0$ reference frame

The double loop voltage regulator consists of an outer VCtrl loop which controls the capacitor voltage v_o and an inner ICtrl loop which controls the filter current i_L. The design of these two controllers are discussed separately. Firstly, the current controller is designed in Figure 2.16 where the red part represents the controller and the black part represents the plant model of the LC filter. The cross coupling terms $\omega L_1 i_{Ld,fb}$ and $-\omega L_1 i_{Lq,fb}$ are included in the controller to cancel out the coupling terms in the plant model, such that d component and q component can be independently controlled. The feedforward loops $V_{od,fb}$ and $V_{oq,fb}$ are included in the controller for the same reason.

The VCtrl is designed in a similar fashion, as shown in Figure 2.17. The inner ICtrl needs to be included in the design. To avoid interference between these two loops, the inner control loop is designed to be at least 10 times faster than the outer control loop. As a consequence, the ICtrl loop can be replaced by a proportional gain of 1.

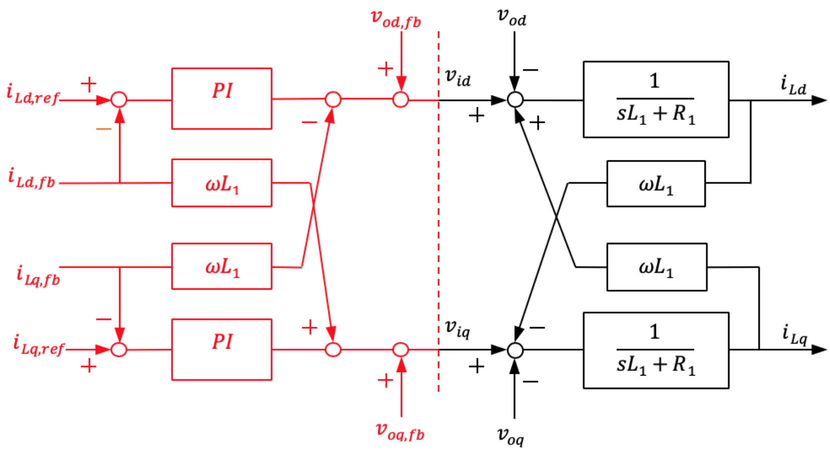

Figure 2.16: Diagram of inner current control in $dq0$ reference frame

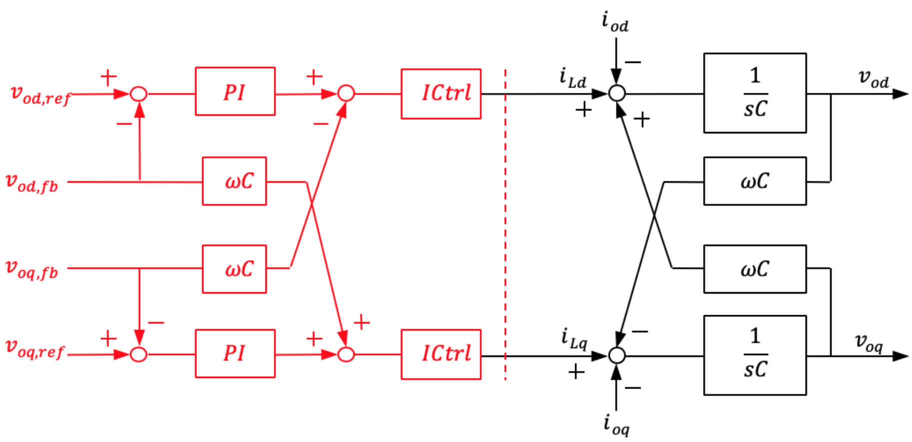

Figure 2.17: Diagram of outer voltage control in $dq0$ reference frame

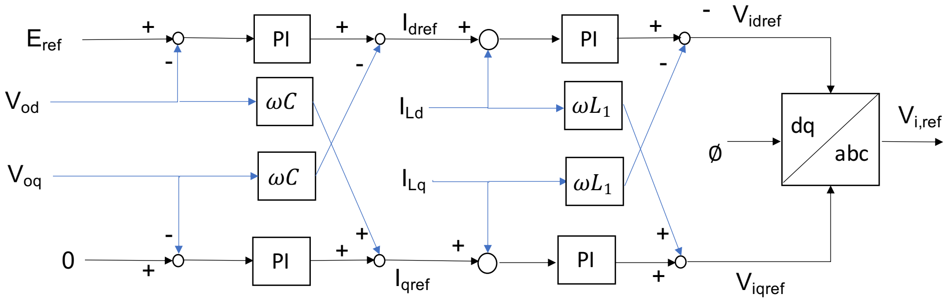

Figure 2.18: Diagram of voltage regulator of VSI output voltage

Combining these two loops together, the double loop voltage regulator is shown in Figure 2.18. Its output $V_{i,ref}$ is the inverter reference voltage for PWM modulation.

2.4 Simulation Results

A hybrid MG is simulated, based on the topology in Figure 2.1. In order to focus on the power sharing strategy, all power sources are represented by ideal DC voltage sources which provide constant DC voltage and dispatchable power generation. Both proportional sharing and the proposed RE-prioritized power sharing are simulated in this section.

2.4.1 Proportional Power Sharing

During the simulated proportional power sharing period, the system experiences a series of step changes in load as shown in Table 2.3. Important parameters of the system operation are shown in Table 2.4.

$t(s)$	0-2	2-4.5	4.5-7	7-9.5
$P(kW)$	25	35	48	58
$Q(kVar)$	5	5	5	10

Table 2.3: Local load conditions in proportional power sharing

All sources share the same frequency and voltage set point (ω_0, E_0). The real power set point (P_0) is the corresponding power rating and the droop coefficient (m) is inversely proportional to the rating. For simplicity, the reactive power set points (Q_0) and reactive droop coefficients (n) are set as identical in all sources. Assume the grid codes allow the system frequency to vary within $(1 \pm 0.5\%)f_{nom}$ ($f_{nom} = 50Hz$) and the grid voltage to vary within $(1 \pm 10\%)V_{nom}$ ($V_{nom} = 230/400V$). The same specifications apply throughout this thesis.

Parameters	Values	Parameters	Values
V_{nom}	$230/400V$	V_{dcref}	$700V$
L_1	$2mH$	L_2	$2mH$
R_1	0.1Ω	R_2	0.1Ω
C	$20\mu F$	$\omega_c(LPF)$	$100rad/s$
Q_0	$0Var$	n	$2.5 \times 10^{-4}V/Var$
P_{0-PV1}	$20kW$	P_{0-PV2}	$10kW$
P_{0-BAT1}	$15kW$	P_{0-BAT2}	$10kW$
P_{0-CVS}	$10kW$	ω_0	$314rad/s$
m_{PV1}	$7.5 \times 10^{-5}rad/(s \cdot W)$		
m_{PV2}	$1.5 \times 10^{-4}rad/(s \cdot W)$		
m_{BAT1}	$1 \times 10^{-4}rad/(s \cdot W)$		
m_{BAT2}	$1.5 \times 10^{-4}rad/(s \cdot W)$		
m_{CVS}	$1.5 \times 10^{-4}rad/(s \cdot W)$		

Table 2.4: System parameters in proportional power sharing

The simulation results are shown in Figure 2.19. According to the real power outputs in Figure 2.19a, the total load is shared by the five sources proportional to their power ratings independent of load changes at t=2s, 4.5s, 7s. Average reactive power sharing is designed in the droop control. However, the mismatch in reactive power outputs shown in Figure 2.19b can be explained by different voltage drops across the coupling line. The higher real power output from PV1 causes a higher voltage drop, which results in a lower reactive power output. The detailed explanation will be discussed in Chapter 5. The underdamped high frequency oscillation in the reactive power measurements after each load change is due to a sub-optimal choice for the reactive power droop coefficient, n. As discussed in Chapter 6, a higher value of n reduces the stability margin. A smaller value of n should be chosen for greater stability.

Figure 2.19c shows that the frequency drops after every increase of real power demand and its value is restricted within the grid acceptable range. The frequency curves were measured at the individual sources as there is no grid common frequency sensor in this method (as it avoids the need for high-bandwidth communication links). The curves differ from each other, most notably during transients, due to the impact of individual source phase angle adjustments on the local frequency measurement method. However, in steady state the frequency measurements converge to a common value in a stable system. The small oscillations in the steady state frequency measurements are a result of implementing PLL measurements on unfiltered output voltages. Grid voltage remains constant during real power disturbances but it drops after the increase of reactive power demand at t=7s, as shown in Figure 2.19d.

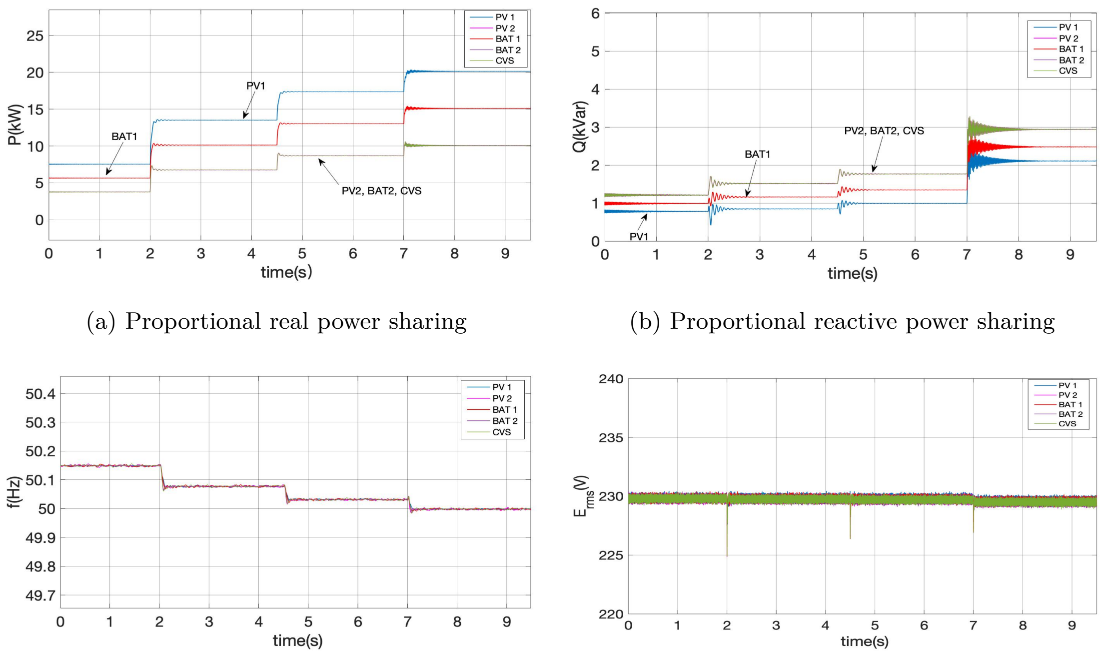

(a) Proportional real power sharing (b) Proportional reactive power sharing

(c) Grid frequency (d) Grid ph-n voltage in RMS value

Figure 2.19: Simulation results of proportional power sharing

2.4.2 RE-Prioritized Power Sharing

Instead of proportional power sharing, RES are given the priority of power supply in this section. The same simulation settings apply except for some changes of the parameters in Table 2.4, as specified in Table 2.5. Moreover, the set point for real power (ω_0, P_0) varies in different power sources. The droop coefficients (m) of the same type of sources are still inversely proportional to their power ratings. The frequency operation region is also divided into three regions based on the grid codes. While the frequency can deviate from f_{nom} ($50Hz$) by $\pm 0.5\%$, the three frequency regions are allocated as follows:

$$\Re\omega_{RES}: (2\pi \times 50)rad/s \sim (2\pi \times 50.25)rad/s$$
$$\Re\omega_{ESS}: (2\pi \times 49.75)rad/s \sim (2\pi \times 50)rad/s$$
$$\Re\omega_{CVS}: (2\pi \times 49.5)rad/s \sim (2\pi \times 49.75)rad/s$$

Parameters	Values	Parameters	Values
P_{0-PV1}	$20kW$	P_{0-PV2}	$10kW$
P_{0-BAT1}	$15kW$	P_{0-BAT2}	$10kW$
ω_{0-PV}	$100\pi rad/s$	ω_{0-BAT}	$99.75\pi rad/s$
P_{0-CVS}	$0kW$	ω_{0-CVS}	$99.75\pi rad/s$
m_{PV1}	$7.5 \times 10^{-5} rad/(s \cdot W)$		
m_{PV2}	$1.5 \times 10^{-4} rad/(s \cdot W)$		
m_{BAT1}	$2.5 \times 10^{-5} rad/(s \cdot W)$		
m_{BAT2}	$3.75 \times 10^{-5} rad/(s \cdot W)$		
m_{CVS}	$7 \times 10^{-5} rad/(s \cdot W)$		

Table 2.5: Modified droop control parameters in RE-prioritized power sharing

The simulation results are shown in Figure 2.20. The system experiences the same loading profile as described in Table 2.3. The real power sharing performance (shown in Figure 2.20a) verifies the effectiveness of the proposed power sharing scheme. The total load is shared by five sources with different priorities. During the first 2s, the load is at a low level, the two PV sources operate at their upper power limits ($20kW/10kW$), providing power for local load consumption and charging batteries. Two batteries are being charged under a rate proportional to their power ratings. During this period, the PV sources operate under PCM while the grid voltage is regulated by batteries.

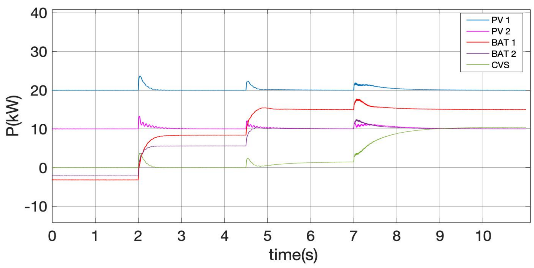

(a) Real power sharing

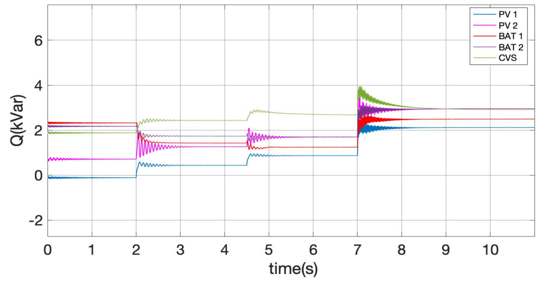

(b) Reactive power sharing

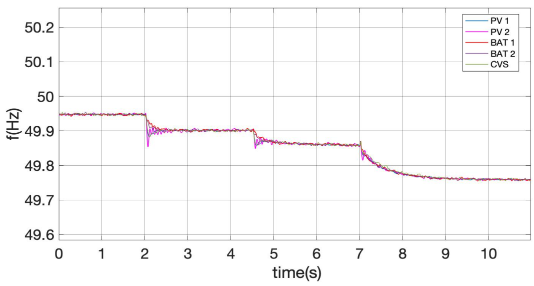

(c) Grid frequency

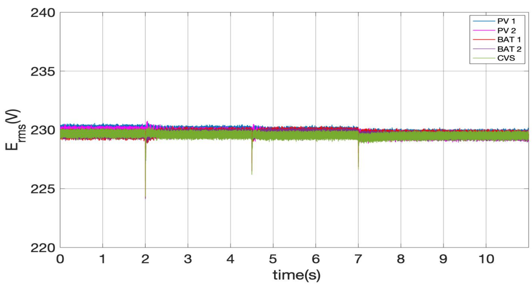

(d) Grid ph-n voltage in RMS value

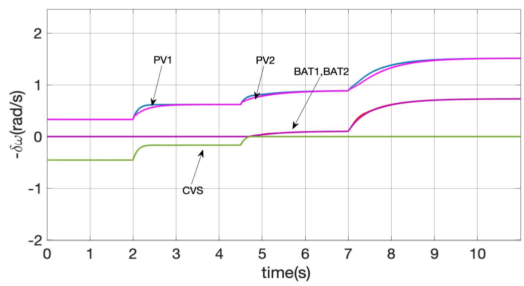

(e) Frequency deviation values in different sources

Figure 2.20: Simulation results of RE-prioritized power sharing in a hybrid MG

At t=2s, the real power demand experiences a step increase. Two batteries start to release energy to support the local load, together with PV generation. Batteries operate in VCM while PV in PCM in this scenario. After t=4.5s, an increase of local load starts to draw power from the CVS as both batteries output their maximum allowed power ($15kW/10kW$). The CVS takes over the responsibility of regulating grid voltage under VCM while all the other sources operate at the maximum power level. The power transients at t=2s, 4.5s and 7s presented in real power curves are attributed to load disturbances and relatively slow responses of droop controllers. All parallel sources instantaneously respond to any power disturbances and will then be regulated by droop control until settling down to steady state. Taking PV1 curve for example, the sudden load increase at t=2s causes a power surge which is beyond its power limit. This additional power output can be supplied from any power storages connected to the unit, such as power reserves, batteries, DC link capacitors. The total consumed energy during this transient is dependent on the response speed of droop control.

Reactive power is also shared differently between units and varies under different load conditions, according to Figure 2.20b. The reason that PV sources share less reactive power is because the voltage drop across the coupling line in PV is larger than that in other sources as a result of larger real power flow. The details will be discussed later in Chapter 5. Nevertheless, it maintains the same pattern during the whole process. On the other hand, frequency (in Figure 2.20c) and magnitude (in Figure 2.20d) of grid voltage behaves similar to the case of proportional power sharing in Section 2.4.1. What is more, the frequency deviation values in every sources are shown in Figure 2.20e. According to the figure, we can see that $\delta\omega_{PV}$ is negative from the beginning and the deviation grows larger after each increase of real power demand. It means PV sources operate at their maximum power level. At the same time, a positive $\delta\omega_{CVS}$ during the first 4.5s means the CVS operate at its lower power limit. The negative value of $\delta\omega_{BAT}$ after t=4.5s also indicates that batteries operate at their upper power limits.

2.5 Conclusions

This chapter discussed real power sharing in an islanded hybrid MG where multiple DG units coordinated with each other. Since the traditional proportional power sharing only works with idealised dispatchable sources, a RE-prioritized power sharing strategy was proposed, for a RE-based MG, which considered the primary sources' capabilities and limits. The new strategy increased the penetration level of RE while considering the capacity restrictions of ESS. Most importantly, the proposed strategy could be easily achieved by modifying droop control to include PI controlled power limits.

The strategy could also effectively respond to variation in the available PV generation due to changing weather conditions. The simulations in this chapter were conducted with ideal DC sources with pre-determined power limits. However, the maximum available PV generation is neither constant nor knowable in advance. In the next chapter, the decentralized implementation of the proposed RE-prioritized power sharing strategy in a PV-based MG is discussed. It will include provision to autonomously track varying PV power generation without relying on inter-unit communications.

Chapter 3

Decentralized Control Strategies in a RE-Prioritized MG

In an islanded MG, the load sharing strategy is critical to stable system operation. Even under the condition of matched power demand and supply, the MG can go unstable if power supply is not shared properly [45]. This is particularly the case if the MG is based on renewables. It can occur when there is either a new connection of load or a reduction of RE generation due to varying weather conditions. To prevent RES from collapsing and to maintain system stability, control strategies for RES have attracted a great attention over the last decade.

This chapter is structured as follows. The control strategy for a PV source in the discussed MG is demonstrated in Section 3.1. It is then followed by the control strategy for a battery source in Section 3.2. The effectiveness of each control strategy is verified through simulations. These proposed strategies can also coordinate with the proposed RE-prioritized power sharing strategy and its performance is shown through a simulation study in Section 3.3. Finally, frequency restoration under the proposed strategies is addressed in Section 3.4. Conclusions are drawn at last in Section 3.5.

3.1 Control of a PV Source

The PV source interfaced to a MG is shown in Figure 3.1. The control methods for both DC/DC boost converter and DC/AC VSI are described respectively in this section.

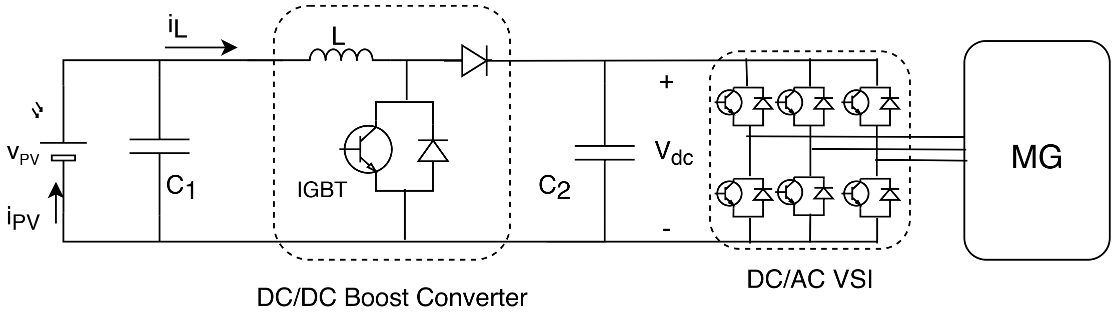

Figure 3.1: Structure of a MG interfaced PV source

3.1.1 DC/DC Boost Converter Control

The aim of the DC/DC converter controller is to balance PV power generation with power demand on the VSI. In normal conditions, the PV source operates under MPPT mode to maximize the efficiency of the PV panels. However, according to the proposed power sharing scheme in Chapter 2, the PV power should be curtailed when the maximum available power is higher than power demand (in Scenario i). Once the system power demand reaches P_{PV-MPP}, PV source should switch to PCM to maintain the maximum power generation. The realization of the mode switching relies on the coordinated operation of the DC/DC boost converter and the DC/AC VSI in a two-stage PV source. The control strategy on the DC/DC boost converter is proposed, based on the PV power characteristics discussed in Section 2.2.1.

The control of the boost converter should take the stability issue into account. Given the PV power characteristics shown in Figure 2.6, V_{PV} should be held above V_{MPP} to maintain PV system stability. However, power disturbances can still potentially drive PV operating point into the unstable region, especially under an increase of load or a decrease of PV power generation (e.g. solar irradiance drop). A mode switching method is proposed for boost converter control as shown in Figure 3.2. An inner PI control loop adjusts boost converter duty cycle to control the output voltage of the PV array to a reference value. The PV array reference voltage is generated by two "parallel" outer control loops: MPPT and DC bus voltage control. Depending on the operating mode of the PV, the outer loops will behave as follows:

a) In Scenario i, where the grid interface inverter is operating in VCM, the V_{dc} control is active and MPPT disabled. Whilst disabled, the MPPT holds the last V_{MPP} value generated prior to deactivation. The V_{dc} control adds an increment δV_{PV} to this V_{MPP}. If the V_{dc} rises (indicative of excess PV generation), the PV array reference voltage is increased lowering the PV arrays output power.

b) In Scenario ii-iv, where the grid interface inverter is operating in PCM, the MPPT is enabled and provides the reference value for PV array voltage ($V_{PVref} = V_{MPP}$). The output of the V_{dc} control is held at zero (indeed it is the return of this signal to zero that enables the MPPT control). The transition to this mode is triggered by the DC bus voltage falling (indicative of insufficient PV generation or increasing load), leading to the PV array reference voltage being lowered and increasing the PV arrays output power until it is effectively limited at the maximum power point.

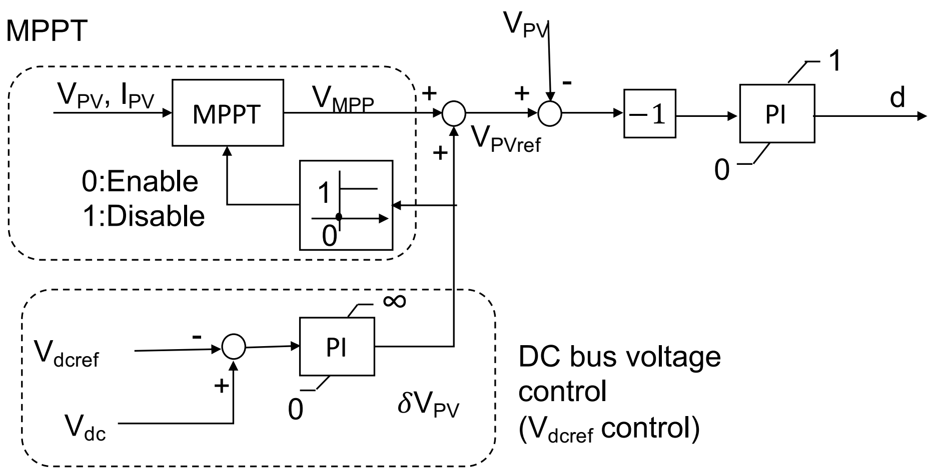

Figure 3.2: Control loop of the DC/DC boost converter

It is worth noting that the range of δV_{PV} is between 0 and $V_{OC} - V_{MPP}$. PV power generation is less sensitive to the value of δV_{PV} (close to 0) when operating close to the MPP, according to Figure 2.5. The steady state value of δV_{PV} is determined by the PI regulation of V_{dc}.

There are several MPPT algorithms and implementation methods for PV sources [96, 97]. These methods include Fixed Duty Cycle, Constant Voltage, Perturb and Observe (P&O) and Modified P&O, Incremental Conductance (IC) and Modified IC. P&O and IC methods are commonly used so they are discussed here.

P&O method observes the variation of the PV generation (P_{PV}) after perturbing the PV voltage (V_{PV}). According to PV power characteristics, if a V_{PV} perturbation, dV_{PV}, moves the operating point towards the MPP, the variation of P_{PV} is positive, i.e. $dP_{PV} > 0$. The next perturbation dV_{PV} should be in the same direction until MPP is reached. If $dP_{PV} < 0$, the algorithm reverses the direction of original V_{PV} perturbation. By repeating this process, the MPP can finally be found. P&O method is simple to implement but oscillations usually appear around the MPP.

The IC method is developed on the fact that $dP_{PV}/dV_{PV} = 0$ at the MPP, which means:

$$\frac{dP_{PV}}{dV_{PV}} = \frac{d(V_{PV}I_{PV})}{dV_{PV}} = I_{PV} + V_{PV}\frac{dI_{PV}}{dV_{PV}} = 0 \tag{3.1}$$

$$\frac{I_{PV}}{V_{PV}} + \frac{dI_{PV}}{dV_{PV}} = 0 \tag{3.2}$$

where $\frac{dI_{PV}}{dV_{PV}}$ is incremental conductance. Instead of observing dP_{PV} as in P&O, $\frac{dI_{PV}}{dV_{PV}}$ is compared with $-\frac{I_{PV}}{V_{PV}}$ in this method. When they are equal, the MPP is reached and perturbation can be stopped. There is no need to calculate P_{PV} thus a fast and accurate tracking of the MPP without oscillation can be achieved. The IC algorithm is adopted in this thesis because of its high tracking accuracy at steady state and its good adaptability to rapidly changing weather conditions.

3.1.2 VSI Control in a PV Source

Because P_{PV-MPP} is varying and hard to predict, the traditional power limiting method as shown in Figure 2.14 is not suitable in a PV source. However, the power balance condition can be indicated by the dynamics of V_{dc}. Instead of employing a direct power limiting method, V_{dc} regulation can be adopted to achieve power regulation.

A power disturbance is reflected in V_{dc} fluctuation. If there is an increase of load or decrease of PV power generation, the stored energy in the DC link capacitor (C_2) will discharge to supplement the power shortage and V_{dc} will decrease. However, the amount of stored energy is limited to the size of the capacitor and the minimum allowable V_{dc} value. The reduced V_{dc} needs to be restored to the nominal value within a certain time period. The V_{dc} regulator thus needs to drive the PV panels to generate more power or command the inverter to reduce power supply to the grid. In Scenario i, regulating V_{dc} means regulating PV power generation as there is reserve capacity in the PV power output. On the other hand, in Scenario ii-iv, regulating V_{dc} means adjusting the frequency reference of the VSI so as to keep PV source operating at its MPP under PCM.

Based on the modified droop control proposed in Chapter 2, a frequency deviation term $\delta\omega$ can help to switch the operation mode. Instead of using the fixed power limit values in ideal DC power sources, the generation of frequency adjustment term $\delta\omega_{PV}$ in the VSI controller is shown in Figure 3.3. In Scenario i, this control loop is disabled by a positive δV_{PV} value which is generated from the V_{dcref} control loop in the boost converter controller. In Scenario ii-iv, it is enabled with a zero value of δV_{PV}. If there is a decrease in V_{dc}, a negative $\delta\omega_{PV}$ will be generated to maintain the output of the VSI at P_{PV-MPP}. It operates under PCM and the power shortage is supplemented by other VCM units. Since the enable/disable signal is also δV_{PV}, the PCM mode is only active under MPPT.

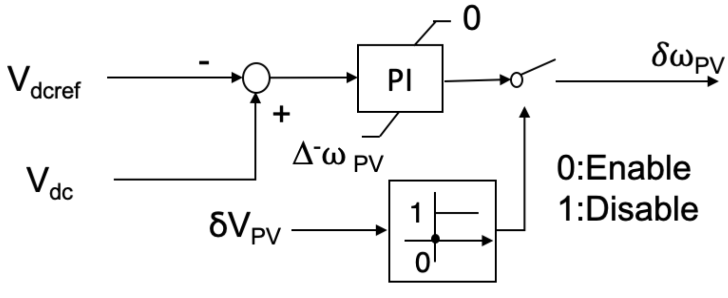

Figure 3.3: $\delta\omega_{PV}$ generation for power limiting

The above two feed-forward loops share the same control variable: V_{dc}. As a consequence, there is a potential that the two controllers will interfere with each other. To separate these two controllers, two techniques are employed: V_{dcref} separation and hysteresis effect, as shown in Figure 3.4.

V_{dc} is regulated to V_{dcref} by the boost converter controller under VCM and drops if the PV unit is overloaded. Under PCM mode, V_{dc} is allowed to operate at a lower value. In the VSI controller, if V_{dc} is regulated to $V_{dcref}^{'}$, $V_{dcref}^{'} < V_{dcref}$, the interference between two controllers can be largely avoided. The V_{dcref} separation should be large enough to overlook V_{dc} oscillation. However, the value of $V_{dcref}^{'}$ should be above the minimum allowed V_{dc} level which is determined by peak AC voltage.

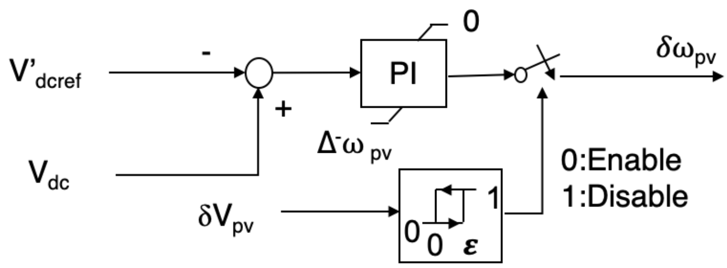

Figure 3.4: $\delta\omega_{PV}$ generation for power limiting with hysteresis effect

Another technique is the hysteresis effect in the VSI controller. The feed-forward loop of $\delta\omega_{PV}$ is enabled when δV_{PV} reaches zero but disabled when δV_{PV} passes a positive value ε. This is to prevent the VSI switching between VCM and PCM due to a small fluctuation in δV_{PV}. For example, in MPPT mode, fluctuations of V_{dc} will lead δV_{PV} to jump around zero. However, the VSI controller should stay in PCM mode rather than switching back and forth between VCM and PCM. The setting of this hysteresis (ε) is dependent on specific applications. Usually, there is a region around the MPP within which the slope of dP_{PV}/dV_{PV} is near zero. It means the power generated within that region is approximate to P_{PV-MPP}.

3.1.3 Simulation of PV Control

3.1.3.1 DC/DC Boost Converter Control

A single two-stage PV source is simulated in this section, as shown in Figure 3.5, to verify the effectiveness of the proposed strategy. The parameters of the solar panels are listed in Table 3.1. According to 2.2, the minimum value of the DC bus capacitance is $13mF$ assuming a time constant of 10 cycles of fundamental period. A $C_{dc} = 20mF$ is chosen as the DC bus capacitance in both the PV sources and battery sources in the simulation studies. This value seems large in practice but it can be reduced by reducing the nominal power rating of the inverter, reducing time constant or increasing DC bus voltage. A highly rated inverter is chosen here in order to demonstrate the power sharing more clearly.

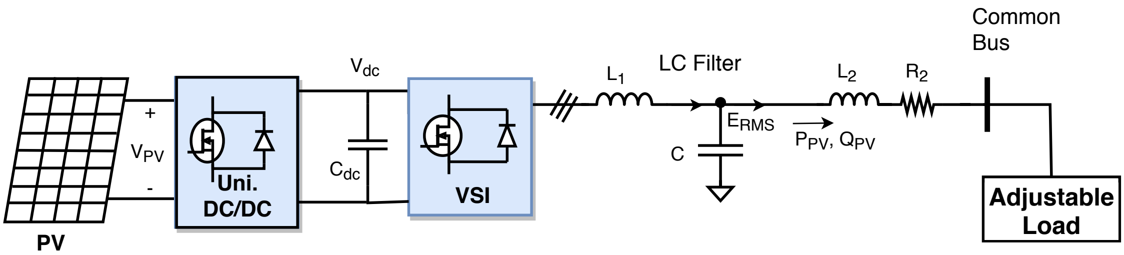

Figure 3.5: Structure of the simulated PV source

Parameters	Values	Parameters	Values
Module	SunPower SPR-305E-WHT-D	Voltage at MPP (V)	273.5
Maximum Power (kW)	17	Current at MPP (A)	63
Open circuit voltage (V)	321	$I_r(W/m^2)$	1000
Short circuit current (A)	77.48	$T_a(^oC)$	25

Table 3.1: Parameters of the simulated solar arrays

In the first simulation, the proposed control strategy for the boost converter controller is implemented while the VSI control adopts the traditional droop method without any power limiting function. The load increases from $14kW$ (below P_{MPP}) to $24kW$ (above

P_{MPP}) at t=2s. Between 0 to 2s, we can see from Figure 3.6a to Figure 3.6c that the real power and reactive power outputs follow the load demand and the grid voltage is at its nominal phase-to-neutral (ph-n) value ($230V$). Meanwhile, Figure 3.6d shows V_{dc} is well regulated at the reference value. As for the solar array, Figure 3.6e shows MPPT algorithm generates a value of V_{MPP} at $273V$ while PV operates at a voltage level of around $300V$ (i.e. $V_{PV} \approx 300V$) as a result of voltage deviation ($\delta V_{PV} \approx 27V$) generated by the V_{dcref} control loop. It shows that the control strategy allows PV curtailment.

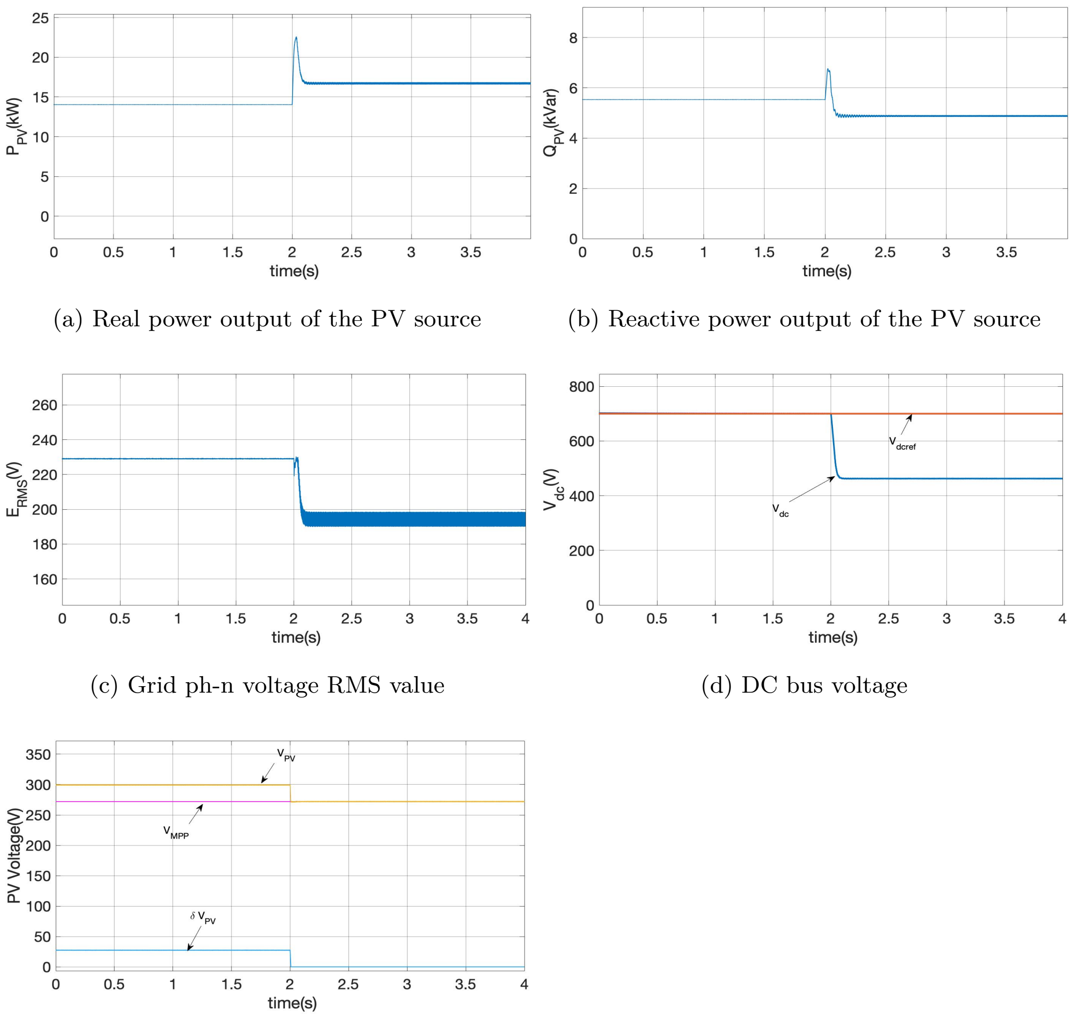

(a) Real power output of the PV source

(b) Reactive power output of the PV source

(c) Grid ph-n voltage RMS value

(d) DC bus voltage

(e) PV voltage

Figure 3.6: Simulation of PV boost converter control

At t=2s, the load increases to a level above P_{MPP}. Figure 3.6e shows δV_{PV} drops to zero after t=2s and V_{PV} starts to track V_{MPP}. Because $P_{PV-MPP} < P_L$, the grid voltage and

DC bus voltage drops below the reference value. As a result, the power quality degrades on the grid side. It is worth noting that the grid voltage oscillates after the transient which is because both real and reactive power flow tries to regulate the voltage level. Real power regulates it in accordance with Ohm's Law in the RL load condition and reactive power regulates it based on the droop method. This phenomenon can be avoided by connecting a backup source to compensate for the power shortage. However, the PV source keeps operating at its MPP, trying to compensate for the power mismatch as much as possible. It can be seen from Figure 3.6e that stable PV operation is maintained during the whole process.

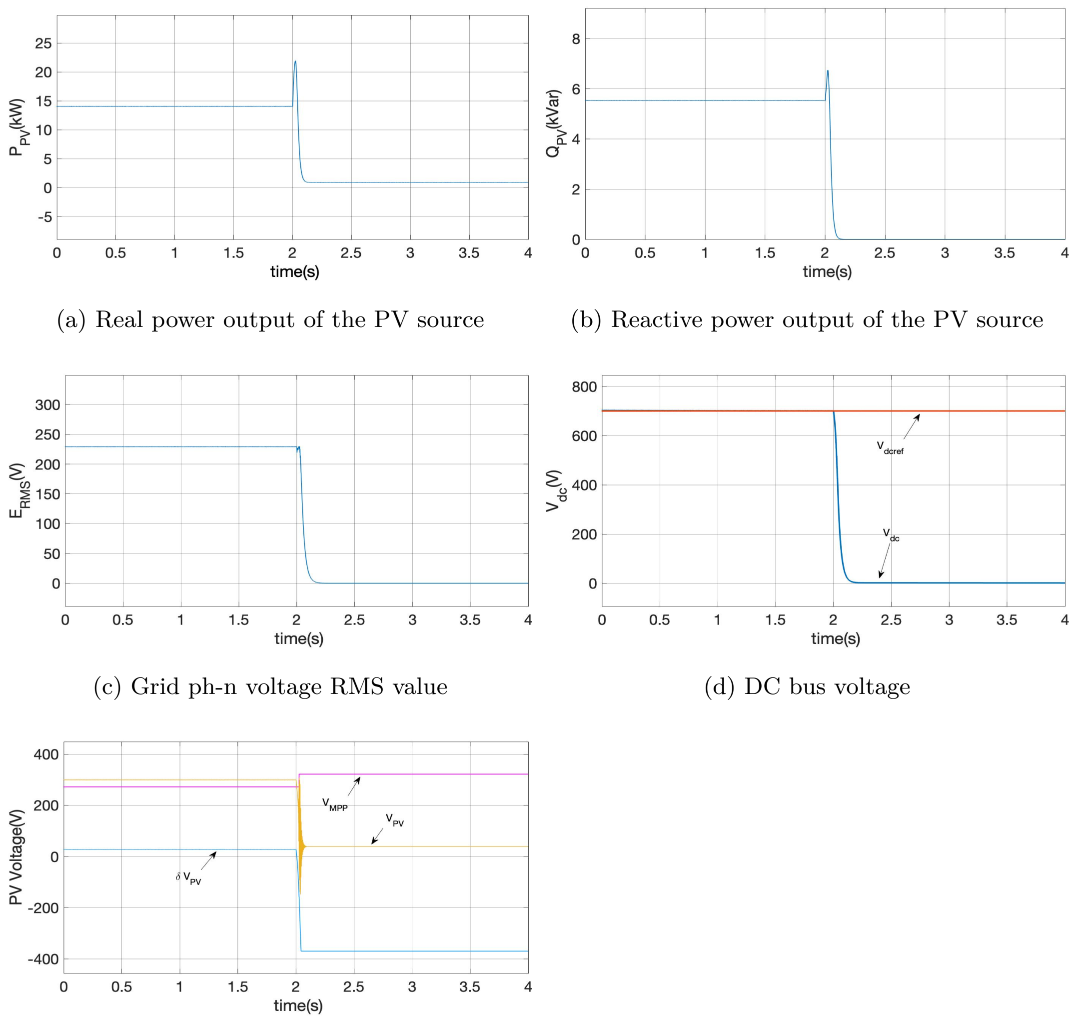

(a) Real power output of the PV source

(b) Reactive power output of the PV source

(c) Grid ph-n voltage RMS value

(d) DC bus voltage

(e) PV voltage

Figure 3.7: Simulation of the stability issue in a PV source

To demonstrate the stability issue associated with a PV source, another simulation is conducted under the topology of Figure 3.5. In the V_{dcref} control loop, the generated V_{PVref} is allowed to go below V_{MPP} such that PV is able to operate on the left-hand-side of the $P_{PV} - V_{PV}$ curve. The other settings remain same as the previous simulation. The modified simulation results are shown in Figure 3.7. It can be seen that the system collapses after the load increases at t=2s. The system shuts down with zero power output and solar panels operates at around the short circuit condition. In conclusion, if PV operates at the left-hand-side of the $P_{PV} - V_{PV}$ curve, it can easily become unstable under power disturbances. Note stability here is referred to in a system (not control) sense in that the output of the DC/DC converter collapses as the PV source operates in its unstable region.

3.1.3.2 Simulation of a PV-Based MG

To compensate for the frequent power shortage from insufficient PV power generation, another source needs to be integrated into the MG. A CVS is connected here as the supplement. It supports the additional power demand when PV reaches its MPP. The simulated grid is structured as shown in Figure 3.8. The settings for droop control follows the proposed prioritized power sharing strategy, as shown in Table 3.2.

The system experiences a load step change at t=1.5s. The available PV power is sufficient for local power demand before t=1.5s while the load exceeds the maximum PV power generation after t=1.5s.

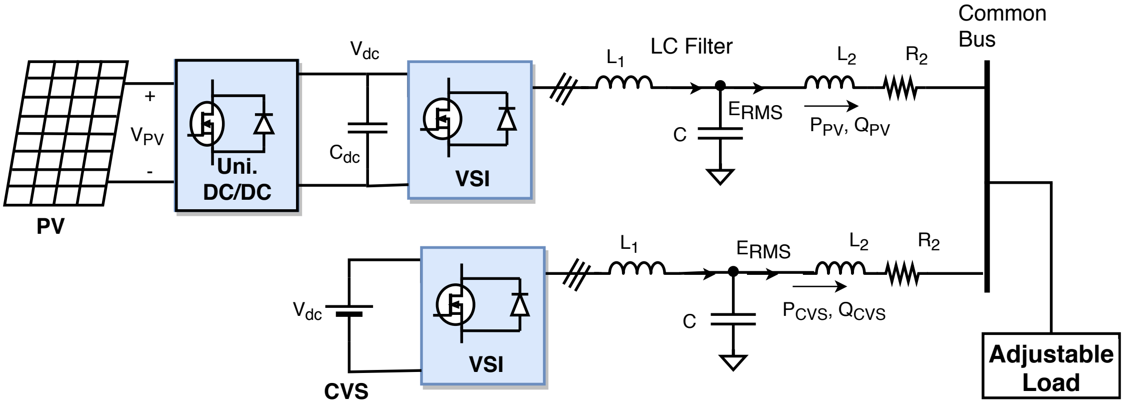

Figure 3.8: Structure of the simulated PV-based MG

Parameters	Values
$\omega_{0PV}/\omega_{0CVS}(rad/s)$	100π
$P_{0PV}(kW)$	20
$P_{0CVS}(kW)$	0
$m_{PV}/m_{CVS}(rad/(s\cdot W))$	7.5×10^{-5}
$E_{0PV}/E_{0CVS}(V)$	230
$Q_{0PV}/Q_{0CVS}(kVar)$	0
$n_{PV}/n_{CVS}(V/Var)$	2.5×10^{-4}

Table 3.2: Settings of droop control in PV operation

Figure 3.9a represents the real power output from two sources during the whole process. At t=1.5s, the PV operation moves to its MPP while the additional load is supported by the CVS. At the same time, reactive power sharing follows the average sharing scheme, shown in Figure 3.9b. The transient induced oscillation in the reactive power measurement (compared to real power) is of slightly higher frequency due to the reactive power droop coefficient chosen. The magnitude of grid voltage (Figure 3.9c) stays constant despite a small transient at t=1.5s.

The grid frequency (Figure 3.9d) drops after an increase of real power demand. Furthermore, Figure 3.9e shows that V_{dc} in the PV source drops to a new reference value after the power shortage and stays constant afterwards. It also explains the big transient in real power output at t=1.5s because some power is released from the DC capacitor. Figure 3.9f also confirms that PV operation switches from VCM to PCM at t=1.5s.

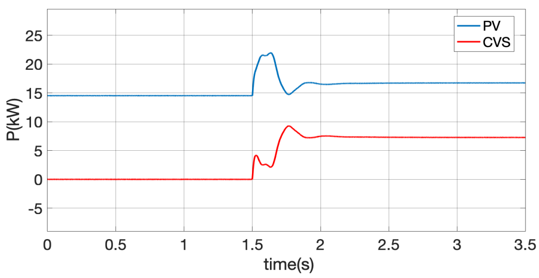

(a) Real power outputs of two sources

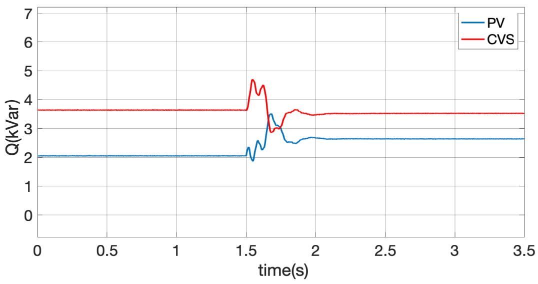

(b) Reactive power outputs of two sources

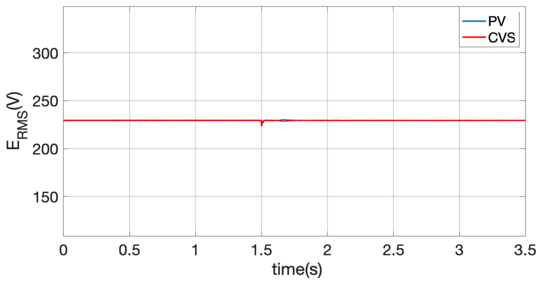

(c) Grid ph-n voltage of the PV-based MG

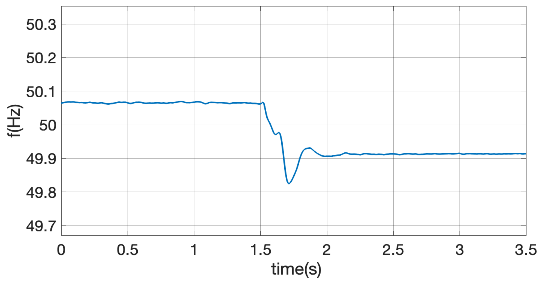

(d) Grid frequency of the PV-based MG

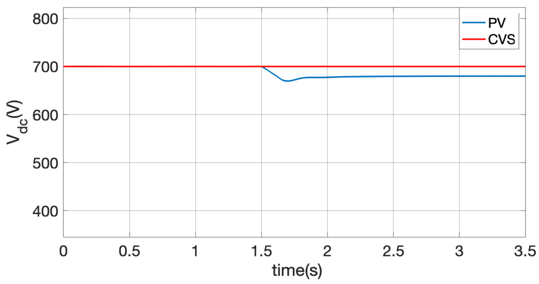

(e) DC bus voltage of the PV source

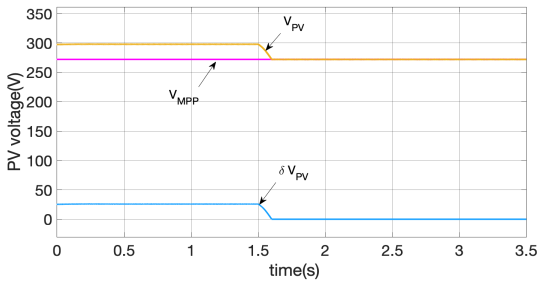

(f) PV voltage

Figure 3.9: Simulation results of a PV-based MG

3.1.3.3 Simulation of MPPT Method

To verify the effectiveness of the proposed strategy under varying I_r, a cloud shadow was simulated in a MG shown in Figure 3.8. From t=2s, the cloud shadow passes over the solar panels and I_r drops from $1000W/m^2$ to $500W/m^2$ over a 2s interval, shown in Figure 3.10a. The PV panel power characteristics at different I_r levels are shown in Figure 3.10b. The load was held constant at $15kW$ during this simulation. Other settings of the system are the same as in the last section.

The simulated cloud overshadows all the connected PV panels so that they have uniformed power characteristics. In reality, partial shading conditions can occur and corresponding improved MPPT strategies can be found in [98,99]. Since MPPT loop operates independently from the DC bus voltage control loop in the proposed boost converter control, traditional IC MPPT algorithm is still deployed here under uniformed solar irradiance, for the sake of simplicity. The investigation of advanced MPPT algorithm is beyond the scope of this thesis.

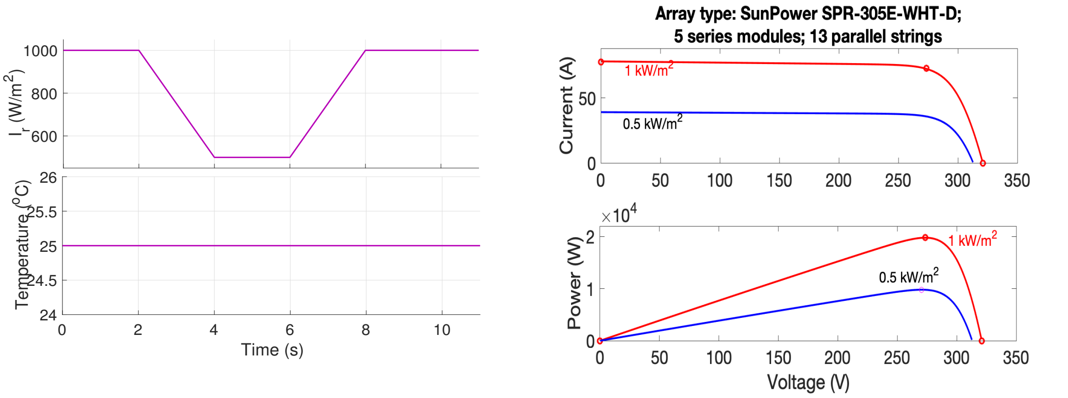

(a) Solar irradiance dynamics

(b) Power characteristics of solar arrays under different I_r levels: $I_r = 1kW/m^2$ and $I_r = 0.5kW/m^2$

Figure 3.10: The dynamics of solar irradiance (left) and its corresponding power characteristics (right)

From Figure 3.11a, we can see that the PV power output starts to drop and track the maximum power from t=3s. When I_r starts to increase after t=6s, the PV generation also increases until the local power demand is met. At the same time, the CVS unit is idle during the first 3s and after 7s during PV power curtailment. Figure 3.11f also confirms that PV operates under PCM with a negative $\delta\omega_{PV}$ between t=3s and t=7s, while the CVS operates under VCM with a zero $\delta\omega_{CVS}$. Reactive power sharing (Figure 3.11b) behaves opposite to real power as a result of the voltage drop across the AC bus. DC bus voltage in Figure 3.11e tracks different reference values during different PV operation modes. The reference value for V_{dc} in the PV source reduces when transitioning from power curtailment to MPPT mode. Note that PV autonomously switches to MPPT operation at around t=3s when I_r reduces to around $750W/m^2$.

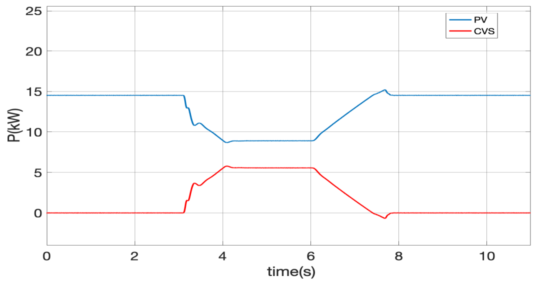

(a) Real power outputs

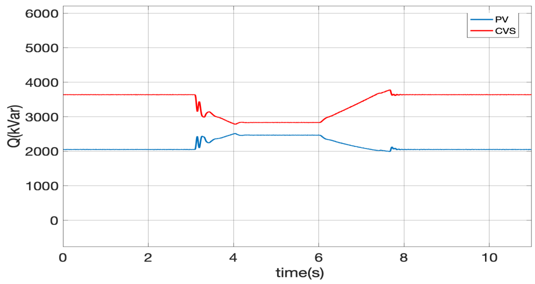

(b) Reactive power outputs

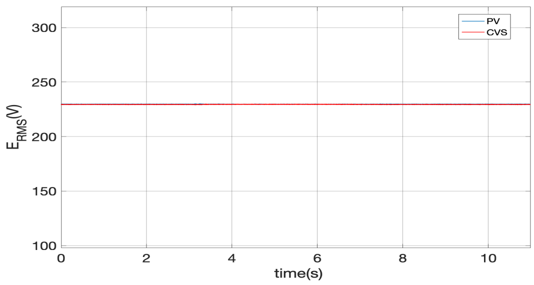

(c) Grid ph-n voltage of PV-based MG

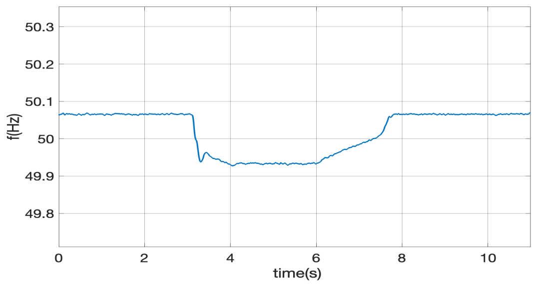

(d) Grid frequency of PV-based MG

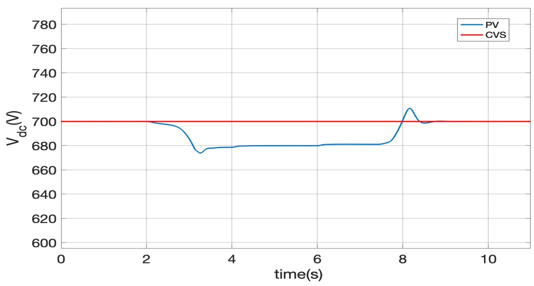

(e) DC bus voltage of PV source

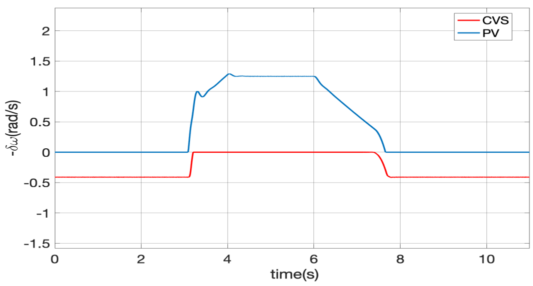

(f) Frequency deviation of each source

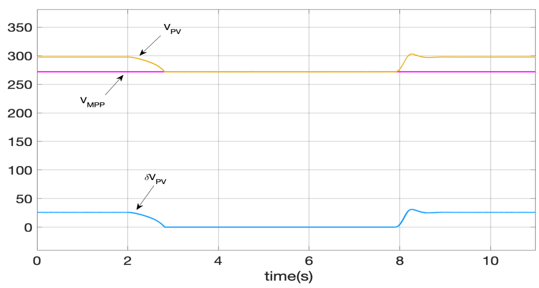

(g) PV voltage

Figure 3.11: Performance of PV source under varying weather conditions

3.2 Control of a Battery Source

The power shortage caused by the intermittent generation of RES can be compensated by ESS such that ESS are indispensable elements in RE-based MGs. However, a co-operative operation of RES and ESS relies on an effective power management strategy. The proposed RE-prioritized power sharing strategy provides a coordinating scheme. In this section, the power characteristics and a general topology of battery sources are illustrated. For the battery source as shown in Figure 3.12, a control strategy is proposed under the proposed power sharing scheme.

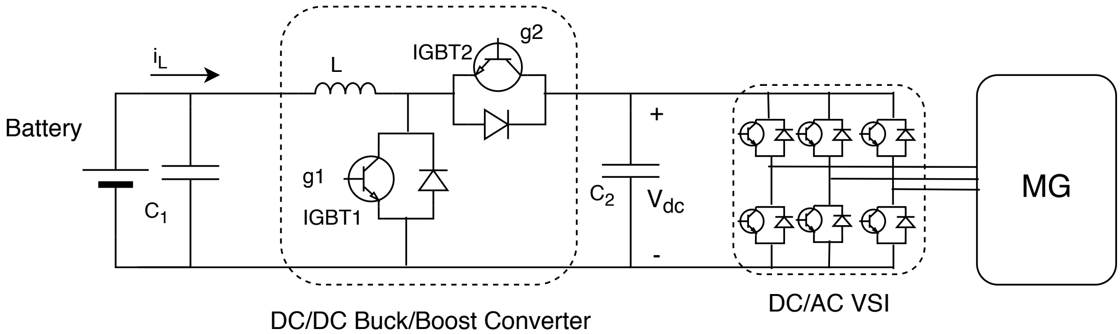

Figure 3.12: Connection structure of a MG interfaced Battery source

3.2.1 Control Strategy in a Battery Source

A battery can be treated as a chargeable DC voltage source. It supplies/draws power demanded/supplied through the VSI in order to maintain power balance. DC bus voltage is again used to indicate the condition of power balance between generation and consumption. It is an easy accessed local signal. Furthermore, the battery output voltage is fairly constant across its operating range so there is no unstable operating region as seen in PV. The limits on charging and discharging rate demonstrated in Chapter 2.2.2 are based on product specifications and applications. The upper and lower power limits can thus be fairly easily estimated so that the $\delta\omega_{BAT}$ generation for the proposed modified droop control can adopt the traditional power limiting method. The control diagram is shown in Figure 3.13.

As for the DC/DC buck/boost converter, it is to regulate V_{dc} to a constant value so as to keep power balance. Two V_{dc} regulation loops are designed for this controller, shown in Figure 3.14. In boost mode, the non-minimum phase phenomenon introduces the inverse response of the output voltage dynamics. As a result, the dynamics of output voltage is not usually directly used for controller design. Instead, the inductor current is widely used as the control variable for boost mode control. In this control topology, an inner current loop is cascaded with an external voltage control loop to regulate output voltage. It provides some advantages: easier-to-design, fast transient response, fast over current protection, as well as its insensitivity to circuit parameters [100].

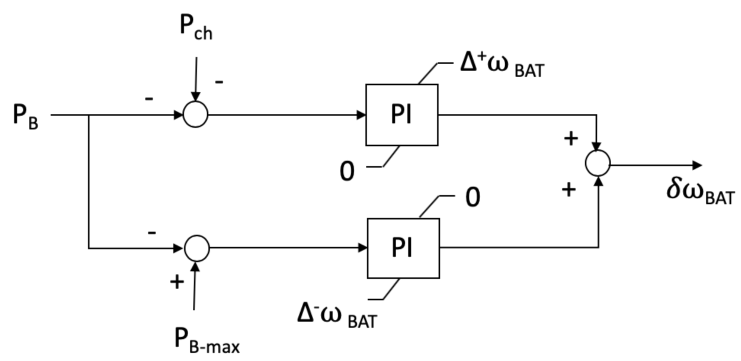

Figure 3.13: Control diagram of $\delta\omega_{BAT}$ generation

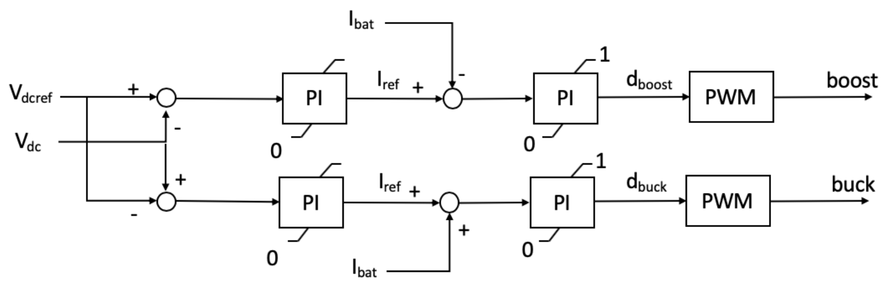

Figure 3.14: Control loop of the buck/boost converter

The IGBT gate drive generation for the buck/boost converter shown in Figure 3.12 is summarised in Table 3.3. In charging mode, the power output P_B is negative and the converter operates in buck mode. Conversely, the converter is in boost mode while P_B is positive under discharging mode.

P_B	> 0	< 0
g_1	*boost*	0
g_2	0	*buck*

Table 3.3: Switching signals in a bidirectional converter

3.2.2 Simulation of Battery Control

A battery can operate alone to supply power demand. However, it needs to connect to the grid or other power sources to be charged. In the simulated MG, a battery source is in parallel with an ideal DC voltage source, as shown in Figure 3.15. It aims to verify the efficacy of the buck/boost converter control and automatic transition between charging mode and discharging mode within the battery source.

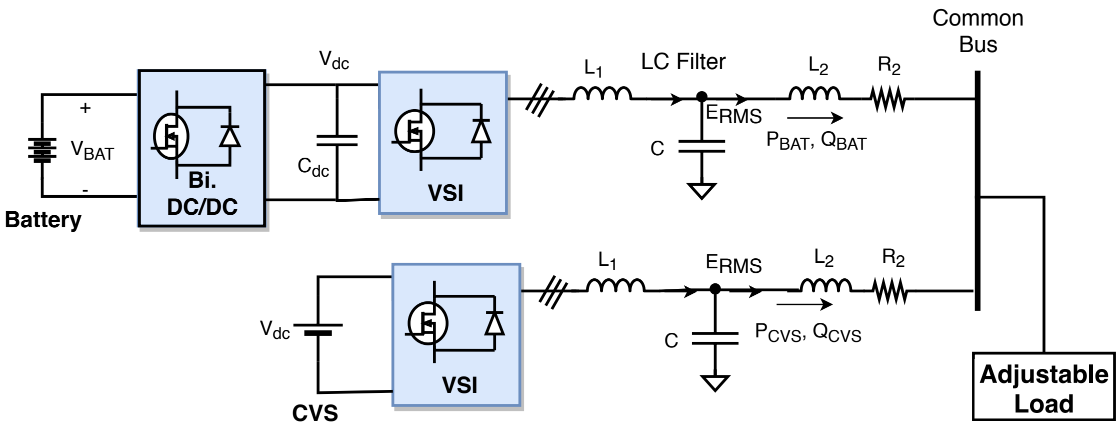

Figure 3.15: Structure of the simulated battery-based MG

The rating of the CVS is $20kW$ and it is set as the prioritized source of power supply. Some parameters with respect to the state of the battery are shown in Table 3.4. The settings of droop control for these two sources are shown in Table 3.5.

Type	Nominal voltage (V)	Rated capacity (Ah)	SOC (%)	Nominal discharge current (A)
Lead-Acid	270	500	80	100

Table 3.4: Parameters of the battery condition

Parameters	Values
$\omega_{0-BAT}(rad/s)$	99.75π
$P_{0-BAT}(kW)$	20
$\omega_{0-CVS}(rad/s)$	100π
$P_{0-CVS}(kW)$	20
$m_{BAT}/m_{CVS}(rad/(s\cdot W))$	7.5×10^{-5}
$E_{0-BAT}/E_{0-CVS}(V)$	230
$n_{BAT}/n_{CVS}(V/Var)$	2.5×10^{-4}
$P_{B0}(kW)$	20

Table 3.5: Settings of droop control in battery operation

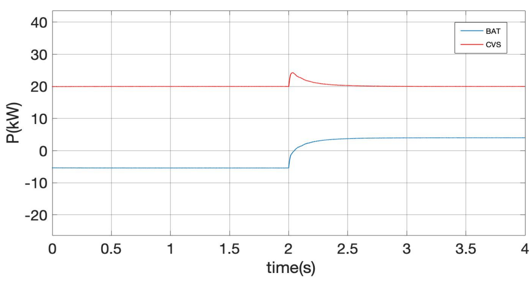

(a) Real power output of the PV source

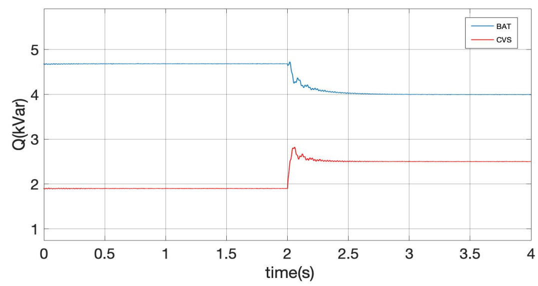

(b) Reactive power output of the PV source

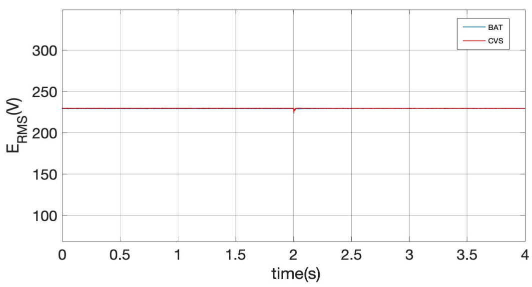

(c) Grid ph-n voltage

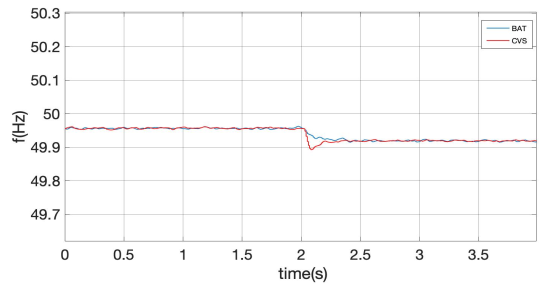

(d) Grid frequency

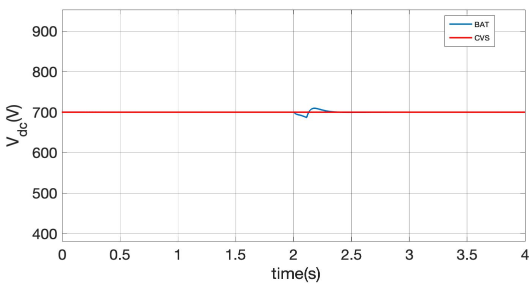

(e) DC bus voltage

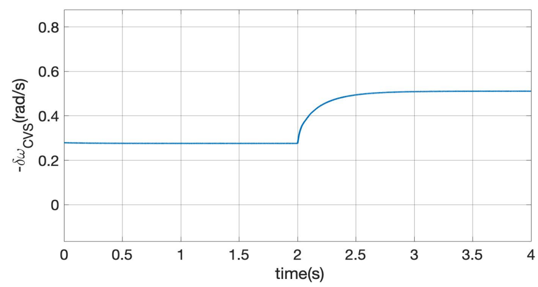

(f) Frequency deviation in the CVS

Figure 3.16: Simulation of control in a battery-based MG

The performance of the control strategy is shown in Figure 3.16. In Figure 3.16a, we can see that during 0 to 2s, when the load ($15kW$) is below the power limit of the CVS, the load is totally supported by the CVS. Meanwhile, the battery is being charged at a rate of $5kW$, which drives P_{CVS} to reach its power limit. At t=2s, the load increases to $25kW$. The battery then switches from charging mode to discharging mode at a discharging rate of $5kW$ to supplement power shortage. During the simulation, grid voltage and frequency are well regulated and within the acceptable range, according to Figure 3.16c and Figure 3.16d. There is a small transient in V_{dc} as shown in Figure 3.16e due to the step increase of load at t=2s. The negative frequency deviation value shown in Figure 3.16f indicates that CVS operates under PCM since t=0s. Note that the SOC level of battery is within the normal range and its variation across the whole process (4s) is minimal.

3.3 Simulation of RE-Prioritized Power Sharing in a Hybrid MG

In this simulation, a hybrid MG was built where the original ideal DC voltage sources (in Section 2.4) were replaced by a two-stage PV, a two-stage battery and a single-stage conventional source. To focus on the cooperation of multiple control strategies, only one unit of each type of source is included in the simulated MG. While the CVS is still represented by an ideal DC voltage source, the grid structure is shown in Figure 3.17.

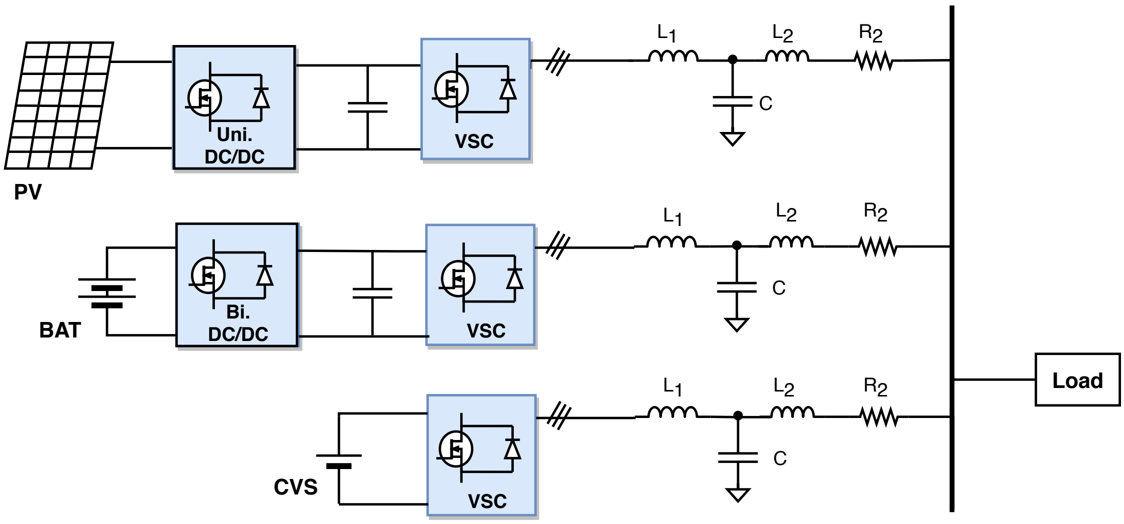

Figure 3.17: Structure of a hybrid MG with three types of sources

The PV source is rated at $17kW$ while battery at $15kW$ and CVS at $15kW$. The system experiences a series of step changes of load, shown in Table 3.6. The grid parameters follows the same settings as in Section 2.4. In order to achieve RE-prioritized power sharing, the design of droop control parameters is based on the power ratings and grid standard, presented in Table 3.7.

$t(s)$	0-2	2-5	5-8	8-11
$P_L(kW)$	15	25	40	30
$Q_L(kVar)$	5	5	5	5

Table 3.6: Local load dynamics in a hybrid MG

Parameters	Values	Parameters	Values
Q_0	$0Var$	n	$2.5 \times 10^{-4} V/var$
P_{0-PV}	$20kW$	ω_{0-PV}	$100\pi rad/s$
P_{0-BAT}	$15kW$	ω_{0-BAT}	$99.75\pi rad/s$
P_{0-CVS}	$0kW$	ω_{0-CVS}	$99.75\pi rad/s$
m_{PV}	$7.5 \times 10^{-5} rad/(s.W)$		
m_{BAT}	$2.5 \times 10^{-5} rad/(s.W)$		
m_{CVS}	$7 \times 10^{-5} rad/(s.W)$		

Table 3.7: System parameters in a hybrid MG

The simulation results are shown from Figure 3.18. According to Figure 3.18a, we can see that the PV source outputs the maximum power throughout the whole process, which can also be seen in Figure 3.18f and Figure 3.18g. In Figure 3.18f, the negative $\delta\omega_{PV}$ value means the PV operates in PCM at MPP. In Figure 3.18g, the PV voltage V_{PV} also aligns with V_{MPP}. During 0 to 2s, PV supports both local load and battery charging at a rate of $2kW$. During 2s to 5s, because of the step increase of load, battery discharges power at a rate of $8kW$. During these first two periods, the battery source operates as a VCM unit which controls the grid voltage and tracks the level of local load. After t=5s, the battery discharges at its maximum rate and transits from VCM to PCM. Meanwhile, the CVS transits from PCM to VCM. It is also indicated in Figure 3.18f that the value of $\delta\omega_{CVS}$ reduces to zero from a positive value at t=5s. During 8s to 11s, when the local load is at a lower level, the CVS transits back to idle condition (PCM) and the battery source transits to VCM again.

The reactive power demand does not change during the whole procedure but the sharing pattern in Figure 3.18b varies with the real power sharing pattern. It is mainly because of the varying voltage drop across the coupling line under different real power flow. The grid voltage in Figure 3.18c is well regulated during the whole procedure and the grid frequency in Figure 3.18d decreases as the total load increases but it is kept within the acceptable range. There are three small transients on V_{dc} performance at the instant of load changes in Figure 3.18e. The short transient time implies the effectiveness of DC bus voltage regulation.

3.4 Decentralized Frequency Restoration

In the proposed RE-prioritized power sharing strategy, the allowed frequency deviation range is divided into three regions and different sources take charge of frequency regulation in different regions. It is important not to deteriorate this mechanism during frequency restoration at secondary level control. It can be achieved by a time-scale separation between primary and secondary control. A simple decentralized strategy is tested in this section based on a three-source MG.

For simplicity, decentralized PI control is selected as the tested strategy. Following the PI control demonstrated in [55–57], the frequency restoration adopts the strategy as shown below:

$$\delta\omega_{i-fres} = \frac{1}{T_{fres}s+1}(k_p + \frac{k_i}{s})(\omega_{ref} - \omega_i) \tag{3.3}$$

where $\delta\omega_{i-fres}$ is the frequency restoration term imposed to primary control in ith unit. The local measurement of the grid frequency is fed into a PI controller. After a low pass filter, it generates a local correction term $\delta\omega_{i-fres}$ adding to primary control. Apart from choosing the same control parameters, the integration error can be minimized by activating the restoration process at the same time for all units. Meanwhile, the initial conditions are also set to be identical.

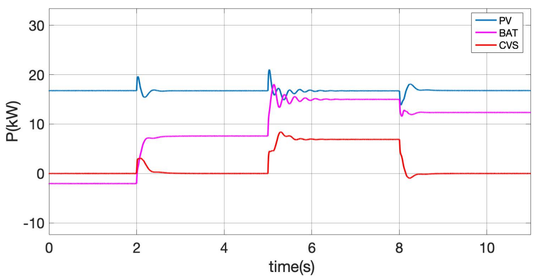

(a) Real power output of the MG sources

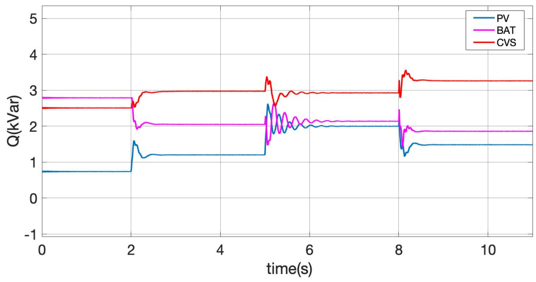

(b) Reactive power output of the MG sources

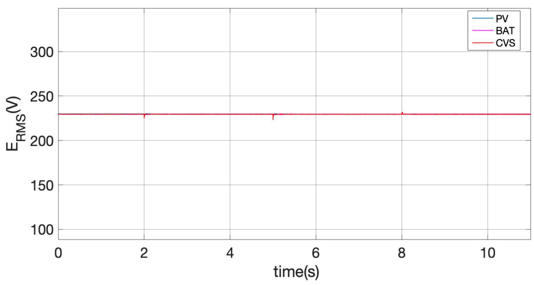

(c) Grid ph-n voltage

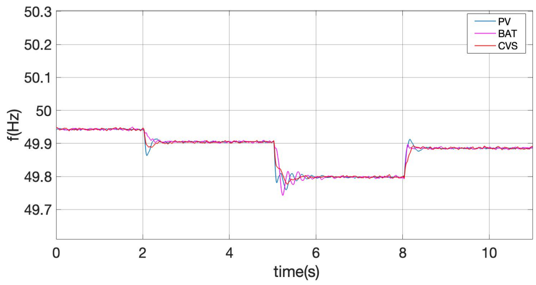

(d) Grid frequency

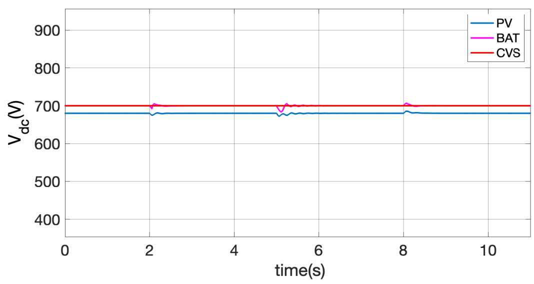

(e) DC bus voltage

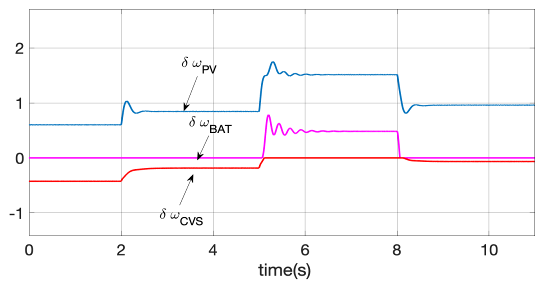

(f) Frequency deviation in three sources

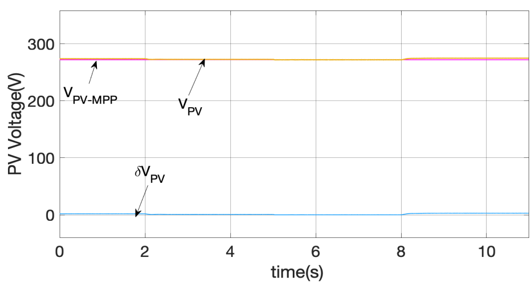

(g) PV voltage

Figure 3.18: Simulation results of RE-prioritized power sharing in a hybrid MG

In simulation, the same sources operate under the same load conditions as in Section 3.3.

However, the time interval lasts longer (5s) under each load condition due to the slow response of secondary control.

In Figure 3.19, the grid frequency value is gradually restored back to the nominal value after each load disturbance. Meanwhile, the real power sharing dynamics are not impacted, compared to Figure 3.18a.

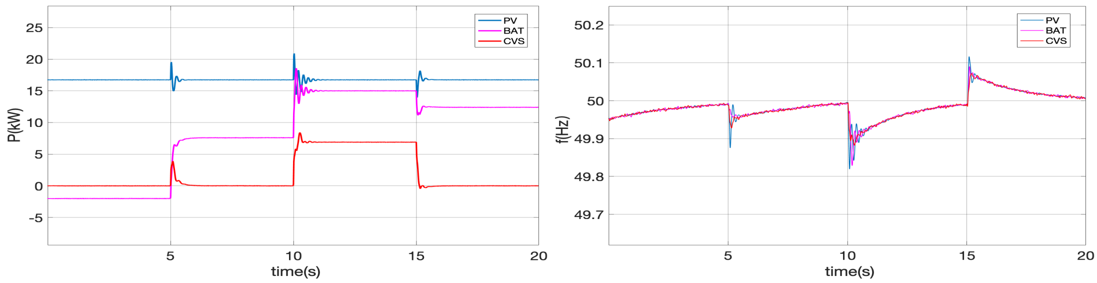

(a) Real power sharing performance

(b) Grid frequency

Figure 3.19: Simulation results of frequency restoration

3.5 Conclusions

This chapter discussed decentralized strategies for the RE-prioritized power sharing strategy. For PV sources, the coordinating strategy for boost converter and VSI were proposed. It could autonomously switch PV operation between MPPT mode and power curtailment mode without inter-unit communications. Meanwhile, the controller for buck-boost converter in a battery source was also designed which was responsible for battery charging and discharging. Finally, all the proposed strategies coordinated with the modified droop control to achieve RE-prioritized power sharing strategy. The simulation performance has shown the proposed strategy is able to prioritize RES in real power supply. It can also respond to varying weather conditions, e.g. varying solar irradiance. As grid frequency deviated from the nominal value under power disturbances, frequency restoration was also discussed without deteriorating primary power sharing.

In the next chapter, the proposed control strategies are verified in a prototype MG.

Chapter 4

Experimental Setup

4.1 Introduction and System Overview

A prototype MG was built at the University of Newcastle with the details of the hardware set up described in this chapter.

The experimental system consists of three sources representing the three different types of DG in a MG: PV, Battery and CVS. Both the PV unit and battery unit are in the two-stage form, i.e. the VSI follows a DC/DC converter which boosts up the output voltage of the power source. The CVS represents a dispatchable source so its VSI is supplied from a DC power source. On the power demand side, resistive and inductive load banks form an RL load. Some step changes of the power demand are realized by changing the resistor values in the resistive load bank. The electrical layout of the prototype MG is shown in Figure 4.1. Its corresponding physical layout is shown in Figure 4.2.

4.2 Hardware Setup

The experimental MG is composed of three paralleled VSIs with each VSI supplied from different DC sources. The power source connects to the VSI directly or through a DC/DC converter. After the VSI, a LCL filter is connected before the common load. In summary, each unit is composed of a power source, an optional DC/DC converter, a VSI, a LCL filter and the coupling line. This section demonstrates the design of each unit and the selection of electrical elements.

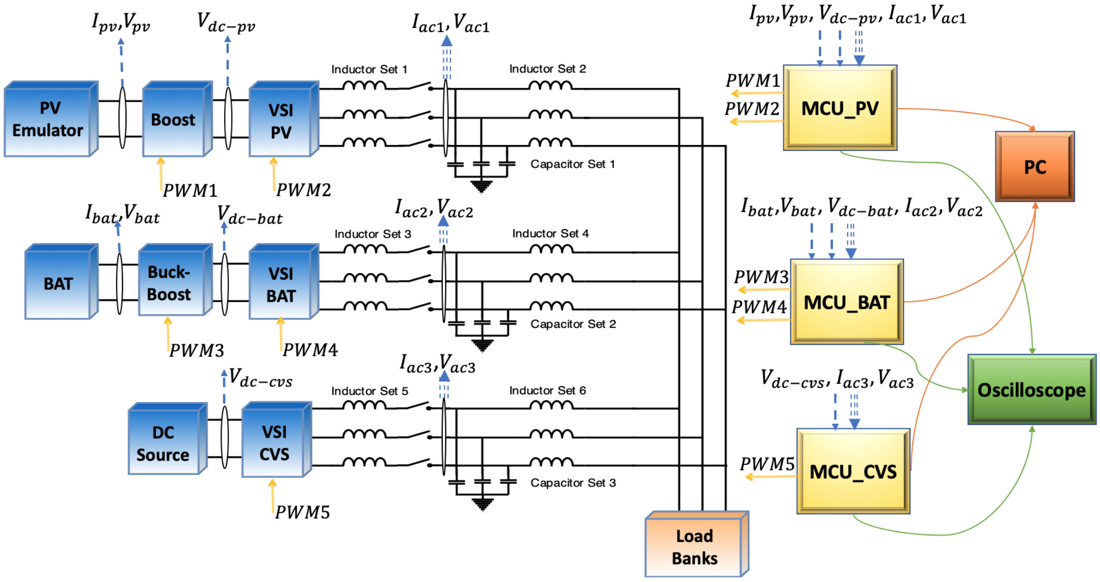

Figure 4.1: Block diagram of the prototype MG

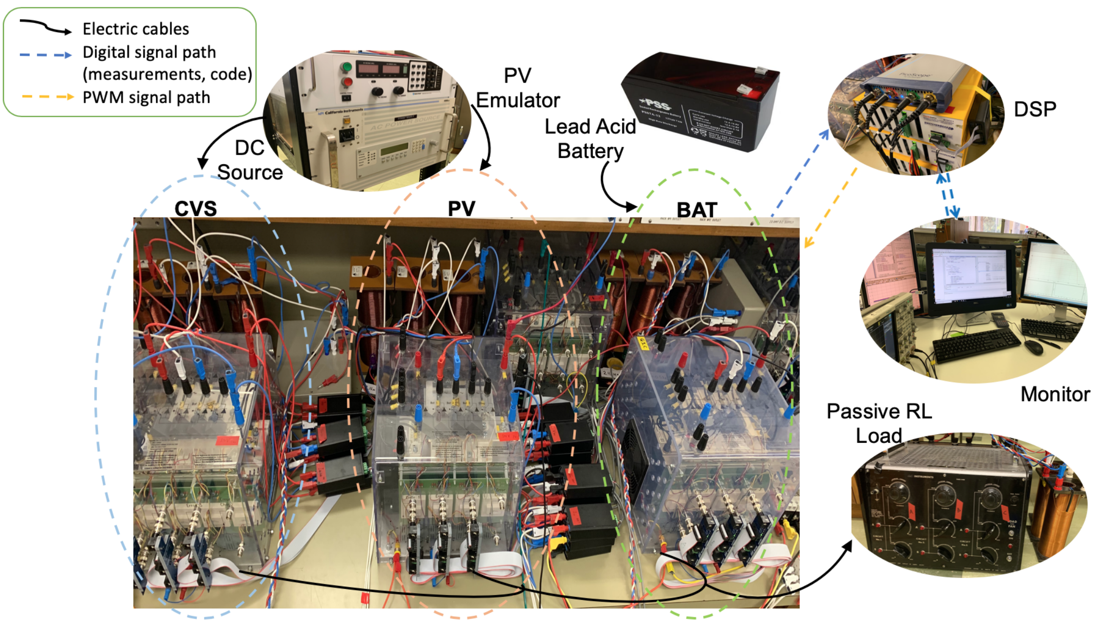

Figure 4.2: Photo of the prototype MG

4.2.1 LCL Filter and Load Banks

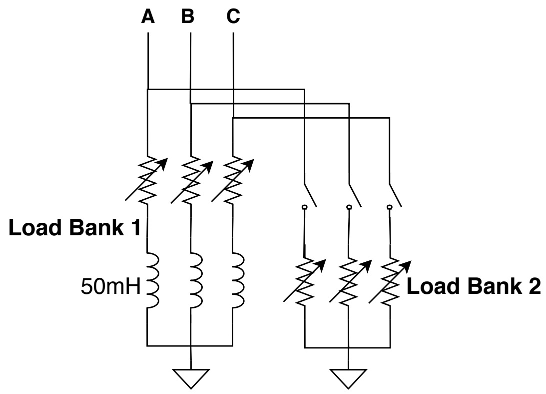

Figure 4.3: Connection structure of RL load banks

Load Bank 1	Load Bank 2	P (W)	Q (Var)
$R = 55\Omega$ $L = 50mH$	off	504	144
	$R = 100\Omega$	804	
	$R = 55\Omega$	1049	
	$R = 40\Omega$	1254	
$R = 30\Omega$ $L = 50mH$	off	785	410
	$R = 100\Omega$	1085	
	$R = 55\Omega$	1330	
	$R = 40\Omega$	1535	

Table 4.1: Different load conditions under the structure in Figure 4.3

In experiments, the elements of the LCL filter are chosen based on the required cutoff frequency and the availability of existing components in the laboratory. The cutoff frequency is relevant to supply frequency and the converter switching frequency, which is explained in Chapter 2. The experimental system operates at $50Hz$ with an inverter switching frequency of $10kHz$. The LC filter cut-off frequency is set to $800Hz$. Consequently, the inverter inductor is chosen as $2mH$ while the grid inductor is $5mH$. The filter capacitor is designed to be $20\mu F$.

The RL load is composed of resistive and inductive load banks. The three phase resistive load bank is adjustable and is in series with three 50mH inductors. The real and reactive power demand can both be changed by adjusting the value of the resistors. The step increase of real power demand is achieved by switching in an additional resistive load bank (Load Bank 2) in parallel with the first load bank (Load Bank 1). The details of the connection is shown in Figure 4.3. The nominal three-phase ph-n RMS voltage is $100V$. At this voltage, the corresponding load conditions are described in Table 4.1.

4.2.2 Components of the PV Source

In the PV unit, solar power is generated from a PV emulator, Magna-Power TSD600-8/+415HS. For this emulator, maximum output voltage is 600V with a current limit of 8A. Considering the system requirement, the reference PV characteristic is configured as shown in Figure 4.4 using the PV emulator software. The PV voltage and power output at the MPP is 163V and 920W respectively while the current is 5.65A. The short circuit current is 6.05A while the open circuit voltage is 193V.

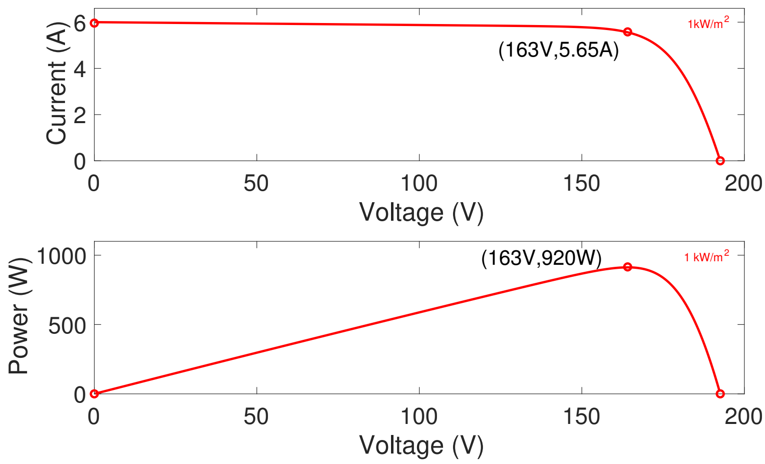

Figure 4.4: Reference PV characteristics: I-V (top); P-V (bottom)

As the PV unit is in two-stage form, the PV emulator is connected to the VSI through a boost DC/DC converter. The VSI adopts the Semikron SEMITEACH 18-kW three phase inverter. The unit includes a three-leg inverter and a fourth leg brake chopper. Each leg consists of two IGBT devices with anti-paralleled diodes. The details of the SEMITEACH Stack can be seen in Appendix A. Another SEMITEACH Stack is used as the DC/DC converter. Only one half-bridge is utilised where the bottom IGBT operates as a switching device and the upper diode restricts the current flow direction. The connection diagram of the PV source is shown in Figure 4.5, where the grey devices are inactive elements. The inductor in this boost converter is chosen as $5mH$ and is connected between the PV emulator and the SEMITEACH Stack.

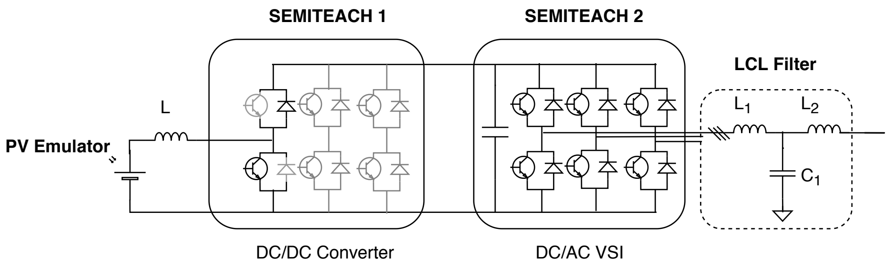

Figure 4.5: Connection diagram of the PV source

4.2.3 Components of the Battery Source

A series of lead-acid batteries are installed in the laboratory and they can provide up to $240V$ DC voltage and $20A$ current. There are multiple tapping points so that different output voltages can be selected. Since the capacity of the installed battery can provide a discharging rate far beyond the power demand, the power limits of the battery are deliberately set as $100W$ for charging rate and $500W$ for discharging rate.

The battery is connected through a buck/boost converter to the VSI, as shown in Figure 4.6. Similar to the PV unit, two SEMITEACH Stacks are used. One of them operates as the VSI while the other one provides a half-bridge to operate as a buck/boost converter. The bottom IGBT switch cooperates with the upper diode while working in the boost mode. Conversely, the upper IGBT switch cooperates with the bottom diode while working in the buck mode. A $5mH$ inductor is also connected between the battery source and the SEMITEACH Stack.

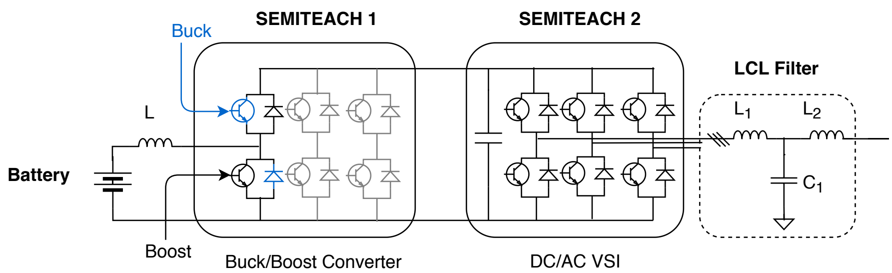

Figure 4.6: Connection diagram of the battery source

4.2.4 Components of the Conventional Source

The power source in the conventional unit can usually supply flexible power generation and is easily controlled. A programmable DC source with flexible output voltage is used to represent the CVS. It connects directly to the DC terminals on the SEMITEACH Stack.

4.2.5 Microcontroller

The DC/DC converters and VSIs are controlled by Microcontroller (MCU) which deploys Texas Instruments (TI) F28335 ControlCARD. It is integrated in a product provided by Denkinetic, SwitcherGear. SwitcherGear is a flexible platform for the rapid development of customised controllers for power converter systems. A module of 4-channel analogue output and two modules of 4-channel analogue input are also integrated. In addition, a hardware interface module which includes control power for the converter is also integrated. All the control signals are transmitted through a single 34-way ribbon cable and released at the SEMITEACH gate drivers through adapters. The current sensors and voltage sensors are also provided by SwitcherGear. The SwitchGear product and associated devices are detailed in Appendix A.

4.2.6 AC Grid Operation

Due to hardware restrictions, the three-phase AC grid operates at $173V/100V$ RMS voltage level and the power rating is down-sized to $1kW$. Consequently, the nominal DC bus voltage is chosen as $320V$. Without losing generality, the experimental setup can still validate the efficacy of the proposed methods.

Note that the start up procedure for droop-controlled units are as follows. One power source unit operates and supplies all the power to the common load, which operates as an AC grid. The other units are synchronised to this existing grid with specified power outputs. The amount of power output can be adjusted as desired under synchronous mode. These units can also switch to droop control mode by enabling the droop control algorithm. The other proposed control methodologies can then be enabled accordingly.

4.3 Experimental Implementation

This section implements the control strategies of real power sharing on the prototype MG. Initially, tests on PV and battery operation are conducted to validate the proposed control strategies for PV and battery sources. Next, both proportional real power sharing and the proposed RE-prioritized real power sharing are implemented. The last section confirms the argument that the MG frequency can be restored back to the nominal value through a secondary level control despite the priority order.

The experimental results are obtained by Picoscope, a 4 channel PC oscilloscope, with the sampling rate set at 5kS/s. While current and voltage values are directly measured, the real and reactive power values are calculated based on the $dq0$ reference frame discussed in Section 2.3.3.1.

4.3.1 PV Operation

In this first experiment, the MG is configured similarly to Figure 4.1 but it is only composed of a PV unit and a CVS unit. Their droop settings are shown in Table 4.2. P_{0-PV} is designed to be the rating of the PV source and P_{0-CVS} is chosen to be the minimum possible CVS generation.

Parameters	Values
$P_{0-PV}(W)$	1000
$P_{0-CVS}(W)$	0
$Q_{0-PV}/Q_{0-CVS}(Var)$	0
$\omega_{0-PV}/\omega_{0-CVS}(rad/s)$	100π
$E_{0-PV}/E_{0-CVS}(V)$	100
$m_{PV}/m_{CVS}(rad/(s\cdot W))$	0.0005
$n_{PV}/n_{CVS}(V/Var)$	0.005

Table 4.2: Droop control settings in PV operation

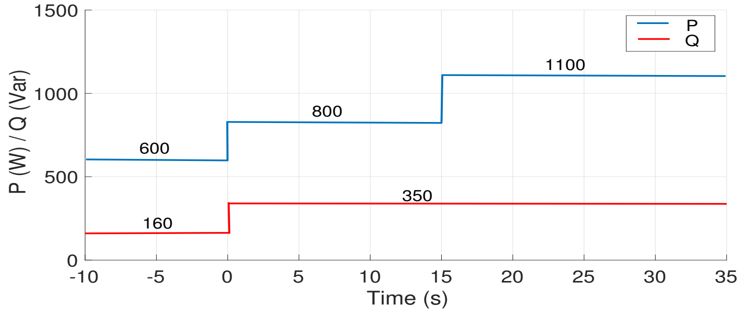

Figure 4.7: Load profiles during PV operation

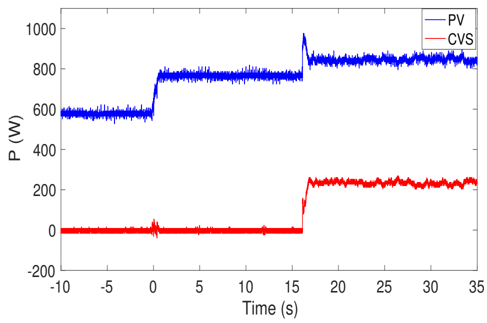

(a) Real power sharing

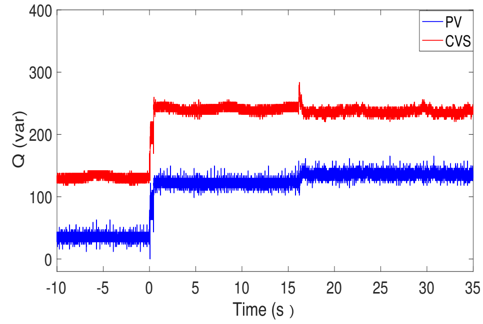

(b) Reactive power sharing

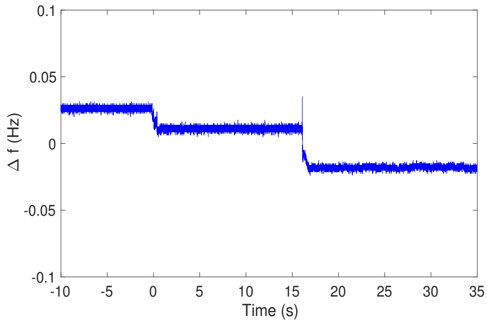

(c) Frequency deviation from nominal value

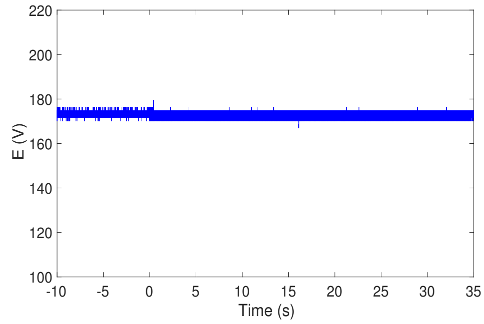

(d) VSI line to line voltage (RMS)

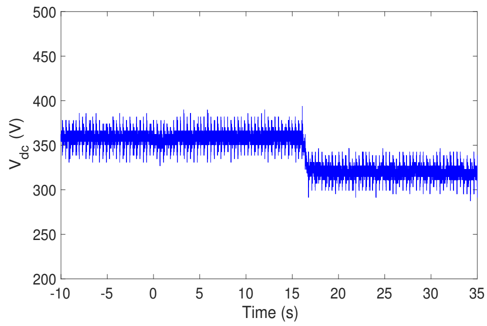

(e) DC bus voltage in PV unit

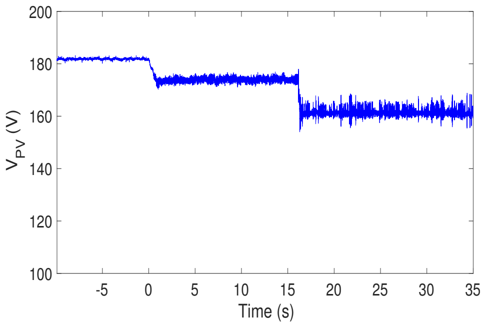

(f) PV output voltage

Figure 4.8: Experimental results of PV operation

Corresponding to the simulation results in Section 3.1.3, experimental results are shown in Figure 4.8. There are two step changes of load during the whole process, as shown in Figure 4.7.

During the first 10s, the power is only provided by PV, according to Figure 4.8a. This condition remains even after an increase of load at t=0s. At t=15s, a further increase of load drives the PV unit to output its maximum power and the CVS unit to supplement the power shortage. Meanwhile, the step increase of reactive power demand happens at 0s and the reactive power outputs are shown in Figure 4.8b. According to Figure 4.8c, the grid frequency decreases at t=0s and t=15s when the real power demand increases. The voltage magnitude decreases at t=0s due to the increase of reactive power demand, according to Figure 4.8d. The value of V_{dc} keeps relatively constant during the first 10s, as shown in Figure 4.8e. However, after PV unit reaching its MPP, V_{dc} drops to the second nominal value V'_{dcref}. Figure 4.8f shows that V_{PV} drops whenever there is an increase in power demand and it stays at V_{PV-MPP} while PV operating at MPPT (after t=15s).

Note that the CVS unit may operate differently in practice, which is determined by the specific system requirements. If the CVS unit is represented by some types of fuel/gas-powered generators (e.g. diesel, gas turbines), it requires a minimum power output threshold to start up the prime mover and there is a delay on start up. Rather than the minimum value of 0 chosen in the experimental settings, a positive threshold is commonly chosen in practice, say 10%. It means the CVS only operates until its real power demand reaches 10% of its power rating. This design can be achieved by droop setting adjustments in cooperation with a hard limit imposed to the CVS. However, the discussion of the detailed design is out of the scope of this thesis.

The following experiment verifies that the PV unit can track a variable MPP under varying weather conditions. In the experiment, the I_r changes from $1000W/m^2$ to $500W/m^2$ from t=10s to t=45s and increases back up to $1000W/m^2$ from t=60s, as shown in Figure 4.9. The corresponding PV power characteristics are also shown on the right. It can be seen that P_{PV-MPP} varies between $920W$ and $450W$ under the varying solar irradiance. In addition, the temperature stays constant at 25^oC and the load is fixed at $770W$.

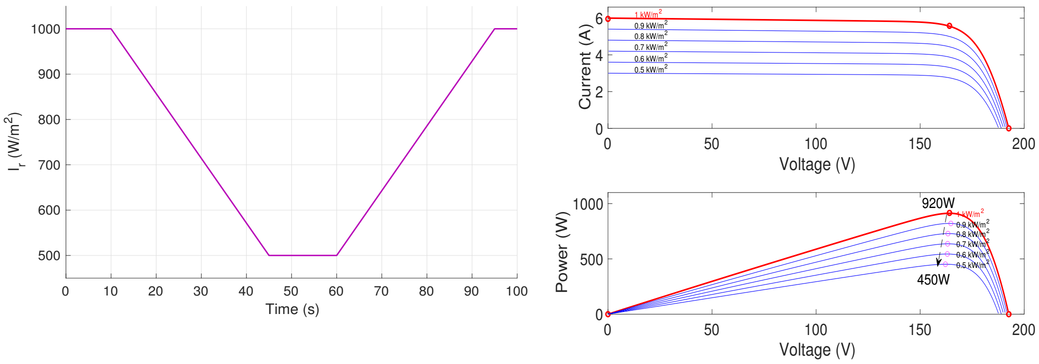

Figure 4.9: Varying solar irradiance (left) and corresponding PV power characteristics (right)

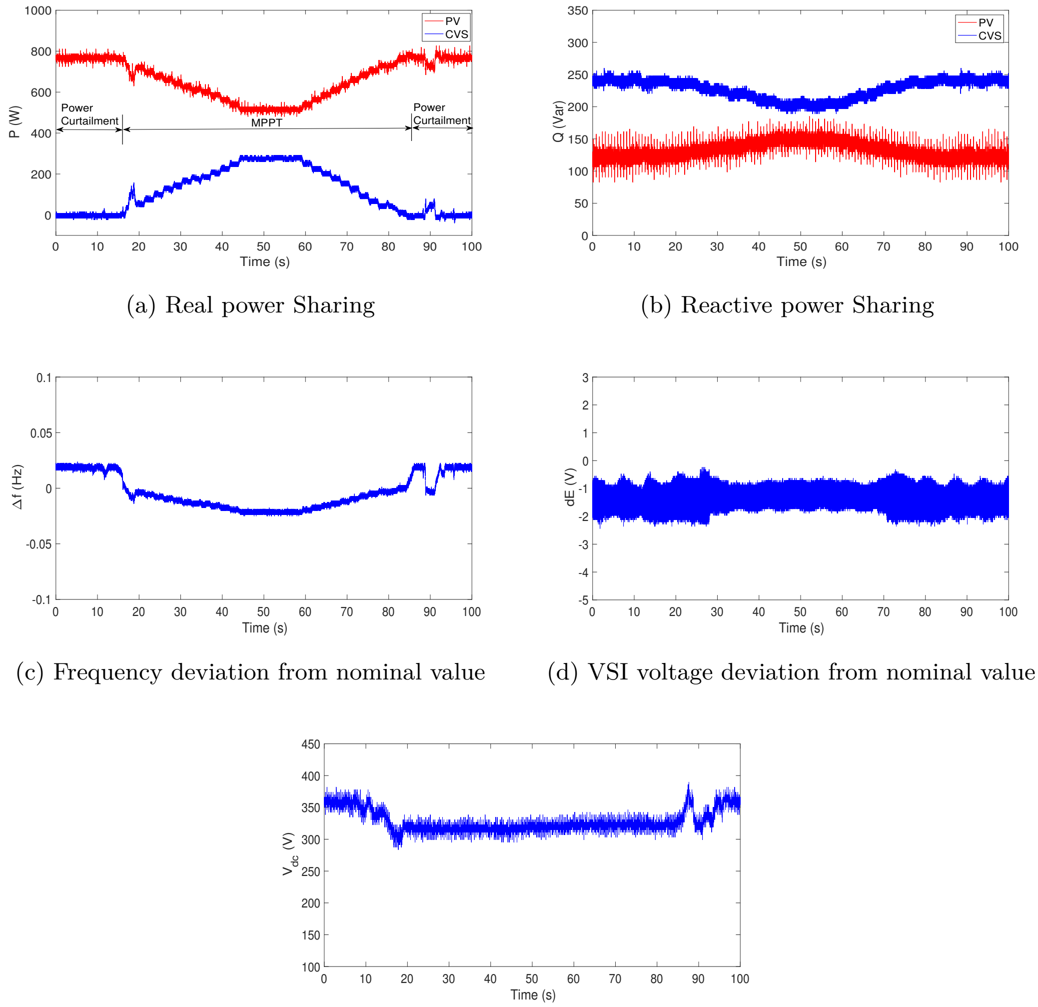

(a) Real power Sharing

(b) Reactive power Sharing

(c) Frequency deviation from nominal value

(d) VSI voltage deviation from nominal value

(e) DC bus voltage in PV unit

Figure 4.10: Performance of power sharing under varying weather conditions

The PV generation is not sufficient to support the power demand at lower irradiance. The performance of real power sharing under the emulated varying solar irradiance I_r is shown in Figure 4.10a. During the first 16s, the solar irradiance is high enough such that PV generation is sufficient to support the local load. As I_r further reduces, the PV unit switches to MPPT mode from power curtailment mode. The power shortage is supplemented by the CVS unit between t=16s and t=86s. When I_r increases back to around $900W/m^2$, the PV unit switches back to power curtailment mode . The V_{dc} value (Figure 4.10e) also indicates the PV mode switching.

4.3.2 Battery Operation

As batteries can be charged and discharged, it is worth testing the control algorithm which should be able to switch battery operating modes responsive to different loading conditions. The filtered power output from the VSI, used in droop control, is used as the signal to enable this transition. In this test, the MG is composed of a battery unit, a CVS unit and RL load. The droop settings of the two units are shown in Table 4.3.

Parameters	Values
$P_{0-BAT}(W)/P_{B-min}(W)$	-100
$P_{0-CVS}(W)/P_{C-max}(W)$	850
$Q_{0-BAT}/Q_{0-CVS}(Var)$	0
$\omega_{0-BAT}/\omega_{0-CVS}(rad/s)$	100π
$E_{0-BAT}/E_{0-CVS}(V)$	100
$m_{BAT}/m_{CVS}(rad/(s \cdot W))$	0.0005
$n_{BAT}/n_{CVS}(V/Var)$	0.005

Table 4.3: Droop control settings in battery operation

The power sharing performance under step changes of load (shown in Figure 4.11) is shown in Figure 4.12. It can be seen from Figure 4.12a that the battery unit is being charged by the CVS unit when the load is lower than P_{C-max}. However, P_{CVS} reaches its maximum output after t=0s and the charging rate of the battery decreases. As the local load further increases, the battery unit starts to discharge power. The reactive power sharing performance in Figure 4.12b performs as desired for average sharing. The grid frequency decreases as the power demand increases, according to Figure 4.12c. It also includes the additional frequency deviation term in the two units. The grid voltage stays relatively constant in Figure 4.12d.

Parameters	Values
$P_0(W)$	0
$Q_0(Var)$	0
$\omega_0(rad/s)$	100π
$E_0(V)$	100
$m(rad/(s \cdot W))$	0.0005
$n(V/Var)$	0.005

Table 4.4: Droop control settings in proportional power sharing

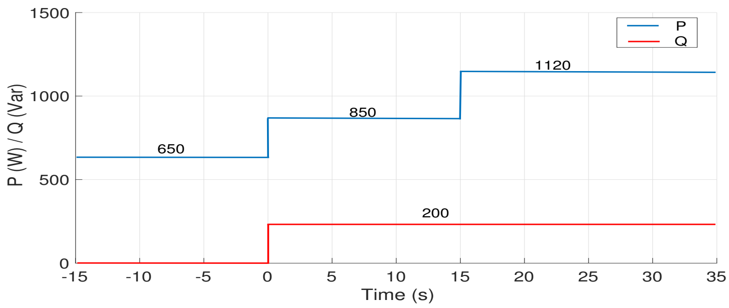

Figure 4.11: Load profile in battery operation

4.3.3 Proportional Power Sharing

Employing the system shown in Figure 4.1, the three types of sources are interfaced. To test proportional power sharing, a reasonable common power rating is assumed for the sources rather than referencing their actual capacity. Note that the allocated power rating is within the minimum capacity of the interfaced sources. The settings of the three droop controllers are also identical, as shown in Table 4.4. During the experimental process, the load dynamics are shown in Figure 4.13.

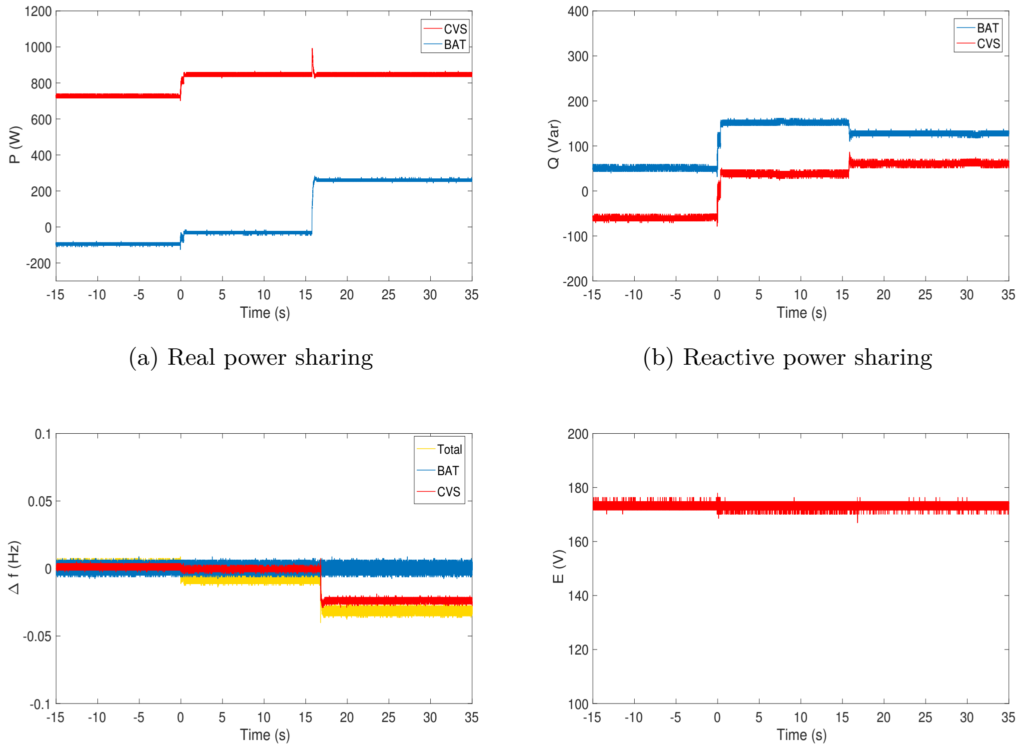

(a) Real power sharing

(b) Reactive power sharing

(c) Frequency deviation from nominal value

(d) VSI line to line voltage (RMS)

Figure 4.12: Experimental results of battery operation

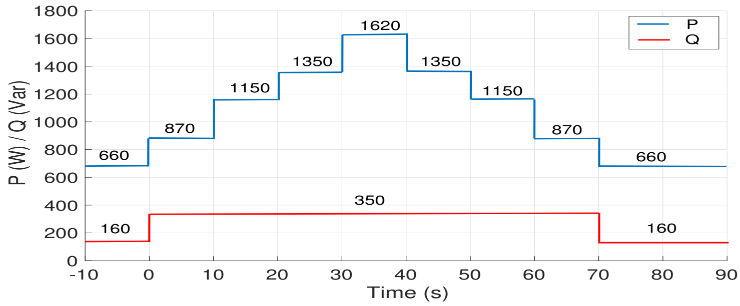

Figure 4.13: Load profiles during the experimental process

The corresponding power sharing performance is shown in Figure 4.14. According to Figure 4.14a and Figure 4.14b, we can see that both real power and reactive power are shared equally, i.e. proportionally to their power ratings. The frequency deviation is shown in Figure 4.14c. It aligns with the droop characteristic where a larger deviation is caused by a higher real power demand. Lastly, the V_{dc} of PV unit in Figure 4.14d shows the effectiveness of the boost converter control. Note that the transients during load step changes are minimal.

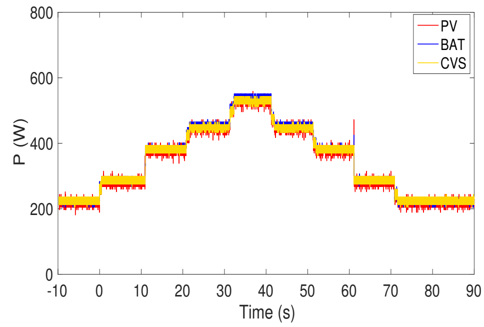

(a) Proportional real power sharing

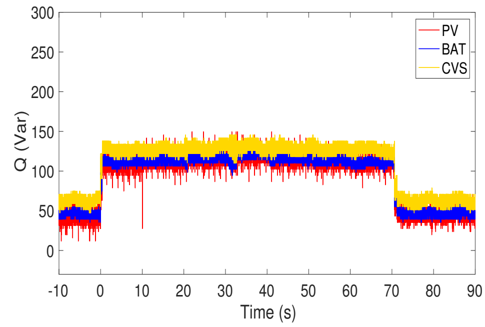

(b) Proportional reactive power sharing

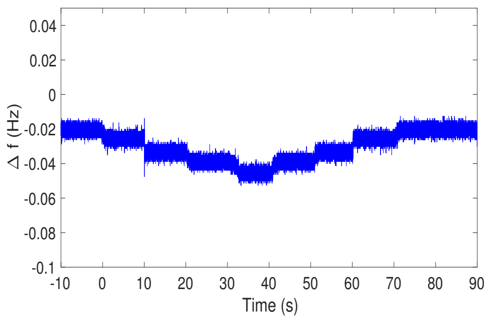

(c) Frequency deviation from nominal value

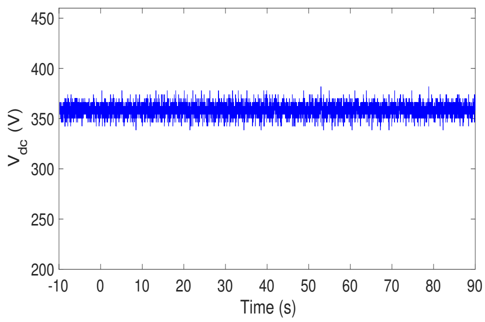

(d) V_{dc} in PV unit

Figure 4.14: Experimental results of proportional real power sharing

4.3.4 RE-Prioritized Real Power Sharing

In this experiment, the MG is composed of three units: PV, battery and conventional sources. Similar to the simulation in Section 3.3, the droop settings are shown in Table 4.5 based on the ratings of the prototype MG. The power limits of the battery unit are chosen based on the overall system design rather than the actual capacity of the lead-acid battery located in the laboratory.

	P_0 (W)	Q_0 (Var)	P_{max} (W)	P_{min} (W)	ω_0 (rad/s)	E_0 (V)	m $(rad/(s\cdot W))$	n (V/Var)
PV	900	0	850	0				
Battery	-100	0	500	-100	$100*\pi$	100	0.0005	0.005
CVS	-600	0	850	0				

Table 4.5: Droop control settings in RE-prioritized real power sharing

Under the load profile shown in Figure 4.13, the performance of prioritized real power sharing is shown in Figure 4.15. The real power outputs and reactive power outputs are shown in Figure 4.15a and Figure 4.15b respectively. Grid frequency and voltage magnitude also drop as the real power demand and reactive power demand increase respectively, shown in Figure 4.15c and Figure 4.15d, aligning with droop characteristics. The transients on V_{dc} in Figure 4.15e also reflect the power output transients. The deviation term of V_{PV} drops to 0 at t=0s which means the PV unit starts to operate at MPPT mode from t=0s and this operation mode lasts for the next 70s. In addition, the output current from PV during the period of transient (around t=0s) is shown in Figure 4.15g.

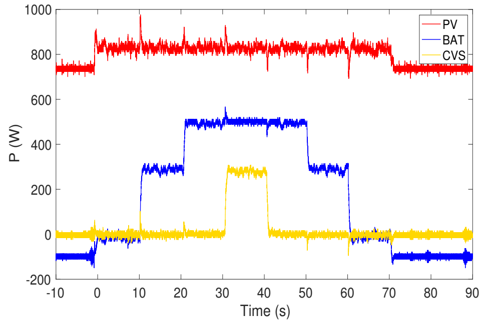

(a) Real power sharing

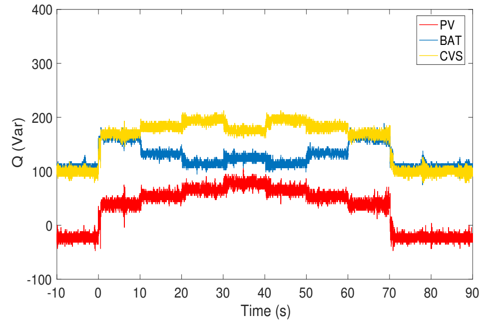

(b) Reactive power sharing

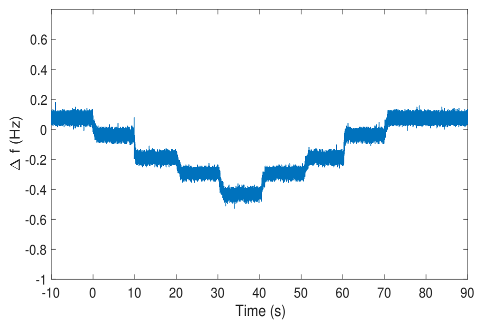

(c) Frequency deviation from the nominal value

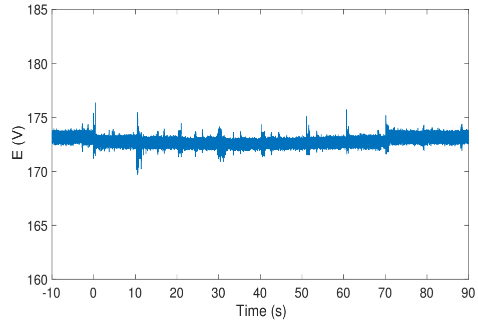

(d) VSI line to line voltage (RMS)

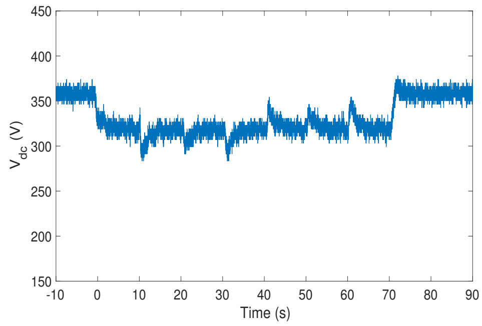

(e) DC bus voltage in PV unit

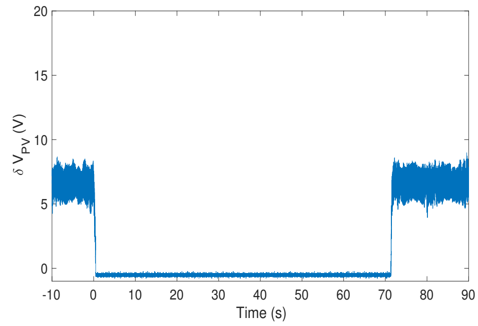

(f) Deviation term of PV bus voltage

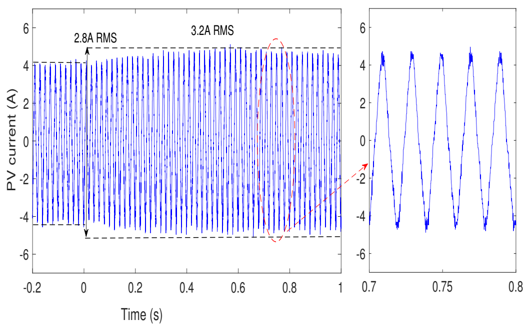

(g) Output current of PV unit

Figure 4.15: Experimental results of RE-prioritized real power sharing

4.3.5 Frequency Restoration

To verify the strategy of frequency restoration discussed in Section 3.4, the secondary level frequency restoration loop is integrated in the experimental implementation. The experimental process of the last section is repeated but with a different time interval of each load condition: 20s. The longer time interval is chosen because the frequency restoration control reacts slower than the primary level control. The results are shown in Figure 4.16. Compared with Figure 4.15a, the real power sharing in Figure 4.16a has a similar performance. However, by comparing Figure 4.15c and Figure 4.16b, we can see that the frequency deviation value in this experiment moves back to zero at each loading condition, which means frequency restores to the nominal value.

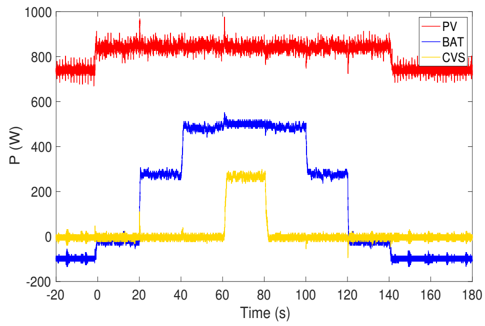

(a) Real power Sharing

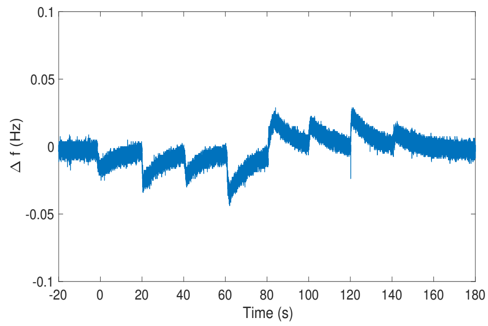

(b) Frequency deviation from nominal value

Figure 4.16: Performance of frequency restoration

4.4 Conclusions

This chapter presented the implementation of control strategies in a prototype MG. The components in the MG were selected based on system design principles as well as hardware availability in the laboratory. The flexible operation of PV source and battery source was first tested. Proportional real power sharing and RE-prioritized real power sharing were then both implemented for comparison. The results showed that the proposed strategy was effective to designate a higher priority of real power supply to PV unit. The system stability was tested by imposing several step changes of load demand. In addition, the frequency deviation resulted from primary control was observed and eliminated by integrating a secondary level control. The time-scale separation successfully prevented the priority order from being deteriorated by the secondary control.

Overall, the experimental results in this chapter match closely with the simulation studies over Chapter 2 to Chapter 3.

Chapter 5

Improved Reactive Power Sharing

Traditionally, reactive power demand is shared proportionally to the VSI power ratings among parallel connected sources. This power management strategy aims to protect VSIs from overloading. However, the reactive power capacity is not only determined by the VSI power rating, but also relevant to its real power flow. Considering the actual reactive power capacity, this chapter proposes two new reactive power sharing strategies with different objectives. First of all, a reliability-enhanced reactive power sharing strategy is proposed, which considers both the power loadings and thermal stresses on converters. It aims to extend the service time of the whole system by adjusting reactive power distribution. Secondly, a RE-prioritized reactive power sharing strategy is proposed focusing on a MG system interfacing with fuel/gas-powered generators. When RES is sufficient to support the active power demand, it is not practical to run micro-turbines merely for reactive power support. The proposed strategy prioritizes RES in reactive power sharing which saves fuel/gas-powered generators' service time. The reliability-enhanced strategy is verified through a long-term numerical analysis while the RE-prioritized strategy is discussed through simulation and experimental studies.

In addition, unlike frequency, voltage varies across a distribution network. The voltage drop across the coupling impedance will reduce the accuracy of reactive power sharing among parallel connected sources. Virtual impedance has been widely adopted to improve reactive power sharing accuracy. This chapter explains the accuracy issue in reactive power sharing and reviews the effect of a virtual impedance. Meanwhile, a Voltage Drop Compensation (VDC) method is proposed and compared with the virtual impedance strategy through mathematical and experimental studies.

5.1 Reliability-Enhanced Reactive Power Sharing

Since most DG units interface with the MG system through converters, the reliability performance of converters is of more and more interest in MG design, operation and maintenance. In a MG, parallel-connected converters complement each other in supporting the load demand. The power sharing strategy impacts on the operational condition of each converter, and consequently its reliability. In proportional power sharing, the droop method cannot effectively avoid converter over-stressing because the thermal stress depends on both its power loading as well as operational and environmental conditions [67,68]. For instance, some ambient temperature (T_a) fluctuations or a failure in the converter cooling system will change junction temperature (T_j) of the critical components in a converter, and hence, affect their thermal stresses. The over-stressing issue has been addressed in DC MGs by presenting a reliability-oriented power sharing strategy in [68]. Unlike the constant droop gain in the conventional droop method, the droop gains in [68] are updated monthly aiming to shift the active power from the high-stressed converters to the low stressed converters. This will extend the aging process of the converters and improve the overall system reliability. Nevertheless, the proposed strategy may overlook the constraints associated with power sources, e.g. intermittent PV generation, and economic efficiency. It is thus worth investigating AC systems, where both active power and reactive power loadings can be adjusted for the purpose of system-level reliability improvement.

5.1.1 Proposed Reliability-Enhanced Reactive Power Sharing Strategy

In the MG with parallel-connected VSIs, power loading on individual converters varies due to their unique source characteristics. The RE-prioritized power sharing strategy proposed in Chapter 3 expects different thermal stresses on different VSIs, especially between PV VSI and battery VSI. Although real power loading has a dominant effect on converter thermal damage, reactive power loading also affects the thermal performance in AC networks. It provides an alternative to improve reliability while maintaining the real power sharing pattern. The principle of the proposed strategy is to shift more reactive power load to the VSI with less thermal damage while relieving the VSI with more damage. This strategy can be achieved by modifying $Q-V$ droop gains since a higher gain corresponds to a smaller fraction of power loading. The droop coefficient can thus be modified from (5.1) into (5.2):

$$n_i = \frac{\Delta V_{max}}{Q_{nom}} \tag{5.1}$$

$$n_i^R = \alpha n_i + (1-\alpha) n_0 (\frac{D_i}{D_0})^{\lambda}, \quad i = 1, \ldots, u+v \tag{5.2}$$

where n_0 is the reference value for $Q-V$ droop coefficient; D_i and D_0 are the estimated and reference value of accumulated VSI damage in the ith unit, respectively. The weighting factor α allows a flexible adjustment between proportional sharing and reliability-enhanced sharing. If $\alpha = 1$, the proportional power sharing is implemented and the thermal damage impact is not considered. If $\alpha = 0$, the adaptive droop coefficient realizes reliability-enhanced power sharing. The selection of λ ($\lambda \geq 1$) tunes the speed of influence from thermal damage. The higher λ, the quicker effect appearing in reactive power shifting. The effect of λ varies with system specifications and it can be designed based on preliminary simulation studies.

The thermal damage of a converter is accumulated over the operation period, which is attributed to both short-term and long-term thermal profiles. The details of thermal damage estimation D_i is demonstrated in Appendix B. It can be seen that electro-thermal mapping plays a critical role. In AC grid operation, the $50Hz$ thermal cycles are identified as the main source of thermal damage [67]. Considering only $50Hz$ thermal cycles allows the on-line estimation of thermal damage which can be realized locally without intensive communication and computation.

5.1.2 Numerical Analysis

A numerical analysis is conducted based on the RE-prioritized real power sharing proposed in Chapter 3 and the proposed reliability-enhanced reactive power sharing. Although the proposed strategy is based on on-line adjustment at primary level, the reliability still needs to be evaluated over long-term because the thermal damage accumulates over the operation period. The simulated system in this section follows the MG structure as shown in Figure 5.1. It is composed of three equivalent PV units and two batteries with the same capacity ($300Ah$). During the operation, the SOC level of battery is estimated and restricted to the specifications in Table 5.2. The interfacing VSIs are designed to be the same for each unit and the specifications are presented in Table 5.1. The three-phase two-level topology is chosen for VSI such that each converter has six IGBT and six diodes. In theory, all IGBTs/diodes in the VSI suffer from the same level of thermal stress such that we can focus on a single device here.

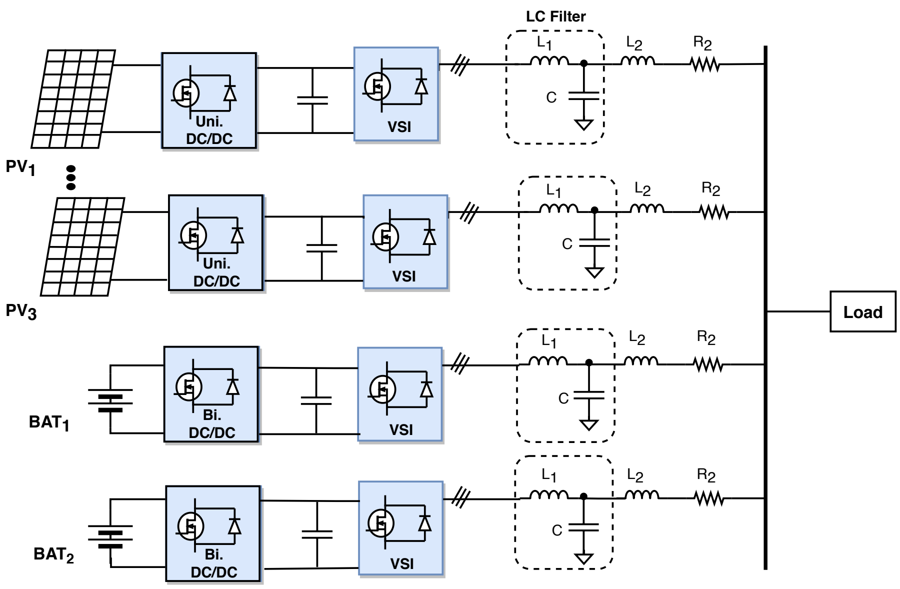

Figure 5.1: Simulated PV-based MG with battery storage

Parameters	Values	Parameters	Values
SOC_{ref}	80%	SOC_{low}	20%
δSOC	10%	P_{B0}	$5kW$
SOC_{01}	50%	SOC_{02}	100%

Figure 5.2: Battery parameters setting

Parameters	VSI
Rated power	5kW
Switching frequency	10kHz
IGBT	IGB20N60H3
Diode	IDV15E65D2

Table 5.1: VSI specifications in numerical analysis

The one-year mission profiles of a hospital in an European city are shown in Figure 5.3 with a sampling rate of one-minute. Note that the load profile is scaled down from practical data to accommodate to power sources in the designed MG. It is also assumed to have a constant power factor of 0.7. The sampling rate restricts the maximum update rate of droop coefficients in the reliability-enhanced power sharing strategy. The update rate in this simulation is set as every minute although it can be set at a slower rate to reduce computation burden.

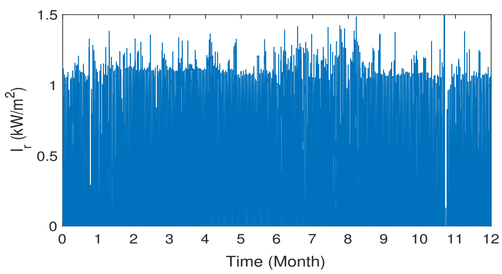

(a) Solar irradiance I_r

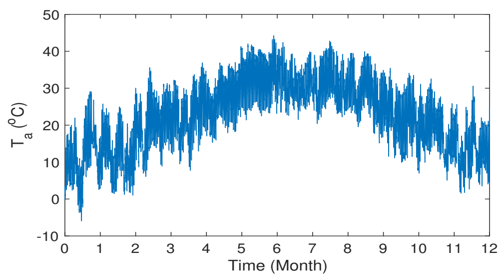

(b) Ambient temperature T_a

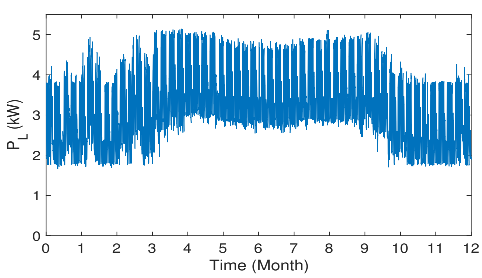

(c) Local load P_L

Figure 5.3: Yearly weather conditions and scaled-down hospital load

5.1.2.1 Case 1 - Proportional Reactive Power Sharing

The yearly power sharing performance based on the RE-prioritized real power sharing and proportional reactive power sharing strategy is shown in Figure 5.4. PV power output is closely related with I_r dynamics. Batteries are charged for most of the days when I_r is high and discharge at night to support local load. Since the system is islanded, batteries are supposed to maintain a high level of SOC in case of power shortages. However, the SOC levels of two batteries reduce dramatically during summer (from June to August), due to the higher load demand but limited battery storage. When the SOC level drops to SOC_{low}, load shedding or some backup sources (e.g. diesel generators) can be activated. Proportional reactive power sharing can also be seen in Figure 5.4. While the $Q-V$ droop coefficients are adaptive to its varying reactive power capacity, reactive power is shared almost equally among these units. The weekly performance of real power outputs from different units can be seen in Figure 5.5. The circled part represents the period of PV power curtailment when battery charging rate is restricted under a high SOC level.

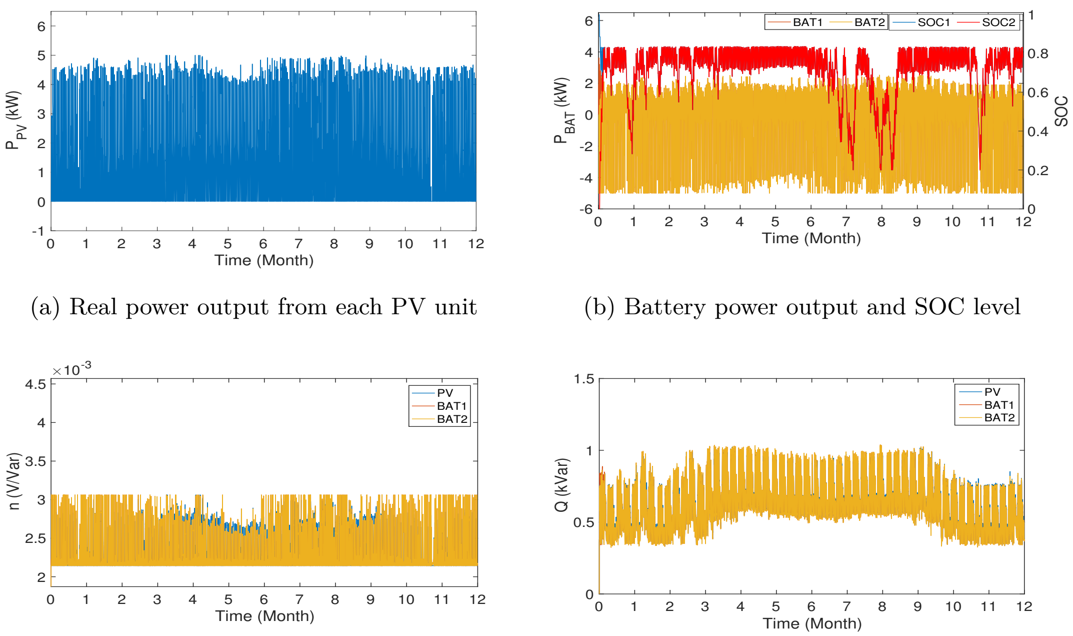

(a) Real power output from each PV unit

(b) Battery power output and SOC level

(c) $Q-V$ droop coefficients n

(d) Reactive power outputs

Figure 5.4: Performance of proportional reactive power sharing in Case 1 for one year

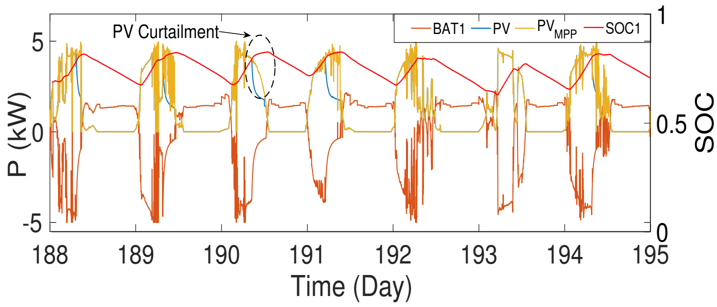

Figure 5.5: Operating Conditions of PV and battery units in Case 1 for one week

5.1.2.2 Case 2 - Reliability-Enhanced Reactive Power Sharing

The results shown in Case 1 have confirmed that power loadings on different VSIs are different, especially between PV VSI and Battery VSI. It is thus necessary to apply the novel reactive power sharing strategy to relieve thermal stresses on the more-stressed VSIs. In the reliability-enhanced power sharing strategy, the reference damage in (5.2) is chosen as $D_0 = D_{pv0} = D_{bat0} = \frac{0.1t}{525600}$ while t is the damage accumulation period in minutes. Meanwhile, $n_0 = 0.002$, $\alpha = 0$ and $\lambda = 3$. The variation of droop coefficient n is shown in Figure 5.6. It can be seen that the value is adaptive to the corresponding VSI damage. The droop coefficients of batteries are higher than that of PV units because of their higher converter damage. The PV droop coefficient drops to a minimal value within the first week in order to share a higher portion of reactive power demand. Meanwhile, the adjusted reactive power performance shows that all of the reactive power demand has been shifted to PV units. The reactive power shared by batteries drops to zero within the first week. This phenomenon can be explained by thermal damage analysis.

The thermal damage of a converter can be estimated by its thermal model combined with operation conditions. The details are demonstrated in Appendix B. With parameters chosen as $A = 9.34e14$, $\alpha_1 = -4.416$, $\beta = 1290$, $\gamma = -0.3$, the damage on VSI under $50Hz$ T_j swing can be calculated. It is compared between proportional reactive power sharing in Case 1 and reliability-enhanced reactive power sharing. It can be seen in Figure 5.7a that battery VSIs suffer more thermal stresses than PV VSIs. The slight difference between BAT1 and BAT2 can be explained by different initial SOC values as

$SOC_{01} = 1$ and $SOC_{02} = 0$. As the adjusted strategy tries to shift reactive power load to PV units, the battery VSIs are relieved by around 15.4% of thermal damage. Since the system reliability is determined by the weakest device, the slight more damage on PV VSI will not deteriorate the overall system reliability. The reliability improvement can also be seen in the lifetime performance based on Monte Carlo analysis [67]. The parameters in the device model and the B1 lifetime model are simulated under normal probability distribution function considering a 5% variation. B1 lifetime is more accurate than thermal damage analysis when discussing device reliability because it considers parameter uncertainties. The reliability of battery VSI is predicted according to [101], and shown in Figure 5.7b for both cases. It can be seen that the B1 lifetimes of battery VSI in Case 1 and Case 2 are around 26 years and 30 years respectively, which presents a 15.4% improvement.

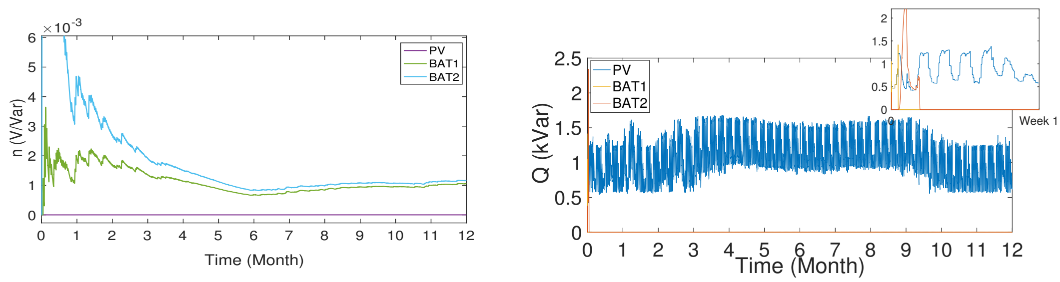

(a) Adjusted $Q-V$ droop gains n_i^R

(b) Battery power output and SOC level

Figure 5.6: Reliability-enhanced reactive power sharing in Case 2 for one year

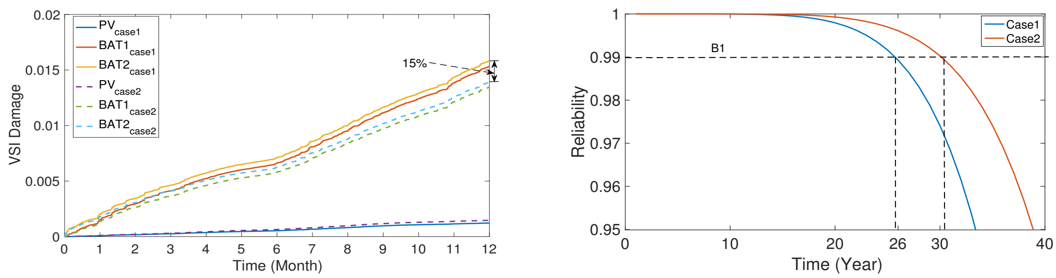

(a) Accumulated damage over one year

(b) Reliability of the battery VSI in Case 1&Case 2

Figure 5.7: Reliability comparison of Case 1 and Case 2

5.2 Reactive Power Sharing in a RE-Prioritized MG

In a MG interfaced with PV sources and CVS, proportional power sharing has not considered the unique power characteristics of individual sources. From a practical point of view, CVS (e.g. diesel generators, microturbines) are not obliged to provide reactive power when no real power is demanded. In addition, the capacity of VSIs ought to be considered which means reactive power control cannot operate independently from real power control [65]. It is thus necessary to share reactive power in accordance with the proposed RE-prioritized real power sharing scheme. This section discusses a RE-prioritized reactive power sharing scheme and its control strategy.

5.2.1 RE-Prioritized Reactive Power Sharing

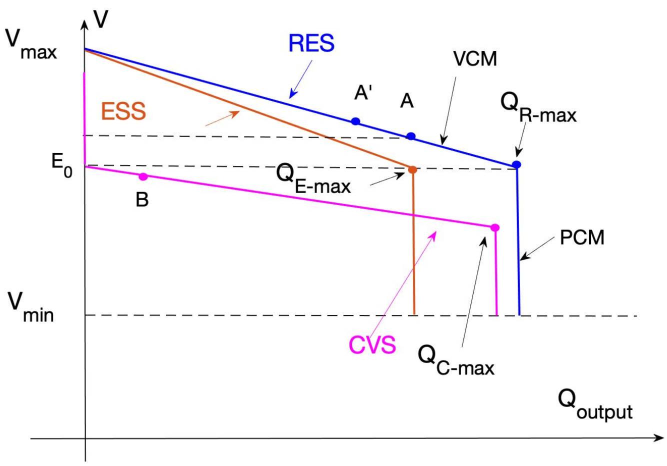

Figure 5.8: Modified $Q - V$ droop curve

In a hybrid microgrid system including RES, ESS and CVS, the real power sharing scheme is designed to draw power from RES in the first place. The ESS and CVS supplement power supply when insufficient RE generation is present. This priority can be designated by modifying $P - \omega$ droop characteristics proposed in Chapter 2. Similarly, for reactive power sharing, the CVS starts to supply reactive power only when the apparent power flowing through the RES/ESS reaches their VSI capacity (shown in Figure 5.8). The sloped section (where $Q < Q_{max}$) applies the traditional $Q - V$ droop control. A voltage increment term is added at Q_{R-max}/Q_{E-max} to limit the reactive power output of RES/ESS, which drives other sources to supply reactive power. The corresponding set point Q_{max} varies with measured real power flow,

$$Q_0 = Q_{max} = \sqrt{S_i^2 - P^2} \tag{5.3}$$

where S_i is the apparent power rating of the VSI and P is the real-time power measurement.

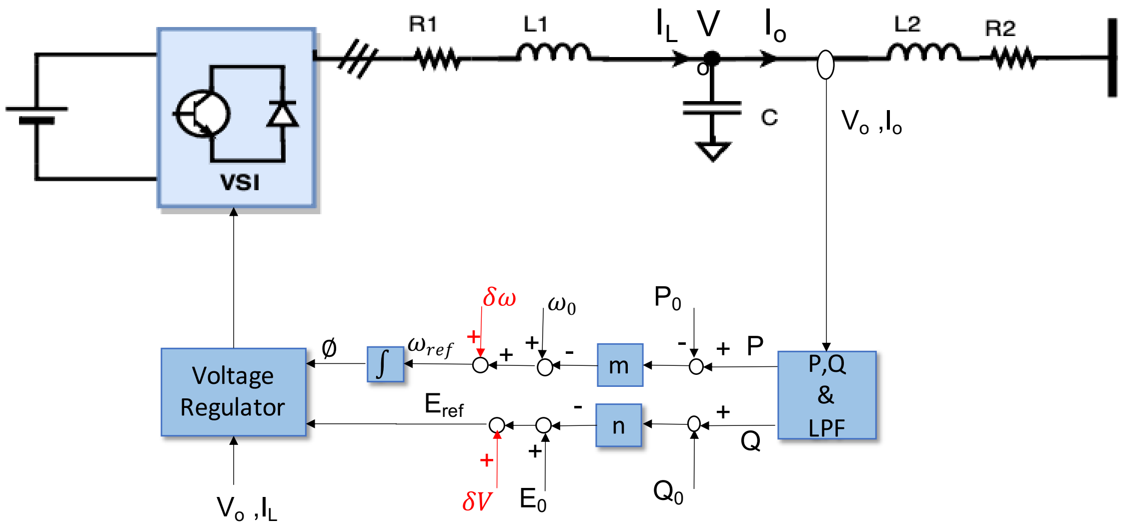

Figure 5.9: Structure of droop control in a RE-Prioritized MG

The overall droop control structure is shown in Figure 5.9. In the $Q-V$ control loop, the power limit of reactive power is imposed to the traditional $Q-V$ droop by a voltage increment term, δV. Consequently, the voltage reference becomes:

$$E_{ref} = E_0 - n(Q - Q_0) + \delta V \tag{5.4}$$

where $-\delta V_{max} < \delta V < \delta V_{max}$ and δV_{max} is determined by the grid specifications on voltage regulation. The generation of δV at Q_{max} is shown in Figure 5.10, which is a basic reactive power limiting loop.

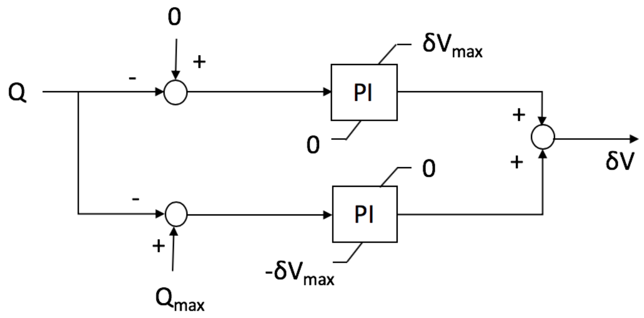

Figure 5.10: Generation of the voltage increment δV

The proposed strategy is easy to implement. However, the issue of reactive power sharing inaccuracy degrades the performance of the proposed strategy. It is demonstrated in the next section through simulations.

5.2.2 Simulation Results

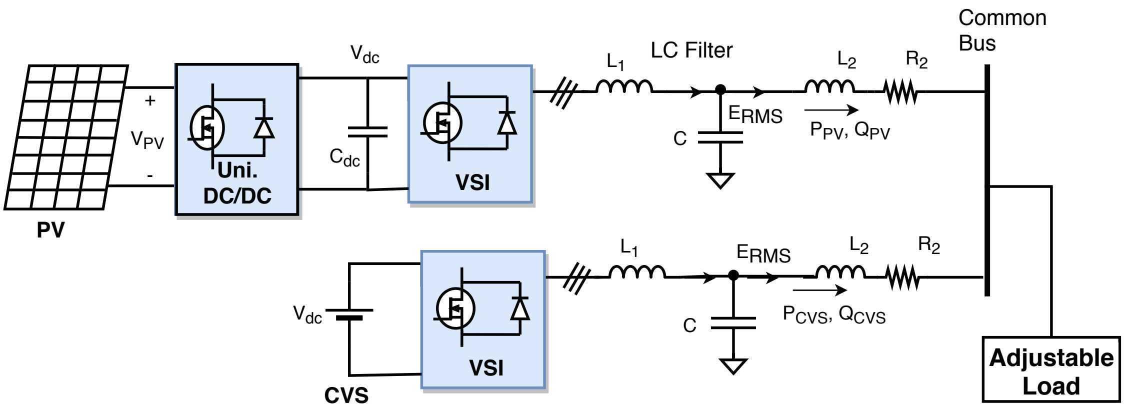

Figure 5.11: Structure of the simulated system

To test the proposed strategy, the simulated MG is composed of a PV source and a conventional source, as shown in Figure 5.11. The network impedance of the two units are set identical. In both real power and reactive power supply, the PV unit has the priority while the conventional unit only serves as the supplement. The power ratings of the VSI and the loading profile through the simulation are presented in Table 5.2. The VSIs are rated at $25kVA$ and $20kW$, with a power factor of 0.8. To achieve RE-prioritized power sharing, the droop control settings are shown in Table 5.3. Across the whole simulation process, the total load is within the power capacity of the PV source.

Simulation results of the RE-prioritized power sharing are shown in Figure 5.12. In real power sharing 5.12a and reactive power sharing 5.12b, we can see that PV is prioritized and the CVS does not supply real power. Nevertheless, it outputs reactive power during the whole process although the total system load is below Q_{PV-max}. It can be seen that the proposed RE-prioritized reactive power sharing is not as effective as real power sharing. It can be explained by the voltage drop across the coupling impedance of each VSI. The VSI output capacitor voltage and grid voltage are shown in 5.12c and 5.12d respectively. The accuracy issue in reactive power sharing is investigated in the next section and a compensation approach is proposed for improvement.

<table>
<tr><td>$P_{PV-max}(kW)$</td><td colspan="2">20</td><td>$S_{PV-max}(kVA)$</td><td colspan="2">25</td></tr>
<tr><td>$P_{C-max}(kW)$</td><td colspan="2">20</td><td>$S_{C-max}(kVA)$</td><td colspan="2">25</td></tr>
<tr><td rowspan="2">$P_L(kW)$</td><td>$0-2s$</td><td>15</td><td rowspan="2">$Q_L(kVar)$</td><td>$0-2s$</td><td>5</td></tr>
<tr><td>$2s-4s$</td><td>15</td><td>$2s-4s$</td><td>10</td></tr>
</table>

Table 5.2: Power ratings and loading profile in RE-prioritized reactive power sharing

Parameters	Values
$P_{0-PV}/P_{PV-max}(kW)$	20
$P_{0-CVS}/P_{C-min}(kW)$	0
$\omega_{0-PV}/\omega_{0-CVS}(rad/s)$	$2\pi * 50$
$Q_{0-PV}/Q_{PV-max}(kVar)$	15
$Q_{0-CVS}/Q_{C-min}(kVar)$	0
$m(rad/(s \cdot W))$	7.5×10^{-4}
$n(V/Var)$	5×10^{-4}
$E_{0-PV}/E_{0-CVS}(V)$	$230\sqrt{2}$

Table 5.3: Droop control settings in RE-prioritized reactive power sharing

5.3 Accuracy Analysis of Reactive Power Sharing

5.3.1 Analysis of Coupling Impedance

Voltage drop across the coupling impedance at the output of the VSI is the main reason for inaccurate reactive power control. It is thus necessary to analyse the characteristics of the output impedance of a VSI unit. Figure 5.13 presents the topology of a single phase VSI and its output interface. It is connected to the load (represented by a varying i_o) through a LC filter. The LC filter is composed of filter capacitor C and filter inductor L_1 with parasitic resistance R_1.

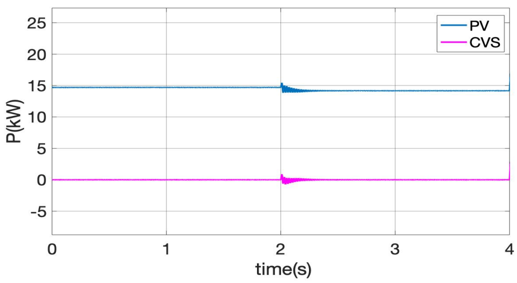

(a) Real power output

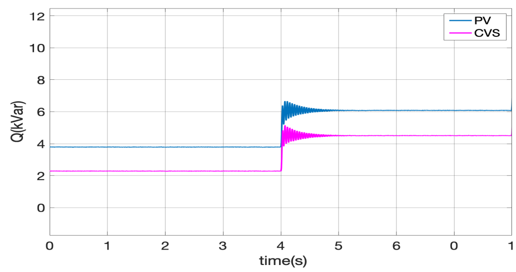

(b) Reactive power output

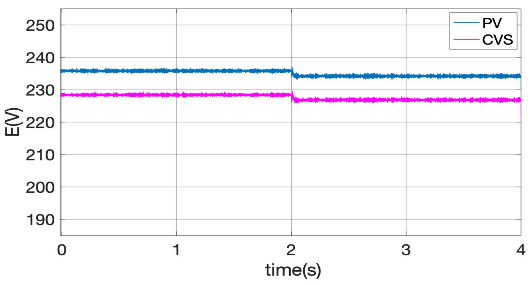

(c) VSI ph-n voltage in RMS value

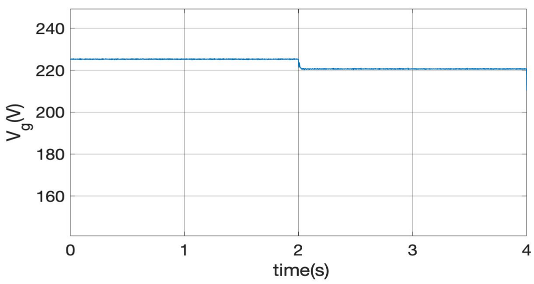

(d) Grid ph-n voltage in RMS value

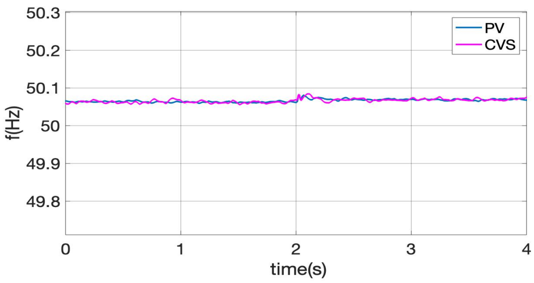

(e) Grid frequency

Figure 5.12: RE-prioritized power sharing

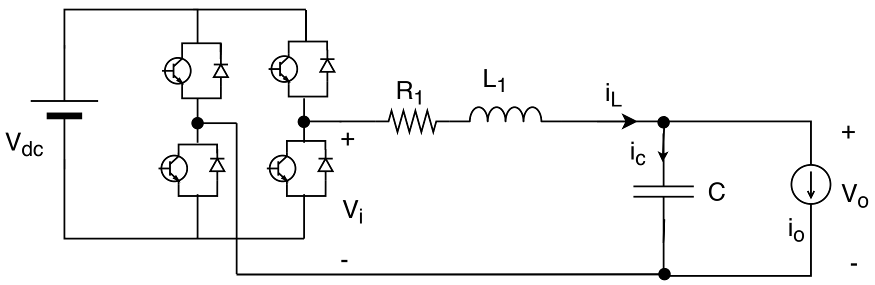

Figure 5.13: Topology of a single phase VSI

The average signal model of this system is:

$$L_1 \frac{di_L}{dt} = V_i - v_o - R_1 i_L \tag{5.5}$$

$$C \frac{dv_o}{dt} = i_c = i_L - i_o \tag{5.6}$$

where V_i is the inverter output voltage; v_o is the instantaneous LC filter output voltage.

The open-loop averaged output-voltage dynamics can be derived as:

$$L_1 C \frac{d^2 v_o}{dt} + R_1 C \frac{dv_o}{dt} + v_o + L_1 \frac{di_o}{dt} + R_1 i_o = V_i \tag{5.7}$$

If there is no voltage regulation loop, reference voltage V_{ref} is generated at the inverter output, i.e. $V_i = V_{ref} = Esin\omega t$. The value of V_{ref} can be generated from a power management strategy, e.g. droop control.

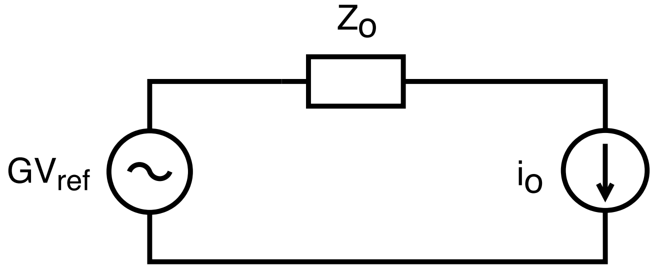

Figure 5.14: Thevenin equivalent circuit of a VSI unit

Apply Laplace transformation to (5.7), output voltage across the filter capacitor can be represented as:

$$v_o = \frac{1}{L_1Cs^2 + R_1Cs + 1}V_{ref} - \frac{L_1s + R_1}{L_1Cs^2 + R_1Cs + 1}i_o \tag{5.8}$$

The single phase VSI combining with output LC filter can be represented by a Thevenin equivalent circuit (shown in Figure 5.14):

$$v_o = GV_{ref} - Z_oi_o \tag{5.9}$$

The new voltage source is GV_{ref} and output impedance is Z_o, where

$$\begin{aligned} G &= \frac{1}{L_1Cs^2 + R_1Cs + 1} \\ Z_o &= \frac{L_1s + R_1}{L_1Cs^2 + R_1Cs + 1} \end{aligned}$$

However, in most cases, a voltage regulator is included to regulate the capacitor voltage tracking the reference value, i.e. $v_o = V_{ref}$. A common PI controller is discussed here. The input of the PI controller is the error between v_o and V_{ref} while the output is inverter implementation voltage V_i.

$$V_i = k_p(V_{ref} - v_o) + k_i\int(V_{ref} - v_o)dt \tag{5.10}$$

Taking the Laplace transform of (5.10) and substituting into (5.7) gives the output voltage across the filter capacitor as:

$$v_o = \frac{k_ps + k_i}{L_1Cs^3 + R_1Cs^2 + (k_p + 1)s + k_i}V_{ref} - \frac{L_1s^2 + R_1s}{L_1Cs^3 + R_1Cs^2 + (k_p + 1)s + k_i}i_o \tag{5.11}$$

The single phase VSI unit combining with a voltage regulator can be represented by a new Thevenin equivalent circuit:

$$v_o = G'V_{ref} - Z_o'i_o \tag{5.12}$$

The new voltage source is $G'V_{ref}$ and output impedance is Z'_o, where

$$G' = \frac{k_p s + k_i}{L_1 C s^3 + R_1 C s^2 + (k_p + 1)s + k_i}$$
$$Z'_o = \frac{L_1 s^2 + R_1 s}{L_1 C s^3 + R_1 C s^2 + (k_p + 1)s + k_i}$$

L_1	R_1	C	k_p	k_i
$2mH$	0.2Ω	$20\mu F$	0.1	100

Table 5.4: Parameters of a single VSI source

Based on the system parameters shown in Table 5.4, the property of the output impedance can be seen in its Bode plot, shown in Figure 5.15. Without the voltage regulation loop, it has resistive characteristic component at fundamental frequency while has inductive dominant characteristic if PI control is included.

Bode plots of the voltage gain in both cases are shown in Figure 5.16. The gain is close to 1 at fundamental frequency. In conclusion, the output voltage regulator can shape the characteristics of the output impedance. It indicates the possibility of manipulating VSI output impedance by designing the voltage regulator.

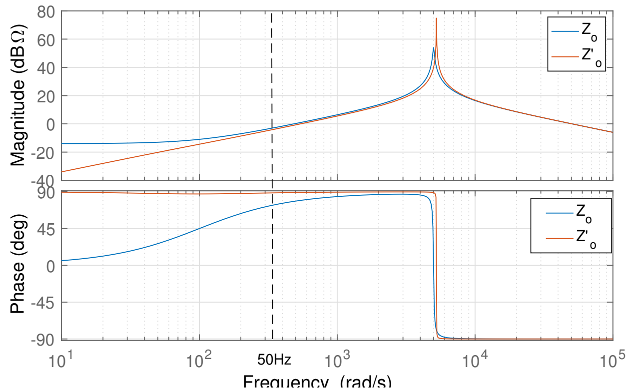

Figure 5.15: Output impedance of VSI without (Z_o) /with (Z'_o) PI control

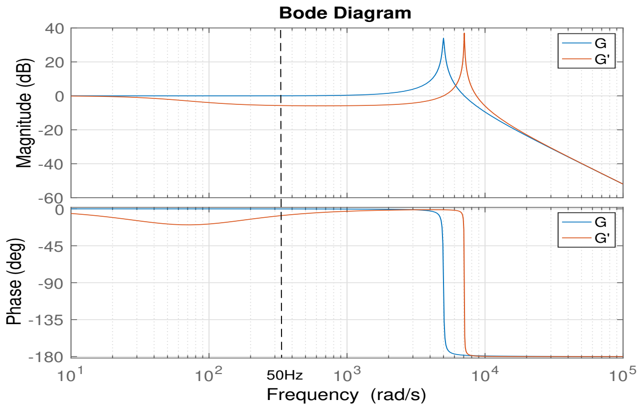

Figure 5.16: Gain of Thevenin equivalent circuit without (G) /with (G') PI control

When the VSI is connected to the AC common bus through a coupling line, of which the impedance is Z_L, the total coupling impedance is:

$$Z_c = Z'_o + Z_L$$

The property of Z_c affects the performance of power sharing in paralleled VSIs. Its impact on reactive power sharing is discussed below.

5.3.2 Inaccurate Reactive Power Sharing

The advantage of implementing $P - \omega$ droop method for real power sharing is that frequency is a common value throughout the system at steady state. In contrast, voltage varies across the network which affects reactive power sharing [23]. To demonstrate the dependence of reactive power sharing on network parameters, the independence of real power sharing is explained first.

Without losing generality, we focus on a system with two paralleled units employing traditional droop control, i_{th} unit and j_{th} unit. For i_{th} unit, the real power flow at steady state is:

$$P_i = \frac{\omega_{0i} - \omega_i}{m_i} + P_{0i} \ . \tag{5.13}$$

where ω_i is the common grid frequency and ω_{0i}, P_{0i} are set points of the ith unit. As a result, P_i can be regulated independently by adjusting ω_{0i}, m_i or P_{0i}. If the j_{th} unit has the same settings, $P_i = P_j$ can be guaranteed. Moreover, any power sharing scheme between i_{th} and j_{th} units can be achieved independently without losing accuracy.

This performance cannot be replicated in reactive power sharing. In a two-unit system, the reactive power flow at steady-state is:

$$Q_i = Q_{0i} + \frac{E_{0i} - E_i}{n_i} \tag{5.14}$$

$$Q_j = Q_{0j} + \frac{E_{0j} - E_j}{n_j} \tag{5.15}$$

In the case that two units share the same droop settings, $E_i = E_j$ is a necessary condition for the realization of $Q_i = Q_j$, according to the formulas above. However, in reality, even with matched VSI output voltage, reactive power mismatch can still occur as a result of mismatched coupling impedance. For example, when $E_i = E_j$, line coupling reactance $X_i < X_j$ can result in $Q_i > Q_j$ at steady state. The reason is that the voltage drop across the coupling impedance affects reactive power sharing.

If the coupling impedance is represented as $Z = R + jX$ while the the LC filter output voltage is $E\angle\phi$ and the grid voltage is V_g, the 3-phase real power flow and reactive power flow are represented respectively as below:

$$P = \frac{3}{2}\frac{E(ER - V_gRcos\phi + V_gXsin\phi)}{R^2 + X^2}$$

$$Q = \frac{3}{2}\frac{E(EX - V_gRsin\phi - V_gXcos\phi)}{R^2 + X^2}$$

Thus,

$$\begin{aligned} PR + QX = &\frac{3}{2}\frac{ER^2(E - V_gcos\phi) + EV_gXRsin\phi}{R^2 + X^2} \\ &+ \frac{3}{2}\frac{EX^2(E - V_gcos\phi) - EV_gXRsin\phi}{R^2 + X^2} \end{aligned}$$

which is equivalent to

$$E - V_g cos\phi = \frac{2}{3}\frac{PR + QX}{E} \tag{5.16}$$

Assuming phase angle ϕ is a small value, (5.16) is simplified into:

$$\Delta V = E - V_g = \frac{2}{3}\frac{PR + QX}{E} \tag{5.17}$$

Where ΔV is the voltage drop across the coupling line. It can be seen that any mismatch in coupling impedance and/or power flow will cause mismatched voltage drop. It in turn causes inaccurate reactive power sharing. Since a larger reactive power flow causes a larger voltage drop, a balanced voltage drop can be achieved by adjusting reactive power sharing. For example, the unit with a larger voltage drop under average power sharing can be adjusted to share less reactive power or even absorb reactive power in extreme conditions. Droop control autonomously adjusts the reactive power sharing among paralleled units, which is shown in Figure 5.17.

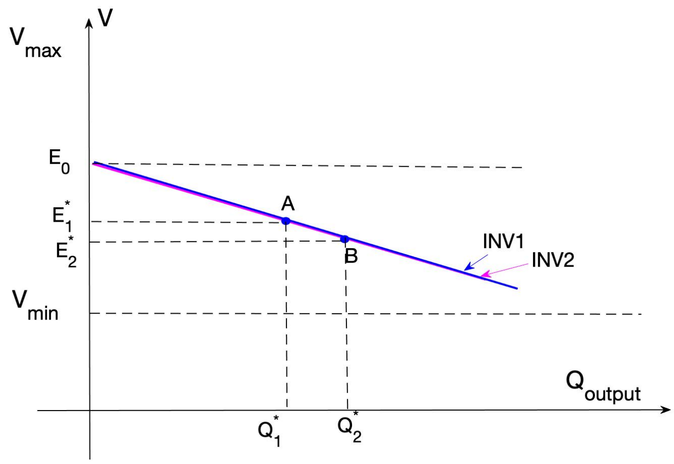

Figure 5.17: Interaction between mismatched voltage drop and droop control

The two droop curves represent two units with identical droop settings. Meanwhile, the two units share the same voltage at the PCC, i.e. $V_1 = V_2$. The voltage drop across the coupling line is dependent on power flows and the line impedance. It is very hard to maintain equivalent voltage drop since the line impedances are normally unknown. In the case of $\Delta V_1 > \Delta V_2$, for example, operating points of two units at VSI output are A

and B respectively. At steady state, the following conditions should be satisfied.

$$
\begin{aligned}
E_1^* &= E_0 - n(Q_1^* - Q_0) \\
E_2^* &= E_0 - n(Q_2^* - Q_0) \\
E_1^* - \Delta V_1 &= E_2^* - \Delta V_2
\end{aligned}
\tag{5.18}
$$

As a result, $Q_1^* < Q_2^*$. The accuracy of reactive power sharing is thus reduced. It also can be noticed that this mismatch can be reduced by increasing $Q - V$ droop coefficient. Virtual impedance is commonly integrated into the reactive power control loop to improve the power sharing accuracy. A new strategy, voltage drop compensation (VDC), is proposed in the next section.

5.4 Accuracy-Improved Reactive Power Sharing

5.4.1 Proportional Reactive Power Sharing

In order to achieve "plug and play" and improve reactive power sharing at the same time, a decentralized control strategy is critical. It does not rely on inter-unit communications or a central controller. Inspired by the idea of grid voltage regulation in [23, 74], a VDC method is proposed based on the estimated value of grid voltage, V_{g-est}. It is proposed on known line impedance and further developed for the case of unknown line impedance.

If line impedance is represented as $Z = R+jX$ and the inverter output voltage magnitude is E, the grid voltage can be estimated as:

$$
V_{g-est} = E - \Delta V = E - \frac{2}{3}\frac{PR + QX}{E}
$$

where P and Q are 3-phase real power flow and reactive power flow through the coupling line respectively. In [23, 74], grid voltage is regulated directly in order to eliminate the impact of voltage drop on reactive power sharing. Similarly, the estimated voltage V_{g-est} can be fed back in case its real value is not available. The voltage regulator effectively regulates V_{g-est} to track the voltage magnitude reference, E_{ref}. Consequently, at steady state,

$$V_{g-est} = E - \frac{2}{3}\frac{PR+QX}{E} = E_{ref}$$
$$E = E_{ref} + \frac{2}{3}\frac{PR+QX}{E}$$

Compared to $E = E_{ref}$ in the traditional voltage regulator, the new inverter output voltage is increased by a value equal to voltage drop ΔV. In implementation, the output voltage reference can increase by ΔV so as to allow V_g to track E_{ref}. The advantage of this VDC method is that reactive sharing and voltage regulation at the grid can be both improved.

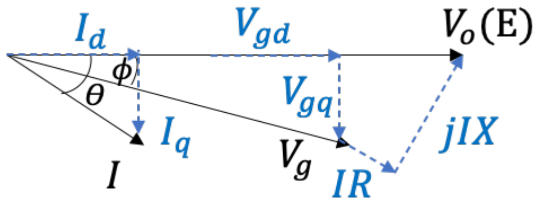

Figure 5.18: Phasor representation of E and V_g

To implement the proposed method in the dq reference frame, the grid voltage is estimated in dq reference frame. According to Figure 5.18, the phase angle of the output voltage $\dot{V_o}$ provides a reference frame, i.e. $\dot{V_o} = E\angle 0^o$, $V_{od} = E$ and $V_{oq} = 0$. Meanwhile, $\dot{V_g} = V_g\angle-\phi$ while the output current is $\dot{I} = I\angle-\theta$. As a result,

$$V_{gd} = V_g cos\phi;\ V_{gq} = -V_g sin\phi$$
$$I_d = Icos\theta;\ I_q = -Isin\theta$$

Furthermore, the relationships between these variables are:

$$V_{od} = V_g cos\phi + IRcos\theta + IXsin\theta = V_{gd} + I_d R - I_q X$$
$$V_{oq} = -V_g sin\phi - IRsin\theta + IXcos\theta = V_{gq} + I_q R + I_d X$$

So,

$$V_g^2 = V_{gd}^2 + V_{gq}^2 = (V_{od} - I_d R + I_q X)^2 + (I_q R + I_d X)^2$$
$$V_{od} = \sqrt{V_g^2 - (I_q R + I_d X)^2} - I_q X + I_d R$$

In order to regulate the grid voltage to the reference value, i.e. $V_g = E_{ref}$, the new output voltage magnitude becomes:

$$E_{est} = \sqrt{E_{ref}^2 - (I_q R + I_d X)^2} - I_q X + I_d R \tag{5.19}$$

where $E_{est}^{\cdot}$ aligns with d axis of the reference frame, i.e.

$$E_{dest} = \sqrt{E_{ref}^2 - (I_q R + I_d X)^2} - I_q X + I_d R$$
$$E_{qest} = 0$$

The implementation of the proposed method is shown in a control topology, Figure 5.19.

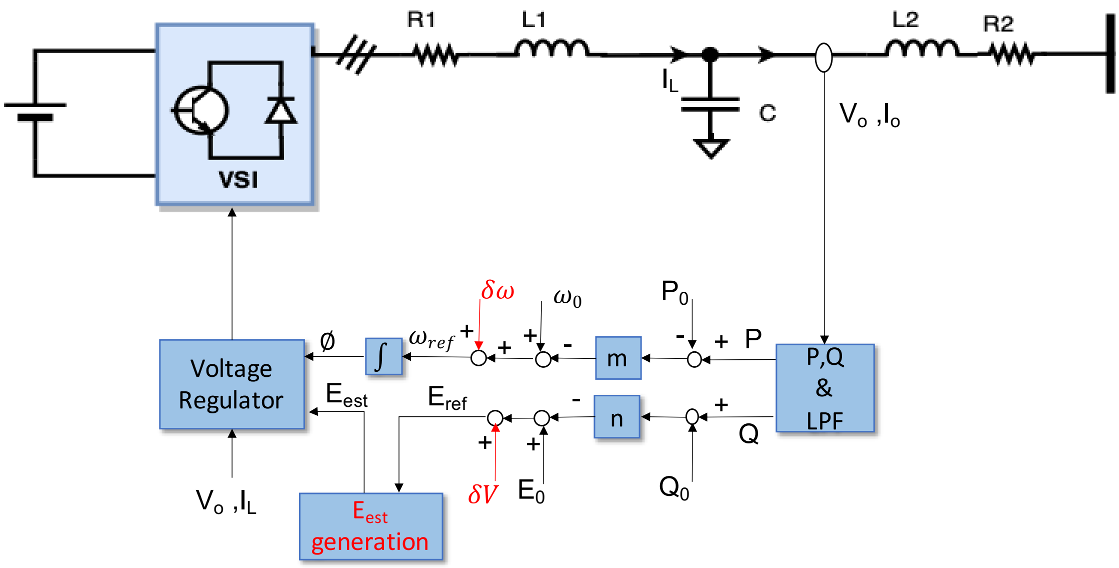

Figure 5.19: Control topology of the proposed VDC strategy

In the case of unknown line impedance, an adaptive line impedance estimation Z_{est} is proposed:

$$Z_{est} = Z^* - jk_a Q$$

where Z^* is a reference impedance value; Q is the measured reactive power output and k_a is a positive proportional gain. The reference impedance value is the value of a relatively large interfacing inductor connected before the coupling line. Besides mitigating harmonics, the existence of a large inductor firstly helps to mitigate reactive power mismatch and secondly, provides a reference value for the proposed VDC. The estimated reactance value is inversely proportional to reactive power measurement, which intends to reduce the mismatch of reactive power between two units.

The implemented voltage at the output of LC filter is:

$$E_{est} = \sqrt{E_{ref}^2 - (I_q R_{est} + I_d X_{est})^2} - I_q X_{est} + I_d R_{est}$$

The estimated line impedance is not accurate and the error will impact the performance of reactive power sharing. It is reasonable to expect a better sharing with a higher proportional gain k_a. It also needs to be noted that if $Z_{est} < 0$, the effect of the proposed method is similar to that of virtual impedance when $Z_v = -Z_{est}$. The comparison between VDC and virtual impedance will be seen in Section 5.4.3.

5.4.2 RE-Prioritized Reactive Power Sharing

The impact of voltage drop across the coupling line is more prominent under the RE-prioritized power sharing scheme. As discussed earlier in this chapter, the voltage drop is dependent on both power flow and coupling impedance. If the power flow in one unit is significant, the voltage drop in that unit is noteworthy regardless of the size of line impedance. The problem caused by this voltage drop is that when RESs supply a large portion of power demand, the voltage drop affects its priority in reactive power supply. Taking Figure 5.8 for example, the inaccuracy in reactive power sharing is explained below.

If the reactive power demand (Q_L) is within the maximum available capacity of the VSI in RES, the operating point can be represented by point A. Ideally, the corresponding reactive power output from the CVS should remain at zero. However, ΔV_{RES} across the line impedance in RES may lower the grid voltage to a value below E_0 . It may result in a new operating condition: the CVS operates at B and the RES operates at a new point A'.

As a development of the proposed VDC method, the line impedance is estimated considering the prioritized power sharing scheme. Assuming the line impedances in different units are matched or slightly mismatched, the voltage drop in the RES is larger than that in others under normal conditions. As a result, the estimated impedance is designed to be proportional to real power flow:

$$Z_{est} = k_b \frac{P}{P_{nom}}$$

where P_{nom} is the nominal value of real power and P is the real-time measured value; k_b is a positive proportional gain. A relatively large inductor (Z^*) is also connected before the coupling line. It provides an upper limit for Z_{est} to prevent the voltage drop being over compensated. The stability analysis regarding the choice of Z_{est} can be seen in Chapter 6.

In implementation, for the sake of simplicity, Z_{est} can be assumed to be inductive, i.e. $Z_{est} = X_{est}$. The new implemented voltage at the output of LC filter becomes:

$$E_{est} = E_{ref} - I_q X_{est} \tag{5.20}$$

Compared to (5.19), (5.20) ignored the term of $I_d X_{est}$. It is because that the ignored term is highly related with real power flow and it counteracts the intention of VDC. As a result, the implemented voltage in dq reference frame is:

$$\begin{aligned} E_{dest} &= E_{ref} - I_q X_{est} \\ E_{qest} &= 0 \end{aligned}$$

The proposed method ensures the priority of RES in both real power and reactive power supply.

5.4.3 Comparison between Virtual Impedance and Proposed VDC

According to droop control, $E_{ref} = E_0 - n(Q - Q_0)$. With the proposed VDC, the output voltage becomes:

$$E_{est} = E_0 - n(Q - Q_0) + \frac{2}{3}\frac{PR_{est} + QX_{est}}{E_{est}} \tag{5.21}$$

Assuming the estimated impedance is predominantly inductive, the approximated (5.21) becomes:

$$\begin{aligned} E_{est} &= E_0 - n(Q - Q_0) + \frac{2}{3}\frac{QX_{est}}{E_{est}} \\ &= E_0 - (n - \frac{2X_{est}}{3E_{est}})Q - nQ_0 \end{aligned} \tag{5.22}$$

It can be seen that, under approximation, the proposed method reduces the effective droop coefficient.

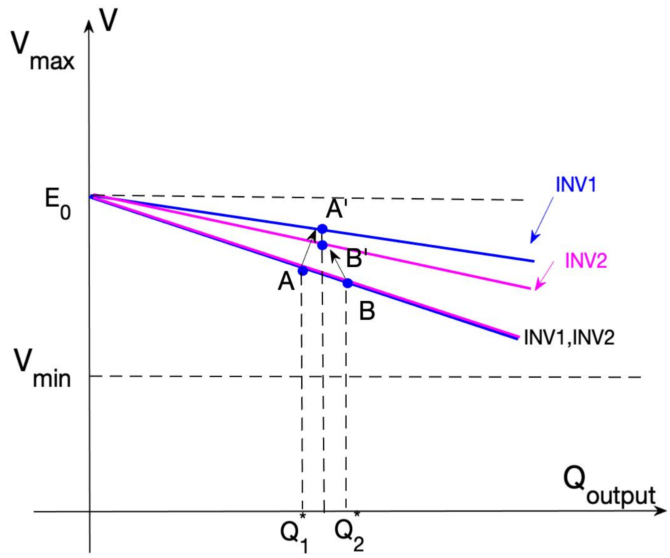

Figure 5.20: $Q - V$ droop characteristics in proportional power sharing based on VDC

The mechanism of the proposed VDC method is illustrated in Figure 5.20 through $Q - V$ characteristics. The VSI voltage is increased by the amount of estimated voltage drop. In case $\Delta V_1 > \Delta V_2$, the compensation term in unit 1 is also larger than that in unit 2.

This discrepancy can be seen by comparing the blue slope and red slope in the figure. If the voltage drop is accurately compensated, operating points A and B move to A' and B' respectively. As a result, two units operate at different voltage levels but reactive power is equally shared.

On the other hand, virtual impedance behaves in the opposite way. The implemented voltage at the output of LC filter is reduced by a voltage drop across the virtual impedance $Z_v = R_v + jX_v$, which means:

$$E_v = E_{ref} - \frac{2}{3}\frac{PR_v + QX_v}{E_v}$$

In the case of inductive virtual impedance, the above equation can be simplified into:

$$\begin{aligned} E_v &= E_0 - n(Q - Q_0) - \frac{2}{3}\frac{QX_v}{E_v} \\ &= E_0 - (n + \frac{2X_v}{3E_v})Q - nQ_0 \end{aligned} \tag{5.23}$$

It can be seen that, under approximation, the virtual impedance increases the effective droop coefficient. The bigger the virtual impedance, the larger the droop coefficient. A larger droop coefficient improves reactive power sharing performance but introduces the risk of instability and poor voltage regulation.

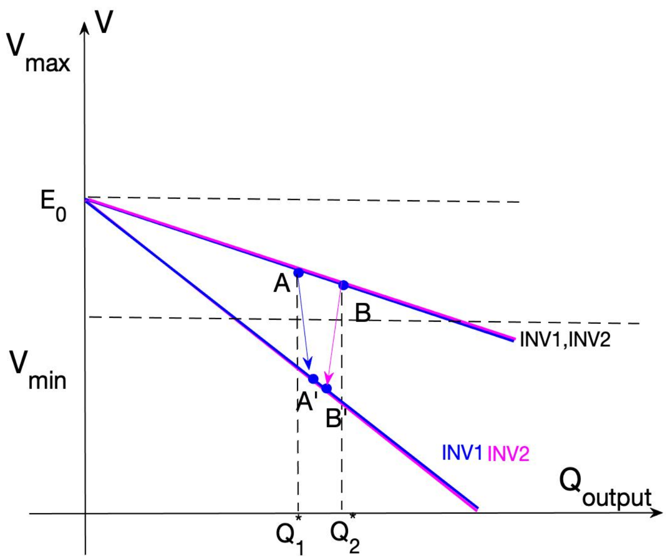

Figure 5.21: $Q - V$ droop characteristics in proportional power sharing based on virtual impedance

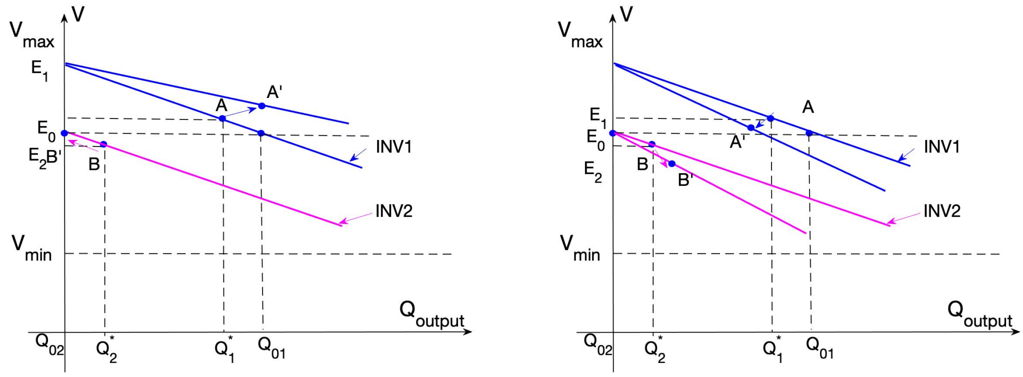

(a) Proposed voltage compensation method (b) Virtual impedance method

Figure 5.22: $Q - V$ droop characteristics in RE-prioritized power sharing

The mechanism of the virtual impedance method is illustrated in Figure 5.21 through $Q-V$ characteristics. The VSI voltage is decreased by the amount of voltage drop across virtual impedance. In the case of unknown line impedance, two identical large virtual impedances are chosen for two units. As a result, two droop slopes change in the same manner. The mismatch of reactive power reduces and can reach zero if the line impedance mismatch is completely compensated.

In RE-prioritized power sharing, the droop characteristics of the two methods are shown in Figure 5.22. In the proposed VDC scheme, the droop slope of INV1 decreases so as to leave a larger drop margin in voltage regulation. If real power output from INV2 is zero, the droop slope of INV2 does not change. When the voltage margin in INV1 is large enough to accommodate the voltage drop across the coupling line, prioritized reactive power sharing can be achieved, i.e. operating points move from A,B to A',B'. On the contrary, the effect of virtual impedance is shown on the right of Figure 5.22. The large voltage drop across virtual impedance in INV1 will lower the voltage at PCC and in turn drives INV2 to output more reactive power. The priority of INV1 in reactive power supply is thus degraded.

The following simulation results test the performance of the proposed VDC method and the performance of virtual impedance method is also shown for comparison.

5.5 Simulation Results

5.5.1 Proportional Reactive Power Sharing

In a two-unit system as shown in 5.11, unit 1 is represented by a PV source and unit 2 is represented by a CVS. The line impedances are intentionally designed to be mismatched and the associated parameters are shown in Table 5.5. The rated power and droop settings of the two units are identical. In a proportional reactive power sharing scheme, two conditions are discussed here: known line impedance values and unknown line impedance values.

Parameters		Values
$P_0(kW)$		10
$Q_0(kVar)$		0
$\omega_0(rad/s)$		$2\pi * 50$
$E_0(V)$		$230 * \sqrt{2}$
$m(rad/(s\cdot W))$		7.5×10^{-4}
$n(V/Var)$		5×10^{-4}
Z_{L1}	R_{L1}	0.3Ω
	L_{L1}	$3mH$
Z_{L2}	R_{L2}	0.2Ω
	L_{L2}	$2mH$

Table 5.5: Parameters in proportional reactive power sharing

5.5.1.1 Known Line Impedance

When line impedances are known, it is possible to achieve accurate reactive power sharing. According to Figure 5.16, the voltage gain is close to 1 at grid frequency. The coupling impedance can thus be approximated to $Z_c' = Z_o' + Z_v + Z_L$. If these two units have the same settings, the two output impedances are equal, $Z'_{o-PV} = Z'_{o-CVS}$. Thus, the selection of virtual impedances can be chosen as below to compensate for the impedance mismatch.

$$Z_{v-PV} = 0;$$
$$Z_{v-CVS} = 0.1\Omega + j\omega_0 * (1mH).$$

As for the proposed VDC method, the compensating impedance is chosen to balance the line impedance. As a result,

$$Z_{est-PV} = 0.3\Omega + j\omega_0 * (3mH);$$
$$Z_{est-CVS} = 0.2\Omega + j\omega_0 * (2mH).$$

Simulation results of the virtual impedance method are shown in Figure 5.23 while those of the VDC are shown in Figure 5.24. It can be seen that when real power generation is equally shared, the mismatch of reactive power output is prominent during the first 1s. At t=1s, when the virtual impedance controller is integrated, the reactive power mismatch is reduced, as shown in Figure 5.23b. The small error is due to the different actual power consumption by the coupling line impedance. At t=3s, the reactive load experiences a step increase and the accuracy of reactive power sharing is maintained. With respect to the VSI output voltage in Figure 5.23c, the PV voltage is higher than the CVS voltage because of the higher voltage drop across the line impedance in PV unit. The grid voltage drops after t=1s when the virtual impedance is switched on. The voltage deviation increases to 1.4% at a power factor of 0.87 during t=1s to t=3s. The deviation will further increase as the power factor decreases.

In the VDC simulation, the performance of real power and reactive power sharing is similar to that in virtual impedance simulation, comparing Figure 5.24a, 5.24b to Figure 5.23a, 5.23b. However, the VSI voltage and the grid voltage increase after the VDC controller is integrated at t=1s. According to Figure 5.24d, the grid voltage restores back to around nominal value ($230V$) after compensating the voltage drop.

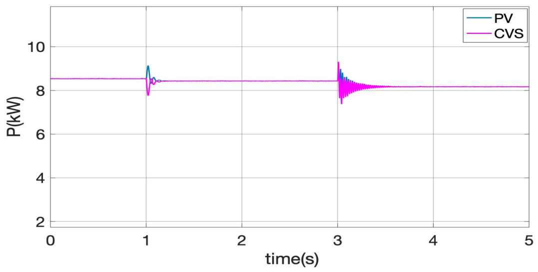

(a) Real power output

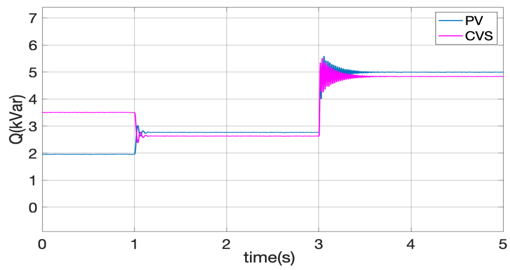

(b) Reactive power output

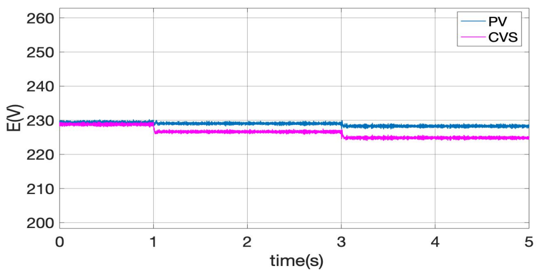

(c) VSI ph-n voltage in RMS value

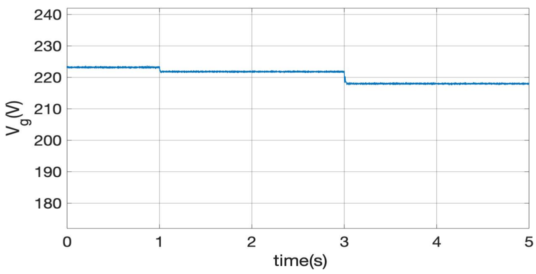

(d) Grid ph-n voltage in RMS value

Figure 5.23: Proportional power sharing under virtual impedance with known line impedances: at t=1s, virtual impedance is integrated; at t=3s, reactive power load increases from 5kVar to 10kVar

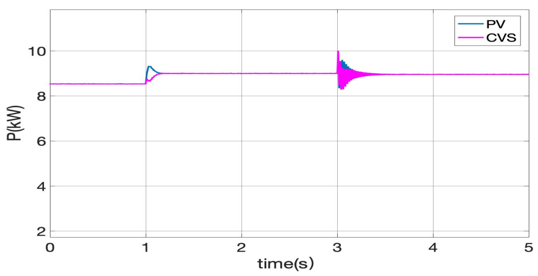

(a) Real power output

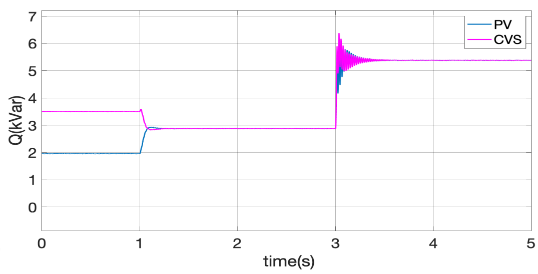

(b) Reactive power output

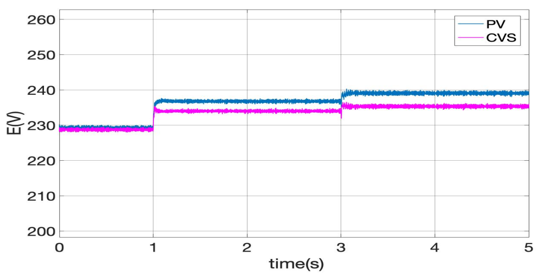

(c) VSI ph-n voltage in RMS value

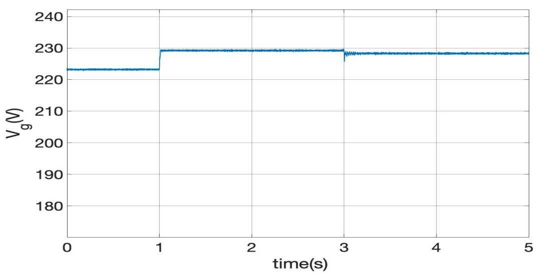

(d) Grid ph-n voltage in RMS value

Figure 5.24: Proportional power sharing under VDC with known line impedances: at t=1s, the compensation control is integrated; at t=3s, reactive power demand increases from 5kVar to 10kVar

5.5.1.2 Unknown Line Impedance

As the line impedances are unknown, a large virtual impedance can be incorporated to minimize the impact of line impedance. Figure 5.25 shows a Bode plot indicating the impact of virtual impedance selection on the total coupling impedance. When there is no virtual impedance, the difference between the two coupling impedances is very obvious, seen from the two blue lines ($Z1, Z_v = 0$ and $Z2, Z_v = 0$) . As the virtual impedance increases, the effect of line impedance mismatch reduces. It can be seen in Figure 5.25 that as Z_v increases from $0mH$ to $5mH$ to $10mH$, the magnitude discrepancy between solid line (Z_1) and dash line (Z_2) reduces. On the other hand, the inductive virtual impedance increases the phase angle at grid frequency which makes the total coupling impedance more inductive. In this simulation, we choose a $5mH$ virtual inductor for both supply units.

The simulation results are shown in Figure 5.26. It can be seen that real power maintains proportional sharing through the whole process. Reactive power sharing is greatly improved after the virtual impedance is incorporated at t=1s and the improvement is maintained during a step change of reactive load at t=3s. However, the VSI voltage and grid voltage drops dramatically at t=1s and t=3s, which is caused by the voltage drop across the relatively large virtual impedance. For example, after t=1s, when the reactive power mismatch drops by 60%, V_g deviates from the nominal value ($230V$) by 3.5%.

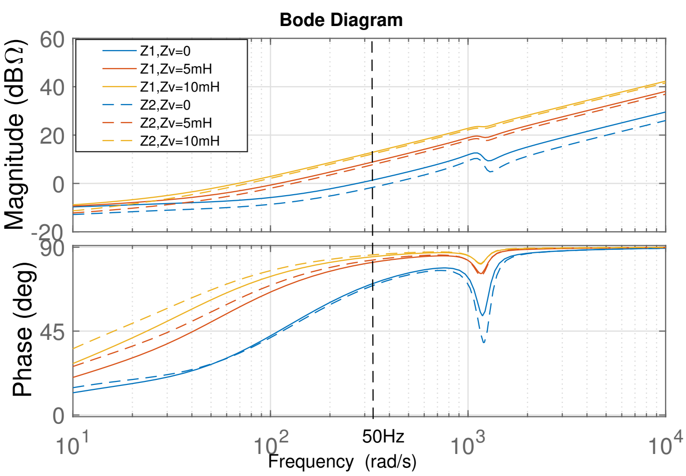

Figure 5.25: Bode plot of two coupling impedances with different virtual impedances

In the VDC method, the estimated line impedance is dependent on the selection of Z^*_{est} and droop coefficient k_a. In this simulation, a physical inductor of $5mH$ is interfaced. Correspondingly, $Z^*_{est} = 1.6\Omega$ is chosen and different values of k_a are tested. The performance of $k_a = 0.0003$, $k_a = 0.0006$, and $k_a = 0.0009$ are shown in Figure 5.27, Figure 5.28 and Figure 5.29 respectively. The real power sharing in the three conditions behaves similarly, which is shown in Figure 5.27a. The reactive power sharing improves as k_a increases. It can be explained by the relationship between Z_{est-pv} and $Z_{est-cvs}$ shown in these three figures. As the network is assumed to be inductive, only line inductance is estimated. In Figure 5.27, both estimated reactances are positive and Z_{est-pv} is slightly larger than $Z_{est-cvs}$. The discrepancy between Z_{est-pv} and $Z_{est-cvs}$ increases as k_a increases to 0.0006, which leads to an improvement in reactive power sharing accuracy. As k_a further increases, shown in Figure 5.29, the estimated impedances turn to negative. The VDC control is equivalent to integrating a virtual impedance. Since $Z_{est-pv} > Z_{est-cvs}$, similar performance of reactive power sharing can be achieved with less voltage degradation. When the reactive power mismatch reduces by around 60%, the V_g deviation is only 2% according to Figure 5.28. In Figure 5.28, during the last 2s, the power sharing improves by 80% with 3% V_g deviation.

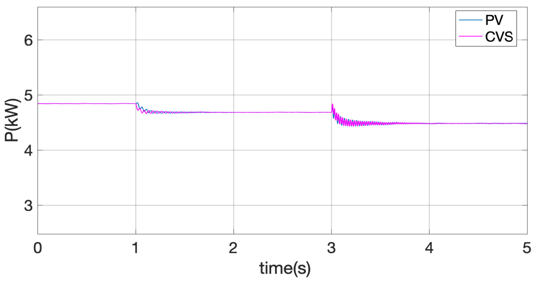

(a) Real power output

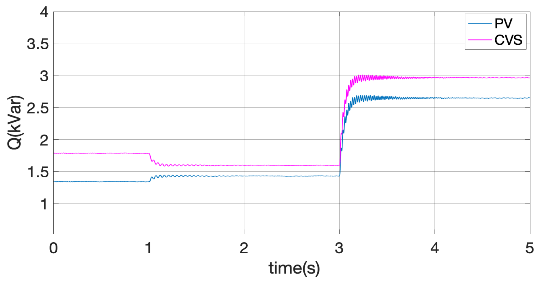

(b) Reactive power output

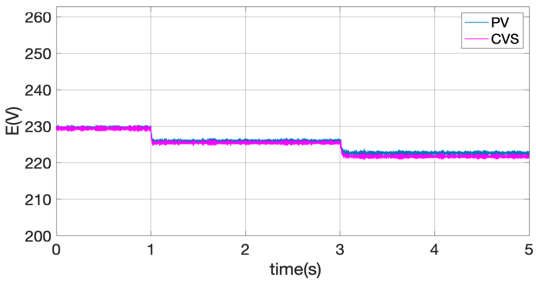

(c) VSI ph-n voltage in RMS value

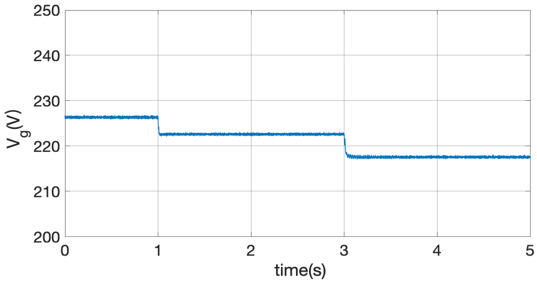

(d) Grid ph-n voltage in RMS value

Figure 5.26: Proportional power sharing under virtual impedance with unknown line impedances

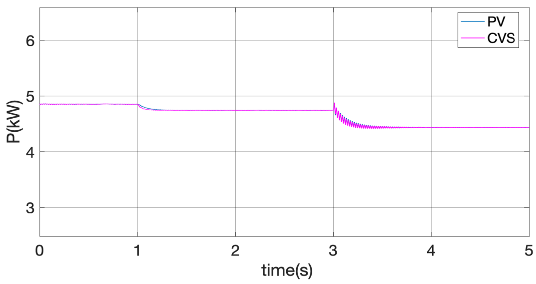

(a) Real power output

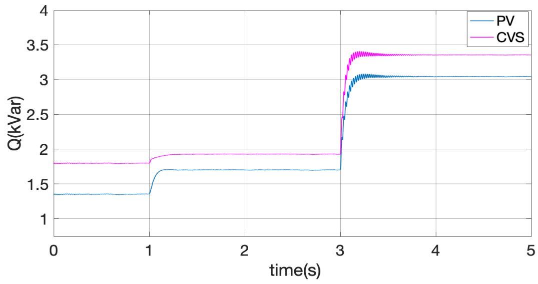

(b) Reactive power output

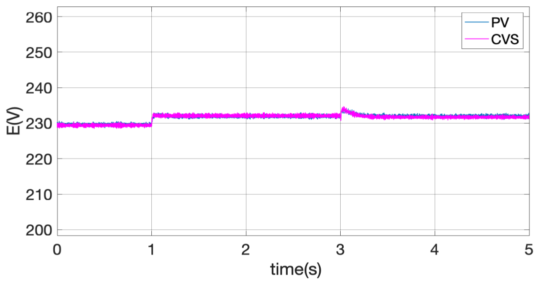

(c) VSI ph-n voltage in RMS value

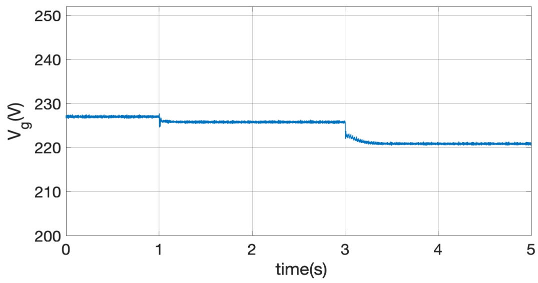

(d) Grid ph-n voltage in RMS value

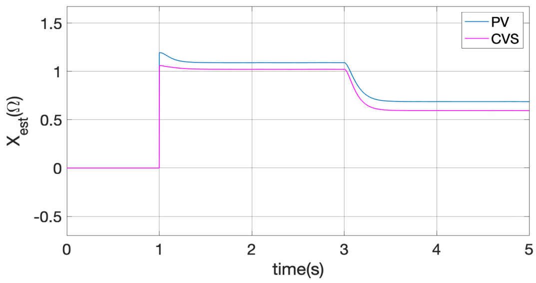

(e) Z_{est}

Figure 5.27: Proportional power sharing under VDC with unknown line impedances, $k_a = 0.0003$

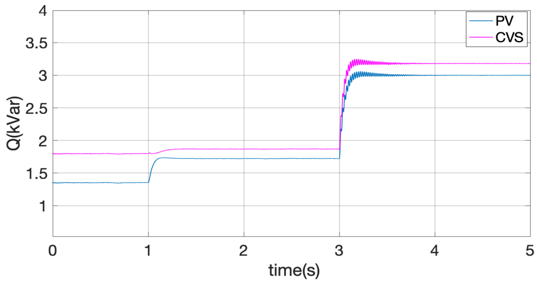

(a) Reactive power output

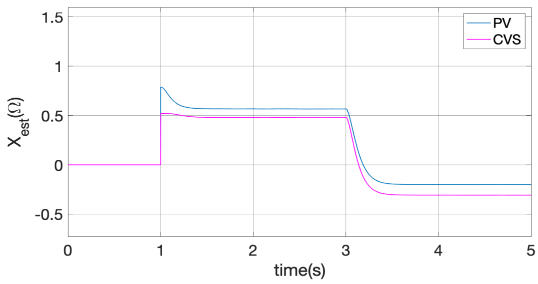

(b) Z_{est}

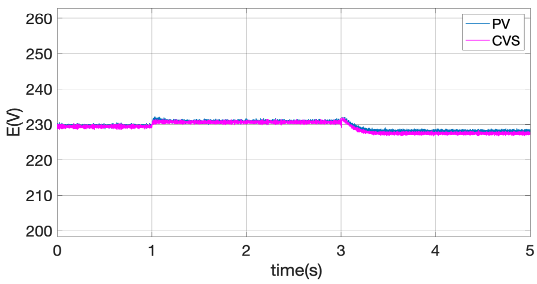

(c) VSI ph-n voltage in RMS value

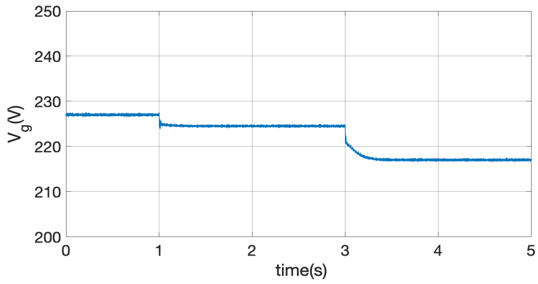

(d) Grid ph-n voltage in RMS value

Figure 5.28: Proportional power sharing under VDC with unknown line impedances, $k_a = 0.0006$

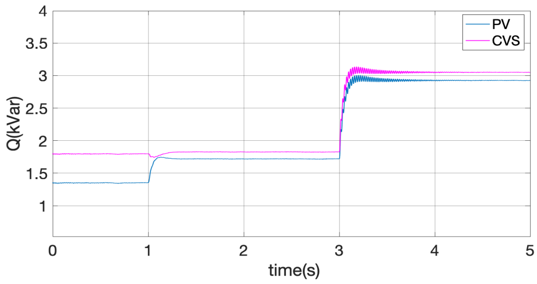

(a) Reactive power output

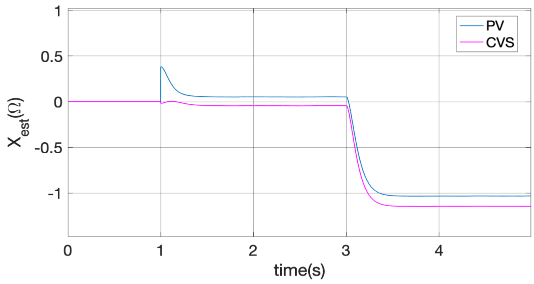

(b) Z_{est}

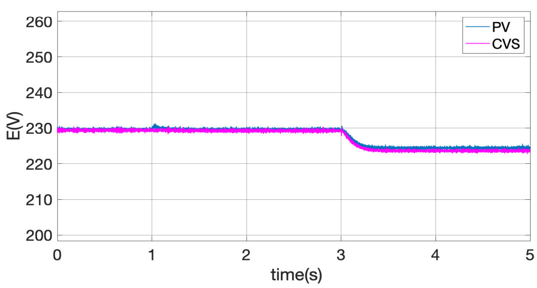

(c) VSI ph-n voltage in RMS value

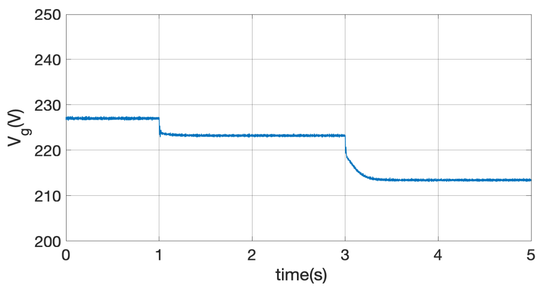

(d) Grid ph-n voltage in RMS value

Figure 5.29: Proportional power sharing under VDC with unknown line impedances, $k_a = 0.0009$

5.5.2 RE-Prioritized Reactive Power Sharing

The error in reactive power sharing, as shown in Figure 5.12b, has degraded the effectiveness of the RE-prioritized power sharing strategy. The proposed VDC method is tested here for power sharing improvement, as shown in Figure 5.30. The interfacing inductor is chosen as $5mH$, $P_{nom} = 20kW$ and k_b is set as 3.

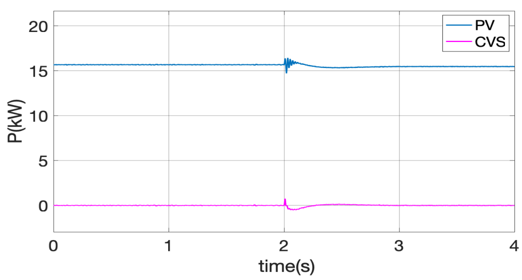

(a) Real Power output

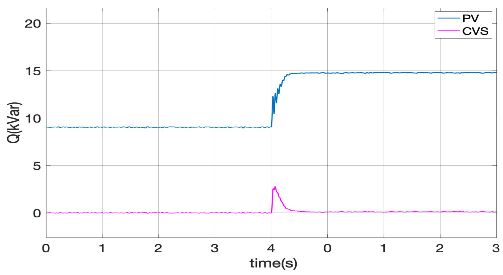

(b) Reactive power output

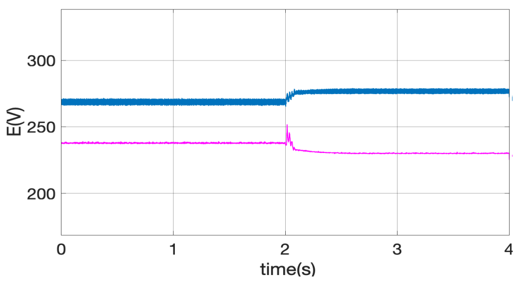

(c) VSI ph-n voltage in RMS value

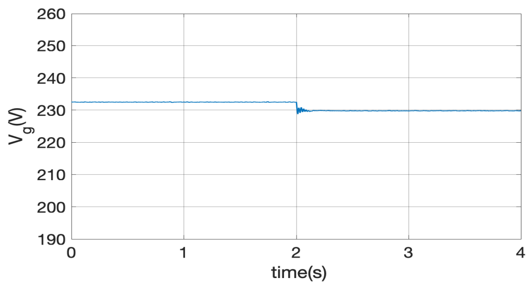

(d) Grid ph-n voltage in RMS value

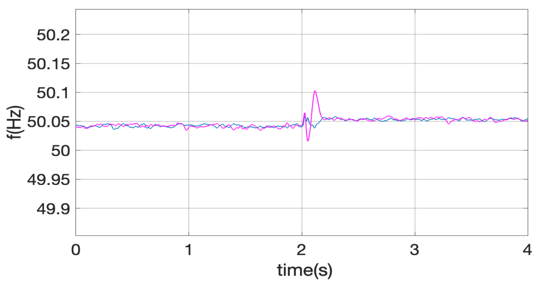

(e) Grid frequency

Figure 5.30: RE-prioritized power sharing with VDC method

It can be seen from the first two subfigures that the PV unit has the priority in both real and reactive power sharing. The CVS unit only outputs power after t=4s when the total load is beyond the capacity of PV VSI. The discrepancy in VSI voltages is not only the result of droop settings but a result of different voltage compensation across X_{est1} and

X_{est2}. Last but not least, the grid voltage is better regulated even in the condition of larger reactive power demand. When Q_L increases to $15kVar$ at a power factor of 0.71, the grid voltage is regulated at around nominal value ($230V$). However, there is a 6.5% voltage drop in Figure 5.12 without VDC integration.

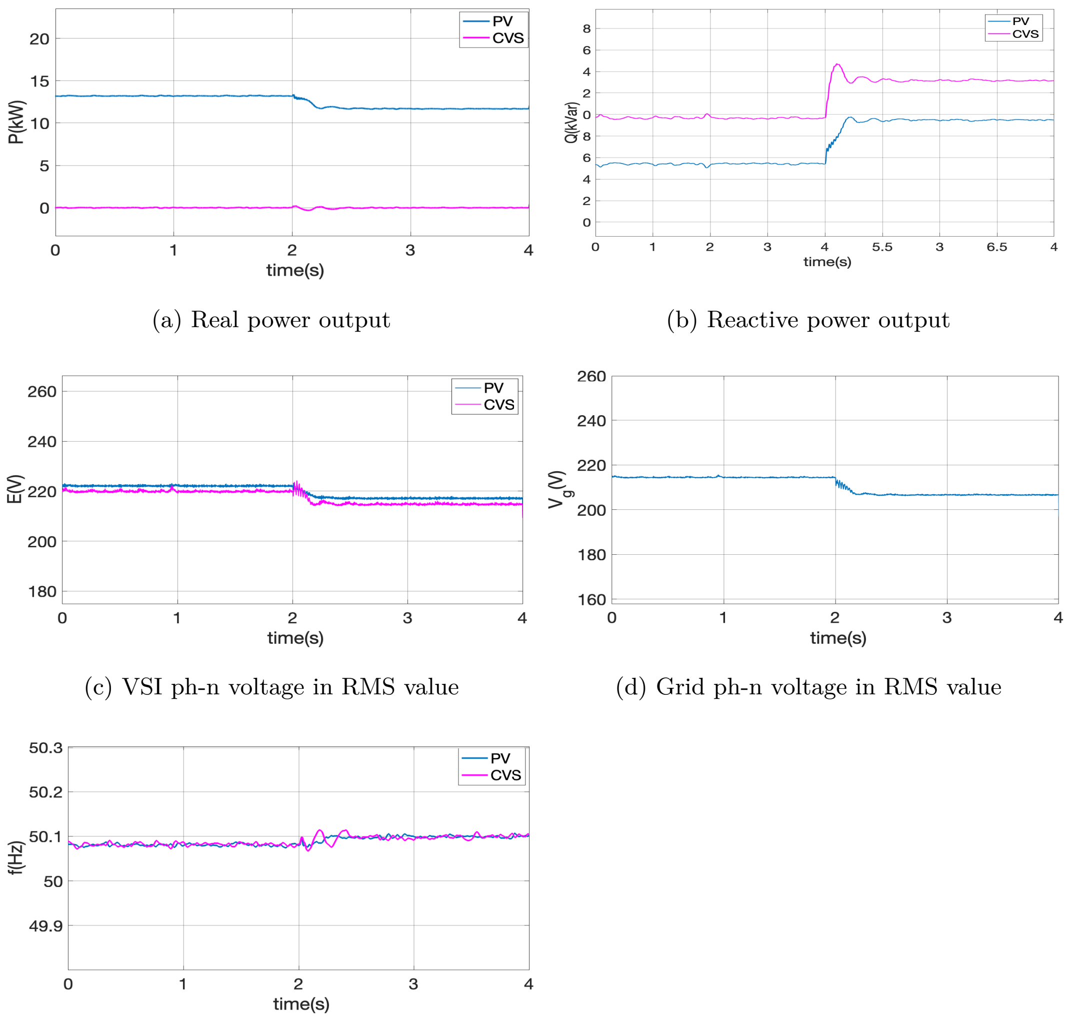

(a) Real power output

(b) Reactive power output

(c) VSI ph-n voltage in RMS value

(d) Grid ph-n voltage in RMS value

(e) Grid frequency

Figure 5.31: RE-prioritized power sharing incorporated with virtual impedance

The following simulation tests the performance of a large virtual impedance in prioritized power sharing. Both units incorporate a $5mH$ virtual inductance. The results are shown in Figure 5.31. The real power sharing still behaves as desired which gives PV unit the priority. However, regarding the reactive power sharing, there is no improvement compared to Figure 5.12. Furthermore, the grid voltage degrades dramatically. It drops to $215V$ during the first 2s and to $205V$ after the reactive load demand increases, which deviates from the nominal value by 11%. It is also worth noting that the overall power consumption is lower than the designed value which is due to the lower grid voltage level. It also explains the frequency increase at t=2s although the designed real power demand is constant.

5.6 Experimental Implementation

The experimental system is configured similarly to the simulation system, which is formed by a PV unit and a CVS unit. In Section 5.6.1, the problem of reactive power sharing with mismatched line impedances is demonstrated. The performance of virtual impedance method and the proposed VDC method are also compared. Similarly, Section 5.6.2 discusses the issues and the improvement in RE-prioritized reactive power sharing by employing the proposed VDC method.

5.6.1 Proportional Reactive Power Sharing

5.6.1.1 Virtual Impedance Method

If the line impedances are known, the mismatched coupling impedances can be compensated in the control loop. In the experiment, the mismatch is created by connecting a $5mH$ inductor on the coupling line for the PV unit and a $2mH$ inductor for the CVS unit. In the virtual impedance method, the mismatch is compensated by integrating a virtual impedance $X_V = 3mH$ in the CVS unit from t=0s. The average real and reactive power sharing is shown in Figure 5.32a and Figure 5.32b respectively. It can be seen that the mismatch of reactive power is improved after integrating the virtual impedance at t=0s. The VSI voltage deviates from the nominal value under reactive load and the deviation is shown in Figure 5.32c.

In the case of unknown coupling impedances, a large virtual impedance needs to be integrated. Under the condition of $2mH$ mismatch ($2mH$ in PV and $0mH$ in CVS) in coupling impedances, the virtual impedance value is chosen to be $10mH$. Figure 5.33 shows reactive power sharing without virtual impedance integration.

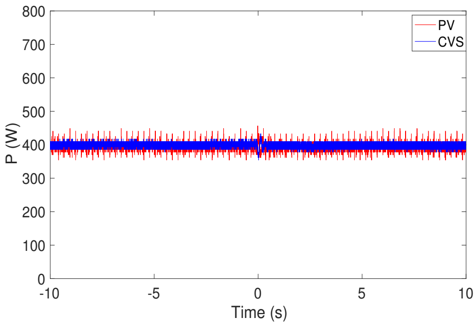

(a) Real power sharing

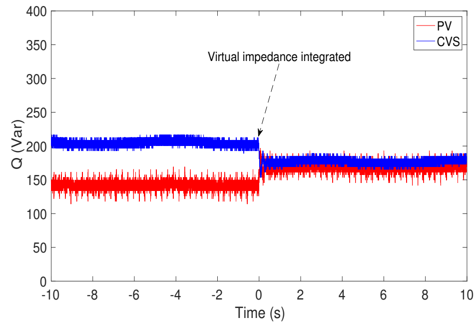

(b) Reactive power sharing

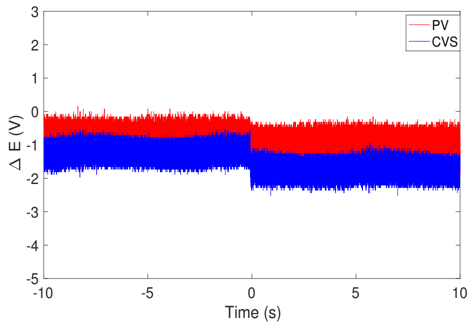

(c) VSI voltage deviation

Figure 5.32: Performance of virtual impedance with known line impedances

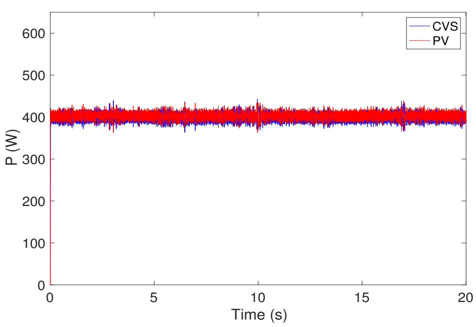

(a) Real power sharing

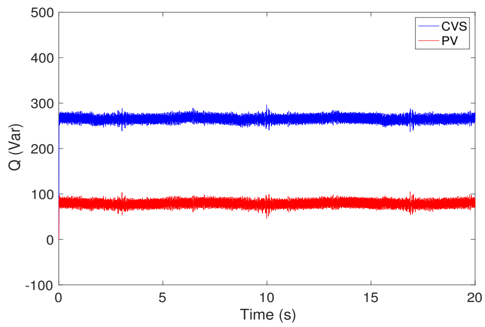

(b) Reactive power sharing

Figure 5.33: The issue in reactive power sharing with mismatched coupling impedances

It can be seen that there is a big mismatch in reactive power outputs between the two sources. Under the same loading conditions, the system performance after integrating the virtual impedance is shown in Figure 5.34. Comparing the performance with Figure 5.33b during the first 10s, the mismatch in reactive power sharing decreases while integrating the virtual impedance. In addition, the step increase of reactive power demand at t=0s demonstrates the stability of this method.

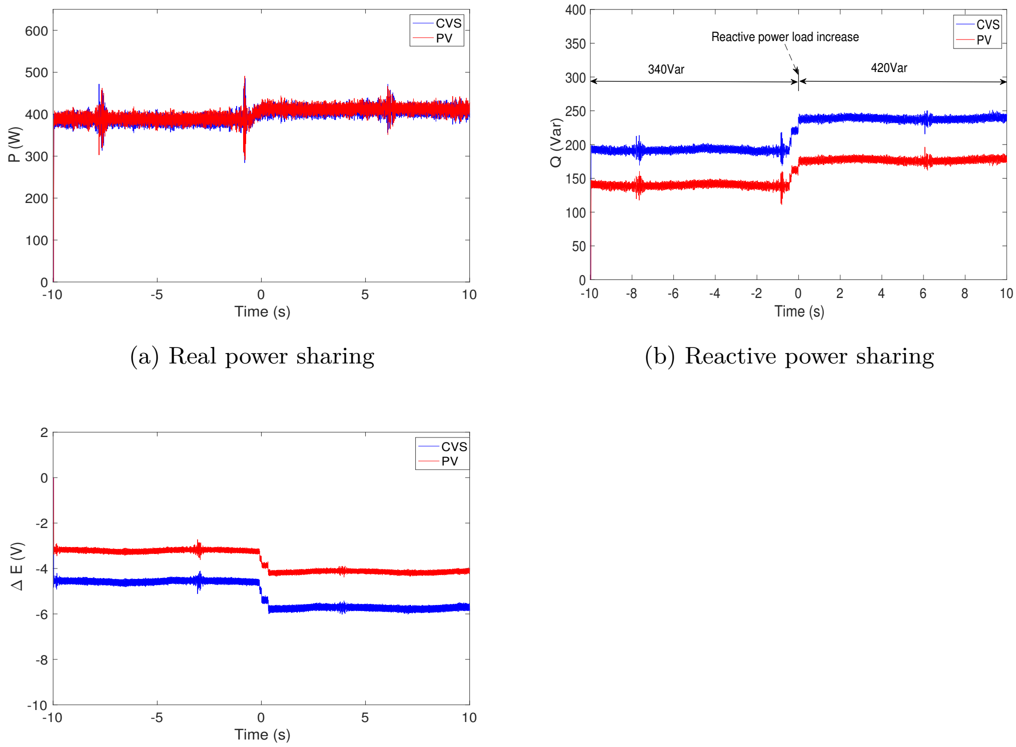

(a) Real power sharing

(b) Reactive power sharing

(c) VSI voltage deviation

Figure 5.34: Performance of virtual impedance with unknown coupling impedances

5.6.1.2 Proposed VDC Method

In the case of known coupling impedances, the experimental procedure is the same as that in the last section except that the compensation method is replaced with the proposed VDC method. In Figure 5.35, the reactive power sharing improvement can be observed from t=0s when the VDC control is integrated. Meanwhile, the VSI voltage deviates from the nominal value to a smaller degree, compared with Figure 5.32c.

If coupling impedances are unknown, a relatively large physical impedance can be interfaced on the coupling line and it is chosen as a $5mH$ inductor in this experiment. The VDC method is adapted based on this value. The reactive power sharing in Figure 5.36 shows the reactive power mismatch is reduced after integrating a large inductance despite the step change of reactive load at t=0s, compared to Figure 5.33b. During VDC integration, the value of parameter k_a has an impact on reactive power sharing accuracy. The experiments in Figure 5.37 prove that a larger k_a leads to a better accuracy. Meanwhile, the real power sharing is not influenced by the choose of k_a so its performance is not included in the results.

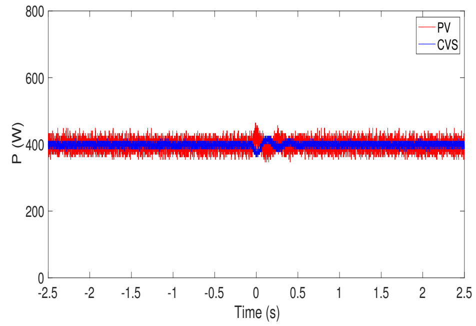

(a) Real power sharing

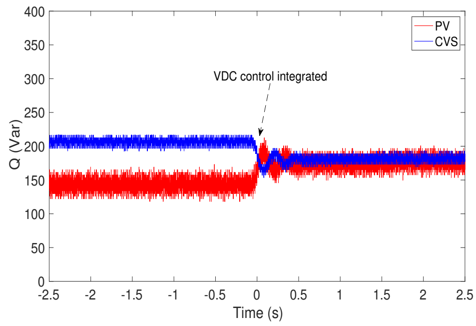

(b) Reactive power sharing

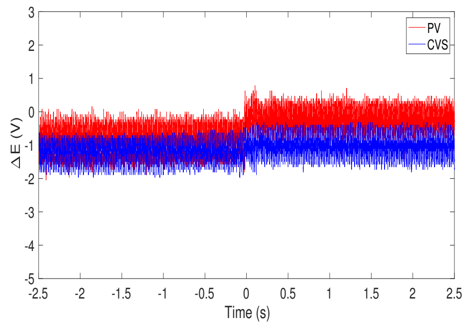

(c) VSI voltage deviation

Figure 5.35: Performance of VDC method with known coupling impedances

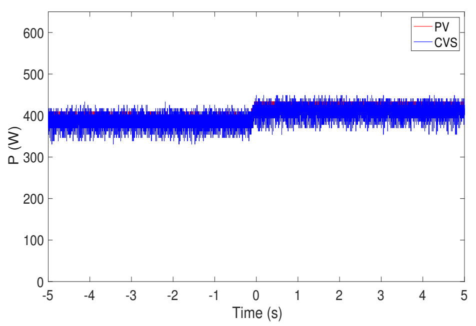

(a) Real power sharing

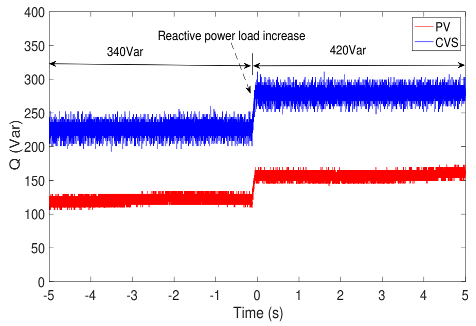

(b) Reactive power sharing

Figure 5.36: Performance after interfacing a physical inductor

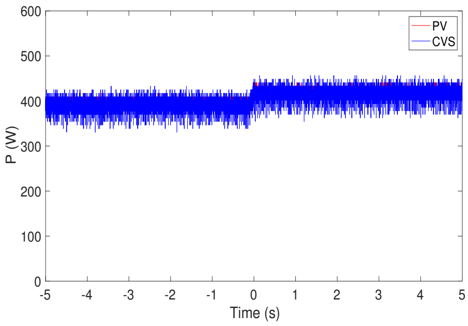

(a) Real power sharing @ $k_a = 0.003$

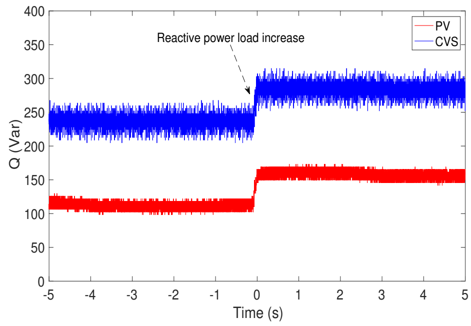

(b) Reactive power sharing @ $k_a = 0.003$

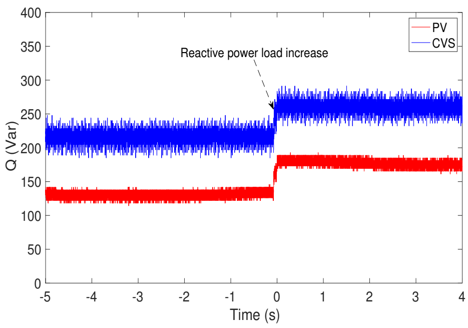

(c) Reactive power sharing @ $k_a = 0.006$

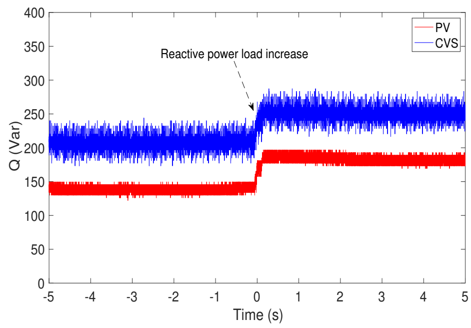

(d) Reactive power sharing @ $k_a = 0.009$

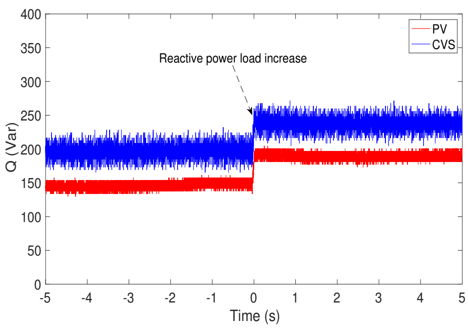

(e) Reactive power sharing @ $k_a = 0.012$

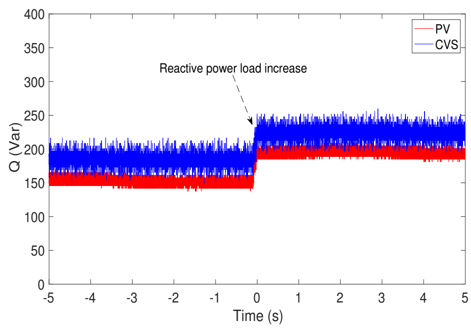

(f) Reactive power sharing @ $k_a = 0.02$

Figure 5.37: Performance of VDC method with unknown coupling impedances

5.6.2 RE-Prioritized Reactive Power Sharing

5.6.2.1 Issues in RE-Prioritized Reactive Power Sharing

In this experiment, the RE-prioritized real power sharing and average reactive power sharing is implemented first and it is followed by the prioritized reactive power sharing. It is worth mentioning that the matched coupling line impedances are employed in this experiment which allows us to focus on power supply priority. The droop settings are shown in Table 5.6 and Q_{0-PV} is changed from 0 to $600Var$ when prioritized reactive power sharing is enabled. If real power sharing is RE-prioritized and reactive power sharing is on average sharing, the PV unit shares less reactive power demand than the CVS unit, shown in Figure 5.38. If the priority of reactive power sharing is also given to the PV unit, the PV unit becomes the dominant source of reactive power supply, shown in Figure 5.39. However, it can also be seen that the CVS unit still shares a portion of reactive power demand, which is not desired. The reason for this phenomenon is that the voltage drop across the coupling impedance in the PV unit degrades its priority in power supply.

Parameters	Values
$P_{0-PV}(W)$	1000
$P_{0-CVS}(W)$	0
Q_{0-PV}	0/600
$Q_{0-CVS}(Var)$	0
$\omega_{0-PV}/\omega_{0-CVS}(rad/s)$	100π
$E_{0-PV}/E_{0-CVS}(V)$	100
$m_{PV}/m_{CVS}(rad/(s\cdot W))$	5×10^{-4}
$n_{PV}/n_{CVS}(V/Var)$	5×10^{-3}

Table 5.6: Droop control settings of reactive power sharing

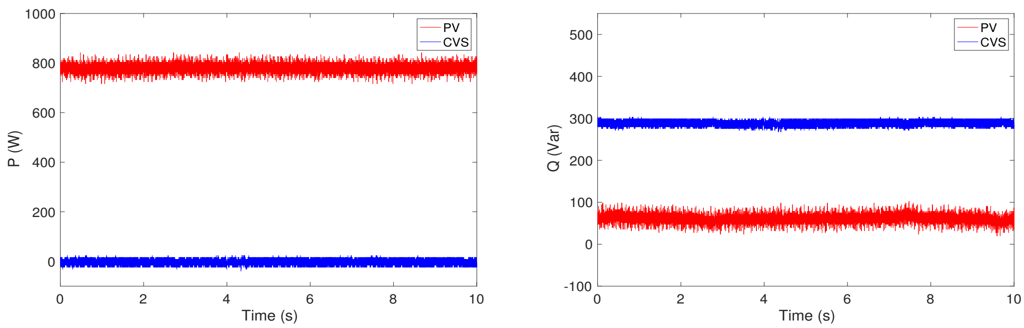

(a) Real power sharing

(b) Reactive power sharing

Figure 5.38: Prioritized real power sharing and average reactive power sharing

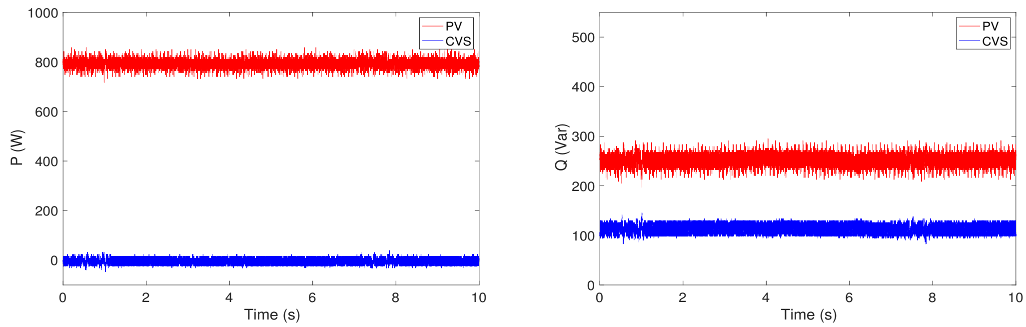

(a) Real power sharing (b) Reactive power sharing

Figure 5.39: Prioritized real power sharing and prioritized reactive power sharing

5.6.2.2 Virtual Impedance Method

The virtual impedance is incorporated here to test its impact on the RE-prioritized reactive power sharing. There is a reactive demand increase at t=0s. According to the results shown in Figure 5.40, the improvement of reactive power sharing could not be observed.

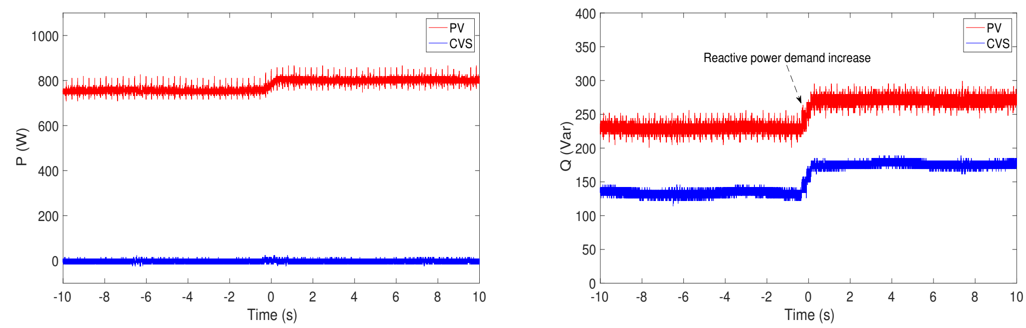

(a) Real power sharing (b) Reactive power sharing

Figure 5.40: Performance of virtual impedance in RE-prioritized reactive power sharing

5.6.2.3 Proposed VDC Method

In the VDC method, a $5mH$ inductor is first connected on the coupling line of each unit and the performance is shown in Figure 5.41. There is no improvement in reactive power sharing compared with Figure 5.39. However, if voltage drops are compensated according to the VDC principle, the CVS unit shares less amount of reactive power demand during the first 5s when the parameter $K_b = 0$ (shown in Figure 5.42b). With a selection of $K_b = 1.5$, all the reactive power demand is supported by the PV unit, which is shown in Figure 5.42b during the last 5s.

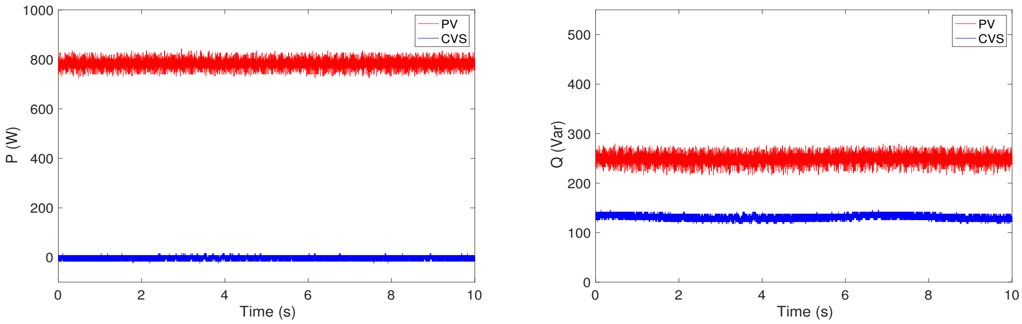

(a) Real power sharing (b) Reactive power sharing

Figure 5.41: RE-prioritized power sharing after interfacing a 5mH inductor

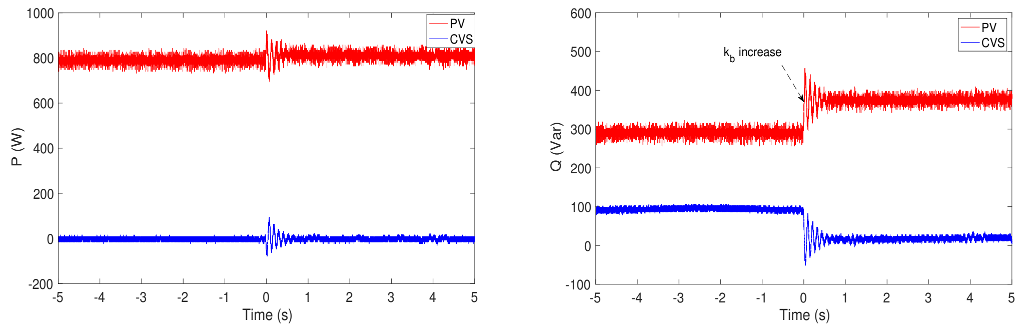

(a) Real power sharing (b) Reactive power sharing

Figure 5.42: RE-prioritized power sharing with VDC method

5.7 Conclusions

This chapter first proposed two reactive power sharing improvement approaches based on the RE-prioritized real power sharing strategy proposed in the Chapter 2. The first approach focused on the over-stressing issues on VSI, which are overlooked by traditional droop control. Different from proportional sharing in most applications, the proposed reliability-enhanced reactive power sharing allocated less reactive power demand to VSIs with more thermal damages, which consequently extends the converter reliability. The one-year numerical analysis proves that the proposed approach could improve system reliability by 15%. The second approach was proposed to relieve the reactive power burden to CVS. It could save CVS from over-running. The approach was realized by modifying traditional $Q-V$ droop and simulations were conducted to test its performance. It was found that RE-prioritized reactive power sharing was not as effective as real power sharing.

The reason of inaccurate reactive power sharing was thus investigated and it could be attributed to mismatched voltage drop across the coupling line between paralleled sources. The well known virtual impedance has been analysed and an innovative VDC method was proposed to improve reactive power sharing. The comparison between these two methods was discussed both theoretically and experimentally. It was found that both method are effective in improving reactive power sharing accuracy under both conditions: known line impedances and unknown line impedances. Meanwhile, the VDC method could achieve better grid voltage regulation. Furthermore, the proposed VDC method was also able to improve the accuracy of RE-prioritized reactive power sharing.

In the next chapter, the stability analysis is conducted for the proposed control strategies from Chapter 2 to Chapter 5. Small signal models are built and eigenvalues are derived under different parameters.

Chapter 6

Small-Signal Model and Stability Analysis

Similar to large-scale transmission grids, the stability of MG operation can also be studied with small-signal analysis. With an accurate model of the plant, small-signal analysis helps to design a robust and stable control loop, including the selection of control parameters. This chapter is divided into two parts: the analysis of control in DC/AC VSI and the analysis of control in DC/DC converter of both PV and battery sources. In Section 6.1, small-signal models of traditional droop control on one VSI are built considering different degrees of freedom. There are 3rd-order, 5th-order, 7th-order and 9th-order models. A reasonable model order reduction is thus discussed. In addition, the stability analysis of modified droop control is conducted. In Section 6.2, the small-signal model of DC/DC converter is built and the stability of the proposed control strategies is analysed.

6.1 Small-Signal Model of Droop-Controlled VSI

A model of VSI controlled by traditional droop method is well established in the literature. A very detailed model of the interfaced inverter in a MG is built and analysed in [102]. Furthermore, a model of a complete MG network interfacing with multiple inverters is analysed in [103]. It considers all internal states of an inverter as well as network dynamics. However, the complex model requires massive computation and accurate network parameters. Model order reduction is thus important which is usually based on time scale separation between different degrees of freedom. In detail, the time scale of network dynamics is determined by the electromagnetic transient time constant L/R, which is usually small (of the order of few milliseconds), below the fundamental cycle period [104]. On the other hand, the time scale of power control combined with a LPF is designed to be large enough (around 0.1s to 0.3s) to realize separation.

Considering different time scales, the model of VSI can be built into four versions: 3rd-order model, 5th-order model, 7th-order model and 9th-order model. The first section will demonstrate the procedure of model building with different degrees of freedom and their corresponding applications. In the second section, the modified $P-\omega$ droop control for real power sharing is discussed. Last but not least, the modified $Q-V$ droop control for reactive power sharing is discussed.

6.1.1 Traditional Droop Control Modelling

6.1.1.1 3rd-Order Model

In stability analysis, the slowest modes draw most attention as they play the dominant role. In traditional droop control method, the power control loop responds at the slowest speed. As a result, the model of droop control can be reduced to a lower order, which is a 3rd-order model. The line current is approximated to its quasi-stationary values derived from Kirchhoff's Law, which neglects the electromagnetic dynamics. This traditional quasi-stationary approximation is also called zero's order approximation, where the line current and power calculation can be represented in algebraic functions:

$$I_o = \frac{V_o e^{j\phi} - V_g}{R_2 + j\omega_0 L_2} \tag{6.1}$$

$$
\begin{aligned}
P &= \frac{V_o^2}{Z}cos\theta - \frac{V_oV_g}{Z}cos(\theta+\phi) \\
&= \frac{V_o^2R_2 - V_oV_gR_2cos\phi + V_oV_gX_2sin\phi}{R_2^2+X_2^2}
\end{aligned} \tag{6.2}
$$

$$
\begin{aligned}
Q &= \frac{V_o^2}{Z}sin\theta - \frac{V_oV_g}{Z}sin(\theta+\phi) \\
&= \frac{V_o^2X_2 - V_oV_gR_2sin\phi - V_oV_gX_2cos\phi}{R_2^2+X_2^2}
\end{aligned} \tag{6.3}
$$

where coupling impedance $Z\angle\theta = R_2 + jX_2 = R_2 + j\omega_0 L_2$; $V_o\angle\phi$ is the voltage at LC filter while $V_g\angle 0$ is the voltage at the common bus. This order reduction is well justified in the case of electromagnetic transient time much smaller than the time constant of power control loop.

To analyse the stability, small-signal models need to be established. A hatted variable $(\hat{})$ represents the small-signal value of the corresponding variable. We first derive small-signal representations of (6.2) and (6.3) at the equilibrium point $[V_{o0}, V_{g0}, \phi_0, \omega_0]$, assuming that the phase angle ϕ_0 at the operating point is very small such that $sin\phi_0 \approx 0$ and $cos\phi_0 \approx 1$:

$$
\hat{P} = \frac{V_{o0}V_{g0}X_2}{Z^2}\hat{\phi} + \frac{2V_{o0}R_2 - V_{g0}R_2}{Z^2}\hat{V}_o + \frac{-V_{o0}R_2}{Z^2}\hat{V}_g \tag{6.4}
$$

$$
\hat{Q} = \frac{-V_{o0}V_{g0}R_2}{Z^2}\hat{\phi} + \frac{2V_{o0}X_2 - V_{g0}X_2}{Z^2}\hat{V}_o + \frac{-V_{o0}X_2}{Z^2}\hat{V}_g \tag{6.5}
$$

Meanwhile, droop control principle gives:

$$
\dot{\hat{\phi}} = \hat{\omega} - \hat{\omega}_g \tag{6.6}
$$

$$
\hat{\omega} = \frac{-m}{1+Ts}\hat{P} \tag{6.7}
$$

$$
\hat{E} = \frac{-n}{1+Ts}\hat{Q} \tag{6.8}
$$

where m, n, T and ω_g are droop coefficients, time constant of LPF in power loop and grid frequency, respectively. Assuming the inverter voltage is equal to reference voltage,

$E = V_o$, the droop-controlled VSI can be represented by a 3rd-order model:

$$\dot{X}_1 = A_1 X_1 + B_1 U_1 \tag{6.9}$$

where $X_1 = [\hat{\phi}\ \hat{\omega}\ \hat{E}]^T$ and $U_1 = [\hat{\omega}_g\ \hat{V}]^T$.

$$A_1 = \begin{bmatrix} 0 & 1 & 0 \\ \frac{-3mV_{o0}V_{g0}X_2}{2TZ^2} & \frac{-1}{T} & \frac{-3m(2V_{o0}R_2 - V_{g0}R_2)}{2TZ^2} \\ \frac{3nV_{o0}V_{g0}R_2}{2TZ^2} & 0 & \frac{-2Z^2 - 3n(2V_{o0}X_2 - V_{g0}X_2)}{2TZ^2} \end{bmatrix}$$

$$B_1 = \begin{bmatrix} -1 & 0 \\ 0 & \frac{3mV_{o0}R_2}{2TZ^2} \\ 0 & \frac{3nV_{o0}X_2}{2TZ^2} \end{bmatrix}$$

This reduced-order model ignores the dynamics of the voltage and current controllers since the inner control bandwidth is much higher than the outer loop power control bandwidth, especially with the use of LPF. However, this model also neglects the dynamics of the power network circuit elements, which is appropriate in slow systems with high inertia. But power electronics-based systems, like MGs, have low inertia. It leads to inaccurate stability margin analysis with this reduced-order model [105]. Instead of small-signal model, Guo et al. have proposed to use a dynamic phasor model to accurately predict the stability margin of the system while considering network dynamics [105].

In addition, the coupling line in a MG is of short length so that the typical property of coupling impedance changes with the role of resistive component becomes more important. Although an increasing R_2 leads to a smaller time constant of network dynamics, the stability issue arises in a resistive network, as discovered by Vorobev et al. [104]. The time-scale separation is not sufficient to support order reduction, which means the electromagnetic dynamics cannot be neglected anymore. In addition to prominent line resistance, the other possible factors are low inertia, short coupling line and small inverter size. In conclusion, network dynamics are necessary to be considered when discussing the stability margin in MG operation.

6.1.1.2 5th-Order Model

The 5th-order model takes network dynamics into account and is built in dq reference form. Note that the small-signal of droop control can still be represented from (6.6) to (6.8).

At the same time, the voltage output of the LC filter can be represented as v_{od} and v_{oq} in dq form. Since we assume the voltage and current control loop reacts much faster, the real value of output voltage can be represented by the reference value, i.e. $v_{od} = E$ while $v_{oq} = 0$. Their dynamics with respect to output current i_{od} and i_{oq} are represented as:

$$v_{od} = v_{gd} + L_2 \frac{di_{od}}{dt} + R_2 i_{od} - \omega_0 L_2 i_{oq} \tag{6.10}$$

$$v_{oq} = v_{gq} + L_2 \frac{di_{oq}}{dt} + R_2 i_{oq} + \omega_0 L_2 i_{od} \tag{6.11}$$

where v_{gd}, v_{gq} are the dq components of voltage at the common bus and its rotating frame is also generated from the inverter, the same reference frame as that for v_o. As a result, v_{gd} and v_{gq} can be represented by

$$v_{gd} = v_g cos\phi \tag{6.12}$$

$$v_{gq} = -v_g sin\phi \tag{6.13}$$

Therefore, their small-signal representations around an operating point $[\phi_0\ \omega_0\ V_{o0}\ I_{o0}\ V_{g0}]$ are:

$$\hat{v}_{gd} = cos\phi_0 \hat{v}_g - V_{g0} sin\phi_0 \hat{\phi} \tag{6.14}$$

$$\hat{v}_{gq} = -sin\phi_0 \hat{v}_g - V_{g0} cos\phi_0 \hat{\phi} \tag{6.15}$$

Meanwhile, the measured power can be represented as:

$$P = \frac{3}{2}(v_{od} i_{od} + v_{oq} i_{oq}) \tag{6.16}$$

$$Q = \frac{3}{2}(v_{oq} i_{od} - v_{od} i_{oq}) \tag{6.17}$$

Take Laplace transformation of above equations and analyse their small signals around the operating point. The system can then be represented in a 5-dimensional state space model:

$$\dot{X}_2 = A_2 X_2 + B_2 U_2 \tag{6.18}$$

where $X_2 = [\hat{\phi}\ \hat{\omega}\ \hat{v}_{od}\ \hat{i}_{od}\ \hat{i_{oq}}]^T$ and $U_2 = [\hat{\omega}_g\ \hat{v}_g]^T$.

$$A_2 = \begin{bmatrix} 0 & 1 & 0 & 0 & 0 \\ 0 & \frac{-1}{T} & \frac{-3mI_{od0}}{2T} & \frac{-3mV_{od0}}{2T} & 0 \\ 0 & 0 & \frac{-2+3nI_{oq0}}{2T} & \frac{-3nV_{oq0}}{2T} & \frac{3nV_{od0}}{2T} \\ \frac{V_{g0}sin\phi_0}{L_2} & 0 & \frac{1}{L_2} & -\frac{R_2}{L_2} & \omega_0 \\ \frac{V_{g0}cos\phi_0}{L_2} & 0 & 0 & -\omega_0 & -\frac{R_2}{L_2} \end{bmatrix}$$

$$B_2 = \begin{bmatrix} -1 & 0 & 0 & 0 & 0 \\ 0 & 0 & 0 & -\frac{cos\phi_0}{L_2} & \frac{sin\phi_0}{L_2} \end{bmatrix}^T$$

6.1.1.3 7th-Order Model

In the full-order model, the dynamics of all degrees of freedom are taken into account. In the cascaded voltage and current control loop, the inner current control loop is considered to have a much higher bandwidth than outer voltage control loop. As a result, the inner loop can be ignored and a 7th-order model can be built. It considers voltage control loop, network dynamics across the coupling line as well as power control loop.

Around an operating point $[\phi_0\ \omega_0\ V_{o0}\ I_{o0}\ V_{g0}]$, the model of network and power control is the same as that of the 5th-order model. The voltage control loop employs PI control combining with cross coupling terms, and generates a current reference value. The current reference can represent the actual current dynamics because of the fast response of the inner current loop. It needs to be noted that the generated reference value is the source-side-inductor current. Based on the control loop and network topology, the output current can be represented by

$$i_{od} = k_p(E - v_{od}) + k_i \int (E - v_{od})dt - C\frac{dv_{od}}{dt} \tag{6.19}$$

$$i_{oq} = k_p(0 - v_{oq}) + k_i \int (0 - v_{oq})dt - Cd\frac{v_{oq}}{dt} \tag{6.20}$$

where the terms $C\frac{dv_{od}}{dt}$ and $C\frac{dv_{oq}}{dt}$ introduce second-order voltage dynamics into the system which can be neglected. Take Laplace transformation of above equations and analyse the small-signal around the operating point. We can derive a state space model of this droop controlled inverter:

$$\dot{X}_3 = A_3X_3 + B_3U_3 \tag{6.21}$$

where $X_3 = [\hat{\phi}\ \hat{P}\ \hat{Q}\ \hat{i}_{od}\ \hat{i}_{oq}\ \hat{v}_{od}\ \hat{v}_{oq}]^T$ and $U_3 = [\hat{\omega}_g\ \hat{v}_g]^T$.

$$A_3 = \begin{bmatrix} 0 & -\frac{3m}{2} & 0 & 0 & 0 & 0 & 0 \\ 0 & -\frac{1}{T} & 0 & \frac{V_{od0}}{T} & \frac{V_{oq0}}{T} & \frac{I_{od0}}{T} & \frac{I_{oq0}}{T} \\ 0 & 0 & -\frac{1}{T} & \frac{V_{oq0}}{T} & -\frac{V_{od0}}{T} & -\frac{I_{oq0}}{T} & \frac{I_{od0}}{T} \\ \frac{V_{g0}sin\phi_0}{L_2} & 0 & 0 & -\frac{R_2}{L_2} & \omega_0 & \frac{1}{L_2} & 0 \\ \frac{V_{g0}cos\phi_0}{L_2} & 0 & 0 & -\omega_0 & -\frac{R_2}{L_2} & 0 & \frac{1}{L_2} \\ -\frac{V_{g0}sin\phi_0}{k_pL_2} & 0 & M^3_{63} & M^3_{64} & M^3_{65} & M^3_{66} & -\frac{3nI_{od0}}{2T} \\ -\frac{V_{g0}cos\phi_0}{k_pL_2} & 0 & 0 & \frac{\omega_0}{k_p} & \frac{R_2}{k_pL_2} & 0 & -\frac{L_2k_i+1}{k_pL_2} \end{bmatrix}$$

$$B_3 = \begin{bmatrix} -1 & 0 & 0 & 0 & 0 & 0 & 0 \\ 0 & 0 & 0 & \frac{-cos\phi_0}{L_2} & \frac{sin\phi_0}{L_2} & \frac{cos\phi_0}{k_pL_2} & \frac{-sin\phi_0}{k_pL_2} \end{bmatrix}^T$$

where

$$
\begin{aligned}
M_{63}^3 &= \frac{3n}{2T} - \frac{3nk_i}{2k_p} \\
M_{64}^3 &= \frac{R_2}{k_pL_2} - \frac{3nV_{oq0}}{2T} \\
M_{65}^3 &= \frac{3nV_{od0}}{2T} - \frac{\omega_0}{k_p} \\
M_{66}^3 &= \frac{3nI_{oq0}}{2T} - \frac{1+k_iL_2}{k_pL_2}
\end{aligned}
$$

The 9th-order model includes the dynamics of the inner current control loop. Current regulation dynamics need to be analysed when designing its control bandwidth. Although the 9th-order model generates a more accurate stability margin analysis, the 7th-order model is sufficient when the inner loop responds much faster than the outer voltage control loop. The following section demonstrates the different behaviour of the 3rd-order, the 5th-order and the 7th-order model in stability performance.

6.1.1.4 Discussion on Model Order Reduction

Root trajectories of a state space model with varying control parameters can indicate the stability margin under different conditions. It also shows the impact of a particular coefficient on stability margin. This technique is used here to verify the effectiveness of the reduced-order model. As we analyse a small-signal model, the selection of the equilibrium point is important. In test, the equilibrium point is chosen by real-time digital simulation in Matlab/Simulink, while it can also be done by power flow analysis. The initial condition is shown in Table 6.1 and Table 6.2 presents the network parameters.

According to literature review, the values of droop coefficients play an important role in stability performance. The following root trajectories track the eigenvalues of the system matrix under varying droop coefficients, m and n. Figure 6.1 shows the eigenvalue trajectories for the 3rd-order model with increasing m and n. The eigenvalues stay within the left-half plane which means the system stays stable. However, in the 5th-order model (Figure 6.2), eigenvalues pass the imaginary axis and move to right-half plane at high droop coefficients. The threshold of m and n are respectively $0.035rad/(s\cdot W)$ and

$0.03V/Var$. In the 7th-order model (Figure 6.3), the stability margin is smaller than that in Figure 6.2 with the same m, which means the voltage control loop affects the system dynamics and stability. However, the impact of n shows little difference between the 5th-order model and the 7th-order model. It can also be found in Figure 6.4 that, the voltage control parameters k_p and k_i change the stability margin under fixed droop coefficients. It is thus necessary to consider the voltage control loop when determining a more accurate threshold of droop coefficients. In conclusion, the 3rd-order model fails to predict the instability under higher droop coefficients; the 5th-order model is sufficient to predict an approximate stability margin of droop-controlled VSI; the 7th-order model generates a smaller stability margin with respect to $P-\omega$ droop coefficient.

I_{od0}	I_{oq0}	V_{od0}	V_{oq0}	V_{g0}	k_p	k_i
$0.8A$	$-0.2A$	$100V$	$0V$	$99V$	0.1	100

Table 6.1: The equilibrium point in stability analysis

m	n	T	L_2	R_2	ω_0
$0.0005rad/(s\cdot W)$	$0.005V/Var$	$0.01s$	$5mH$	0.5Ω	$314rad/s$

Table 6.2: Network and control parameters

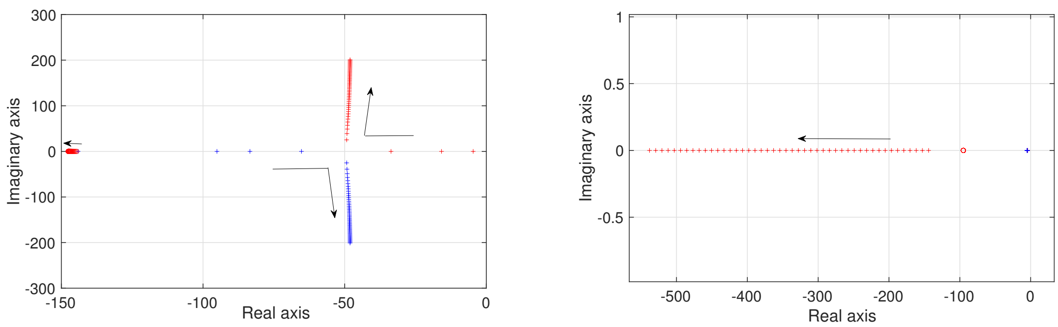

(a) $m(rad/(s\cdot W))$: 0.0005 to 0.05 (step interval:0.001) (b) $n(V/Var)$: 0.005 to 0.05 (step interval:0.001)

Figure 6.1: Eigenvalue trajectories under increasing m and n in 3rd-order model

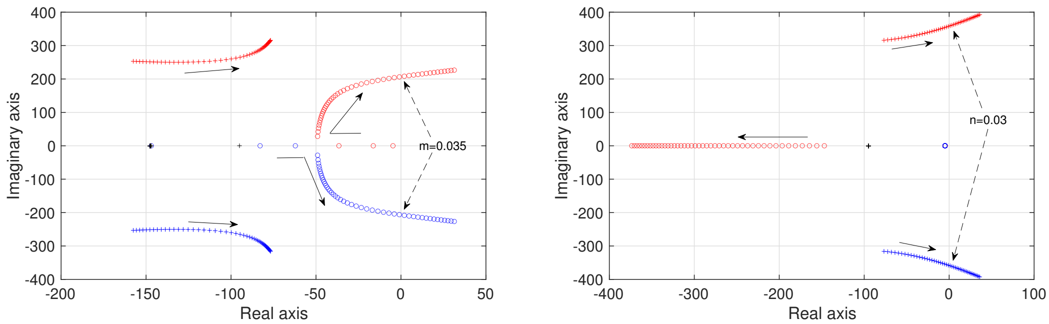

(a) $m(rad/(s{\cdot}W))$: 0.0005 to 0.05 (step interval:0.001)

(b) $n(V/Var)$: 0.005 to 0.05 (step interval:0.001)

Figure 6.2: Eigenvalue trajectories under increasing m and n in 5th-order model

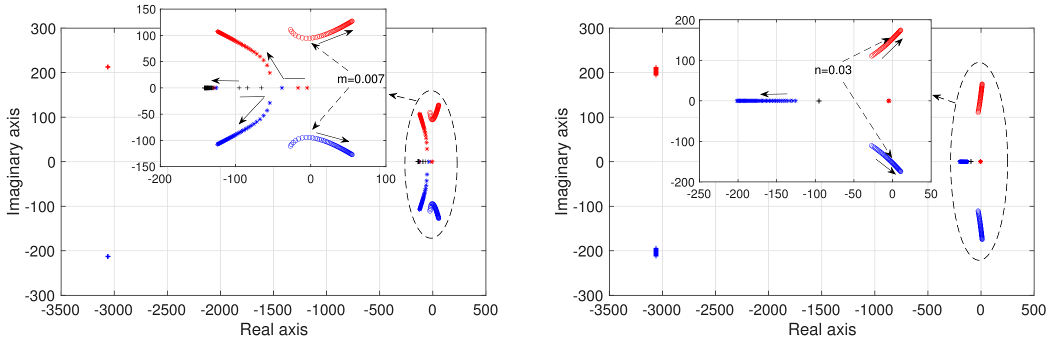

(a) $m(rad/(s{\cdot}W))$: 0.0005 to 0.05 (step interval:0.001)

(b) $n(V/Var)$: 0.005 to 0.05 (step interval:0.001)

Figure 6.3: Eigenvalue trajectories under increasing m and n in 7th-order model

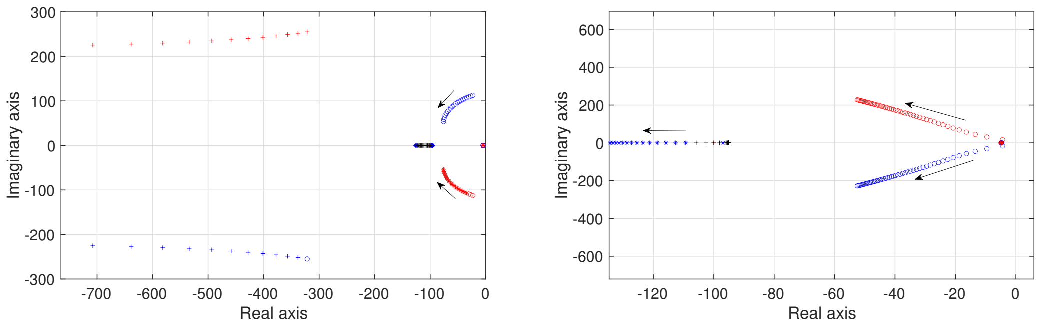

(a) k_p: 0.05 to 1 (step interval:0.05), $k_i = 100$

(b) k_i: 10 to 500 (step interval:10), $k_p = 0.1$

Figure 6.4: Eigenvalue trajectories under increasing k_p and k_i in 7th-order model

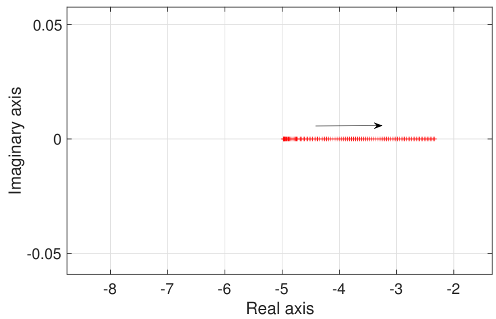

Figure 6.5: The effect of coupling resistance on stability performance

This phenomenon can also be explained from the perspective of physical meaning. It is more explicit to analyse the system in phasor form. According to (6.1), output current from inverter to the grid I_o can be represented by

$$I_o = \frac{E\angle\phi - V}{R_2 + j\omega_0 L_2} \tag{6.22}$$

$$I_o = \frac{E\angle\phi - V}{(sL_2 + R_2) + j\omega_0 L_2} \tag{6.23}$$

where (6.22) represents the current ignoring its dynamics and (6.23) takes it into account. It can instantly be noted that the original R_2 is replaced by $sL_2 + R_2$ in the model including network dynamics. In other words, the line resistance value increases by an increment which is determined by the coupling inductance and frequency. The effect of line resistance on stability can be seen in the root trajectory of the 3rd-order model. In Figure 6.5, the dominant eigenvalue moves towards the imaginary axis under an increasing R_2 . This phenomena can roughly explain the influence of network dynamics on system stability. A detailed analysis of the reason is discussed in [104].

To conclude, 5th-order model is chosen to analyse droop control stability for the sake of simplicity and appropriate accuracy.

6.1.1.5 Simulation Verification of Model Accuracy

To verify the accuracy of established model in predicting system stability, a simulation is conducted based on two droop-controlled converters connected in parallel. The stable operating point is set according to Table 6.1 and the control parameters are set as Table 6.2. The droop coefficients m and n are tested separately. Firstly, the real power droop coefficient m is increased through step changes, as shown in Figure 6.6 (a). The corresponding system power sharing performance is shown in Figure 6.6 (b). It can be seen that the system becomes underdamped after m reaches $0.007 rad/(s{\cdot}W)$ and turns to unstable after m reaches $0.009 rad/(s{\cdot}W)$ while the 7th-order model estimates the stability boundary is $m = 0.007 rad/(s{\cdot}W)$. This slight error in small-signal analysis can provide the system with more stability margin.

Secondly, the reactive power droop coefficient n is increased through step changes, as shown in Figure 6.7 (a). The corresponding system power sharing performance is shown in Figure6.7 (b). It can be seen that the system becomes underdamped after n reaches $0.02V/Var$ and turns to unstable after n reaches $0.04V/Var$ while the 7th-order model estimates the stability boundary is $n = 0.03V/Var$. It is worth noting that the small-signal analysis based on the established droop control model can estimate the system stability boundary with a slight error. It is effective enough as a guidance for control parameters selection.

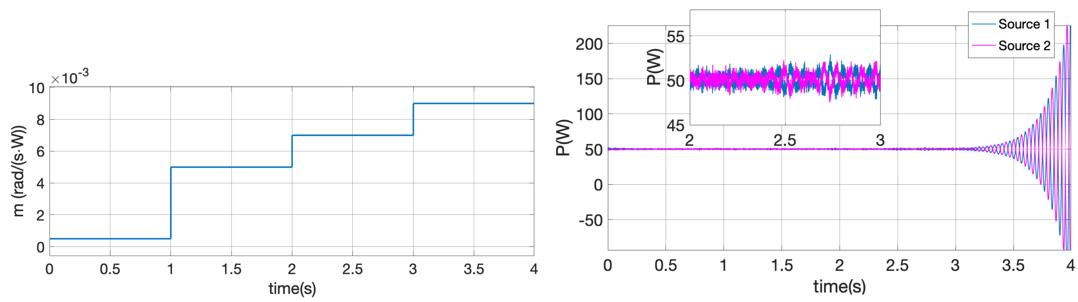

(a) Step changes of m (b) Real power sharing performance

Figure 6.6: Stability simulation of increasing m

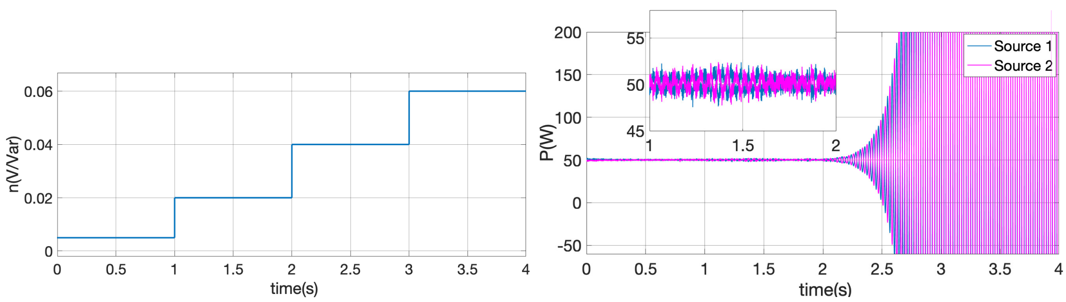

(a) Step changes of n (b) Real power sharing performance

Figure 6.7: Stability simulation of increasing n

6.1.2 Modified $P - \omega$ Control Modelling

The modified $P - \omega$ control strategy for VSI was discussed in Chapter 2. The frequency reference value is adjusted by a frequency deviation term $\delta\omega$. In batteries and CVS, the $\delta\omega$ is generated by PI power limiting method while it is generated by DC voltage bus regulation in RES. The small-signal model of the modified droop control in different sources are now discussed.

6.1.2.1 Modified P–ω Control Modelling for Conventional & Battery Sources

According to the control topology proposed in Chapter 2, $\delta\omega$ is generated from a PI controller:

$$\delta\omega = (k_p + \frac{k_i}{s})(P_{max} - P) \tag{6.24}$$

The modified small-signal model can be represented as:

$$\dot{\hat{\phi}} = \hat{\omega} - \hat{\omega}_g + \hat{\delta\omega} \tag{6.25}$$

$$\hat{\omega} = \frac{-m}{1 + Ts}\hat{P} \tag{6.26}$$

$$\hat{E} = \frac{-n}{1 + Ts}\hat{Q} \tag{6.27}$$

$$\hat{\delta\omega} = -(k_p + \frac{k_i}{s})\hat{P} \tag{6.28}$$

As the model of power calculation has not changed, the state space model can be modified into, what is now a 6-dimensional model:

$$\dot{X}_4 = A_4 X_4 + B_4 U_4 \tag{6.29}$$

where $X_4 = [\hat{\phi}\ \hat{\omega}\ \hat{v}_{od}\ \hat{i}_{od}\ \hat{i}_{oq}\ \hat{\delta\omega}]^T$ and $U_4 = [\hat{\omega}_g\ \hat{v}_g]^T$.

$$A_4 = \begin{bmatrix} 0 & 1 & 0 & 0 & 0 & 1 \\ 0 & \frac{-1}{T} & \frac{-3mI_{od0}}{2T} & \frac{-3mV_{od0}}{2T} & 0 & 0 \\ 0 & 0 & \frac{-2+3nI_{oq0}}{2T} & \frac{-3nV_{oq0}}{2T} & \frac{3nV_{od0}}{2T} & 0 \\ \frac{V_{g0}sin\phi_0}{L_2} & 0 & \frac{1}{L_2} & -\frac{R_2}{L_2} & \omega_0 & 0 \\ \frac{V_{g0}cos\phi_0}{L_2} & 0 & 0 & -\omega_0 & -\frac{R_2}{L_2} & 0 \\ \frac{-3k_pV_{od0}V_{g0}sin\phi_0}{2L_2} & 0 & M_{63}^4 & M_{64}^4 & M_{65}^4 & 0 \end{bmatrix}$$

$$B_4 = \begin{bmatrix} -1 & 0 & 0 & 0 & 0 & 0 \\ 0 & 0 & 0 & \frac{-cos\phi_0}{L_2} & \frac{sin\phi_0}{L_2} & 0 \end{bmatrix}^T$$

where

$$M_{63}^4 = -\frac{3k_p}{2}\left(\frac{V_{od0}}{L_2} + \frac{(-2+3nI_{oq0})I_{od0}}{2T}\right) - \frac{3k_iI_{od0}}{2}$$
$$M_{64}^4 = \frac{3k_p}{2}\left(\frac{V_{od0}R_2}{L_2} + \frac{3nV_{oq0}I_{od0}}{2T}\right) - \frac{3k_iV_{od0}}{2}$$
$$M_{65}^4 = -\frac{3k_p}{2}\left(\omega_0V_{od0} + \frac{3nV_{od0}I_{od0}}{2T}\right)$$

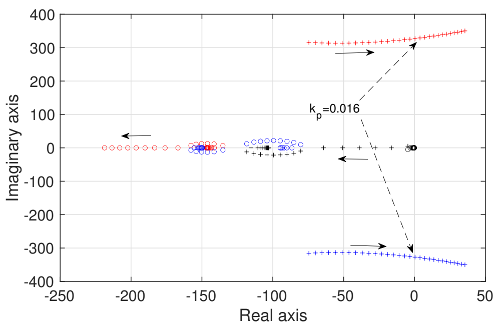

(a) k_p: 0.0005 to 0.03 (step interval:0.001)

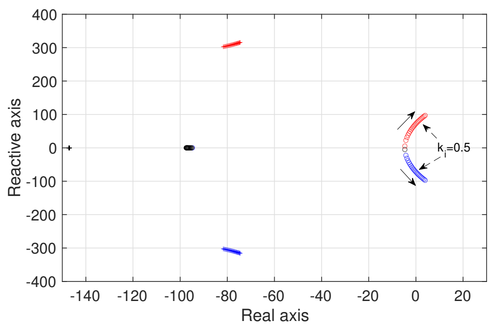

(b) k_i: 0.005 to 1 (step interval:0.05)

Figure 6.8: Eigenvalue trajectories under increasing k_p, k_i in modified droop control for CVS/Batteries

In simulation, the parameters are chosen consistently with those used for traditional droop control while the PI parameters in power limiting are set as $k_p = 0.0005$ and $k_i = 0.005$ as the nominal value. The root trajectories of varying m and n are similar to that of 5th-order model. Meanwhile, the impact of k_p and k_i can also be seen in root trajectories, shown in Figure 6.8. The increasing k_p or k_i reduces the stability margin which indicates a boundary for PI parameters.

6.1.2.2 Modified $P - \omega$ Control Modelling for PV Sources

According to the control topology proposed in Chapter 2, $\delta\omega$ in PV is generated from the DC link voltage regulation loop:

$$\delta\omega = (k_p + \frac{k_i}{s})(V_{dc} - V_{dcref}) \tag{6.30}$$

Since V_{dc} is related to the energy stored in the DC capacitor, a decrease of V_{dc} means energy loss. The detailed relationship is shown below:

$$\delta E = \frac{C}{2}(V_{dc}^2 - V_{dcref}^2)$$

where δE represents the amount of energy exchange after V_{dc} deviates from its nominal value V_{dcref}.

The small-signal model of above equation is:

$$\hat{P}_{net} = sCV_{dcref}\hat{V}_{dc} \tag{6.31}$$

where $\hat{P}_{net}$ represents the net power injected into the DC link capacitor. Ignoring power losses in converters, the power output of VSI equals the power consumption on DC capacitor. The power injection is assumed to be constant since weather conditions vary at a slow speed. The power output of the VSI can thus be represented as:

$$\hat{P} = -sCV_{dcref}\hat{V}_{dc} \tag{6.32}$$

Combining (6.30) and (6.32), the small-signal of $\delta\omega$ relative to $\hat{P}$ can be expressed as:

$$\hat{\delta\omega} = (k_p + \frac{k_i}{s})\frac{-1}{sCV_{dcref}}\hat{P} \tag{6.33}$$

We introduce a new variable α here to transform the second-order system (6.33) into first-order by defining:

$$\hat{\alpha} = sCV_{dcref}\hat{\delta\omega}$$

As a result, (6.33) can be presented in two equations:

$$\hat{\delta\omega} = \frac{1}{sCV_{dcref}}\hat{\alpha}$$
$$\hat{\alpha} = -(k_p + \frac{k_i}{s})\hat{P}$$

The small-signal state space model of modified droop control in PV source can be represented as:

$$\dot{X}_5 = A_5X_5 + B_5U_5 \tag{6.34}$$

where $X_5 = [\hat{\phi}\ \hat{\omega}\ \hat{v}_{od}\ \hat{i}_{od}\ \hat{i}_{oq}\ \hat{\alpha}\ \hat{\delta\omega}]^T$ and $U_5 = [\hat{\omega}_g\ \hat{v}_g]^T$.

$$A_5 = \begin{bmatrix} 0 & 1 & 0 & 0 & 0 & 0 & 1 \\ 0 & \frac{-1}{T} & \frac{-3mI_{od0}}{2T} & \frac{-3mV_{od0}}{2T} & 0 & 0 & 0 \\ 0 & 0 & \frac{-2+3nI_{oq0}}{2T} & \frac{-3nV_{oq0}}{2T} & \frac{3nV_{od0}}{2T} & 0 & 0 \\ \frac{V_{g0}sin\phi_0}{L_2} & 0 & \frac{1}{L_2} & -\frac{R_2}{L_2} & \omega_0 & 0 & 0 \\ \frac{V_{g0}cos\phi_0}{L_2} & 0 & 0 & -\omega_0 & -\frac{R_2}{L_2} & 0 & 0 \\ \frac{-3k_pV_{od0}V_{g0}sin\phi_0}{2L_2} & 0 & M_{63}^5 & M_{64}^5 & M_{65}^5 & 0 & 0 \\ 0 & 0 & 0 & 0 & 0 & \frac{1}{CV_{dcref}} & 0 \end{bmatrix}$$

$$B_5 = \begin{bmatrix} -1 & 0 & 0 & 0 & 0 & 0 & 0 \\ 0 & 0 & 0 & \frac{-cos\phi_0}{L_2} & \frac{sin\phi_0}{L_2} & 0 & 0 \end{bmatrix}^T$$

where

$$M_{63}^5 = -\frac{3k_p}{2}(\frac{V_{od0}}{L_2} + \frac{(-2+3nI_{oq0})I_{od0}}{2T}) - \frac{3k_iI_{od0}}{2}$$
$$M_{64}^5 = \frac{3k_p}{2}(\frac{V_{od0}R_2}{L_2} + \frac{3nV_{oq0}I_{od0}}{2T}) - \frac{3k_iV_{od0}}{2}$$
$$M_{65}^5 = -\frac{3k_p}{2}(\omega_0V_{od0} + \frac{3nV_{od0}I_{od0}}{2T})$$

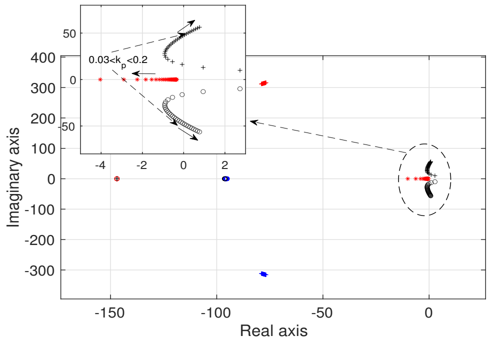

(a) k_p: 0.005 to 0.3 (step interval:0.01), $k_i = 0.1$

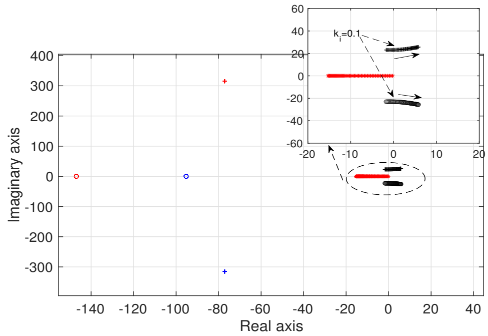

(b) k_i: 0.01 to 1 (step interval:0.02), $k_p = 0.05$

Figure 6.9: Eigenvalue trajectories under increasing k_p and k_i in modified $P-\omega$ control for PV

A simulation is conducted to plot root trajectories with increasing PI parameters. The nominal values of proportional and integral gain are respectively $k_p = 0.05$ and $k_i = 0.1$. In Figure 6.9, we can see that both a very small and large k_p can lead to system instability while a large k_i can also cause instability.

6.1.3 Modified $Q-V$ Control Modelling

6.1.3.1 RE-Prioritized Reactive Power Sharing Modelling

According to the RE-prioritized reactive power sharing strategy proposed in Chapter 5, δV is generated from a PI power limiting controller:

$$\delta V = (k_p + \frac{k_i}{s})(Q_{max} - Q) \tag{6.35}$$

Note that one input of the above PI controller is the filtered reactive power measurement and the other one Q_{max} is dependent on the real-time active power measurement. However, we assume the value of Q_{max} is constant during the analysis of reactive power dynamics. The modified small-signal droop control model can be represented as:

$$
\begin{aligned}
\dot{\hat{\phi}} &= \hat{\omega} - \hat{\omega}_g \\
\hat{\omega} &= \frac{-m}{1+Ts}\hat{P} \\
\hat{E} &= \frac{-n}{1+Ts}\hat{Q} + \frac{\delta\hat{V}}{1+Ts} \\
\delta\hat{V} &= -(k_p + \frac{k_i}{s})\hat{Q}
\end{aligned}
$$

As the model of power calculation has not changed, the state space model can be modified into:

$$\dot{X}_6 = A_6 X_6 + B_6 U_6 \tag{6.36}$$

where $X_6 = [\hat{\phi}\ \hat{\omega}\ \hat{v}_{od}\ \hat{i}_{od}\ \hat{i}_{oq}\ \delta\hat{V}]^T$ and $U_6 = [\hat{\omega}_g\ \hat{v}_g]^T$.

$$
A_6 = \begin{bmatrix}
0 & 1 & 0 & 0 & 0 & 0 \\
0 & \frac{-1}{T} & \frac{-3mI_{od0}}{2T} & \frac{-3mV_{od0}}{2T} & 0 & 0 \\
0 & 0 & \frac{-2+3nI_{oq0}}{2T} & \frac{-3nV_{oq0}}{2T} & \frac{3nV_{od0}}{2T} & \frac{1}{T} \\
\frac{V_{g0}sin\phi_0}{L_2} & 0 & \frac{1}{L_2} & -\frac{R_2}{L_2} & \omega_0 & 0 \\
\frac{V_{g0}cos\phi_0}{L_2} & 0 & 0 & -\omega_0 & -\frac{R_2}{L_2} & 0 \\
M_{61}^6 & 0 & M_{63}^6 & M_{64}^6 & M_{65}^6 & 0
\end{bmatrix}
$$

$$
B_6 = \begin{bmatrix}
-1 & 0 & 0 & 0 & 0 & 0 \\
0 & 0 & 0 & \frac{-cos\phi_0}{L_2} & \frac{sin\phi_0}{L_2} & \frac{3k_p(V_{od0}sin\phi_0 + V_{oq0}cos\phi_0)}{2L_2}
\end{bmatrix}^T
$$

where

$$M_{61}^6 = \frac{3k_pV_{g0}(V_{od0}cos\phi_0 - V_{oq0}sin\phi_0)}{2L_2}$$
$$M_{63}^6 = \frac{3k_p}{2}(-\frac{V_{oq0}}{L_2} + \frac{(-2+3nI_{oq0})I_{oq0}}{2T}) + \frac{3k_iI_{oq0}}{2}$$
$$M_{64}^6 = \frac{3k_p}{2}(\frac{V_{oq0}R_2}{L_2} - \frac{3nV_{oq0}I_{oq0}}{2T} - \omega_0V_{od0}) - \frac{3k_iV_{oq0}}{2}$$
$$M_{65}^6 = \frac{3k_p}{2}(\frac{-V_{od0}R_2}{L_2} - \omega_0V_{oq0} + \frac{3nV_{od0}I_{oq0}}{2T}) + \frac{3k_iV_{od0}}{2}$$

In simulation, the parameters are chosen consistently with those used in traditional droop control while the PI parameters are set as $k_p = 0.005$ and $k_i = 0.05$. The root trajectories of varying m and n are similar to that of the 5th-order model. The impact of proportional and integral gain can also be seen in the root trajectories, shown in Figure 6.10. It shows that k_p will have more impacts on the system stability comparing to k_i. The system tends to be unstable as k_p increases. In consequence, the selection of k_p should be kept within a reasonable range.

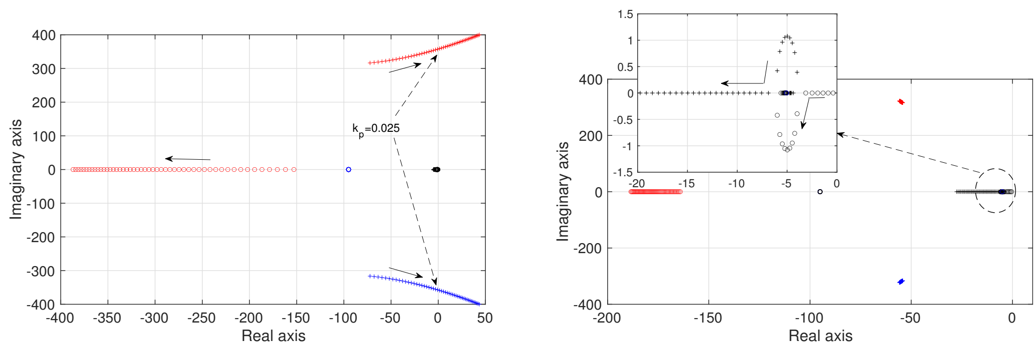

(a) k_p: 0.001 to 0.1 (step interval:0.001) (b) k_i: 0.01 to 0.5 (step interval:0.01)

Figure 6.10: Eigenvalue trajectories under increasing k_p and k_i in modified $Q-V$ characteristics

6.1.3.2 Modelling of Proposed VDC

According to the VDC strategy proposed in Chapter 5, the new voltage reference is generated with a modified droop coefficient:

$$E = E_0 - \frac{1}{1+Ts}(n - \frac{2X_{est}}{3E_{est}})Q - nQ_0 \tag{6.37}$$

In proportional reactive power sharing, $X_{est} = X^* - k_aQ$. The small-signal of the new voltage reference $\hat{E}$ is:

$$\hat{E} = \frac{-1}{1+Ts}(n - \frac{2X^*}{3E_0} + \frac{4k_a Q_0}{3E_0})\hat{Q}$$

assuming $E_0 = E_{est}$ and $Q_0 = V_{oq0}I_{od0} - V_{od0}I_{oq0}$.

It is to be noted that the droop coefficient n is replaced by a new value n' where,

$$n' = n - \frac{2X^*}{3E_0} + \frac{4k_a Q_0}{3E_0}$$

The system model can thus be represented by (6.18) with a new droop coefficient n'.

Using the same parameters as in Model (6.18), the influence of VDC method on system stability is discussed regarding to different selection of m, n, k_a and X^*. The nominal values of these variables are set as: $m = 0.0005rad/(s\cdot W), n = 0.005V/Var, k_a = 0.0005, X^* = 1.57$. The root trajectories due to varying variables are shown in Figure 6.11.

Compared to Model (6.18), the impact of m has not changed much while the stability margin of n has improved. It can be explained by $n' < n$. As for the proportional gain k_a, the root trajectory (c) suggests that the system has a better performance in stability as k_a increases. The next figure (d) suggests that a larger X^* will lead to system instability. In the case of line inductance being $5mH$, there is a maximum allowed X^* which corresponds to a reference inductance $L^* = 7mH$. This aligns with the theoretical analysis in Chapter 4. The selection of X^* is usually kept below the line impedance and in practice, it is achieved by interfacing a relatively large inductor on the coupling line. If $X^* = \omega_0 * 10mH$ while the line inductance stays at $5mH$, a pole is moved to the unstable region, shown in (e). However, if the line inductance is increased to $10mH$, the pole moves back to left-hand side of the s plane, as shown in (f).

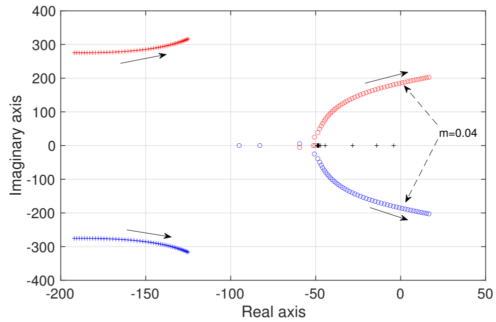

(a) m: 5e-4 to 0.05 (step interval:0.001)

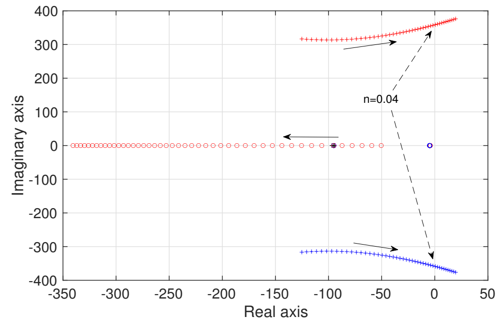

(b) n: 0.005 to 0.05 (step interval:0.001)

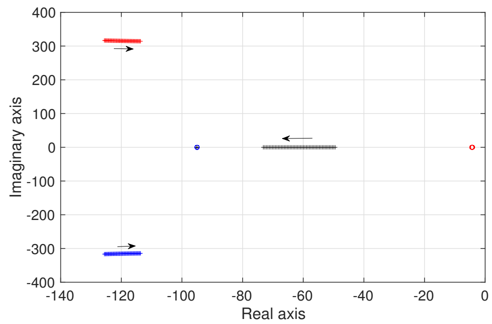

(c) k_a: $1e-4$ to 0.01 (step interval:$2e-4$)

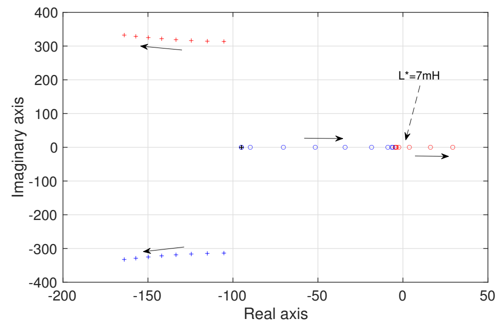

(d) X^* increases as a result of inductance increasing from $3mH$ to $10mH$ with a step of $1mH$

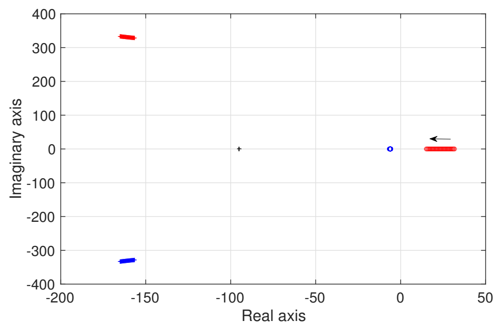

(e) k_a: $1e-4$ to 0.01 (step interval:$2e-4$), $X^* = 3.14, L_2 = 5mH$

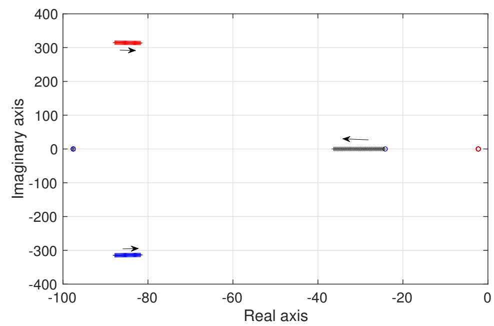

(f) k_a: $1e-4$ to 0.01 (step interval:$2e-4$), $X^* = 3.14, L_2 = 10mH$

Figure 6.11: Eigenvalue trajectories under VDC for proportional power sharing

In RE-prioritized Q sharing, $X_{est} = \frac{k_b P}{P_0}$. The small signal of the new voltage reference $\hat{E}$ is:

$$\hat{E} = \frac{-1}{1+Ts}(n - \frac{2k_b}{3E_0})\hat{Q} + \frac{2k_b Q_0}{3E_0 P_0(1+Ts)}\hat{P}$$

assuming $E_0 = E_{est}$, $P_0 = V_{od0}I_{od0} + V_{oq0}I_{oq0}$ and $Q_0 = V_{oq0}I_{od0} - V_{od0}I_{oq0}$.

It is to be noted that the droop coefficient n is replaced by a new value n' where

$$n' = n - \frac{2k_b}{3E_0}$$

The system model is modified based on (6.18) with a new droop coefficient n':

$$\dot{X_7} = A_7 X_7 + B_7 U_7 \tag{6.38}$$

where $X_7 = [\hat{\phi}\ \hat{\omega}\ \hat{v_{od}}\ \hat{i_{od}}\ \hat{i_{oq}}]^T$ and $U_7 = [\hat{\omega_g}\ \hat{v_g}]^T$.

$$A_7 = \begin{bmatrix} 0 & 1 & 0 & 0 & 0 \\ 0 & \frac{-1}{T} & \frac{-3mI_{od0}}{2T} & \frac{-3mV_{od0}}{2T} & 0 \\ 0 & 0 & \frac{-2+3n'I_{oq0}}{2T} + \frac{k_b Q_0 I_{od0}}{TP_0 V_{od0}} & \frac{-3n'V_{oq0}}{2T} + \frac{k_b Q_0}{TP_0} & \frac{3n'V_{od0}}{2T} + \frac{k_b Q_0 V_{oq0}}{TP_0 V_{od0}} \\ \frac{V_{g0} sin\phi_0}{L_2} & 0 & \frac{1}{L_2} & -\frac{R_2}{L_2} & \omega_0 \\ \frac{V_{g0} cos\phi_0}{L_2} & 0 & 0 & -\omega_0 & -\frac{R_2}{L_2} \end{bmatrix}$$

$$B_7 = \begin{bmatrix} -1 & 0 & 0 & 0 & 0 \\ 0 & 0 & 0 & -\frac{cos\phi_0}{L_2} & \frac{sin\phi_0}{L_2} \end{bmatrix}^T$$

The root trajectories of Model (6.38) are also analysed. The nominal value of k_b is 1.5. The impact of m and n are similar to that of Model (6.18) except that the stability boundary of n in model (6.38) is increased. It can be explained by a reduction of the value of n. From Figure 6.12, it can be seen that large k_b leads to instability. It makes sense because a larger k_b corresponds to a larger X_{est} whose boundary is related with the coupling line impedance. By comparing (b) and (a), the stability margin can be increased by interfacing a large inductor on the coupling line. This finding also suggests to interface a large inductor on the coupling line for stability improvement.

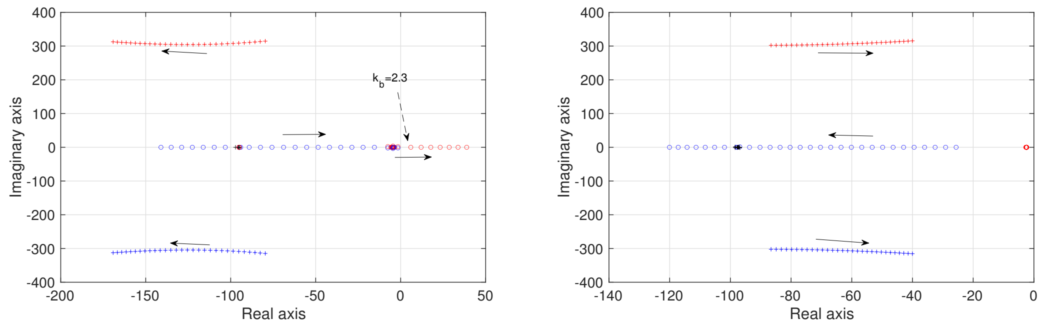

(a) k_b: 0.1 to 3 (step interval:0.1), $L_2 = 5mH$ (b) k_b: 0.1 to 3 (step interval:0.1), $L_2 = 10mH$

Figure 6.12: Eigenvalue trajectories under VDC for RE-prioritized reactive power sharing

6.2 Small-Signal Model of DC/DC Converter

Both PV and battery sources are of two-stage form, the interaction between DC/DC converter and DC/AC inverter is inevitable. Having a good understanding of the dynamics of DC/DC converter operation can help with the control design.

6.2.1 Small-Signal Model of Boost Converter Control

PV arrays are controlled by boost converter controller. A DC/DC boost converter is a nonlinear, time variant system of which the controller is difficult to design. However, it can be linearised in the incremental components of inputs and outputs around a chosen operating point, i.e. small-signal model. In the proposed PV control strategy in Chapter 3, it is composed of inner control loop and outer control loop. The outer control loop generates a reference value of PV voltage, which regulates PV arrays to operate under MPPT or power curtailment mode. In the mean time, the inner control loop is to track V_{PVref} by adjusting duty ratio. From the perspective of control theory, the inner control loop should react faster than the outer loop. As PI control is the fundamental strategy in each control loop, the tuning of proportional and integral gain plays an important role in designing the bandwidth of control loop.

6.2.1.1 Inner Control Loop

Given the boost converter topology shown in Figure 6.13, the inner control loop regulates v_{PV} by adjusting duty ratio d of the switching device.

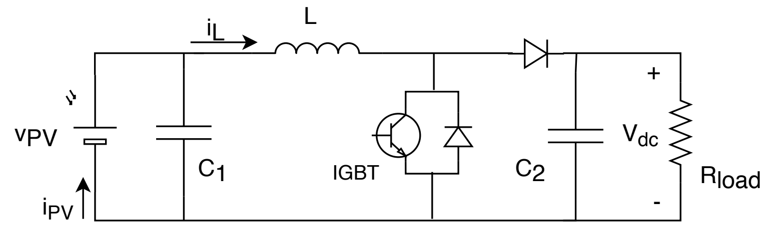

Figure 6.13: Structure of DC/DC boost converter

As the output voltage V_{dc} is regulated by the outer loop, we assume it is constant when analysing the dynamics of the inner loop. The small-signal model of the boost converter can thus be built as:

$$\begin{bmatrix} \dot{\hat{i_L}} \\ \dot{\hat{v_{PV}}} \end{bmatrix} = \begin{bmatrix} \frac{-R_L}{L} & \frac{1}{L} \\ \frac{-1}{C_1} & \frac{1}{r_{PV}C_1} \end{bmatrix} \begin{bmatrix} \hat{i_L} \\ \hat{v_{PV}} \end{bmatrix} + \begin{bmatrix} V_{dcref}/L \\ 0 \end{bmatrix} \hat{d}$$

$$\hat{y} = \begin{bmatrix} 0 & 1 \end{bmatrix} \begin{bmatrix} \hat{i_L} \\ \hat{v_{PV}} \end{bmatrix}$$

where r_{PV} represents the photovoltaic dynamic resistance which is dependent on the operating point and weather conditions. As [106] proposes, $r_{PV} \approx \frac{\hat{v_{PV}}}{\hat{i_{PV}}}$. The value of it changes with the operating point but can be simplified into three regions (current source region, power source region and voltage source region) on each I-V curve of PV, Figure 6.14. Its average value can be used to build this model, calculated at the extrema of the voltage source and current source regions [3].

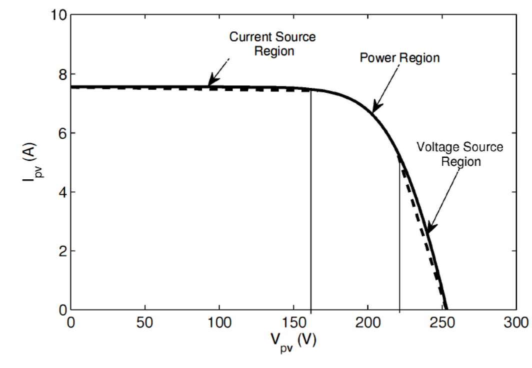

Figure 6.14: PV operating regions [3]

The transfer function of $v\hat{_{PV}}$ relative to $\hat{d}$ can be derived from the model:

$$G_{v_{PV}-d} = \frac{v\hat{_{PV}}}{\hat{d}} = \frac{-V_{dcref} r_{PV}}{C_1 L r_{PV} s^2 + (C_1 R_L r_{PV} - L)s + r_{PV} - R_L} \tag{6.39}$$

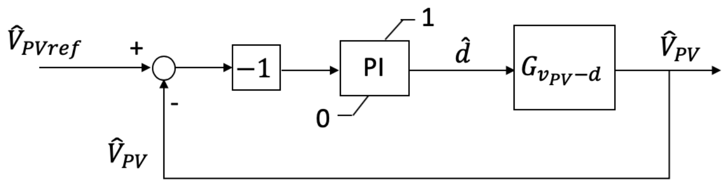

Figure 6.15: Topology of inner control loop of boost converter

The design of the inner control loop can be based on this transfer function, which is shown in Figure 6.15. The PI parameters of this inner loop controller can be selected by root locus technique. In the simulation example, the parameters of the boost converter are shown in Table 6.3. The bandwidth of the inner control loop should be at least 10 times smaller than IGBT switching frequency ($10kHz$) to avoid noises. The proportional gain k_p and integral gain k_i are selected as 0.05 and 10 respectively.

C_1	L	r_{PV}	R_L	V_{dcref}	C_2
$100\mu F$	$5mH$	-0.2Ω	0.5Ω	$700V$	$2200\mu F$

Table 6.3: Parameters of the boost converter in a PV source

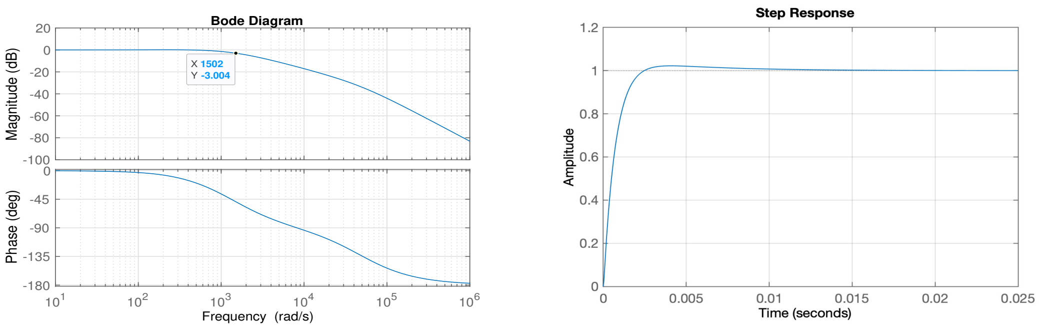

(a) Bode plot (b) Step response

Figure 6.16: Performance of the inner control loop in boost converter

The corresponding Bode plot of this closed loop transfer function is shown in Figure 6.16a. The bandwidth is around $1500 rad/s$. Meanwhile, the step response is also shown in Figure 6.16b.

6.2.1.2 Outer Control Loop

The outer control loop has two parts, the MPPT loop and V_{dcref} tracking loop. As the IC method is widely adopted in MPPT and well studied, we only focus on the V_{dcref} tracking loop in this small-signal analysis.

The relationship between DC bus voltage and power disturbances can be seen in (6.31). In the PV boost converter, any power disturbances on the capacitor are attributed to the power imbalance between power generation from PV panels (P_{PV}) and power consumption by the VSI (P_L), i.e.

$$\hat{P_{net}} = \hat{P_{PV}} - \hat{P_L} \tag{6.40}$$

We assume the load P_L is constant and modeled by a negative current source $I_s = P_L/V_{dc}$. According to power characteristics of PV arrays, Figure 2.6, we can derive a model of P_{PV} with respect to V_{PV}. On the right hand side of the characteristic curve, the P_{PV}, V_{PV} relationship is approximated as below:

$$P_{PV} = aV_{PV} + b \tag{6.41}$$

where $a = P_{MPP}/(V_{MPP} - V_{OC}) < 0$, $b = (-P_{MPP}V_{OC})/(V_{MPP} - V_{OC})$ and V_{OC} is the open circuit voltage of PV arrays.

Small-signal model of the above equation is

$$\begin{aligned} \hat{P_L} &= 0 \\ \hat{P_{PV}} &= a\hat{V_{PV}} \end{aligned} \tag{6.42}$$

Combining (6.31), (6.40) and (6.42), the relationship between V_{PV} and V_{dc} is thus derived, as shown in (6.43). It represents the plant model in the outer control loop, $G_{v_{dc}-v_{pv}}$,

$$\begin{aligned} a\hat{V_{PV}} &= sCV_{dcref}\hat{V_{dc}} \\ G_{v_{dc}-v_{pv}} &= \frac{\hat{V_{dc}}}{\hat{V_{PV}}} = \frac{a}{sCV_{dcref}} \end{aligned} \tag{6.43}$$

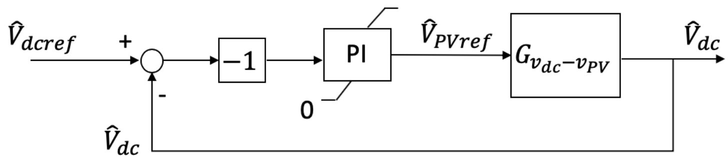

Figure 6.17: Topology of outer control loop of boost converter

Based on the plant model, the control loop diagram of V_{dc} regulation is represented in Figure 6.17. The parameters of the PI controller are tuned to meet the specification of control loop bandwidth, which is smaller than the inner control loop. In a simulation, V_{OC} of the PV arrays is $321V$ while its V_{MPP} is $273V$ and P_{MPP} is $20kW$. The gain of the PV model is derived as $a = -417$. Using root locus technique, the k_p and k_i are selected as 0.3 and 10 respectively to ensure a bandwidth of around $100rad/s$. Figure 6.18a and Figure 6.18b show the performance of the outer control loop.

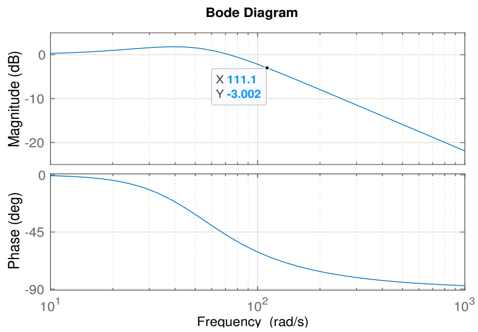

(a) Bode plot

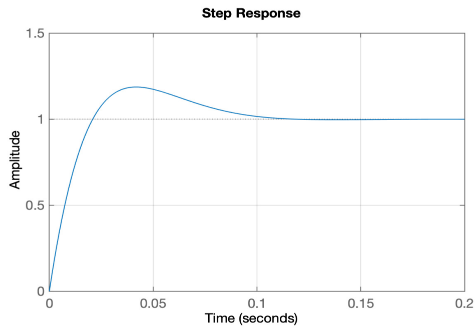

(b) Step response

Figure 6.18: Performance of the outer control loop in boost converter

6.2.2 Small-Signal Model of Buck/Boost Converter Control

As the adopted buck/boost converter is simply a combination of a single boost converter and a single buck converter, we discuss the boost mode and the buck mode separately. Referring to Figure 6.19, when IGBT1 is active and IGBT2 is open, it is in boost mode. The inductor current i_L flows from the battery source to load whose value is defined as positive. On the contrary, when IGBT1 is open and IGBT2 is active, it is in buck mode. A negative i_L means the current is flowing from the load side to the battery source.

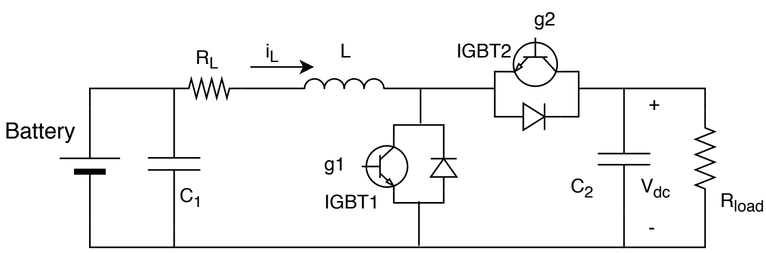

Figure 6.19: Structure of a buck/boost converter

The steady state model of the boost converter is first built. It generates the steady state values needed in the small-signal model.

$$\begin{bmatrix} 0 \\ 0 \end{bmatrix} = \begin{bmatrix} \frac{-R_L}{L} & \frac{D-1}{L} \\ \frac{1-D}{C_2} & \frac{-1}{R_{load}C_2} \end{bmatrix} \begin{bmatrix} I_L \\ V_{dc} \end{bmatrix} + \begin{bmatrix} \frac{1}{L} \\ 0 \end{bmatrix} V_{BAT}$$

$$\begin{bmatrix} I_L \\ V_{dc} \end{bmatrix} = \begin{bmatrix} 1 & 0 \\ 0 & 1 \end{bmatrix} \begin{bmatrix} I_L \\ V_{dc} \end{bmatrix}$$

where L, R_L are the output inductance and resistance respectively, the values of which ensure continuous mode and appropriate damping; C_2 is the capacitance value on DC bus side and R_{load} is the equivalent resistance of the load; D, I_L, V_{dc} and V_{BAT} are duty ratio, inductor current, DC bus voltage and battery output voltage respectively under steady state.

Once the steady state values, V_{dc} and I_L, are obtained, the small-signal model of the boost mode can be written as below:

$$\begin{bmatrix} \dot{\hat{i_L}} \\ \dot{\hat{v_{dc}}} \end{bmatrix} = \begin{bmatrix} \frac{-R_L}{L} & \frac{D-1}{L} \\ \frac{1-D}{C_2} & \frac{-1}{R_{load}C_2} \end{bmatrix} \begin{bmatrix} \hat{i_L} \\ \hat{v_{dc}} \end{bmatrix} + \begin{bmatrix} \frac{V_{dc}}{L} \\ -\frac{I_L}{C_2} \end{bmatrix} \hat{d} + \begin{bmatrix} \frac{1}{L} \\ 0 \end{bmatrix} \hat{v_{BAT}}$$

$$\hat{y} = \begin{bmatrix} 1 & 0 \\ 0 & 1 \end{bmatrix} \begin{bmatrix} \hat{i_L} \\ \hat{v_{dc}} \end{bmatrix}$$

Similarly, for the buck mode model, its steady state model is:

$$\begin{bmatrix} 0 \\ 0 \end{bmatrix} = \begin{bmatrix} \frac{-R_L}{L} & \frac{-D}{L} \\ \frac{D}{C_2} & \frac{-1}{R_{load}C_2} \end{bmatrix} \begin{bmatrix} I_L \\ V_{dc} \end{bmatrix} + \begin{bmatrix} \frac{1}{L} \\ 0 \end{bmatrix} V_{BAT}$$

$$\begin{bmatrix} I_L \\ V_{dc} \end{bmatrix} = \begin{bmatrix} 1 & 0 \\ 0 & 1 \end{bmatrix} \begin{bmatrix} I_L \\ V_{dc} \end{bmatrix}$$

The small-signal model of buck mode is:

$$\begin{bmatrix} \dot{\hat{i_L}} \\ \dot{\hat{v_{dc}}} \end{bmatrix} = \begin{bmatrix} \frac{-R_L}{L} & \frac{-D}{L} \\ \frac{D}{C_2} & \frac{-1}{R_{load}C_2} \end{bmatrix} \begin{bmatrix} \hat{i_L} \\ \hat{v_{dc}} \end{bmatrix} + \begin{bmatrix} \frac{-V_{dc}}{L} \\ \frac{I_L}{C_2} \end{bmatrix} \hat{d}$$

$$\hat{y} = \begin{bmatrix} 1 & 0 \\ 0 & 1 \end{bmatrix} \begin{bmatrix} \hat{i_L} \\ \hat{v_{dc}} \end{bmatrix}$$

As the control strategy proposed in Chapter 2 includes inner current loop and outer voltage loop. The two control loops are discussed separately. The inner current loop regulates i_L while the outer loop regulates V_{dc}. According to the state space model established above, we can derive the transfer function of both boost mode and buck mode under the assumption that battery output voltage is constant.

$$\begin{aligned} G_{Bat-boost} &= \frac{\hat{i_L}}{\hat{d}} \\ &= \frac{R_{load}C_2V_{dc}s + V_{dc} + R_{load}(1-D)I_L}{R_L + R_{load} + Ls + D^2R_{load} - 2DR_{load} + C_2LR_{load}s^2 + C_2R_LR_{load}s} \end{aligned} \tag{6.44}$$

$$G_{Bat-buck} = \frac{\hat{i_L}}{\hat{d}} = \frac{-V_{dc}C_2R_{load}s - R_{load}DI_L - V_{dc}}{R_L + Ls + D^2R_{load} + C_2LR_{load}s^2 + C_2R_LR_{load}s} \tag{6.45}$$

where the value of inductor current is negative under buck mode. Meanwhile, the load is replaced with a power source which is represented by a negative R_{load} .

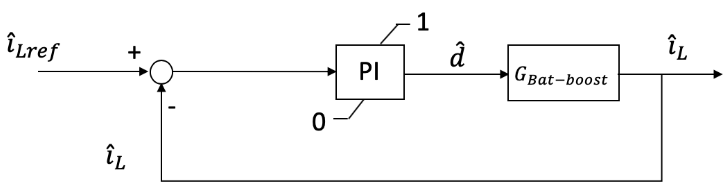

Figure 6.20: Topology of inner control loop in boost mode

C_1	L	R_L	V_{BAT}	V_{dcref}	C_2	R_{load}
$100\mu F$	$5mH$	0.5Ω	$240V$	$700V$	$2200\mu F$	49Ω

Table 6.4: Parameters of the buck/boost converter in a battery source

The inner control loop for boost mode is shown in Figure 6.20. Parameters of PI control are tuned to realize a high bandwidth in the control loop. In the simulation, the parameters of the buck/boost converter are shown in Table 6.4. The selection of $k_p = 0.01$, $k_i = 10$ can achieve a bandwidth of around $1500rad/s$. The Bode plot and step response of the closed loop is shown in Figure 6.21.

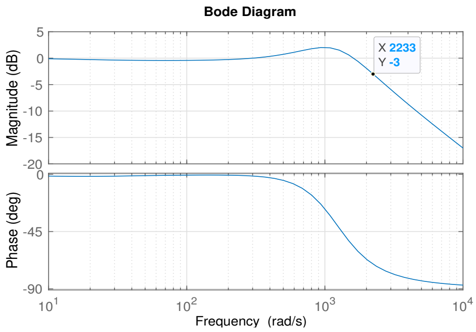

(a) Bode plot

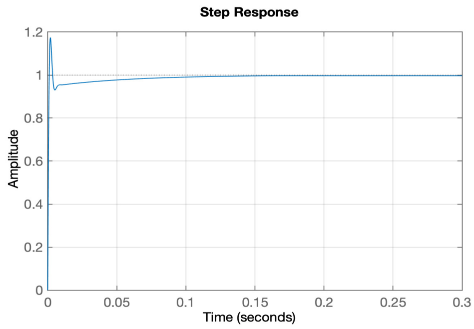

(b) Step response

Figure 6.21: Performance of the inner control loop of boost mode in a buck/boost converter

As for the outer control loop in boost mode, the process of model building is similar to Section 6.2.1.2. The power disturbance here is represented by the battery generation disturbance, which is $\hat{P}_{BAT} = V_{BAT}\hat{i}_L$. As a result, the transfer function of the plant model in outer loop is:

$$G_{v_{dc}-i_{Bat}} = \frac{V_{dc}}{i_L} = \frac{V_{BAT}}{sCV_{dcref}}$$

The tuning of the PI parameters is based on the closed loop shown in Figure 6.22. A selection of $k_p = 2$, $k_i = 20$ achieves a bandwidth of around $300rad/s$ for closed loop. The Bode plot and step response of the closed loop are shown in Figure 6.23.

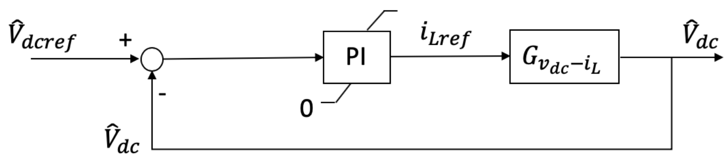

Figure 6.22: Topology of outer control loop in boost mode

In buck mode, the topology of the control loop is different due to the opposite direction of current flow. The inner control loop and outer control loop are shown in Figure 6.24.

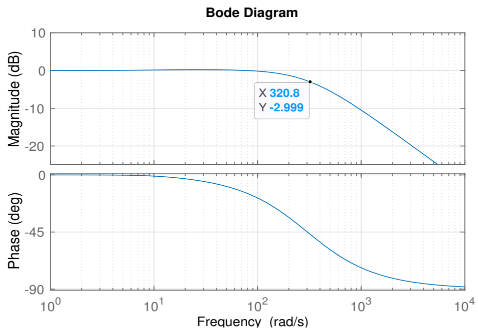

(a) Bode plot

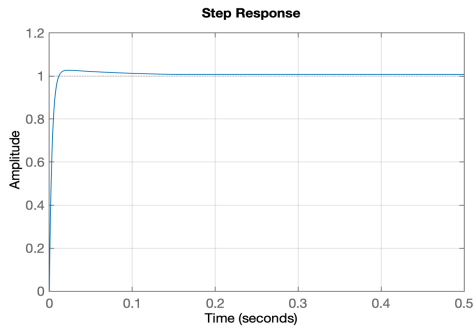

(b) Step response

Figure 6.23: Performance of the outer control loop of boost mode in a buck/boost converter

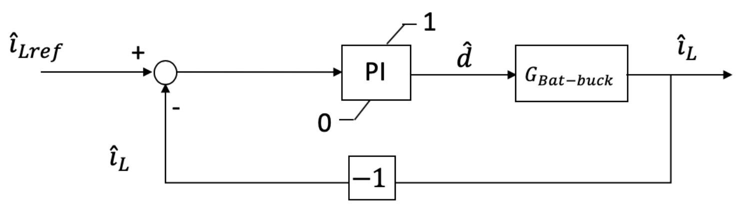

(a) Inner control loop

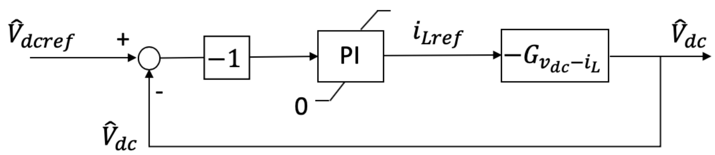

(b) Outer control loop

Figure 6.24: Topology of control loops in buck mode

It needs to be noted that, in simulation, the value of R_{load} is set as -49Ω to represent a power source at the DC bus side. In inner control loop, a set of $k_p = 0.01$, $k_i = 10$ produces a bandwidth of $2000 rad/s$ and the performances are shown in Figure 6.25. As for the outer control loop, as battery is absorbing power and the generated current reference value is designed to be positive, the plant model is the opposite of $G_{v_{dc}-i_{Bat}}$, i.e. $-G_{v_{dc}-i_{Bat}}$. As a result, the closed loop of outer voltage control in buck mode is same as that in boost mode. The parameters are thus chosen the same to achieve the same response speed.

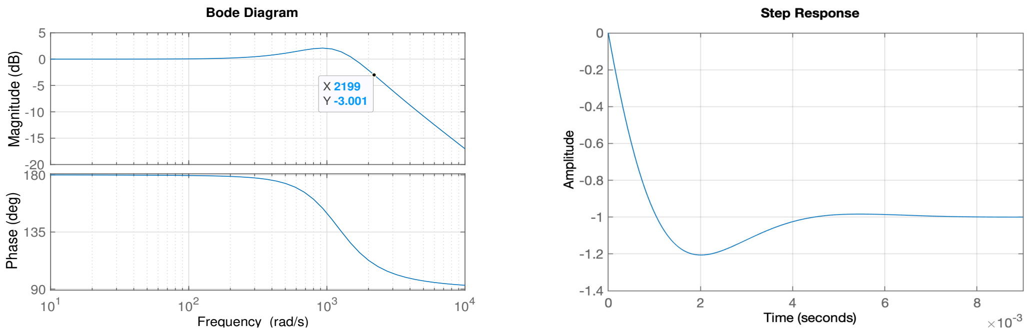

(a) Bode plot

(b) Step response

Figure 6.25: Performance of the inner control loop of buck mode in a buck/boost converter

6.3 Conclusions

This chapter discusses system stability issue based on small-signal analysis under different control topologies. Firstly, a 5th-order model for droop-controlled VSI is deemed as effective to analyse stability. It was found that droop coefficients are restricted for system stability. With modified $P-\omega$ droop control, a 6th-order model and a 7th-order model are built for Conventional & Battery sources and PV sources respectively. Large proportional and integral gains can both drive system unstable. In addition, a small proportional gain in PV also leads to instability. In the modified $Q-V$ droop control, the proportional gain has a predominant impact on system stability. In the proposed VDC method, the impedance reference value is critical for system stability. In the case of unknown line impedance, a relatively large inductor is suggested to be connected before the coupling line. As for the DC/DC converter, the boost converter model of a PV source and buck/boost converter model of a battery source are discussed separately. With the help of Bode plot and step response performance, the inner control loop was designed to be around 10 times faster than the outer loop.

Chapter 7

Conclusions and Contributions

This thesis has investigated strategies for use in a microgrid that maximise PV power integration, which effectively improves RE penetration level. MG technology facilitates reliable, efficient and economic operation of DG sources, such as RES and ESS. In an autonomous MG with a high RE penetration level, the main grid or a prevalent SG is no longer present, which poses challenges in MG operation. This thesis enables ancillary services from RES, i.e. frequency regulation and voltage support, when they operate in VCM. These functionalities can be achieved through the primary control, together with an appropriate power sharing scheme. The proposed RE-prioritized real power sharing scheme can effectively improve RE penetration level in an islanded MG while enabling "peer to peer' and "plug and play" functionalities. Meanwhile, the battery management strategy protects the interfaced batteries from over-charging or too deeply discharging. Furthermore, the reactive power sharing issues are also investigated and the proposed solutions can improve the system performance from different perspectives.

7.1 Summaries and Contributions

The major contributions of each chapter are summarised as follows:

- Chapter 1 introduced the concept of the MG and its hierarchical control strategy with multiple objectives. As this thesis focuses on the primary control, real-time power management strategies were reviewed and proportional power sharing scheme based on droop control was examined in detail. Since DG sources are mostly interfaced with the grid through VSIs, the control strategies for VSI operation were thoroughly reviewed. The VSI operating modes can be classified into two categories: VCM for grid-forming function and PCM for grid-following function. While PV sources traditionally operate as grid-following units, the increasing demand of RE penetration poses new challenges on PV integration. After reviewing the issues and state-of-the-art solutions, the motivations and objectives of this thesis were summarised.

- Chapter 2 proposed a RE-prioritized power sharing strategy which aims to improve RE penetration level within the system. A hybrid MG interfacing multiple DG units was first introduced. In the context of a hybrid MG interfacing PV, battery and conventional sources, the proposed strategy considered the unique power characteristics of individual sources, such as the intermittent and varying nature of PV generation, and limited charge/discharge rates of a battery source. The realization of the proposed power sharing strategy was by modifying traditional droop method at primary level. It thus enabled PV sources with grid-forming functionality and an autonomous switch between VCM and PCM operation. Simulation results of both proportional real power sharing and RE-prioritized real power sharing were presented and the efficacy of the proposed control strategy was validated.

- Chapter 3 proposed a decentralized implementation of the RE-prioritized real power sharing strategy. Due to intermittent, uncertain and fluctuating PV generation, VSI power limiting cannot be achieved by traditional PI control as implemented in battery and conventional sources. The modified droop control on a PV VSI combining with its boost converter control could constrain the PV power output within its local capacity without relying on a supervisory control or inter-unit communications. Additionally, it enabled autonomous switching of the PV operation mode between power curtailment and MPPT. On the other hand, the proposed battery power management was based on the coordinated battery VSI control and buck/boost converter control. It achieved autonomous switch between battery charging and discharging and could effectively maintain charging/discharging rate within battery capacity. Simulations of both PV operation and battery operation have shown the desired performance of the proposed strategies. The ideal DC sources in the simulated MG of Chapter 2 were then replaced with PV and battery sources with actual power characteristics. The simulated power sharing performed as expected. Meanwhile, the performance of MPPT under varying weather conditions was also verified. Last but not least, the frequency restoration in a RE-prioritized MG was also verified with a simulation study. It proved that the frequency restoration at secondary level does not interfere with the priority order of power supply at the primary level.

- Chapter 4 verified the effectiveness of the proposed decentralized control strategies on a prototype MG. The experimental system layout, elements selection and testing conditions were first described. The PV and battery control were tested and it was found that PV generation could effectively track varying MPP while the battery could autonomously switch between charging and discharging modes. Furthermore, the proportional and RE-prioritized power sharing strategies were implemented. The results showed that the PV unit could effectively switch between PCM and VCM under RE-prioritized real power sharing strategy. Last but not least, secondary-level frequency restoration was also implemented on the prototype MG and the frequency deviation as a result of primary control was eliminated.

- Chapter 5 investigated reactive power sharing issues in a RE-prioritized MG and proposed improvement approaches from different perspectives. First of all, the over-stressing issues on VSIs were addressed and a reliability-enhanced reactive power sharing approach was proposed to improve overall system reliability. The numerical analysis based on a simulated MG has verified that the proposed strategy can improve the system reliability by 15%. Secondly, the reactive power allocation on CVS in a RE-prioritized MG was proposed to be minimised from the perspective of practical and economic performance. Both of the strategies were achieved by locally implemented adaptive droop control techniques. Moreover, the accuracy issue in reactive power sharing due to mismatched coupling impedances was studied.

While the virtual impedance could effectively improve power sharing performance according to literatures, an innovative VDC method was proposed to achieve similar effects with better voltage regulation. The proposed VDC method was compared to virtual impedance through theoretical analysis and simulation studies. Meanwhile, the proposed VDC method was also tested and shown to be effective under the proposed RE-prioritized reactive power sharing scheme while virtual impedance shows no improvement. Last but not least, the proposed strategies in reactive power sharing improvement were implemented on the experimental prototype MG and the results align with simulation findings.

- Chapter 6 studied the stability performance of the proposed strategies based on small-signal analysis. Firstly, it discovered that the small-signal model of droop-controlled VSI should consider network dynamics for accuracy. After comparing with the 3rd-order model and the 7th-order model, the 5th-order model was chosen to represent traditional droop-controlled VSI. Based on this finding, the proposed RE-prioritized real power sharing strategy requires a 6th-order model for a battery or conventional source and a 7th-order model for a PV source. Meanwhile, the proposed RE-prioritized reactive sharing was also studied with a 6th-order model. It was found that the impact of droop coefficients maintains in the proposed control strategies. In addition, the parameters of PI controller in the modified droop control should be carefully designed to maintain system stability. As for the DC/DC converter control, the inner loop controller was designed to be around 10 times faster than the outer loop with the help of Bode plot and step response simulation.

7.2 Future Work

The future investigation based on the work presented in this thesis can be divided into two areas. Firstly, the proposed control strategy can be extended to a MG with resistive networks. The $P-\omega$ and $Q-V$ droop principles should be adjusted accordingly. Additionally, the harmonics distribution should be also considered in power sharing to prevent VSI overloading.

In the second area, the secondary and tertiary control based on the proposed primary control can be investigated. An optimal power distribution can be realized at secondary level with multiple objectives, such as maximum RE penetration level, minimum fossil fuel consumption, lowest operation cost, etc. Unit commitment is also worth studying in an islanded MG. The sizing of the installed PV, battery and conventional sources will not only impact on the initial cost but influence system future performance. It is valuable to obtain an optimization method that coordinates various power sources based on different applications and system specifications.

Appendix A

Experimental System

A.1 Introduction

This appendix outlines the experimental system used in this thesis. The hardware configuration and the structure of the software are presented.

A.2 Hardware Configuration

A.2.1 SEMITEACH Stack

The SEMITEACH stack by Semikron is a multi-function IGBT converter constructed for use in a teaching, learning and research environment (Figure A.1). It includes a three phase inverter, a brake chopper and also a front-end three phase passive rectifier. The circuit diagram is shown in Figure A.2. The maximum output current is 30 ARMS while the maximum input current is 30 ADC. The output AC voltage can reach as high as 400V while the maximum DC bus voltage is 750V. The maximum frequency for output voltage is 500Hz and the maximum switching frequency is 50kHz.

A.2.2 MCU Setup

The DSP product (SwitcherGear) provided by Denkinetic is a flexible platform for the

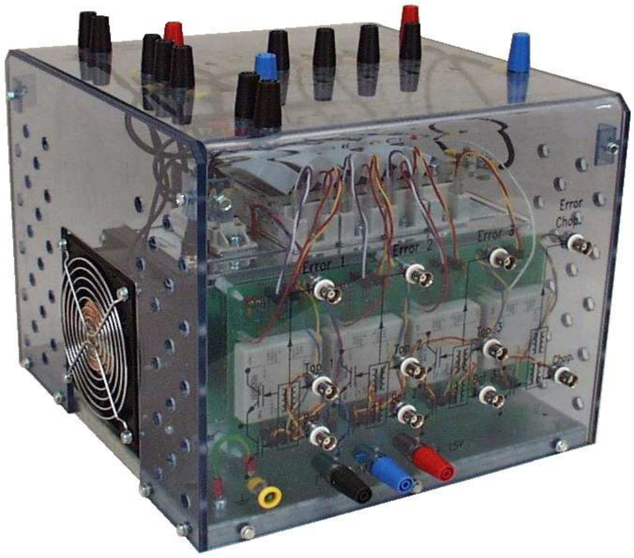

Figure A.1: The SEMITEACH Stack

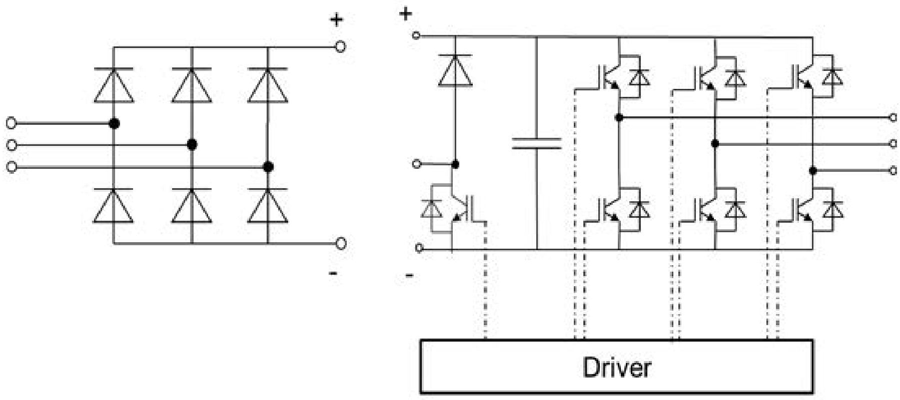

Figure A.2: The circuit diagram of SEMITEACH Stack

rapid development of customised controllers for power converter systems. It operates from a single 24 VDC power supply input. Secondary supplies for external devices such as gate drivers, current and voltage sensors are generated on-board by the installed modules. It is designed to accept host MCUs in the format of DIMM 100-pin TI controlCARDs. The 14-pin debug probe interface also allows the use of all standard development tools and libraries for C2000. TI XDS100v2 14-pin debug probe is used.

The used MCU features TMS320F28377D dual-core 200 MHz microcontroller from TI and it also features 16 channel ADC. An on-board 16 MB SDRAM is added for buffering large amounts of real-time data.

A voltage output module is used to output analogue signals which can be seen on oscilloscopes. Its output voltage range is between $\pm 10V$ while the current range is $\pm 20mA$. The three phase converter interface allows the MCU to be connected to the gate drivers of power converters. It connects to SEMITEACH IGBT through 20-way ribbon cables and adapters.

The used current sensor is a closed-loop Hall-Effect current sensor with a measurement range of $\pm 50A$ (Figure A.3 left). The maximum measured current can be 25 ARMS. The output current range is of $\pm 50mA$. The gain accuracy is 0.5%. The sensor is galvanically isolated from the primary current conductor. The enclosed voltage sensor can measure voltage up to $\pm 1000V$ with a gain accuracy of 0.4(Figure A.3 right). The output gain is $20\mu A/V$. It has internal shield which reduces interference from switch-mode converters. The sensor output connects to a current input module with configurable current input range and polarity mode for each channel. The current input is converted to a voltage output in the range of 0 to 3 V, which is routed to the ADC of the host MCU.

Figure A.3: The current sensor (left) and voltage sensor (right)

A.2.3 PV Emulator

Magna-Power Electronics programmable DC power supplies combine DC power processing with microprocessor embedded control. The remote control is enabled by RS232. The selected model TSD600-8/+415HS allows an output with 600V maximum DC voltage and 8A maximum current. The deployed product also features high slew rate output. The output stage consists of low capacitance film and aluminum electrolytic capacitors. It allows output voltage to change from 0 to 63% within 4ms and current to change from

0 to 63% within 8ms. This feature benefits the emulation of photovoltaic behavior.

Figure A.4: Magna-Power DC power supply

Appendix B

Reliability Modelling of a Converter

B.1 Introduction

The lifetime consumption of a converter can be identified based on its lifetime model combined with temperature monitoring. Without losing accuracy, the calculation of thermal damage on a converter usually focuses on the most vulnerable components. It is acknowledged that semiconductor devices are critical components in the converter reliability assessment [107]. The thermal damage on semiconductors is thus used as the indicator of converter reliability in the reliability predication in Chapter 5.

B.2 Lifetime Model of a Converter

The junction temperature swing (ΔT_j) is critical to the lifetime of electronic devices [108]. According to [109], the lifetime model of semiconductor devices, insulated-gate bipolar transistor (IGBT) and diode, can be represented by its number of cycles to failure (N), as shown below:

$$N = A \cdot \Delta T_j^{\alpha} \cdot exp(\frac{\beta}{T_{jm} + 273.15})t_{on}^{\gamma} \tag{B.1}$$

where T_{jm} and ΔT_j represent minimum junction temperature and temperature swing of the cycle, respectively; t_{on} is the heating time; A, α, β, and γ are constants obtained from long-term lifetime tests [109]. The aging of the device can then be calculated based on its thermal cycling:

$$D = \sum_t \frac{n_t}{N_t} \tag{B.2}$$

where D is the damage of the device under n_t thermal cycles during operation period of t. N_t is the number of cycles to failure derived from (B.1)under the corresponding thermal cycle with T_{jm}, ΔT_j, and t_{on}.

As IGBT and diode have different thermal performances, the damage on each device needs to be calculated separately. The total damage on a VSC can then be represented by:

$$D_{VSC} = max\{D_{g_T}^{(T)}, D_{g_D}^{(D)}\}, \tag{B.3}$$

where $g_T \in \{1, ..., M^{(T)}\}$, $g_D \in \{1, ..., M^{(D)}\}$ and $M^{(T)}$, $M^{(D)}$ are numbers of IGBT and diodes in each VSC; $D_{g_T}^{(T)}$ and $D_{g_D}^{(D)}$ represent the damage on a single IGBT and diode respectively in the discussed VSC.

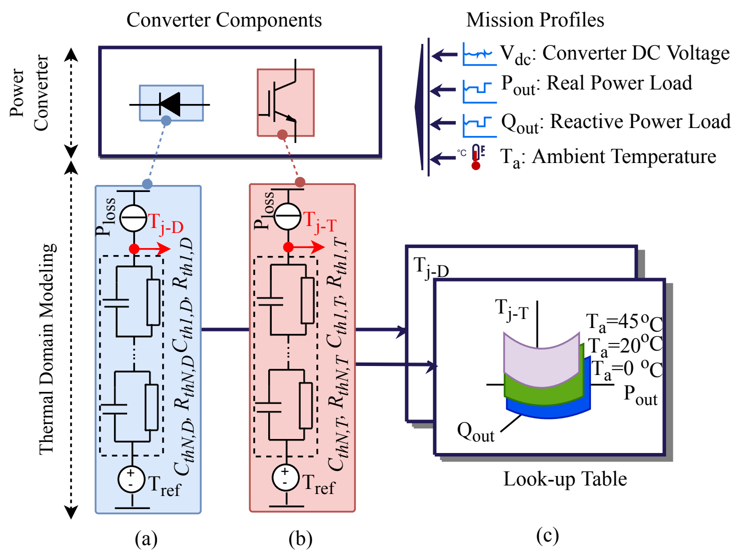

Figure B.1: The procedure of electro-thermal mapping in the power converter: (a) Diode (b) IGBT (c) Look-up Table

The thermal performance of a converter during operation can be attained from electro-thermal mapping procedure [68] or direct temperature measurements [110]. It is not common to install temperature sensors in every DG because of the extra cost. In electro-thermal mapping, as shown in Figure B.1, the thermal model of IGBT and diode should first be established. It includes parameters for thermal impedances, turn on-off switching energy, and V-I curves when conducting. Power losses on devices dissipate through their thermal impedances, which causes junction temperature increase. The steady-state junction temperature is mainly dependent on the thermal resistance R_{th} while its dynamic behaviour is mostly dependent on thermal capacitance C_{th}. These values can be obtained from the component datasheet and imported into a simulation platform, PLECS. The behaviour of T_j under a certain operating condition is automatically calculated by PLECS. As the power sources connect to the system in the two-stage form, the DC link voltage is relatively constant. VSC loading and ambient temperature thus become the main concerns of the operating conditions. The junction temperatures are stored in a look-up table for each component under different operating conditions. It can then be recalled when creating T_j profiles under specified mission profiles.

Once T_j profiles of every devices are created, the VSC damage can be derived based on (B.1) to (B.3). Thermal cycles over a long operation period include both short-term cycles and long-term cycles. It is assumed that short-term cycle is equivalent to $50Hz$ cycle in AC grid. Long-term cycles are dependent on fluctuations in mission profiles, such as I_r, T_a and P_L. A cycle counting algorithm, called rain flow counting, can convert the randomly changed T_j profile into categorized thermal cycles. It identifies all the long-term thermal cycles existing in the temperature profile and extracts parameters for each thermal cycle, i.e. T_{jm}, ΔT_j, t_{on} and n_t [111]. The thermal damage on a component is the sum of damage from all thermal cycles according to (B.2).

Bibliography

[1] Pinomelean, "Li-ion battery charging," *https://www.instructables.com/id/Li-ion-battery-charging/*, 2018.

[2] H. Mahmood, D. Michaelson, and J. Jiang, "Strategies for independent deployment and autonomous control of pv and battery units in islanded microgrids," *IEEE Journal of Emerging and Selected Topics in Power Electronics*, vol. 3, no. 3, pp. 742–755, 2015.

[3] ——, "Control strategy for a standalone pv/battery hybrid system," in *IECON 2012-38th Annual Conference on IEEE Industrial Electronics Society*. IEEE, 2012, pp. 3412–3418.

[4] https://www.iea.org/reports/world-energy-outlook 2019, "Iea (2019), "world energy outlook 2019", iea, paris," 2019.

[5] Z. Wang, A. Scaglione, and R. J. Thomas, "Electrical centrality measures for electric power grid vulnerability analysis," in *49th IEEE conference on decision and control (CDC)*. IEEE, 2010, pp. 5792–5797.

[6] A. Zahedi, "Smart grid opportunities & challenges for power industry to manage the grid more efficiently," in *2011 Asia-Pacific Power and Energy Engineering Conference*. IEEE, 2011, pp. 1–4.

[7] J. Eto, R. Lasseter, B. Schenkman, J. Stevens, D. Klapp, H. VolkommeRr, E. Linton, H. Hurtado, and J. Roy, "Overview of the certs microgrid laboratory test bed," in *Integration of Wide-Scale Renewable Resources into the Power Delivery System, 2009 CIGRE/IEEE PES Joint Symposium*. IEEE, 2009, pp. 1–1.

[8] K. Tan, P. So, Y. Chu, and M. Chen, "Coordinated control and energy management of distributed generation inverters in a microgrid," *IEEE transactions on power delivery*, vol. 28, no. 2, pp. 704–713, 2013.

[9] T. Logenthiran, R. T. Naayagi, W. L. Woo, V.-T. Phan, and K. Abidi, "Intelligent control system for microgrids using multiagent system," *IEEE Journal of Emerging and Selected Topics in Power Electronics*, vol. 3, no. 4, pp. 1036–1045, 2015.

[10] J. P. Lopes, C. Moreira, and A. Madureira, “Defining control strategies for microgrids islanded operation,” *IEEE Transactions on power systems*, vol. 21, no. 2, pp. 916–924, 2006.

[11] J. M. Guerrero, J. C. Vasquez, J. Matas, L. G. De Vicuña, and M. Castilla, “Hierarchical control of droop-controlled ac and dc microgrids: A general approach toward standardization,” *IEEE Transactions on industrial electronics*, vol. 58, no. 1, pp. 158–172, 2011.

[12] Q. Shafiee, J. M. Guerrero, and J. C. Vasquez, “Distributed secondary control for islanded microgrids: A novel approach,” *IEEE Transactions on power electronics*, vol. 29, no. 2, pp. 1018–1031, 2014.

[13] C.-L. Chen, Y. Wang, J.-S. Lai, Y.-S. Lee, and D. Martin, “Design of parallel inverters for smooth mode transfer microgrid applications,” *IEEE Transactions on Power Electronics*, vol. 25, no. 1, pp. 6–15, 2010.

[14] S. Bae and A. Kwasinski, “Dynamic modeling and operation strategy for a microgrid with wind and photovoltaic resources,” *IEEE Transactions on Smart Grid*, vol. 3, no. 4, pp. 1867–1876, Dec 2012.

[15] B. Hong and Z. Zheng, “Stochastic multi-objective dynamic optimal dispatch for combined heat and power microgrid,” in *2016 IEEE PES Asia-Pacific Power and Energy Engineering Conference (APPEEC)*, Oct 2016, pp. 2369–2373.

[16] A. C. Luna, N. L. Diaz, M. Graells, J. C. Vasquez, and J. M. Guerrero, “Mixed-integer-linear-programming-based energy management system for hybrid pv-wind-battery microgrids: Modeling, design, and experimental verification,” *IEEE Transactions on Power Electronics*, vol. 32, no. 4, pp. 2769–2783, April 2017.

[17] P. C. Sekhar, S. Mishra, and R. Sharma, “Data analytics based neuro-fuzzy controller for diesel-photovoltaic hybrid ac microgrid,” *IET Generation, Transmission Distribution*, vol. 9, no. 2, pp. 193–207, 2015.

[18] C. Chen and S. Duan, “Optimal integration of plug-in hybrid electric vehicles in microgrids,” *IEEE Transactions on Industrial Informatics*, vol. 10, no. 3, pp. 1917–1926, Aug 2014.

[19] T. Wang, D. O. Neill, and H. Kamath, “Dynamic control and optimization of distributed energy resources in a microgrid,” *IEEE Transactions on Smart Grid*, vol. 6, no. 6, pp. 2884–2894, Nov 2015.

[20] Y. Pei, G. Jiang, X. Yang, and Z. Wang, “Auto-master-slave control technique of parallel inverters in distributed ac power systems and ups,” in *Power Electronics Specialists Conference, 2004. PESC 04. 2004 IEEE 35th Annual*, vol. 3. IEEE, 2004, pp. 2050–2053.

[21] T. Caldognetto and P. Tenti, "Microgrids operation based on master–slave cooperative control," *IEEE Journal of Emerging and Selected Topics in Power Electronics*, vol. 2, no. 4, pp. 1081–1088, 2014.

[22] M. C. Chandorkar, D. M. Divan, and R. Adapa, "Control of parallel connected inverters in standalone ac supply systems," *IEEE Transactions on Industry Applications*, vol. 29, no. 1, pp. 136–143, 1993.

[23] C. K. Sao and P. W. Lehn, "Autonomous load sharing of voltage source converters," *IEEE Transactions on Power Delivery*, vol. 20, no. 2, pp. 1009–1016, 2005.

[24] J. M. Guerrero, J. C. Vasquez, J. Matas, M. Castilla, and L. G. de Vicuna, "Control strategy for flexible microgrid based on parallel line-interactive ups systems," *IEEE Transactions on industrial Electronics*, vol. 56, no. 3, pp. 726–736, 2009.

[25] A. Bidram and A. Davoudi, "Hierarchical structure of microgrids control system," *IEEE Transactions on Smart Grid*, vol. 3, no. 4, pp. 1963–1976, 2012.

[26] Y.-Y. Tzou, R.-S. Ou, S.-L. Jung, and M.-Y. Chang, "High-performance programmable ac power source with low harmonic distortion using dsp-based repetitive control technique," *IEEE Transactions on Power Electronics*, vol. 12, no. 4, pp. 715–725, 1997.

[27] C. Chiarelli, L. Malesani, S. Pirondini, and P. Tomasin, "Single-phase, three-level, constant frequency current hysteresis control for ups applications," in *Power Electronics and Applications, 1993., Fifth European Conference on.* IET, 1993, pp. 180–185.

[28] S. Buso, S. Fasolo, and P. Mattavelli, "Uninterruptible power supply multiloop control employing digital predictive voltage and current regulators," *IEEE Transactions on Industry Applications*, vol. 37, no. 6, pp. 1846–1854, 2001.

[29] N. M. Abdel-Rahim and J. E. Quaicoe, "Analysis and design of a multiple feedback loop control strategy for single-phase voltage-source ups inverters," *IEEE Transactions on power electronics*, vol. 11, no. 4, pp. 532–541, 1996.

[30] P. C. Loh, M. J. Newman, D. N. Zmood, and D. G. Holmes, "A comparative analysis of multiloop voltage regulation strategies for single and three-phase ups systems," *IEEE Transactions on Power Electronics*, vol. 18, no. 5, pp. 1176–1185, 2003.

[31] A. Paquette and D. Divan, "Transient droop for improved transient load sharing in microgrids," in *Energy Conversion Congress and Exposition (ECCE), 2014 IEEE.* IEEE, 2014, pp. 84–91.

[32] P. C. Loh and D. G. Holmes, “Analysis of multiloop control strategies for lc/-cl/lcl filtered voltage-source and current-source inverters,” *IEEE Transactions on Industry Applications*, vol. 41, no. 2, pp. 644–654, 2005.

[33] P. J. Hart, A. Nelson, R. Lasseter, and T. Jahns, “Effect of power measurement filter properties on certs microgrid control performance,” in *Power Electronics for Distributed Generation Systems (PEDG), 2015 IEEE 6th International Symposium on*. IEEE, 2015, pp. 1–8.

[34] A. Tavakoli, M. Negnevitsky, and K. M. Muttaqi, “A decentralized model predictive control for operation of multiple distributed generators in an islanded mode,” *IEEE Transactions on Industry Applications*, vol. 53, no. 2, pp. 1466–1475, 2017.

[35] T. Dragičević, “Model predictive control of power converters for robust and fast operation of ac microgrids,” *IEEE Transactions on Power Electronics*, vol. 33, no. 7, pp. 6304–6317, 2018.

[36] Q. Chen, Y. Li, and J. E. Seem, “Bumpless transfer-based inter-region controller switching of wind turbines for reducing power and load fluctuation,” *IEEE Transactions on Sustainable Energy*, vol. 7, no. 1, pp. 23–31, Jan 2016.

[37] J. Lin, Y. Sun, Y. Song, W. Gao, and P. Sorensen, “Wind power fluctuation smoothing controller based on risk assessment of grid frequency deviation in an isolated system,” *IEEE Transactions on Sustainable Energy*, vol. 4, no. 2, pp. 379–392, April 2013.

[38] N. Modi, R. Yan *et al.*, “Low inertia power systems: Frequency response challenges and a possible solution,” in *Power Engineering Conference (AUPEC), 2016 Australasian Universities*. IEEE, 2016, pp. 1–6.

[39] W. Du, Q. Jiang, M. J. Erickson, and R. H. Lasseter, “Voltage-source control of pv inverter in a certs microgrid,” *IEEE Transactions on Power Delivery*, vol. 29, no. 4, pp. 1726–1734, 2014.

[40] R. B. Godoy, D. B. Bizarro, E. T. de Andrade, J. de Oliveira Soares, P. E. M. J. Ribeiro, L. A. Carniato, M. L. Kimpara, J. O. Pinto, K. Al-Haddad, and C. A. Canesin, “Procedure to match the dynamic response of mppt and droop-controlled microinverters,” *IEEE Transactions on Industry Applications*, vol. 53, no. 3, pp. 2358–2368, 2017.

[41] J. Li, F. Li, X. Li, H. Liu, F. Chen, and B. Liu, “S-shaped droop control method with secondary frequency characteristics for inverters in microgrid,” *IET Generation, Transmission & Distribution*, vol. 10, no. 13, pp. 3385–3392, 2016.

[42] A. M. Egwebe, M. Fazeli, P. Igic, and P. M. Holland, "Implementation and stability study of dynamic droop in islanded microgrids," *IEEE Transactions on Energy Conversion*, vol. 31, no. 3, pp. 821–832, 2016.

[43] A. Elrayyah, Y. Sozer, and M. E. Elbuluk, "Modeling and control design of microgrid-connected pv-based sources," *IEEE Journal of Emerging and Selected Topics in Power Electronics*, vol. 2, no. 4, pp. 907–919, 2014.

[44] A. Elrayyah, Y. Sozer, and M. Elbuluk, "Microgrid-connected pv-based sources: a novel autonomous control method for maintaining maximum power," *IEEE Industry Applications Magazine*, vol. 21, no. 2, pp. 19–29, 2015.

[45] H. Liu, Y. Yang, X. Wang, P. C. Loh, F. Blaabjerg, W. Wang, and D. Xu, "An enhanced dual droop control scheme for resilient active power sharing among paralleled two-stage converters," *IEEE Transactions on Power Electronics*, vol. 32, no. 8, pp. 6091–6104, 2017.

[46] H. Nikkhajoei and R. H. Lasseter, "Distributed generation interface to the certs microgrid," *IEEE Transactions on Power Delivery*, vol. 24, no. 3, pp. 1598–1608, 2009.

[47] S. M. Lukic, S. G. Wirasingha, F. Rodriguez, J. Cao, and A. Emadi, "Power management of an ultracapacitor/battery hybrid energy storage system in an hev," in *Vehicle Power and Propulsion Conference, 2006. VPPC'06. IEEE.* IEEE, 2006, pp. 1–6.

[48] N. Hamsic, A. Schmelter, A. Mohd, E. Ortjohann, E. Schultze, A. Tuckey, and J. Zimmermann, "Increasing renewable energy penetration in isolated grids using a flywheel energy storage system," in *Power Engineering, Energy and Electrical Drives, 2007. POWERENG 2007. International Conference on.* IEEE, 2007, pp. 195–200.

[49] D. Wu, F. Tang, T. Dragicevic, J. C. Vasquez, and J. M. Guerrero, "A control architecture to coordinate renewable energy sources and energy storage systems in islanded microgrids," *IEEE Transactions on Smart Grid*, vol. 6, no. 3, pp. 1156–1166, 2015.

[50] Y. Karimi, H. Oraee, and J. M. Guerrero, "Decentralized method for load sharing and power management in a hybrid single/three-phase-islanded microgrid consisting of hybrid source pv/battery units," *IEEE Transactions on Power Electronics*, vol. 32, no. 8, pp. 6135–6144, 2017.

[51] H. Mahmood and J. Jiang, "Autonomous coordination of multiple pv/battery hybrid units in islanded microgrids," *IEEE Transactions on Smart Grid*, vol. 9, no. 6, pp. 6359–6368, 2018.

[52] ——, “Decentralized power management of multiple pv, battery, and droop units in an islanded microgrid,” *IEEE Transactions on Smart Grid*, 2017.

[53] P. Kundur, N. J. Balu, and M. G. Lauby, *Power system stability and control.* McGraw-hill New York, 1994, vol. 7.

[54] Q. Shafiee, J. M. Guerrero, and J. C. Vasquez, “Distributed Secondary Control for Islanded Microgrids A Novel Approach,” *IEEE Transactions on Power Electronics*, vol. 29, no. 2, pp. 1018–1031, Feb. 2014.

[55] M. C. Chandrokar, D. M. Divan, and B. Banerjee, “Control of distributed UPS systems,” in *Proceedings of 1994 Power Electronics Specialist Conference - PESC'94*, vol. 1, Jun. 1994, pp. 197–204 vol.1.

[56] R. Lasseter and P. Piagi, “Providing premium power through distributed resources,” in *Proceedings of the 33rd Annual Hawaii International Conference on System Sciences*, Jan 2000, pp. 9 pp.–.

[57] M. Velasco, P. MartAÂ, A. Camacho, J. Miret, and M. Castilla, “Synchronization of local integral controllers for frequency restoration in islanded microgrids,” in *IECON 2016 - 42nd Annual Conference of the IEEE Industrial Electronics Society*, Oct. 2016, pp. 3906–3911.

[58] J. W. Simpson-Porco, F. DArfler, and F. Bullo, “Synchronization and power sharing for droop-controlled inverters in islanded microgrids,” *Automatica*, vol. 49, no. 9, pp. 2603–2611, Sep. 2013. [Online]. Available: http://www.sciencedirect.com/science/article/pii/S0005109813002884

[59] J. W. Simpson-Porco, Q. Shafiee, F. DArfler, J. C. Vasquez, J. M. Guerrero, and F. Bullo, “Secondary frequency and voltage control of islanded microgrids via distributed averaging,” *IEEE Transactions on Industrial Electronics*, vol. 62, no. 11, pp. 7025–7038, Nov. 2015.

[60] F. Guo, C. Wen, J. Mao, and Y. Song, “Distributed Secondary Voltage and Frequency Restoration Control of Droop-Controlled Inverter-Based Microgrids,” *IEEE Transactions on Industrial Electronics*, vol. 62, no. 7, pp. 4355–4364, Jul. 2015.

[61] A. Pilloni, A. Pisano, and E. Usai, “Robust Finite-Time Frequency and Voltage Restoration of Inverter-Based Microgrids via Sliding-Mode Cooperative Control,” *IEEE Transactions on Industrial Electronics*, vol. 65, no. 1, pp. 907–917, Jan. 2018.

[62] J. M. Guerrero, L. G. De Vicuna, J. Matas, M. Castilla, and J. Miret, “Output impedance design of parallel-connected ups inverters with wireless load-sharing control,” *IEEE Transactions on industrial electronics*, vol. 52, no. 4, pp. 1126–1135, 2005.

[63] W. Yao, M. Chen, J. Matas, J. M. Guerrero, and Z.-M. Qian, "Design and analysis of the droop control method for parallel inverters considering the impact of the complex impedance on the power sharing," *IEEE Transactions on Industrial Electronics*, vol. 58, no. 2, pp. 576–588, 2011.

[64] H. Mahmood, D. Michaelson, and J. Jiang, "Accurate reactive power sharing in an islanded microgrid using adaptive virtual impedances," *IEEE Transactions on Power Electronics*, vol. 30, no. 3, pp. 1605–1617, 2015.

[65] M. M. A. Abdelaziz, "Effect of detailed reactive power limit modeling on islanded microgrid power flow analysis," *IEEE Transactions on Power Systems*, vol. 31, no. 2, pp. 1665–1666, 2016.

[66] A. Milczarek, M. Malinowski, and J. M. Guerrero, "Reactive Power Management in Islanded Microgrid:Proportional Power Sharing in Hierarchical Droop Control," *IEEE Transactions on Smart Grid*, vol. 6, no. 4, pp. 1631–1638, Jul. 2015.

[67] P. D. Reigosa, H. Wang, Y. Yang, and F. Blaabjerg, "Prediction of bond wire fatigue of igbts in a pv inverter under a long-term operation," *IEEE Transactions on Power Electronics*, vol. 31, no. 10, pp. 7171–7182, 2015.

[68] S. Peyghami, P. Davari, and F. Blaabjerg, "System-level reliability-oriented power sharing strategy for dc power systems," *IEEE Transactions on Industry Applications*, vol. 55, no. 5, pp. 4865–4875, 2019.

[69] A. Tuladhar, H. Jin, T. Unger, and K. Mauch, "Control of parallel inverters in distributed ac power systems with consideration of line impedance effect," *IEEE Transactions on Industry Applications*, vol. 36, no. 1, pp. 131–138, 2000.

[70] C.-T. Lee, C.-C. Chu, and P.-T. Cheng, "A new droop control method for the autonomous operation of distributed energy resource interface converters," *IEEE Transactions on Power Electronics*, vol. 28, no. 4, pp. 1980–1993, 2013.

[71] A. Haddadi, A. Shojaei, and B. Boulet, "Enabling high droop gain for improvement of reactive power sharing accuracy in an electronically-interfaced autonomous microgrid," in *2011 IEEE Energy Conversion Congress and Exposition*, Sep. 2011, pp. 673–679.

[72] L. Lu and C. Chu, "Autonomous power management and load sharing in isolated micro-grids by consensus-based droop control of power converters," in *2013 1st International Future Energy Electronics Conference (IFEEC)*, Nov. 2013, pp. 365–370.

[73] A. Tuladhar, Hua Jin, T. Unger, and K. Mauch, "Control of parallel inverters in distributed AC power systems with consideration of line impedance effect," *IEEE Transactions on Industry Applications*, vol. 36, no. 1, pp. 131–138, Jan. 2000.

[74] Q.-C. Zhong, “Robust droop controller for accurate proportional load sharing among inverters operated in parallel,” *IEEE Transactions on Industrial Electronics*, vol. 60, no. 4, pp. 1281–1290, 2013.

[75] L. Asiminoaei, R. Teodorescu, F. Blaabjerg, and U. Borup, “A digital controlled PV-inverter with grid impedance estimation for ENS detection,” *IEEE Transactions on Power Electronics*, vol. 20, no. 6, pp. 1480–1490, Nov. 2005.

[76] N. Ishigure, K. Matsui, and F. Ueda, “Development of an on-line impedance meter to measure the impedance of a distribution line,” in *ISIE 2001. 2001 IEEE International Symposium on Industrial Electronics Proceedings (Cat. No.01TH8570)*, vol. 1, Jun. 2001, pp. 549–554 vol.1.

[77] J. He, Y. W. Li, J. M. Guerrero, F. Blaabjerg, and J. C. Vasquez, “An islanding microgrid power sharing approach using enhanced virtual impedance control scheme,” *IEEE Trans. Power Electron*, vol. 28, no. 11, pp. 5272–5282, 2013.

[78] Y. Zhu, F. Zhuo, F. Wang, B. Liu, R. Gou, and Y. Zhao, “A Virtual Impedance Optimization Method for Reactive Power Sharing in Networked Microgrid,” *IEEE Transactions on Power Electronics*, vol. 31, no. 4, pp. 2890–2904, Apr. 2016.

[79] J. Schiffer, T. Seel, J. Raisch, and T. Sezi, “A consensus-based distributed voltage control for reactive power sharing in microgrids,” in *2014 European Control Conference (ECC)*, Jun. 2014, pp. 1299–1305.

[80] C. A. Macana and H. R. Pota, “Adaptive synchronous reference frame virtual impedance controller for accurate power sharing in islanded ac-microgrids: A faster alternative to the conventional droop control,” in *2017 IEEE Energy Conversion Congress and Exposition (ECCE)*, Oct. 2017, pp. 3728–3735.

[81] H. Zhang, S. Kim, Q. Sun, and J. Zhou, “Distributed Adaptive Virtual Impedance Control for Accurate Reactive Power Sharing Based on Consensus Control in Microgrids,” *IEEE Transactions on Smart Grid*, vol. 8, no. 4, pp. 1749–1761, Jul. 2017.

[82] R. Rahmani, M. Tayyebi, M. Majid, M. Hassan, and H. Rahman, “Designing dynamic controller and passive filter for a grid connected micro-turbine,” in *2011 IEEE Applied Power Electronics Colloquium (IAPEC)*. IEEE, 2011, pp. 165–169.

[83] M. Rezkallah, S. Singh, A. Chandra, B. Singh, M. Tremblay, M. Saad, and H. Geng, “Comprehensive controller implementation for wind-pv-diesel based standalone microgrid,” *IEEE Transactions on Industry Applications*, vol. 55, no. 5, pp. 5416–5428, 2019.

[84] A. Elmitwally and M. Rashed, “Flexible operation strategy for an isolated pv-diesel microgrid without energy storage,” *IEEE transactions on energy conversion*, vol. 26, no. 1, pp. 235–244, 2010.

[85] X. Li, Z. Li, L. Guo, J. Zhu, Y. Wang, and C. Wang, “Enhanced dynamic stability control for low-inertia hybrid ac/dc microgrid with distributed energy storage systems,” *IEEE Access*, vol. 7, pp. 91 234–91 242, 2019.

[86] G. R. Walker and P. C. Sernia, “Cascaded dc-dc converter connection of photovoltaic modules,” *IEEE transactions on power electronics*, vol. 19, no. 4, pp. 1130–1139, 2004.

[87] S. Masri and P. Chan, “Design and development of a dc-dc boost converter with constant output voltage,” in *Intelligent and Advanced Systems (ICIAS), 2010 International Conference on.* IEEE, 2010, pp. 1–4.

[88] H.-S. Kim and S.-K. Sul, “A Novel Filter Design for Output LC Filters of PWM Inverters,” *Journal of Power Electronics*, vol. 11, no. 1, pp. 74–81, 2011. [Online]. Available: http://www.koreascience.or.kr/article/JAKO201115037857700.page

[89] G. L. Calzo, A. Lidozzi, L. Solero, and F. Crescimbini, “LC filter design for on-grid and off-grid distributed generating units,” *IEEE Transactions on Industry Applications*, vol. 51, no. 2, pp. 1639–1650, Mar. 2015.

[90] A. Reznik, M. G. Simoes, A. Al-Durra, and S. M. Muyeen, “Lcl filter design and performance analysis for grid interconnected systems,” *IEEE Transactions on Industry Applications*, vol. 50, no. 2, pp. 1225–1232, Mar. 2014.

[91] M. J. Erickson, “Improved power control of inverter sources in mixed-source microgrids,” Ph.D. dissertation, The University of Wisconsin-Madison, 2012.

[92] G. L. Soloveichik, “Battery technologies for large-scale stationary energy storage,” *Annual review of chemical and biomolecular engineering*, vol. 2, pp. 503–527, 2011.

[93] D. G. Photovoltaics and E. Storage, “Ieee guide for optimizing the performance and life of lead-acid batteries in remote hybrid power systems,” 2008.

[94] R. H. Lasseter, “Extended certs microgrid,” in *2008 IEEE Power and Energy Society General Meeting - Conversion and Delivery of Electrical Energy in the 21st Century*, July 2008, pp. 1–5.

[95] J. Liu, Y. Miura, and T. Ise, “Comparison of dynamic characteristics between virtual synchronous generator and droop control in inverter-based distributed generators,” *IEEE Transactions on Power Electronics*, vol. 31, no. 5, pp. 3600–3611, 2015.

[96] M. A. De Brito, L. P. Sampaio, G. Luigi, G. A. e Melo, and C. A. Canesin, "Comparative analysis of mppt techniques for pv applications," in *Clean Electrical Power (ICCEP), 2011 International Conference on.* IEEE, 2011, pp. 99–104.

[97] R. A. Mastromauro, M. Liserre, and A. Dell'Aquila, "Control issues in single-stage photovoltaic systems: Mppt, current and voltage control," *IEEE Transactions on Industrial Informatics*, vol. 8, no. 2, pp. 241–254, 2012.

[98] H. Patel and V. Agarwal, "Maximum power point tracking scheme for pv systems operating under partially shaded conditions," *IEEE transactions on industrial electronics*, vol. 55, no. 4, pp. 1689–1698, 2008.

[99] J. Gosumbonggot, D.-D. Nguyen, and G. Fujita, "Partial shading and global maximum power point detections enhancing mppt for photovoltaic systems operated in shading condition," in *2018 53rd International Universities Power Engineering Conference (UPEC).* IEEE, 2018, pp. 1–6.

[100] Y. Wang, B. Ren, and Q.-C. Zhong, "Robust control of dc-dc boost converters for solar systems," in *2017 American Control Conference (ACC).* IEEE, 2017, pp. 5071–5076.

[101] S. Peyghami, Z. Wang, and F. Blaabjerg, "A guideline for reliability prediction in power electronic converters," *IEEE Transactions on Power Electronics*, 2020.

[102] Y. A. I. Mohamed and E. F. El-Saadany, "Adaptive Decentralized Droop Controller to Preserve Power Sharing Stability of Paralleled Inverters in Distributed Generation Microgrids," *IEEE Transactions on Power Electronics*, vol. 23, no. 6, pp. 2806–2816, Nov. 2008.

[103] N. Pogaku, M. Prodanovic, and T. C. Green, "Modeling, Analysis and Testing of Autonomous Operation of an Inverter-Based Microgrid," *IEEE Transactions on Power Electronics*, vol. 22, no. 2, pp. 613–625, Mar. 2007.

[104] P. Vorobev, P. Huang, M. A. Hosani, J. L. Kirtley, and K. Turitsyn, "High-Fidelity Model Order Reduction for Microgrids Stability Assessment," *IEEE Transactions on Power Systems*, vol. 33, no. 1, pp. 874–887, Jan. 2018.

[105] X. Guo, Z. Lu, B. Wang, X. Sun, L. Wang, and J. M. Guerrero, "Dynamic Phasors-Based Modeling and Stability Analysis of Droop-Controlled Inverters for Microgrid Applications," *IEEE Transactions on Smart Grid*, vol. 5, no. 6, pp. 2980–2987, Nov. 2014.

[106] W. Xiao, W. G. Dunford, P. R. Palmer, and A. Capel, "Regulation of photovoltaic voltage," *IEEE Transactions on Industrial Electronics*, vol. 54, no. 3, pp. 1365–1374, 2007.

[107] H. Wang, M. Liserre, F. Blaabjerg, P. de Place Rimmen, J. B. Jacobsen, T. Kvisgaard, and J. Landkildehus, "Transitioning to physics-of-failure as a reliability driver in power electronics," *IEEE Journal of Emerging and Selected Topics in Power Electronics*, vol. 2, no. 1, pp. 97–114, 2013.

[108] F. Blaabjerg, K. Ma, and D. Zhou, "Power electronics and reliability in renewable energy systems," in *2012 IEEE International Symposium on Industrial Electronics.* IEEE, 2012, pp. 19–30.

[109] R. Bayerer, T. Herrmann, T. Licht, J. Lutz, and M. Feller, "Model for power cycling lifetime of igbt modules-various factors influencing lifetime," in *5th International Conference on Integrated Power Electronics Systems.* VDE, 2008, pp. 1–6.

[110] P. Asimakopoulos, K. Papastergiou, T. Thiringer, M. Bongiorno, and G. Le Godec, "On v_{ce} method: In situ temperature estimation and aging detection of high-current IGBT modules used in magnet power supplies for particle accelerators," *IEEE Transactions on Industrial Electronics*, vol. 66, no. 1, pp. 551–560, 2018.

[111] M. Musallam and C. M. Johnson, "An efficient implementation of the rainflow counting algorithm for life consumption estimation," *IEEE Transactions on Reliability*, vol. 61, no. 4, pp. 978–986, 2012.